NASA Contractor Report 177626

IN-02
190830
130P

Aerodynamic Control of NASP-Type Vehicles Through Vortex Manipulation

Volume III

Wing Rock Experiments

Carlos J. Suárez, Brooke C. Smith, Brian R. Kramer, T. Terry Ng, Lih-Yenn Ong, and Gerald N. Malcolm

CONTRACT NAS2-13196
September 1993

National Aeronautics and
Space Administration

NASA Contractor Report 177626

Aerodynamic Control of NASP-Type Vehicles Through Vortex Manipulation

Volume III

Wing Rock Experiments

Carlos J. Suárez, Brooke C. Smith, Brian R. Kramer, T. Terry Ng, Lih-Yenn Ong, and Gerald N. Malcolm

Eidetics International, Inc.
3415 Lomita Blvd.
Torrance, CA 90505

Prepared for
Ames Research Center
CONTRACT NAS2-13196
September 1993

National Aeronautics and
Space Administration

Ames Research Center
Moffett Field, California 94035-1000

TABLE OF CONTENTS

NOMENCLATURE

Water Tunnel Test

A_{ref}	reference wing area
b	wing span
C_μ	momentum coefficient of blowing = $\dot{m}_j V_j / q A_{ref}$
C_n	yawing moment coefficient = $Y_M / q A_{ref} b$
f	wing rock frequency
k	reduced frequency = $\pi f b / V_\infty$
L	reference length = total length of the model
LF	left forebody vortex (from a pilot's view point)
LW	left wing vortex (from a pilot's view point)
$\dot{m}_j$	mass flow rate of the blowing jet
q	free-stream dynamic pressure
RF	right forebody vortex
RW	right wing vortex
t^*	convective time = $t V_\infty / L$
V_∞	free-stream velocity
V_j	average exit velocity of the blowing jet
α, AOA	angle of attack
Φ	azimuth angle (from the windward meridian)
ϕ	roll angle
YM	yawing moment

Wind Tunnel Test

Cl	rolling moment coefficient = $RM / q A_{ref} b$
Cl(b)	body axis rolling moment coefficient
Cn(b)	body axis yawing moment coefficient
CN	body axis normal force coefficient
CY	body axis side force coefficient
Cp	pressure coefficient
ΔCp	difference between Cp on the left and right wings
β	sideslip angle
RM	rolling moment
Ixx	moment of inertia
L/R60	blowing on the left /right side with a reservoir pressure of 60 psi
B60	blowing on both sides with a reservoir pressure of 60 psi
Phi dot	first derivative of roll angle with respect to time (angular velocity)
Phi ddot	second derivative of roll angle with respect to time (angular acceleration)

LIST OF FIGURES

Page

Water Tunnel Test

Wind Tunnel Test

SUMMARY

Free-to-roll tests were conducted in a water tunnel and in a wind tunnel in an effort to investigate in detail the mechanisms of wing rock on a NASP-type vehicle. The configuration tested consisted of a highly-slender forebody and a 78° swept delta wing. In the water tunnel, extensive flow visualization was performed and roll angle histories were obtained. The fluid mechanisms governing the wing rock motion of this configuration were identified. Different means of suppressing wing rock by controlling the forebody vortices using small blowing jets were also explored. Steady blowing was found to be capable of suppressing wing rock, but significant vortex asymmetries had to be induced at the same time. On the other hand, alternating pulsed blowing on the left and right sides of the forebody was demonstrated to be a potentially effective means of suppressing wing rock and eliminating large asymmetric moments at high angles of attack. In the wind tunnel test, the roll angle, forces and moments, and limited forebody and wing surface pressures were measured during the wing rock motion. A limit cycle oscillation was observed for angles of attack between 22° and 30°. The amplitude of the motion was smaller for the tail off configuration, denoting a strong interaction between the forebody vortices and the vertical tail. In general, the wind tunnel test confirmed that the main flow phenomena responsible for the wing-body-tail wing rock are the interactions between the forebody and the wing vortices. The variation of roll acceleration (determined from the second derivative of the roll angle time history) with roll angle clearly showed the energy balance necessary to sustain the limit cycle oscillation. Various blowing techniques were also evaluated in this test as means of wing rock suppression. Blowing tangentially aft from leeward side nozzles near the forebody tip can damp the roll motion at low blowing rates and stop it completely at higher blowing rates. At the high rates, the disadvantages of aft blowing as a wing rock control method observed in the water tunnel were confirmed in this test, i.e., significant vortex asymmetries are created, causing the model to stop at a non-zero roll angle. Forward blowing and alternating pulsed blowing appear to be more efficient techniques for suppressing wing rock, in the sense that the motion can be damped at lower blowing rates and, apparently, without large asymmetries as denoted by the roll angle at which the model stops. In general, good agreement is observed between the results of the water tunnel and wind tunnel tests.

AERODYNAMIC CONTROL OF NASP-TYPE VEHICLES THROUGH VORTEX MANIPULATION

VOLUME III: WING ROCK EXPERIMENTS

1.0 INTRODUCTION

Modern fighter aircraft are operating in a flight regime that requires maximum maneuverability and controllability to be effective in the combat arena. One of the limitations to combat effectiveness for all fighter aircraft is the phenomenon of wing rock -- a moderate to high angle-of-attack dynamic motion manifested primarily in a limit-cycle oscillation in roll with, in some cases, a coupled oscillation in yaw. Generally, the onset of wing rock is attributed to a loss of stability in the lateral/ directional mode. Wing rock is also a phenomenon experienced by configurations with highly-swept wings at moderate angles of attack. Configurations considered for supersonic to hypersonic speeds, such as NASP, may be susceptible to wing rock problems at low speeds and the moderate and high angles of attack associated with take off and landing.

The aerodynamics of wing rock have been studied extensively; however, this event is not thoroughly understood. On a modern fighter configuration, wing rock can simultaneously involve many different aerodynamic phenomena. On straight or moderately swept wings, the flow mechanism causing wing rock is closely related to dynamic stall[1]. During the wing rock motion, the left and right wings experience alternatively aerodynamic phenomena that are akin to the up and down pitching phases of a dynamic stall. On highly-swept delta wings, the susceptibility to wing rock is determined by the vortex interaction as dictated by the strength and proximity of the leading edge vortices. While vortex characteristics such as vortex liftoff and breakdown can significantly affect the intensity of wing rock, their existence is not necessary for sustaining wing rock. Results from different studies (e.g., Ref. 2) have shown that the time-lag associated with vortex strength or position alone is sufficient to sustain wing rock.

At high angles of attack, the vortices emanating from the forebody of an aircraft can be very strong. Studies[3,4] have shown that these vortices are primarily responsible for wing rock in this flight regime. While this form of wing rock is undoubtedly configuration dependent, it is generally believed that interactions between asymmetric forebody vortices and the other surfaces on the aircraft at sideslip conditions are the main mechanisms that drive the motion. If an aircraft is perturbed when flying at a high angle of attack and begins to roll, a sideslip is induced. Depending on the forebody geometry, significant asymmetries can be induced in the forebody vortices even at relatively small sideslip angles. These asymmetric vortices then act on surfaces such as the wings and the tails to produce a rolling moment. The variation of the vortex asymmetry induced by the aircraft motion eventually produces a restoring rolling moment, thereby leading to limit-cycle wing rock. The results of Ref. 3 on a generic fighter show that the forebody shapes that provide the highest levels of static stability may also cause the highest susceptibility to wing rock and vice versa. Once the rocking motion is initiated, dynamic flow phenomena over the moderately-swept wings and highly-swept LEX's may also contribute to the building-up of wing rock.

Attempts have been made in recent years on specific aircraft configurations[5,6] using a variety of both controls-oriented and aerodynamic fixes to cure wing-rock problems. For instance, the wind tunnel and drop-test results in Ref. 7 indicate that the X-29A aircraft exhibits negative roll damping at angles of attack above about 18°. A conventional roll damper can eliminate wing rock below about $\alpha = 35°$, but is ineffective at higher angles of attack where wing rock is induced by forebody vortices. The loss of effectiveness of a conventional roll damper at high angle of attack is likely to be common for many modern fighters and can severely limit aircraft capabilities in a rather critical flight regime. Even if the conventional control surfaces, such as the aileron and rudder, can effectively control wing rock, the level of control power remaining for maneuvering may be insufficient to meet the high-angle-of-attack maneuverability requirements. On the configuration investigated in this report, representative of a supersonic or hypersonic transport such as NASP, the reduction of the vertical tail might be desirable to reduce weight and drag and to improve high-speed performance. An alternative source for roll stability control would help to solve the wing rock problem.

The powerful forebody vortices are one of the main causes of aircraft instabilities at high angles of attack. An effective means of suppressing the instabilities in this flight regime is therefore to directly control these vortices. Recent research efforts on fighter-type aircraft indicated that some of the most promising methods for Forebody Vortex Control (FVC) are movable forebody strakes[8], rotatable nose-tip[9] and nose-boom devices[10], and blowing on the forebody surface. Two main forms of blowing have been studied: (1) blowing from a localized jet[8,11,12] and (2) blowing from a tangential slot[12-14]. In either form, blowing was found to be highly effective in controlling the vortex orientation. The Phase I technical results of this research program (Ref. 15) showed that it is potentially feasible to utilize vortex manipulation with blowing to provide the necessary control forces for a NASP-type configuration at low speeds.

Up to now, however, most of the studies of FVC have concentrated on directional control. In situations where wing rock is induced by the forebody vortices, FVC obviously would have an impact on the wing rock motion. The basic idea behind the present study was not only to study the mechanism of wing rock in detail, but to determine if blowing can be used as a practical method for suppressing the wing rock motion as well. The experiments were intended to reveal if controlling the vortex asymmetries during wing rock can induce sufficiently strong roll damping so that the limit-cycle motion can be suppressed, and to identify an effective means of control.

Tests were performed both in a water tunnel and in a wind tunnel on a model of a generic NASP-type configuration. The model possesses characteristics that may be considered as similar to certain forebody/leading edge extension (LEX) and missile forebody/canard combinations. It is important to note that at the time the research contract with NASA was awarded, there was no specific design for the NASP yet selected. The models used in the preceding SBIR Phase I study and in this investigation (SBIR Phase II Contract) are based on drawings of a generic, preliminary NASP configuration provided by the duPont Aerospace Co., Inc. The configuration that now appears from the consolidated NASP design team, however, is significantly different. Even though it still has highly-swept wings, the fuselage has a blunt forebody, so the lateral/directional stability problems will be different. This by no means diminishes the value of this research program; the general results obtained in this study can be applied to similar configurations, such as the High Speed Civil Transport (HSCT) or any other supersonic/hypersonic advanced configuration. Despite the dissimilarity between the current NASP and the configurations used in this investigation, the models will still be referred to as NASP-type configurations.

This SBIR Phase II research effort includes static and dynamic (free-to-roll) experiments. Water tunnel and wind tunnel static tests are discussed in Volumes I and II, respectively. It is the intention of this report (Volume III of a Final Report) to summarize the results of the wing rock experiments performed first in the Eidetics water tunnel and later in the NASA Ames Research Center 7 x 10 ft wind tunnel.

2.0 WATER TUNNEL TEST

2.1 Technical Objectives

The specific objectives of the water tunnel test were:

1. Investigate possible causes of wing rock on this highly-slender forebody-wing configuration.

2. Study the vortex flows over the wing and forebody during wing rock.

3. Explore the effectiveness of forebody vortex control in the form of blowing jets operating near the forebody tip in controlling the wing rock of this configuration.

A detailed flow visualization of phenomena related to the causes of wing rock was obtained in the water tunnel tests. The roll angle history was obtained from the video-taped data. The method of FVC used in this study was blowing from small jets near the tip of the forebody. Two methods of blowing were investigated: (1) steady blowing and (2) alternating pulsed blowing from both sides of the forebody.

2.2 Experimental Setup

The experiment was conducted in the Eidetics 2436 Flow Visualization Water Tunnel. The facility is a continuous flow tunnel with a horizontal test section 0.91 m high x 0.61 m wide x 1.83 m long (36" x 24" x 72"). The test section is a channel constructed of tempered glass that allows both side and planform views. In addition, a downstream transverse window provides an upstream end view. The tunnel speed can be varied from 0 to 30 cm/sec. Most of the tests were conducted at a flow speed of about 20.3 cm/sec (8 in/sec). A pressurized dye-injection system was used for flow visualization. Dye patterns created by the model flow field were recorded using both a 35-mm camera and a 3/4-in. video tape recorder. The vortex flow was visualized using either regular flood-light or a laser sheet. Selected video recordings were digitized using a video digitizer, and the resulting images were enhanced and analyzed on a Macintosh computer.

A sketch of the model is shown in Fig. 1. The forebody of the model has a length-to-base-diameter ratio of 6, and was circular in cross-section with a projected side-profile as shown which resulted in a nominal apex angle of about 18.5°. The tip of the model was rounded off slightly. The wings were sharp-edge delta wings with a 78° sweep. Tests were conducted on the model with no vertical tail, or with one of the two different tails shown in Fig. 1. Blowing ports were located near the tip of the forebody 1.9 cm (0.75 in) from the apex, with the 0.76 mm (0.03 in) diameter nozzles pointing directly aft along the $\Phi = \pm 150°$ meridians. The blowing fluid was supplied by a pressurized canister and metered by a rotometer. Blowing on the left and right sides were turned on or off by fast-acting solenoid valves. Indicator lights of different colors, positioned to appear in the video recording, were used to indicate when the left and/or right blowings were on. For the pulsed blowing, the steady blowing rate was set initially with the valve opened. Dye ports were located along the windward sides of the forebody and the wings.

Two bearings spanned on a mounting bracket along the centerline of the fuselage allow a single degree-of-freedom, "free-to-roll" motion about the body axis. The model was balanced so that its center of gravity aligned closely with the roll axis. The roll angle was indicated by markings at the tail end of the model and a pointer on the support sting. Close-up video recordings of the tail end during wing rock allowed the roll angle history to be obtained in subsequent data processing.

The free-to-roll experiments were conducted at angles of attack from 0° to 30°. Additional tests at higher angles of attack were conducted for specific configurations. All the free-to-roll tests were started with the model being released from near the zero-roll position. The time history of roll motion and flow behaviors were recorded on video tapes. Blowing was initiated after the model had either reached an equilibrium steady position or a limit cycle wing rock motion, and the subsequent motions were recorded.

3.0 WATER TUNNEL TEST RESULTS AND DISCUSSION

3.1 Roll Angle History

Tests were performed with the model mounted on the free-to-roll bracket to investigate the effect of releasing the constraint on the roll axis. Three model configurations were tested: the model with no vertical tail (Model O), with tail A (Model A), and with tail B (Model B). A roll angle that results in a clock-wise motion with a right-wing-down attitude is designated as positive; a left-wing-down attitude is negative.

Figures 2a - 2d show the roll angle history at different angles of attack for Model O. The result at $\alpha = 20°$ is shown in Fig. 2a. For α's below 23°, the model will roll to a certain negative (left-wing-down) roll angle when released from rest. However, no wing rock was observed. Therefore, the natural flow/model asymmetry causes the model to roll to a negative roll position that is both statically and dynamically stable in roll. Above $\alpha = 23°$, as shown by the results of $\alpha = 24°$, 25° and 29° in Figs. 2b, 2c and 2d, respectively, a limit-cycle wing rock occurs with the amplitude increasing with the angle of attack. Beyond the angle of attack range where wing rock initially occurs, the model oscillates in a relatively regular frequency about a negative mean roll position. The time required to establish a limit-cycle wing-rock motion decreases with angle of attack - an indication of a reduction in roll damping. At higher angles of attack, the limit cycle behavior is usually established within about one cycle of motion. The roll angle history results of Models A and B are qualitatively similar to those of Model O, as seen in Figs. 3 and 4, respectively.

3.2 Contributions of Model Components to Wing Rock

It is of interest to determine the roles of various components in the wing-rock motion of this model. Figure 5 shows the peak-to-peak wing rock amplitudes for the three models as a function of angle of attack. As demonstrated in Fig. 5, the presence of a vertical tail delays the onset and reduces the amplitude of wing rock. One of the principle effects of the vertical tail is therefore to provide additional roll damping. The results, however, also show that a larger tail (tail B) can result in less overall roll damping than a smaller one (tail A). This suggests that interaction between the tail surface and the flow around other parts of the model can be an important factor to wing rock. Nevertheless, the results indicate that the net effect of a vertical tail is to increase roll damping. Figure 6 shows the reduced frequency as a function of the angle of attack. Below α of about 28° the presence of a vertical tail increases the wing rock frequency, indicating an increase in the static lateral stability. Above α of about 28°, effects of the tail on the amplitude and frequency are reduced significantly, probably a result of the tail being enveloped in the wake of the wing and fuselage.

Tests were performed with the forebody removed and the fuselage operating in a flow-through mode to study the role of the wings in wing rock. Flow visualization did not reveal any strong direct effects on the wing vortices due to the removal of the forebody. Obviously, the interaction between the forebody and wing vortices at higher angles of attack is absent. At conditions where the forebody vortices are strongly asymmetric, such as the case of $\alpha = 30°$, interaction between the vortices causes vortex breakdown to occur over only one of the wings as described earlier. Removal of the forebody, on the other hand, results in vortex breakdown over both wings. Thus, one effect of the interaction between the forebody and wing vortices is to delay vortex breakdown over one wing.

Without the forebody, no wing rock was observed over the range of angles of attack tested (up to 50°). Any roll motion induced by random disturbances was readily damped out. Thus, in the absence of the forebody, the wing flow alone is not capable of establishing a limit-cycle wing-rock motion. In comparison, a pure delta wing with the same sweep (i.e., without a fuselage component) can be expected to wing rock for an angle of attack range from about 24° to 50°.

Since the forebody and fuselage are circular in cross-section, the asymmetry in surface pressure cannot induce a roll moment about the centrally located roll axis on the body alone. Thus, except for possibly a small effect from the skin friction, the above results suggested that wing rock of this configuration was induced by interactions between the forebody vortices and the wing or tail surfaces of the model. To understand the process more thoroughly, flow visualization was used to study the vortex flow in detail.

Figure 7 shows an example of the off-surface flow over Model A during wing rock at $\alpha = 29°$. Through the wing rock cycle, the forebody vortices lift off alternatively from the body surface. A strong convective time-lag was observed with the vortex lift-off. Strong interactions between the forebody and the wing vortices can also be observed, especially towards the trailing half of the wings. Due to the natural forebody flow asymmetry, the main interactions are concentrated over the right wing with the rear portion of the wing vortex being lifted farther from the wing surface. Selected photos in Fig. 8 complement the digitized images and show the vortex interactions in more detail.

Figure 9 shows the laser sheet visualization results at model Station B during wing rock at $\alpha = 29°$. At this station, there is very little direct interaction between the forebody and wing vortices. The left and right forebody vortices lift alternatively from the surface during the wing rock motion. On the other hand, positions of the left and right wing vortices relative to the respective wings do not change significantly. There is an absence of the distinct vortex lift-off behavior commonly observed on highly-swept flat plate delta wings during wing rock (e.g., Ref. 2). These vortex flow behaviors persist until farther downstream where the forebody vortex asymmetry develops sufficiently for the forebody vortices to interact directly with the wing vortices, such as the case at Station C.

Figure 10 shows the laser sheet visualization results at model station C during one cycle of wing rock motion at $\alpha = 29°$. At $t^* = 0$ (arbitrary starting time), the wing vortices are approximately symmetric at this station while the forebody vortices are highly asymmetric with the right vortex at a high position. At $t^* = 0.29$, vortex breakdown propagates upstream of the left wing trailing edge and crosses Station C. A negative rolling motion is generated, causing the model to roll in a counter clockwise direction. During this phase of the model motion, the right forebody vortex moves continuously towards the surface. Contrary to what may be expected for pure delta wings, at $t^* = 0.60$ vortex breakdown over the left and thus windward wing moves downstream of the trailing edge. This breakdown behavior is apparently a result of the interaction between the forebody and wing vortices. At $t^* > 0.60$, the left forebody vortex begins to lift farther off the surface than the right vortex. At $t^* = 0.77$, the forebody vortices become highly asymmetric with the left forebody vortex at a position far from the surface. Vortex breakdown briefly moves upstream of the trailing edge of the right wing but does not seem to have significant effects on the roll motion. The model continues to roll in the counter clockwise direction until $t^* = 1.14$. At this t^*, the right forebody vortex begins to move underneath the right wing vortex and the right wing vortex begins to lift off the surface. The processes continue, and at $t^* = 1.28$ the left vortex begins to move towards the right wing. From $t^* = 1.32$ to 1.36, both forebody vortices are residing over the right wing. Correspondingly, the right wing vortex is lifted farther from the wing surface. During the sequence of events from $t^* = 1.14$ to 1.46, a positive rolling moment is produced to eventually induce a positive (clockwise) rolling motion. Note that a clockwise rolling moment is generated when the forebody vortices are both residing over the right wing. Therefore, the rolling moment that may have been generated by these vortices acting on the right wing is apparently small compared with that generated by the wing vortices. As the positive roll motion progresses, the forebody vortices move to the left with the right forebody vortex continuing to lift from the surface at the same time. At $t^* = 1.76$, one cycle of wing rock motion is approximately completed.

Thus, flow visualization reveals that a combination of the breakdown of the left wing vortex and the lift-off of the right wing vortex is sustaining the wing rock motion. As indicated by both the static and dynamic results, interactions between the forebody and wing vortices are the primary mechanism that drives this process. Even though the wing vortices seem to provide the necessary rolling moments for wing rock, the behavior of the wing vortices and their relationship to the wing motion is controlled mainly by the behavior of the forebody vortices.

3.3 Control of Wing Rock by Forebody Blowing

Since the forebody vortices are controlling the wing rock of this configuration, a means of suppressing the wing rock motion is to directly control the forebody vortices. Two methods of control were investigated: steady and alternating forebody jet blowing. Examples of the results are shown below.

3.3.1 Steady Blowing

Figure 11 shows the effect of blowing on the roll angle history of Model O. At $\alpha = 20°$, shown in Fig. 11a, blowing on the left side causes the model to roll from the naturally negative roll position to a positive roll position. At this condition, wing rock does not occur with or without blowing. The cases of $\alpha = 24°$, 25° and 29° in Figs. 11b, c and d, respectively, show the condition where wing rock occurs naturally without blowing. Under this condition, the wing rock motion can be damped within about one cycle of motion by steady blowing on either side of the forebody. The blowing has to be above a certain blowing rate that is dependent on the angle of attack and natural flow asymmetry. However, it is not possible to suppress wing rock while maintaining a zero-roll position. Blowing on the left side forces the left forebody vortex to be closer to the fuselage and wing on that side, creating a higher suction over the left wing and causing the model roll to the right to a new orientation where the rolling moment is zero. Results for Models A and B, are similar to those of Model O, as seen in Fig. 12 for $\alpha = 29°$.

Flow visualization results shown in Fig. 13 reveal that steady blowing on either side of the forebody suppresses wing rock by "locking" the forebody vortex asymmetry into a pattern that prevents the forebody vortices from freely interacting with the wing vortices. In addition to the non-zero roll angle, an adverse yawing moment will most likely result from the highly asymmetric forebody vortex pattern. These side effects may make this means of control undesirable, because some other means, perhaps conventional control surfaces, would have to be employed to bring the wings level.

An attempt was made to eliminate the vortex asymmetry while simultaneously suppressing wing rock by blowing on both sides of the forebody. In this experiment, blowing on one side was fixed initially at a rate that would suppress wing rock. After steady state was reached for the blowing condition, blowing on the other side was turned on. The model motion and vortex flow were observed and, at selected conditions, the roll angle history was determined. Examples of roll angle history of the cases of fixing the blowing rate on the left side and varying the blowing on the right are shown in Figs. 14 and 15.

In Fig. 14, the left blowing is fixed at $C_\mu = 0.27 \times 10^{-3}$ - a rate that is just sufficient to suppress wing rock with left blowing alone. Increasing the right blowing from $C_\mu = 0$ to 0.02×10^{-3} causes the model to roll initially in the negative direction, but the effect diminishes and the steady-state model behavior is essentially the same as left blowing alone. Increasing the right blowing to $C_\mu = 0.2 \times 10^{-3}$ again causes the model to roll initially in the negative direction. However, a wing rock motion with a bias towards negative roll is eventually established. The peak-to-peak wing-rock amplitude is about 22°, compared with 35° for the no-blowing case. At a right-blowing rate of $C_\mu = 0.27 \times 10^{-3}$, the model rolls initially to a negative angle of about 20°. Eventually, the model reaches a steady-state roll angle of -10° after a relatively long transient period. The behaviors with right-side blowing rates of $C_\mu = 0.46 \times 10^{-3}$ and 0.77×10^{-3} are essentially the same, except that the transient period decreases and the magnitude of the steady-state roll angle increases with increasing blowing.

In Fig. 15, the left blowing is fixed at $C_\mu = 0.46 \times 10^{-3}$ - a rate that is higher than needed to suppress wing rock. Increasing the right blowing from $C_\mu = 0$ to 0.27×10^{-3} has no effect on the roll angle. At a right blowing rate of $C_\mu = 0.46 \times 10^{-3}$, the model rolls in the negative direction upon turning on the blowing and eventually reaches a steady-state negative roll angle. The behavior at a right-side blowing C_μ of 0.77×10^{-3} is similar.

The simultaneous steady blowing results show that the configuration becomes unstable in roll and starts to rock when the blowing rates on the two sides are adjusted to maintain a near symmetric forebody vortex pattern. That is, without creating a sufficiently large forebody vortex asymmetry that minimizes interactions between the forebody and wing vortices, wing rock will persist. One of the reasons for this behavior is revealed by the flow visualization of the static model (see Volume I of this report). When the forebody flow is forced by blowing to become almost symmetric at high angles of attack, a strong interaction between the forebody and wing vortices occurs. This vortex interaction, as has been demonstrated, is the mechanism responsible for wing rock of this model. Thus, using steady blowing to suppress wing rock but without creating a large forebody vortex asymmetry may not be feasible for this configuration.

3.3.2 Alternating Pulsed Blowing

Since steady blowing cannot be used to achieve wing rock suppression without potentially undesirable aerodynamic side effects, another means of control based on pulsed blowing was attempted. Blowing on the left and right sides was alternatively switched on and off. There were two main limitations with the present experimental setup. First, the square-wave depiction is a highly idealized representation of the actual situation. Even though the solenoid valves are relatively fast-acting, there are always transient lags associated with turning on and off the blowing. Second, the present experimental set-up allowed only manual control of the solenoid valves and the actual pulsing rate was determined afterward from the video recording based on the indicator lights. Even though the pulsing rates in most cases turned out to be surprisingly steady and controlled, the scheme did not allow very fine control of the rate. Nevertheless, the results do demonstrate (at least qualitatively) the potential of such a control scheme.

At slow alternating rates, the blowing does not have significant effects on wing rock. The wing rock amplitude begins to decrease when the rate is increased. The trend continues and at sufficiently high alternating rates (in this case, approximately 8 pulses per wing rock cycle, or every 0.25 t^*), wing rock is completely suppressed. Figure 16 shows an example of the off-surface flow visualization results of blowing at such an alternating rate. In the flow visualization the vortices show a wavy pattern, likely due to the convective time lag associated with pulsed blowing on both sides. Most importantly, as opposed to steady blowing at the same peak rates either individually or simultaneously on the left and right sides, a zero-roll position is maintained while at the same time wing rock is suppressed.

Results of laser sheet visualization at Stations B and C of Model A, at $\alpha = 29°$ and pulsing the blowing at a frequency that appears to be the most efficient for suppressing the motion, are shown in Fig. 17. At Station B, the forebody vortices oscillate between two asymmetric patterns with smaller degrees of asymmetry than the case without blowing. There is no direct interaction between the forebody and wing vortices just as in the case without blowing. Thus, the effect of alternating pulsed blowing has relatively minor effects on the vortex behaviors at this station. In comparison, at Station C where, without blowing, the forebody vortices interact strongly with the wing vortices, the blowing has much stronger effects on the flow. The forebody vortices again oscillate between two asymmetric patterns with smaller degrees of asymmetry than the case without blowing. The forebody vortex asymmetry never develops sufficiently to result in strong interactions with the wing vortices.

Therefore, the mechanism responsible for the wing rock of this configuration is suppressed.

Thus, the source of wing rock for this configuration is eliminated while at the same time maintaining a zero-roll attitude by alternating pulsed blowing on the left and right sides. The forebody vortex flow can be considered to be symmetric on a time-averaged basis. In addition, the natural vortex asymmetric at any given instant is significantly reduced. At sufficiently high pulsing rates, another potential benefit of this control scheme can be the alleviation of asymmetric yawing moments at high angles of attack.

4.0 WIND TUNNEL TEST

4.1 Technical Objectives

Following the water tunnel tests, this configuration was also tested in the wind tunnel to investigate the expected wing rock characteristics and to evaluate the potential of blowing as a method for controlling wing rock.

The specific objectives of the wind tunnel test were:

1. Measure the roll-oscillation amplitude and frequency over an angle of attack range from 0° to 30°.

2. Measure surface pressures during the wing rock motion. Endevco dynamic pressure transducers were utilized on the wing and a PSI pressure system was used to measure static pressures at selected locations on the forebody.

3. Perform limited force and moment measurements.

4. Evaluate different blowing techniques as means of wing rock suppression.

4.2 Experimental Setup

The experiments were conducted in the NASA Ames 7 x 10 Foot Wind Tunnel. It is a closed-throat, single return atmospheric tunnel with about 10% air exchange accomplished by means of a ventilating tower. The tunnel is powered by a single 8-blade, 8.5 m (28 ft) diameter fan driven by a 1600 HP synchronous motor located in the nacelle in the return passage.

The model used in this test (which was twice the scale of the water tunnel model), can be seen in Figs. 18 and 19. Two low-friction bearings (Fig. 19a) allow the model to rotate "freely" around its longitudinal axis. A rotational transducer is used to measure the roll angle history and mechanical stops prevent the model from rolling a complete turn. An electro-magnetic brake was used to release the model from the static position, and later to stop the wing rock motion. Two basic configurations were tested: tail on and tail off. Each configuration is statically mass-balanced in roll by means of lead weights bolted to the top stringers.

The forebody of the model is provided with three rings of static pressure ports at F.S. 7.6 cm, 20.3 cm and 47 cm (3", 8" and 18.5"). The first two stations have 20 static pressure ports each, while the last station has 8 ports on the leeward side. A PSI system (electronic pressure scanner) was used to monitor the surface pressures at each of the ports during the wing rock motion. Endevco dynamic pressure transducers, located on each wing at 93 cm and 118.4 cm (36.6" and 46.6") from the tip, provided wing pressure data. A 6-component sting balance was utilized to acquire force data.

The blowing ports are located at F.S. 3.2 cm (1.25") and at $\Phi = 150°$ radially, as seen in Fig. 19b. Two different blowing schemes were tested: aft blowing and forward blowing. The blowing was controlled by two fast-acting solenoid valves (Fig. 19c). The total pressure and temperature in a chamber very close to each of the nozzle exits were measured to determine the mass flow rate and the blowing coefficient $C\mu$. The interference of the blowing lines with the wing rock motion was minimized by leaving a large service loop behind the model.

Even though the static tests on this configuration were performed earlier at a dynamic pressure $q = 1915$ Pa (40 psf), most of the wing rock experiments were conducted at a dynamic pressure range from 718 Pa (15 psf) to 1436 Pa (30 psf) to avoid exciting the resonance frequency of the model/balance/sting system (7.9 Hz). This dynamic pressure range corresponds to free stream velocities between 35 m/sec and 48.5 m/sec, and Reynolds numbers from 280,000 to 400,000 based on the body diameter. The test was performed for an angle of attack range from 0° to 30° and for a sideslip angle range from -10° to 10°. The model is sting mounted in the center of the test section with the wings in the vertical plane (Fig. 19d).

5.0 WIND TUNNEL TEST RESULTS AND DISCUSSION

5.1 Roll Angle History

The angular displacement transducer was used to measure the roll angle during the wing rock motion at different angles of attack. Data were acquired during 3 seconds at 200 samples/second/channel, providing an accurate roll angle history. Data were also taken with an OscilloGraph Recorder (OGR) for longer periods of time to investigate wing rock build-up and wing rock suppression by blowing.

5.1.1 Tail On Configuration

Data from OGR strips for the wing rock motion at different angles of attack at $q = 958$ Pa are presented in Fig. 20. In this graph, time $t = 0$ corresponds to the release of the brake, illustrating the complete wing rock build-up. The wing rock behavior is established within the first cycle, but it takes 4 or 5 cycles, or approximately 1.5 seconds, for the motion to reach its maximum amplitude.

Detailed roll angle histories at various angles of attack are shown in Figs. 21, 22 and 23 for different dynamic pressures: 718 Pa, 958 Pa and 1436 Pa (15 psf, 20 psf and 30 psf), respectively. Time $t = 0$ on these graphs does not correspond to the release of the brake. The roll angle, forces and pressures were measured for three seconds after the wing rock motion was well established. In general, the wing rock motion starts at $\alpha = 22^\circ$; for angles of attack below 22°, the model either rolls to a position that is statically and dynamically stable, or experiences a very irregular motion. A multi-exposure photo (Fig. 24) illustrates the limit cycle motion at $\alpha = 30^\circ$.

Figure 25 shows a comparison between the maximum peak-to-peak amplitude for the runs at different dynamic pressures. The curves for the two low dynamic pressures present similar trends, even though the amplitude of the oscillations is smaller and the wing rock motion appears to start later at the lowest q. Both curves show a maximum peak-to-peak amplitude at $\alpha = 28^\circ$ (74° and 84°, for $q = 718$ Pa and 958 Pa, respectively). At $q = 1436$ Pa, trends are similar up to $\alpha = 25^\circ$, but noticeable differences appear at higher angles of attack. The maximum amplitude at this condition occurs earlier, at $\alpha = 26^\circ$, and that is followed by a dramatic decrease in the wing rock amplitude, especially at $\alpha = 30^\circ$. Differences may be attributed to the fact that the model was vibrating significantly at this higher dynamic pressure. These vibrations can strongly influence the vortex flow field and the vortex interactions, which are principally responsible for the wing rock motion.

In general, the frequency of wing rock increases with angle of attack (from 2 Hz to 3 Hz between $\alpha = 20^\circ$ and 30° at $q = 958$ Pa), as seen in Fig. 26a. The roll motion equation:

$$[(Ixx)\ (\ddot{\phi}) = RM = (Cl)\ (q)\ (Aref)\ (b)],$$

with $\ddot{\phi}$ being proportional to f^2, would indicate that, if Cl were the same at the different q levels, then the wing rock frequency f would be proportional to the free stream velocity V_∞. Figure 26b (cross-plot of the data shown in Fig. 26a) reveals slight non-linearities for some angles of attack (between 24° and 30°). The reduced frequency curves for the same conditions (Fig. 27a) do not collapse together, and the cross-plot presented in Fig. 27b clearly shows that the reduced frequency is not constant with free stream velocity with the exception of $\alpha = 22^\circ$. This indicates that the wing rock frequency is not a function of just the free stream velocity, but is also influenced by a change in the total rolling moment coefficient, which varies with tunnel velocity or Reynolds number. The reduced frequency of wing rock is significantly lower than in the water tunnel test, but that is expected because of the difficulty in inertially scaling the models for air and water in order to match the reduced frequencies.

The wing rock motion with a mean sideslip angle was also investigated. Results for the cases at $\beta = -5^\circ$ and $\beta = -10^\circ$ are revealed in Figs. 28 and 29, respectively. At low angles of attack (less than 20°), the model rolls to a stable position, which can exceed a roll angle of 70° at $\alpha = 0^\circ$. Wing rock starts between 22° and 24° angle of attack, and the maximum peak-to-peak amplitude of the motion is slightly smaller for the sideslip conditions, as Fig. 30a indicates. A significant decrease in the wing rock amplitude is observed at $\alpha = 30^\circ$. Another interesting difference is that the mean roll angle, i.e., the angle halfway between peaks, increases with sideslip, varying from

$\phi = 0°$ for $\beta = 0°$ to $\phi = 20°$ for $\beta = -10°$ (Fig. 30b). Results of Ref. 16 show that a flat 80° delta wing does not exhibit wing rock when a mean sideslip angle of 10° is introduced. With a negative mean sideslip angle, this configuration exhibits a strong wing rock, although the amplitude of the motion is smaller and the model assumes a right-wing-down attitude. This is an indication of the differences between the wing rock mechanisms, i.e., between slender wing rock (pure delta wing) and "body-wing-tail" wing rock. The interactions among vortices and aircraft components are major participants in the wing rock phenomena observed in this type of configuration.

5.1.2 Tail Off Configuration

The vertical tail was removed and the model was statically re-balanced in roll. The wing rock motion for the tail off configuration presents similar characteristics, as shown in Fig. 31. The major difference between the two configurations is illustrated by comparing the plots in Fig. 32 with the appropriate plots in Fig. 20 (tail on). For angles of attack below 30°, the limit cycle behavior for the tail off case takes longer to develop, approximately 1 second. The interaction between the vertical tail and the forebody vortices is an important contributor to wing rock. The absence of the tail appears to delay the onset of the limit cycle oscillation, but once the motion is established, other aerodynamic events are able to maintain the "rocking". At $\alpha = 30°$, the strong natural asymmetry is sufficient to trigger wing rock much faster; the motion is established within one cycle, as in the tail on case.

Figure 33 reveals that the maximum peak-to-peak amplitude of wing rock is smaller for the tail off configuration than for the tail on case. This contradicts the water tunnel test results (Fig. 5), where it was found that the amplitude was larger for the tail off configuration. The water tunnel test, however, also showed that the amplitude of wing rock was larger for a configuration with a larger tail, denoting once again the importance of the interaction between the forebody vortices and the vertical tail, and probably, an effect of tail size. In the wind tunnel, only one vertical tail was tested, therefore, no conclusions on tail size effects can be drawn. At this test condition, the vortex/tail interactions appear to play a key role in the amplitude and development of wing rock, and the net effect of the vertical tail is to decrease roll damping. The difference in reduced frequencies between the water tunnel and wind tunnel tests could be, in part, responsible for the discrepancy in the motion amplitude. Brandon and Nguyen[3] showed in a wind tunnel test that the removal of the vertical tail on a generic fighter configuration (slender forebody-moderately swept wing) significantly increased the amplitude of wing rock for angles of attack greater than 30°. Their data also showed that for angles of attack below 30°, the amplitude of the wing rock motion exhibited by the tail on and tail off configurations were similar, and in some cases, such as at $\alpha = 24°$, the amplitude of the motion for the no tail configuration was smaller. This indicates that the interaction of the vortices and the vertical tail occurs at low to moderate angles of attack. At higher α's, the interactions are minimized and the vertical tail provides a stabilizing influence. Unfortunately, insufficient data are available from this experiment to confirm this theory. The wing rock frequency and reduced frequency for the tail off and tail on cases present no major differences (Figs. 34a and 34b).

5.2 Phase Plots

The analysis of the motion obtained during the free-to-roll experiments provides the means to estimate the roll angular velocity $\dot{\phi}$ and the roll acceleration $\ddot{\phi}$. The roll angle data obtained with the rotational transducer were smoothed graphically and then differentiated numerically, yielding $\dot{\phi}$. The angular velocity data were smoothed and differentiated again, and the roll acceleration was obtained. This acceleration $\ddot{\phi}$ is proportional to the total aerodynamic rolling moment coefficient, so the behavior of the rolling moment as a function of time or roll angle can be carefully investigated. The plots of $\dot{\phi}$ vs. ϕ and $\ddot{\phi}$ vs. ϕ are commonly referred to as phase plots.

Depicted in Fig. 35 are phase plots for one cycle of the wing rock motion at $\alpha = 25°$ and $q = 958$ Pa. The roll angular velocity $\dot{\phi}$ (Phi dot, in deg./sec.) shows the expected behavior : starting at $\phi = 0°$, the angular velocity is maximum. As the model moves right-wing-down, the angular velocity decreases to zero when the model is at the maximum roll angle. The motion reverses its direction and the velocity starts to increase (negatively), reaching the maximum negative magnitude when the model is at $\phi = 0°$ again. The roll angular acceleration $\ddot{\phi}$ (Phi ddot, in deg./sec.^{2}), which closely represents rolling moment, yields the typical wing rock hysteresis loops[17,18] when plotted as a function of roll angle. In this graph, a clockwise loop denotes an area where energy is being added to the system, i.e., the oscillations are being driven (destabilizing). The counter-clockwise loops near the maximum roll angle represent areas where the system is consuming energy, and therefore the motion is being damped (stabilizing). Figure 35b reveals that the areas contained within the destabilizing and stabilizing loops are about equal, indicating an energy balance which is required to sustain the limit cycle wing rock. The cross points in this plot are roll angles at which the total roll damping goes to zero, and for this particular case, they are -20° and 12°. The lack of symmetry in these roll angles for the right-wing-down and left-wing-down portions of the cycle could be due to aerodynamic reasons (asymmetric flow field) or mechanical reasons (non-constant bearing friction). Cycles during the buildup phase of the wing rock motion at $\alpha = 25°$, such as cycles 3 and 4 in Fig. 36, were also analyzed. In these cycles, energy is being fed to the system, and the roll angle and the angular velocity are increasing, as Fig. 37a indicates. Larger clockwise loops (destabilizing) in the rolling moment graph reveal the unbalance in energy necessary to initiate the oscillatory motion.

As discussed in the previous section, the maximum amplitude of the wing rock motion occurs at $\alpha = 28°$, and the oscillations are very steady (Fig. 38). Any arbitrary cycle during the motion exhibits similar characteristics. Figures 40 and 41 present roll angular velocity and acceleration, respectively, for the cycles depicted in Fig. 39. The shape and magnitude of the curves for each cycle are almost identical, denoting a very steady oscillatory motion. The data for all the cycles at 28° angle of attack are presented in Fig. 42.

The phase plots for a cycle at $\alpha = 30°$ and $q = 958$ Pa, illustrated in Fig. 43, reveal similar characteristics. Small deformations in the $\dot{\phi}$ vs. ϕ plot might indicate non-linearities in the restoring moment. A direct relationship between the roll angle and the roll velocity and acceleration is presented in Fig. 44.

5.3 Forces and Pressures During Wing Rock

The balance-fixed normal and side forces were acquired also at 200 samples/second/channel, and later reduced and converted to body-fixed coordinates by applying a simple transformation to account for the roll angle (recall that the balance is fixed to the sting and that the model rolls about the balance). Tares and balance interactions were not applied, and the actual magnitude of the coefficients could present a small error. The actual magnitude, however, is not very important in this case; the behavior of the forces and their relationship with the motion are the useful information that these data will provide. Pressures were measured on the wings with Endevco pressure transducers. Endevcos 7 and 9 are on the left wing, while Endevcos 8 and 10 are on the right wing (Fig. 18). The pressures on the forebody were monitored at selected ports using the PSI electronic pressure scanner.

5.3.1 Normal and Side Forces Changes During Wing Rock

Figures 45a and 45b present normal force and side force during the wing rock motion at $\alpha = 28°$, where the maximum amplitude occurs. As expected, the normal force oscillates at twice the frequency of wing rock, with the maximum peaks observed when the model is at $\phi = 0°$. The normal force is minimum when the model reaches the maximum positive or negative roll angles. There is an additional input to the normal force gages as evidenced by the irregularity of the output plot. The frequency of this additional component could be related to the model/balance/sting system structural frequency (7.9 Hz), or it may be an aerodynamic input related to the interaction of the forebody vortices with the vertical tail. This will be discussed further below. The side force response to the roll motion is obviously quite different, as it should be. If there was no influence on the balance side force gages other than the body normal force component due to roll angle, then the side force would behave exactly like the roll angle. If the side force is non zero at $\phi = 0°$, either there is a lag in the response of the flow field to the roll motion or there could be, for example, an interaction of the forebody vortices with the vertical tail that induces a yawing moment and side force in addition to that expected from the body normal force variation. Figure 45b indicates a substantial input to the side force gages at zero roll angle. It is possible that the higher frequency components of the balance output are related to the structural resonance frequency of 7.9 Hz, but they appear to have a periodic regularity tied to the roll motion, as would be expected if there were a vortex interaction phenomena taking place. This notion of a vortex interaction with the tail is strongly supported by the data in Fig. 46, where the vertical tail has been removed. In these figures, the irregularities in the normal force output have nearly disappeared. The side force behavior is as expected: zero (or near zero) at $\phi = 0°$ and maximum and minimum at the roll angle extremes. There are still small disturbances in the overall side force output, but they are minor compared to the total output level. This is strong evidence that the vertical tail, even at $\alpha = 28°$, plays a significant role in the body forces and moments during the wing rock cycle. The hysteresis loops for the normal force CN and the side force CY for the tail on and tail off configurations (Fig. 47) also reveal a strong influence of the vertical tail, as indicated by the difference in the shape of the curves in each case. The variation observed in the normal and side forces with roll angle for the vertical tail off configuration are very similar to data presented in Ref. 19 for a pure delta wing.

5.3.2 Forebody Pressure Distribution During Wing Rock

The forebody pressures at three ports located at station 1 (Fig. 18) at $\Phi = 0°$, 144° (right side) and -144° (left side), are shown in Fig. 48a. Since the ports are moving with the model, they can pass through regions of separated and attached flows. The pressure outputs are actually showing local flow characteristics depending on the position of the port. At the port located at the windward meridian ($\Phi = 0°$), the pressure is fluctuating at twice the wing rock frequency as expected, with the maximum pressure when the model is at $\phi = 0°$. The pressures at the two other ports provide interesting information. When the model has a right-wing-down attitude, the right pressure port is probably in a region of attached flow, and the pressure remains constant for most of this portion of the motion cycle. On the other hand, the pressure on the left port presents more fluctuations and a higher value (actually, a less negative value) for roll angles greater than 20°. In this roll angle range, the left port is in a region of mostly separated flow. The opposite occurs in the left-wing-down portion of the motion, even thought the magnitudes of the pressure differences are not the same because of the initial vortex flow field asymmetry. The water tunnel test performed on this configuration and the wind tunnel test on a generic fighter in Ref. 3 revealed that the forebody vortices switch twice during each oscillation cycle, and during that switching process, the vortices appear to wrap around one another. The pressures in Fig. 48a are probably showing some of that vortex behavior, especially when the model is at an approximately wings-level position. At forebody station 3, which is farther away from the tip, the pressure data reveal similar characteristics, as illustrated in Fig. 48b.

The pressure measurements from this test provide a way to analyze the pressure distribution at selected forebody stations and selected roll angles during a cycle of the wing rock motion. The wing rock at $\alpha = 25°$ is depicted again in Fig. 49, and the pressure distribution at station 2 for cycle A is presented in Fig. 50 in the following manner: the first two plots show pressure distributions at arbitrary roll angles during the right-wing-down portion of the oscillation, one for the motion between $\phi = 0°$ and the maximum roll angle and the other for the motion between the maximum amplitude and $\phi = 0°$. The left-wing-down portion is arranged similarly. A shift in the pressures measured in the windward ports is evident from these data, clearly showing the movement of the ports. Therefore, in order to get the actual forebody pressure distribution in a wind tunnel fixed reference frame, the roll angle for each condition was subtracted from the port geometric angular location. The pressures in Fig. 51 are plotted as a function of this "corrected" azimuth. As expected, no major changes are observed at the forebody region where the flow is still attached, as denoted by the curves collapsing together for azimuth angles between 0° and 90° and between 270° and 360°. If the forebody vortices were fixed in the wind tunnel reference system, the curves would collapse together even between 90° and 270°. Major differences are observed in this forebody region, therefore, the forebody vortices are moving in this reference frame. In Fig. 51a, when the model is at $\phi = 0°$, the pressures are lower on the right side, indicating a right-vortex-low asymmetry. This is very similar to the natural asymmetric pattern found in the static test at this angle of attack (see Volume II of this Final Report). As the model moves right-wing-down, the asymmetry in the pressures is reversed, as seen when the model is at $\phi = 16°$. It appears that the left vortex moves closer to the surface while, at the same time, the right vortex moves farther away from the body. As the roll oscillation progresses, the right vortex continues moving up, and a maximum left-vortex-low asymmetry is observed when the model is close to the maximum positive roll angle. When the motion reverses its direction (Fig. 51b), the left vortex appears to remain static and the right vortex moves closer to the surface. The asymmetry is reversed again and the vortex pattern at $\phi = 0°$ is very similar to the starting condition in the previous figure. In the left-wing-down portion of the cycle (Figs. 51c and 51d), not much activity is observed. The rolling motion in this direction tends to enhance the initial asymmetry, but apparently, the disturbance produced by the oscillation is not enough to cause a much larger asymmetry. The right vortex stays almost at the same position, while the left vortex moves up for roll angles between -30° and -38°, reinforcing the right-vortex-low pattern.

The forebody pressure distribution during cycle A of the wing rock motion at $\alpha = 30°$ (Fig. 52) is presented in Fig. 53 (versus uncorrected azimuth) and in Fig. 54 (versus corrected azimuth). Figure 54a reveals large forebody vortex movements. Starting from a right-vortex-low pattern, the right vortex moves up and the left vortex moves down, reversing the initial asymmetry completely when the model approaches the maximum roll amplitude. The opposite occurs when the model goes to $\phi = 0°$ again. Hysteresis is evident in the left-wing-down portion, where not much activity in the vortex movement is observed. Another cycle, shown in Fig. 55 as cycle B, was investigated to evaluate the repeatability of the pressure measurements, and the results presented in Fig. 56 show strong consistency and agreement with the trends observed for cycle A.

5.3.3 Wing Pressure Distribution During Wing Rock

The pressure measurements and the relationship with lift on the right and left wing upper surfaces are extremely useful for understanding the wing rock mechanism. Figures 57a and 57b present the pressure on the left and right wings at two different stations during one cycle of motion at 28° angle of attack. A detailed analysis of Fig. 57b reveals that at $\phi = 0°$, with the model moving in the direction of right-wing-down, the pressure over the right wing (End. 10) is slightly higher (i.e., less negative) than over the left wing (End. 9), which would be indicative of a net rolling moment in the clockwise direction. At about 10° roll angle, the pressures are the same on both wings. As the right wing continues moving down, the pressure starts building up on the left wing and decreasing on the right wing, creating a negative rolling moment. This restoring rolling moment retards the clockwise motion, and eventually, the model starts moving in the opposite direction. When the model passes again through $\phi = 0°$ in the opposite direction, the pressure on the left wing is still slightly higher than on the right wing and the resulting moment is therefore still negative, continuing to drive the model in the left-wing-down direction. At approximately $\phi = -10°$, the pressures are again equal on both wings, and as the motion continues, the pressure on the right wing increases and a positive rolling moment is induced. This rolling moment variation with roll angle is the cause of the limit cycle motion classified as wing rock. Figures 57c and 57d show the same pressures plotted against roll angle. In both cases, a strong hysteresis is observed, i.e., the pressure at a certain point is different at the same roll angle depending on the direction of the rotation.

Another means of relating the rolling moment to the roll angle history is by subtracting the pressure on the left wing from the pressure on the right wing at a specific time and plotting it against time. It should be noted that this is only one pressure location, and despite being indicative of the wing lift characteristics, it is not an accurate measurement of the wing total loading. Figures 58a and 58b show ΔCp, that closely represents the local rolling moment, at the two wing stations. The behavior is similar in both figures: starting at $\phi = 0°$, and with the right wing moving down, the rolling moment starts to decrease from a slightly positive value to a negative value. After reaching a maximum negative magnitude, ΔCp increases (absolute value decreases) slightly until the model passes through the maximum roll angle, and then it remains constant for most of the time the model presents a positive ϕ. This rolling moment retards the clockwise motion, and eventually forces the model to start moving in the opposite direction. Before the model passes through $\phi = 0°$, the rolling moment starts increasing and it reaches a maximum positive value when the model is at $\phi = -30°$. This positive moment retards the counter-clockwise rotation and forces the model to roll in the opposite direction. Due to the lag in the rolling moment response to the roll motion, a limit cycle oscillation, or wing rock, has been established.

Figures 58c and 58d present the same ΔCp data plotted against roll angle. Since ΔCp is a close representation of the rolling moment, then these plots should be similar to the hysteresis loops presented in Section 5.2. The difference in the areas of the clockwise and counter-clockwise loops in Figs. 58c and 58d denotes an unbalance in the total energy. This is due to the fact that the pressure measurement at one wing location provides an indication of the rolling moment, but by no means represents accurately the total rolling moment. Also, the friction in the roll bearings or in the wiring and pressure lines attached to the model (energy consumed) are not being accounted for in these graphs. Figures 59a-d present Cp and ΔCp data for the case at $\alpha = 30°$, and the trends and behavior are very similar to the data at $\alpha = 28°$.

5.4 Effect of Blowing on Wing Rock

Blowing from small nozzles located near the tip of the model strongly influences the vortex flow field both in the static case and in the one-degree-of-freedom wing rock. The flow visualization performed in the water tunnel showed that the wing rock mechanism depends on the communication between the forebody and wing vortices. When blowing is turned on, this communication between the vortices is interrupted and, eventually, a strong forebody vortex asymmetry is induced. The amplitude of the motion is reduced significantly, and in some cases, wing rock is totally suppressed. Even though flow visualization was not performed during the wind tunnel test, it seems that the mechanisms of wing rock and wing rock suppression with blowing are similar to those observed in the water tunnel. Most of the blowing experiments were performed at $\alpha = 25°$ and 30°. At this last angle of attack, a strong asymmetry in the yawing moment curve was observed in the static tests, denoting a right-vortex-low pattern. The following sections discuss in detail the effect of blowing on the wing rock motion during the wind tunnel tests.

5.4.1 Aft Blowing - Tail On Configuration

Aft blowing strongly influences the vortex flow field at moderate and high angles of attack, generating sizable forces and moments that can be utilized to enhance the controllability of the aircraft (see Volume II of this Final Report). As demonstrated in the water tunnel test, aft blowing also has a strong effect on wing rock. Figure 60 presents the roll angle history for the non-blowing case, and for the left, right and simultaneous blowing cases at $\alpha = 25°$. At this blowing coefficient ($C\mu = 0.0028$), this technique is not effective in stopping the motion completely but it reduces the amplitude of wing rock significantly (about 35% of the non-blowing amplitude). At 30° angle of attack, with the strong asymmetry in the baseline flow, the fluid mechanics resulting from blowing on the left and the right-hand-sides are totally different, as observed in the water tunnel test. Blowing on the left side means, in this case, blowing under the high vortex, and the impact on the forebody vortex flow field is to eliminate and eventually reverse the asymmetry. It appears that this blowing coefficient is not sufficient to reverse the asymmetry, so the vortices are probably in a symmetric or close-to-symmetric state. Therefore, the forebody vortices are still interacting with the wing vortices and the motion cannot be stopped completely, although the amplitude is again reduced (Fig. 61b). Blowing on the right-hand-side, or blowing under the low vortex, is very efficient and totally suppresses wing rock, as seen in Fig. 61c. By blowing under the low vortex, the asymmetry has probably been enhanced, and the communication between the forebody and wing vortices has been greatly diminished. The motion is stopped with the model presenting a right-wing-down attitude at a roll angle of approximately 10°. Blowing on both sides simultaneously (Fig. 61d) does not suppress the limit cycle behavior. Figure 62 shows OGR strip data at 30° angle of attack for the three blowing conditions discussed above. Blowing on the left side and on both sides simultaneously reduce the amplitude of the motion; blowing on the right side completely damps the motion in about three cycles (1 second).

By increasing the blowing coefficient to $C\mu = 0.0037$, or actually by running the test at a lower dynamic pressure and blowing at the same total pressure, blowing becomes very efficient for suppressing wing rock. Figure 63 reveals the results for non-blowing, left, right, and simultaneous blowing at $\alpha = 25°$. Blowing completely suppresses the motion in all cases, with the only difference being the roll angle at which the model stops. For the left blowing case, the model stops with a roll angle $\phi = -10°$, i.e., a left-wing-down attitude. For the other two cases, the model stops with the wings almost at $\phi = 0°$. The equilibrium roll angle for each of these cases will be determined by the relative lift contributions of the left and right wings and the resulting rolling moment. The lift contribution from each wing will depend strongly on the influence of the forebody and wing vortices, which are affected significantly by the forebody jet blowing. This "bias" in the steady state roll angle in the wind tunnel tests is in the opposite direction to that observed in the water tunnel test. In the water tunnel, left side blowing suppressed the wing rock motion and the model rolled to a steady positive roll angle (right wing down). Flow visualization in the water tunnel showed that when blowing on the left side of the forebody, the left forebody vortex was closer to the left wing than the right forebody vortex was to the right wing, thereby resulting in higher suction on the left wing, producing a positive (right-wing-down) roll angle. The locations of the wing vortices over each wing are not significantly different. However, as a result of blowing on the left forebody, the left wing vortex bursts somewhat forward of the wing trailing edge and the right wing vortex bursts behind the trailing edge. If these were the only vortices affecting the lift, the difference in burst location would usually imply that there would be more lift on the right wing than the left wing (because the burst vortex over the left wing would result in less overall suction). It appears that in this case, since the roll moment is positive rather than negative, the asymmetric forebody vortices produced by the blowing are more dominant than the resulting changes in the wing vortices and the result is a positive roll angle.

Since there was no flow visualization in the wind tunnel tests, it is impossible to determine where the vortices are with respect to the model in order to compare to the water tunnel tests. From the static yawing moment results, it is known that blowing on the left produces a left yawing moment and negative rolling moment (left wing down). The yawing moment result is consistent with a forebody vortex pattern where the left vortex is closest to the forebody. On the basis of other water and wind tunnel tests on generic fighter configurations, which have slender forebodies and wing leading-edge extensions (LEX), the direction of the rolling moment (negative) is also consistent. In past flow visualization experiments on generic fighters, blowing on the left forebody resulted in the left forebody vortex being nearest the forebody and also nearer the wing. This usually results in the wing LEX vortex on the left side bursting much farther forward than the LEX vortex on the right, which could support an argument for less lift on the left wing than the right wing thereby producing a negative rolling moment. This same argument could support the wind tunnel results on the NASP model, where the wing vortices are analogous to the wing LEX vortices on generic fighters.

Explanation of the difference responses in roll to forebody blowing between the water and wind tunnel tests can only be speculated. As discussed above, the direction of the roll moment and consequent response in determining a steady state bias in the roll angle is influenced by both the forebody and wing vortices. The interaction of the forebody and wing vortices with each other and with the wing surface is quite complex and may be quite sensitive to Reynolds number, which differs by an order of magnitude between the water and wind tunnel tests. The relative influence of the forebody and wing vortices on the wing will be highly dependent on the vortex strengths, positions relative to the wing upper surface, and the burst location. Even though the equilibrium roll angle resulting from steady blowing is different in the water tunnel and wind tunnel tests, the dynamic characteristics of the wing motion and the influence of blowing are very similar.

At 30° angle of attack, the trends are very similar to the previous case (Fig. 64). Blowing suppresses wing rock completely, even when blowing under the high vortex; it appears that this blowing coefficient is sufficient to switch the asymmetry and stop the motion at a negative roll angle, as seen in Fig. 64b. Figure 65 shows OGR data of the three blowing schemes at $\alpha = 30°$ and $C\mu = 0.0037$, illustrating clearly the effectiveness of blowing as a wing rock suppression method. It can be speculated that, with further refinements, optimized nozzle location and the proper mass flow rate on the left and right sides of the aircraft, the wing rock motion might be stopped without the induced asymmetry and the resulting steady rolling moment.

Aft blowing was also investigated as a method for controlling the wing rock of this configuration with a mean sideslip angle. At $\alpha = 30°$, blowing at the high $C\mu = 0.0037$ stops the motion when blowing on the left, right and both sides (Figs. 66b, c and d). The bias in the roll angle is magnified at this condition, but that is strongly related to the natural bias in the mean roll angle observed for the non blowing cases. The model stops the motion at $\phi = -5°$ when blowing on the left side, at $\phi = 10°$ when the blowing is applied on both sides simultaneously, and at $\phi = 25°$ when blowing on the right side.

5.4.2 Forward Blowing - Tail On Configuration

Forward blowing can also be used to modify the vortex flow field and the lateral/directional characteristics of an aircraft. Many investigations (Ref. 8 and Volume I of this Final Report) have reported that, for enhanced control forces and moments, forward blowing is very unpredictable and that the changes in forces and moments are non-linear with angle of attack or blowing coefficient. This study reveals that forward blowing appears to be more effective than aft blowing in the sense that it can suppress wing rock at the lower blowing coefficient ($C\mu = 0.0028$). An important point is that the mechanism which appears to be significant in suppressing wing rock is the decoupling of the forebody and wing vortices. Forward blowing, whether it produces larger or smaller yawing and rolling moments than aft blowing, is more efficient at decoupling. It is conceivable that the optimum blowing technique for wing rock suppression and aerodynamic control for yaw and roll are not the same. Figure 67 shows left and right blowing at $\alpha = 25°$ and 30°, and it is clear that both blowing cases (left and right) reduce the amplitude of wing rock significantly. In spite of the fact that forward blowing is never able to completely stop the motion at this blowing coefficient, the general behavior of left and right blowing is more uniform than in the aft blowing case, i.e., it appears to be indifferent whether the blowing is applied under the low vortex or under the high vortex. For the same reason, no difference in the roll angle bias was observed when using this blowing technique; for most cases, the model stops the motion at a slightly positive roll angle.

5.4.3 Aft Blowing - Tail Off Configuration

As discussed in Section 5.1.2, the tail off configuration exhibits wing rock between 22° and 30° angles of attack, although the amplitude of the motion is smaller than for the tail on configuration. The amplitude of the wing rock motion at α = 25° and α = 30° is shown again in Figs. 68a and b, respectively.

Aft blowing on this configuration is very efficient in controlling wing rock, and even blowing at $C\mu = 0.0028$ provides adequate damping for the motion. The absence of the tail makes it easier for blowing to stop the communication between vortices and components. When the vertical tail is on, the forebody vortices can impinge on that surface, complicating the elimination of vortex interactions. Figures 69a and 69b show results of blowing on the left and right sides, respectively, with $C\mu = 0.0028$ and at 25° angle of attack. The motion is suppressed almost completely in both cases, and the bias in the roll angle is observed again. Right blowing stops the model with a right-wing-down attitude (positive roll angle) and vice versa. A similar behavior is shown in Figs. 69c and 69d for α = 30°, with the model again stopping at a positive roll angle when blowing on the right side and at a negative roll angle when blowing on the left side. Figure 70 presents OGR strip data for two blowing cases: left blowing at α = 25° and right blowing at α = 30°. It takes about 6 cycles for the motion to stop completely in the first case, and about 3-4 cycles at 30° angle of attack.

5.4.4 Forward Blowing - Tail Off Configuration

Forward blowing was also investigated on this configuration. Figures 71a and 71b for α = 25°, and Figs. 71c and 71d for α = 30°, reveal that it is possible to suppress the wing rock motion when blowing on the left or right sides with $C\mu = 0.0028$. No bias in the roll angle is observed at α = 25°; at 30° angle of attack, the motion is stopped with the model assuming a right-wing-down attitude, especially when blowing on the right-hand-side. Since no major differences were found between the tail on and tail off cases, it appears that the mechanism by which forward blowing stops wing rock is less dependent on the interaction between the forebody vortices and the vertical tail.

5.4.5 Alternating Pulsed Blowing

The results presented in the previous sections clearly showed that steady blowing can efficiently control wing rock. However, the disadvantages of steady blowing found in the water tunnel experiments were confirmed in this test: the model does not stop with a wings-level attitude, resulting in large part from forebody vortex asymmetries, which induce a steady rolling moment at $\phi = 0°$ (sideslip equals to zero). Forward blowing appears to minimize these problems but it is not able to completely suppress the motion. Aft blowing on both sides simultaneously suppresses wing rock at an almost zero roll angle at α = 25°, but only when blowing at the highest $C\mu$. In an effort to eliminate these side effects, blowing was pulsed between the left and right nozzles at several frequencies. The flow visualization performed in the water tunnel showed that by pulsing the blowing, it is possible to stop the motion with a forebody vortex pattern that, on a time-averaged basis, is symmetric.

Figure 72a shows again the limit cycle motion at α = 30°, and Figs. 72b - 72f reveal the effect of pulsed blowing on wing rock when blowing with a $C\mu = 0.0028$ at a variety of frequencies. Pulsing the blowing between 6 and 9 Hz (2-3 times the wing rock frequency) reduces the amplitude of the motion; however, pulsed blowing at these frequencies is not able to damp the oscillations completely. When blowing at frequencies close to the wing rock frequency, the wing rock motion can be either enhanced or damped, depending on the phase relationship between the motion and the blowing. The data presented in Fig. 72c show a larger wing rock amplitude than in the non-blowing case when pulsing the blowing at 3 Hz (approximately the wing rock frequency at $\alpha = 30°$). Blowing at frequencies higher than 9 Hz was not effective, probably because the pulsing was too fast for the blowing pressure at the nozzles to reach the required levels for effectiveness.

Figure 73 presents OGR data of the effect of pulsing the blowing at 6 Hz. The amplitude of the motion is reduced, as noted in Fig. 72b, but the model still experiences a limit cycle oscillation at approximately the same frequency as the pulsing frequency (twice the wing rock frequency). The blowing signals reveal that it takes about one second after the valves are opened for the pressures to reach the maximum value. A decrease in the amplitude of the motion occurs after approximately 2 seconds, with the model presenting a slightly positive mean roll angle. The major advantage of pulsed blowing appears to be the fact that it is able to suppress wing rock without creating a large forebody asymmetry and, of course, for a given blowing coefficient, the required total mass flow for a given time period is less than that for continuous blowing. Figure 74 shows the yawing moment for the model in a static position. For the range of the useful pulsing frequencies (6 to 9 Hz), the yawing moment is almost zero, indicating that pulsed blowing interrupts the communication between the vortices without creating large asymmetries.

5.5 Forces and Pressures During Wing Rock Suppression

5.5.1 Side Force Changes

The side force after blowing has stopped the wing rock motion at $\alpha = 25°$ and $\alpha = 30°$ can be seen in Figs. 75a and 75b, respectively. The three curves on each graph correspond to left, right and simultaneous blowing. As expected, right blowing produces a positive side force and left blowing produces a negative side force, but these values are strongly dependent on the roll angle at which the model stops. Referring back to Figs. 63 and 64, right and left blowing stopped the model at a positive and at a negative roll angle, respectively. At $\alpha = 25°$, simultaneous blowing was able to stop wing rock at an almost zero roll angle, and Fig. 75a reveals that the mean side force value is close to zero, indicating the absence of a large forebody asymmetry. This trend is not repeated at higher angles of attack (Fig. 75b), where the non-zero side force indicates an asymmetric flow field.

5.5.2 Forebody Pressure Changes

Figure 76 presents pressure distributions at different forebody stations after the motion is stopped with right blowing and left blowing ($\alpha = 30°$, tail off, $C\mu = 0.0028$). The pressures are plotted as a function of corrected azimuth, i.e., the difference between the geometric azimuth angle and the roll angle at which the motion is stopped. The asymmetries created in each case are evident in stations 2 and 3. Left blowing pulls the left vortex down, creating a lower pressure on that side of the forebody, while right blowing does the opposite. The same trend for the tail on configuration at station 3 is observed in Fig. 77. When blowing on the right side, the motion is stopped at a positive roll angle, and the right vortex appears to assume a lower position, as denoted by the lower pressure on that side of the forebody.

5.5.3 Wing Pressure Changes

The pressures on the left and right sides of the wing at the two Endevco locations after left blowing is initiated ($\alpha = 30°$, tail off, $C\mu = 0.0028$) are depicted in Fig. 78a and 78b. When blowing on the left side, wing rock is stopped at a negative roll angle, and the Endevco output shows that the left wing has a higher pressure at both stations. The forebody pressure distribution showed that when blowing on the left side, the left forebody vortex was pulled down. This vortex interacts with the left wing vortex, making it burst earlier or lift off the surface, explaining the higher pressure over this wing at these locations. It is important to emphasize that since the rolling moment is zero (the wing rock motion has been suppressed), the total lift on both wings should be equal (or nearly equal for the tail-on configuration if there is some influence of the vertical tail on the rolling moment), so these pressures represent only local flow characteristics. When the blowing is applied on the right-hand-side (Figs. 78c and 78d), the transducers show a lower pressure on the left wing at the forward station but a slightly higher pressure on the left wing at the rearward Endevco station. This lack of perfectly reversed asymmetry from the left to right blowing configurations shows that the vortex flow field cannot be forced easily to equal and opposite asymmetric conditions when starting with a highly asymmetric flow field. There is a substantial bias in the flow that persists.

In general, the pressures over each wing are strongly dependent on the roll angle at which the model stops. When forward blowing is used and wing rock is stopped at a roll angle close to zero, the pressures over the left and right wings are almost equal (Fig. 79).

6.0 CONCLUSIONS

6.1 Water Tunnel Test

The wing rock characteristics of a highly slender (NASP-type) configuration were investigated in a water tunnel. Different means of suppressing wing rock by controlling the forebody vortices were also explored. Several conclusions can be made:

1. Wing rock for the highly-slender configuration tested is caused by the forebody vortices interacting with the wing flow. While the wing vortices seem to provide most of the rolling moments, the wing rock motion is controlled by the forebody vortices.

2. The presence of physical barriers such as a fuselage between the left and right wing vortices prevents the type of wing rock observed on delta wings with the same sweep. Furthermore, the vortex liftoff observed on slender delta wings during roll or sideslip was not observed at similar conditions.

3. Steady blowing can suppress wing rock but only at the expense of the creation of significant vortex asymmetries, resulting in a steady-state roll angle bias.

4. Alternating pulsed blowing on the left and right sides of the forebody can potentially be an effective means of suppressing wing rock and eliminating large asymmetric moments at high angles of attack.

The exact forms of interactions between the forebody flow and the other components of a configuration are no doubt dependent on the specific configuration. Nevertheless, it is believed that the concept of suppressing wing rock by controlling the forebody vortex flow should be generally applicable for situations where the primary cause of wing rock is the forebody vortices.

6.2 Wind Tunnel Test

The mechanics of wing rock and wing rock suppression by blowing were further investigated in the wind tunnel test. Roll angle, forces and pressures were measured in an effort to understand the phenomena and assess similarities and/or differences with the wing rock experiment performed in the water tunnel. The main conclusions of this investigation are summarized as follows:

1. The NASP-type configuration tested exhibits a strong wing rock motion between 22° and 30° angle of attack, with a maximum amplitude that can exceed roll angles of about +/- 40°. The frequency of wing rock (about 3 Hz at $\alpha = 30°$) increases with angle of attack, and, at each angle of attack, is not directly proportional to free stream velocity, indicating that the total rolling moment coefficient is also changing with velocity. The configuration also exhibits wing rock even when a mean sideslip angle of -10° was introduced.

2. The amplitude of the wing rock motion is smaller for the tail off than for the tail on configuration, and the onset of wing rock is delayed when the vertical tail is not present. This is the major discrepancy with the water tunnel test results, where the no tail case presents a larger amplitude. It seems that the interaction between the forebody vortices and the vertical tail plays a major role in the wind tunnel test, with the vertical tail enhancing the roll amplitude for angles of attack below 30°.

3. The angular velocity and the angular acceleration were obtained from the roll motion. Phase plots of the angular acceleration, that is directly proportional to the total rolling moment, showed undamped loops at small roll angles and damped loops at large roll angles. The areas of the stabilizing and destabilizing loops are equal, indicating the balance of energy necessary to sustain wing rock.

4. Forces and pressures provided valuable data to understand wing rock, and again, the interaction between the forebody and wing vortices appears to be the principal contributor to this oscillatory motion. The side force change during the wing rock reveals clear differences between the tail on and tail off cases, indicating also some interactions between the forebody vortices and the vertical tail.

5. Aft blowing can stop the wing rock motion completely, but only when blowing with $C\mu = 0.0037$. At lower blowing coefficients, the motion is totally damped only for selected cases, although the amplitude of the oscillations is reduced in all cases. The disadvantages of this technique detected in the water tunnel test are also observed in this investigation: the motion is not stopped at a wings-level position and large forebody vortex asymmetries are introduced. Forces and pressures after the motion has been damped clearly show those asymmetries. In general, less blowing is required to suppress wing rock when the vertical tail is off.

6. Forward blowing appears to control wing rock more effectively than aft blowing, i.e., it suppresses the motion at the low blowing coefficient and the effects of blowing on the right or left sides are almost equal. No bias in the mean roll angle between right and left blowing is observed. As in the water tunnel, alternating pulsed blowing is also an effective means of controlling wing rock. Results are strongly dependent on the pulsing frequency, with the optimum being 2-3 times the wing rock frequency, and the flow field after the motion has been stopped appears to be symmetric.

In general, the wing rock motions and the forebody vortex control suppression results from the water tunnel and wind tunnel tests are in good agreement. The force and pressure data obtained in the wind tunnel confirm the mechanisms causing wing rock and wing rock suppression which were observed in the flow visualization experiments performed in the water tunnel.

7.0 ACKNOWLEDGMENTS

Support for this work is provided by NASA-Ames Research Center under contract NAS2-12989. The technical monitor is Mr. Larry Meyn of the Fixed-Wing Aerodynamics Branch. We would also like to acknowledge the efforts of Mr. Bert Ayers for his consistent high quality work in constructing the water tunnel and wind tunnel models.

8.0 REFERENCES

1. Ericsson, L.E., "The Various Sources of Wing Rock," AIAA-88-4370-CP, 1988.

2. Ng, T. T., Malcolm, G. N., and Lewis, L. C., "Flow Visualization Study of Delta Wings in Wing-Rock Motion," AIAA-89-2187, July 31-August 1-2, 1989.

3. Brandon, J.M. and Nguyen, L.T., "Experimental Study of Effects of Forebody Geometry on High Angle of Attack Static and Dynamic Stability," AIAA-86-0331, August 1986.

4. Brandon, J.M., Murri, D.G., and Nguyen, L.T., "Experimental Effects of Forebody Geometry on High Angle of Attack Static and Dynamic Stability and Control," 15th Congress of the ICAS, September 1986.

5. Nguyen, L.T., Gilbert, W.P., Gera, J., Iliff, K.W., and Enovoldson, E.K., "Application of High-α Control System Concepts to a Variable-Sweep Fighter Airplane," AIAA Flight Mechanics Conference, August 1980.

6. Ross, A. Jean, "Lateral Stability at High Angle of Attack, Particularly Wing Rock," AGARD-CP-260, 1985.

7. Fratello, D.J., Croom, M.A., Nguyen, L.T., and Domack, C.S., "Use of the Updated NASA Langley Radio-Controlled Drop-Model Technique for High-Alpha Studies of the X-29A configuration," AIAA-87-2559, August 1987.

8. Malcolm, G.N., Ng, T.T., Lewis, L.C., and Murri, D.G., "Development of Non-Conventional Control Methods for High Angle of Attack Flight Using Vortex Manipulation," AIAA-89-2192, July 31-August 1-2, 1989.

9. Ng, T. T. and Malcolm, G. N., "Aerodynamic Control Using Forebody Strakes," AIAA-91-0618, January 1991.

10. Suárez, C. J., Malcolm, G. N., Ng, T. T., "Forebody Vortex Control with Miniature, Rotatable Nose-boom Strakes", AIAA-92-0022, January 1992.

11. Guyton, R. W., Maerki, G., "X-29 Forebody Jet Blowing", AIAA-92-0017, January 1992.

12. LeMay, S. P., Sewall, W. G., Henderson, J. F., "Forebody Vortex Flow Control on the F-16C Using Tangential Slot and Jet Nozzle Blowing", AIAA-92-0019, January 1992.

13. Tavella, D.A., Schiff, L.B., and Cummings, R.M., "Pneumatic Vortical Flow Control at High Angles of Attack," AIAA-90-0098, January 1990.

14. Ng, T. T. and Malcolm, G. N., "Aerodynamic Control Using Forebody Blowing and Suction," AIAA-91-0619, January 1991.

15. Ng, T. T., "Aerodynamic Control of NASP-type Vehicles Through Vortex Manipulation", Eidetics International TR 89-009, 1989.

16. Nguyen, L. T., Yip, L., Chambers, J. R., "Self-Induced Wing Rock of Slender Delta Wings", AIAA-81-1883, August 1981.

17. Levin, D., Katz, J., "Self-Induced Roll Oscillations of Low-Aspect Ratio Rectangular Wings", AIAA-90-2811, August 1990.

18. Levin, D., Katz, J., "Dynamic Load Measurements with Delta Wings Undergoing Self-Induced Roll-Oscillations", AIAA-82-1320, 1982.

19. Konstadinopoulos, P., Mook, D. T., Nayfeh, A. H., "Subsonic Wing Rock of Slender Delta Wings", AIAA-85-0198, 1985.

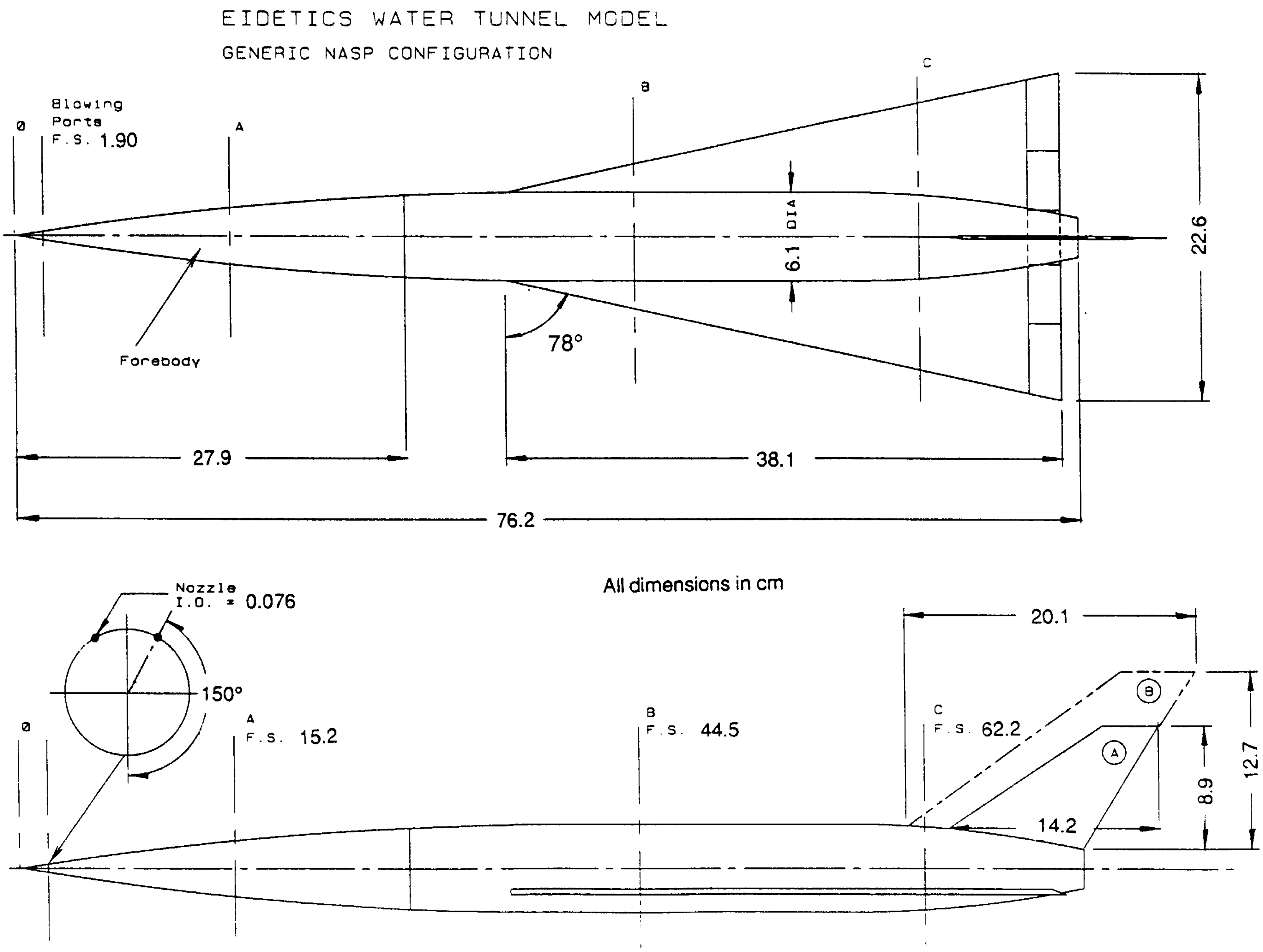

Figure 1 - Schematic of the Water Tunnel Model

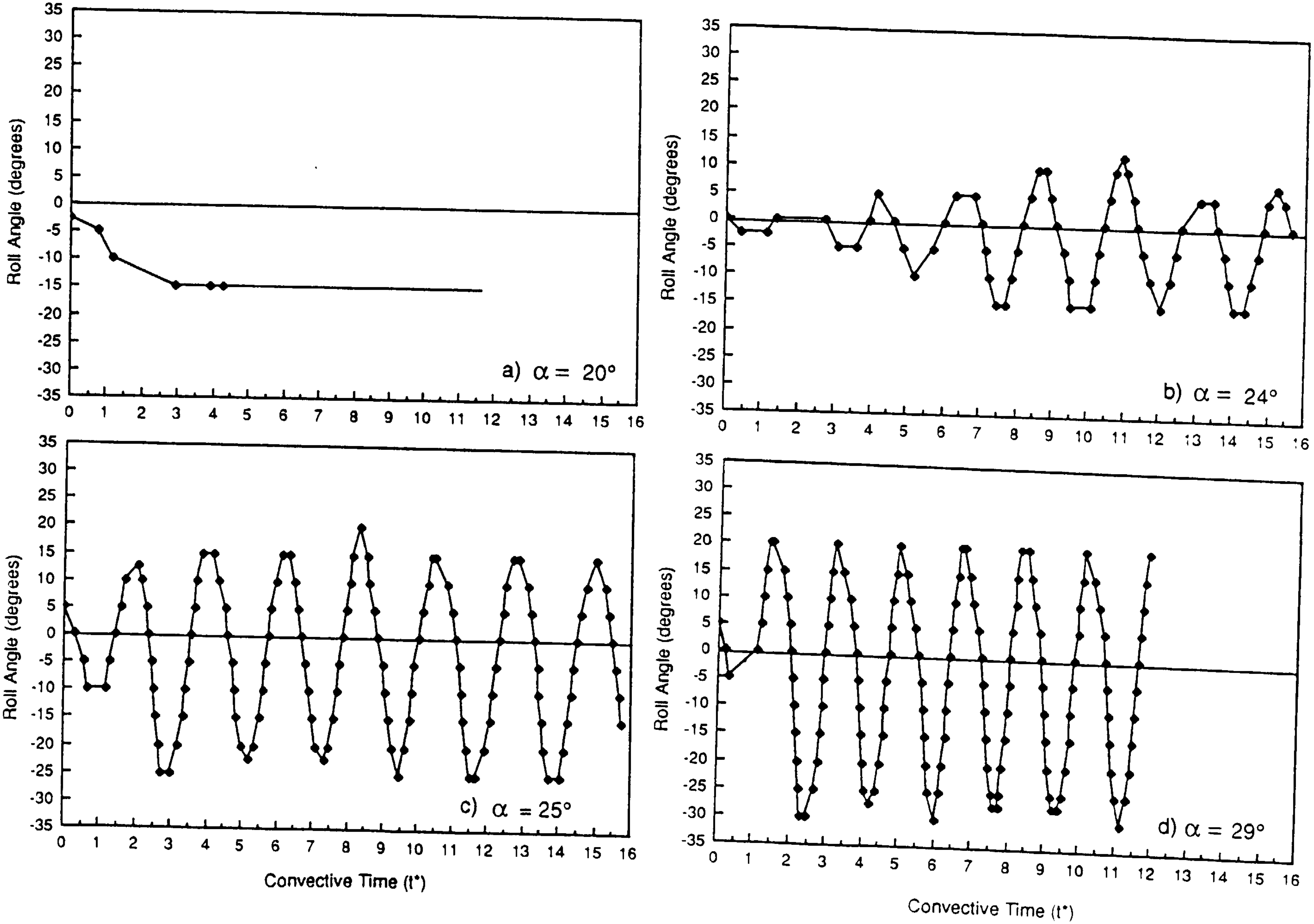

Figure 2 - Roll Angle History of Model O (No Tail)

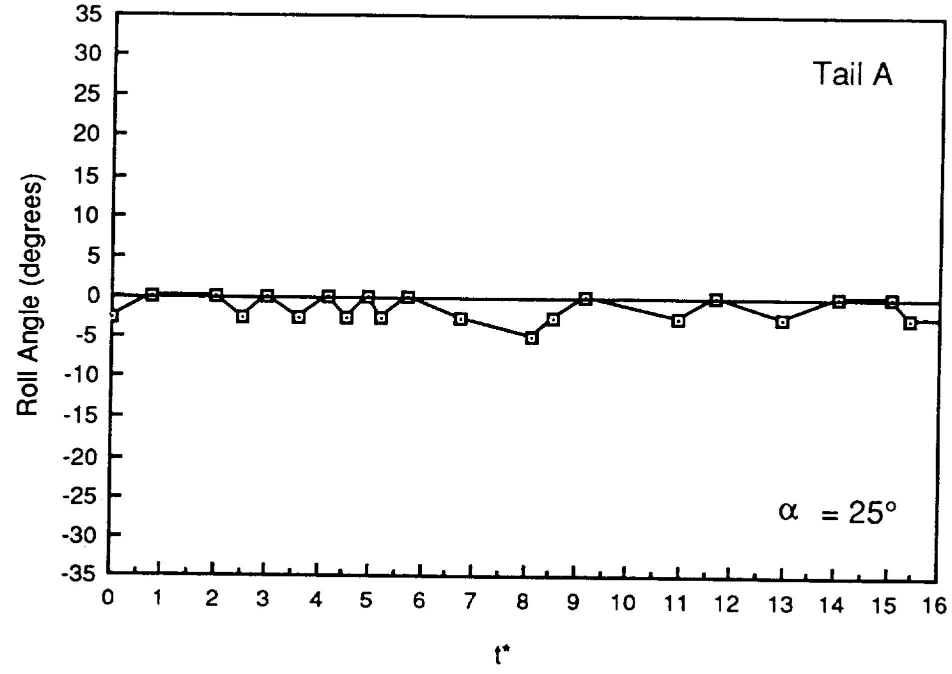

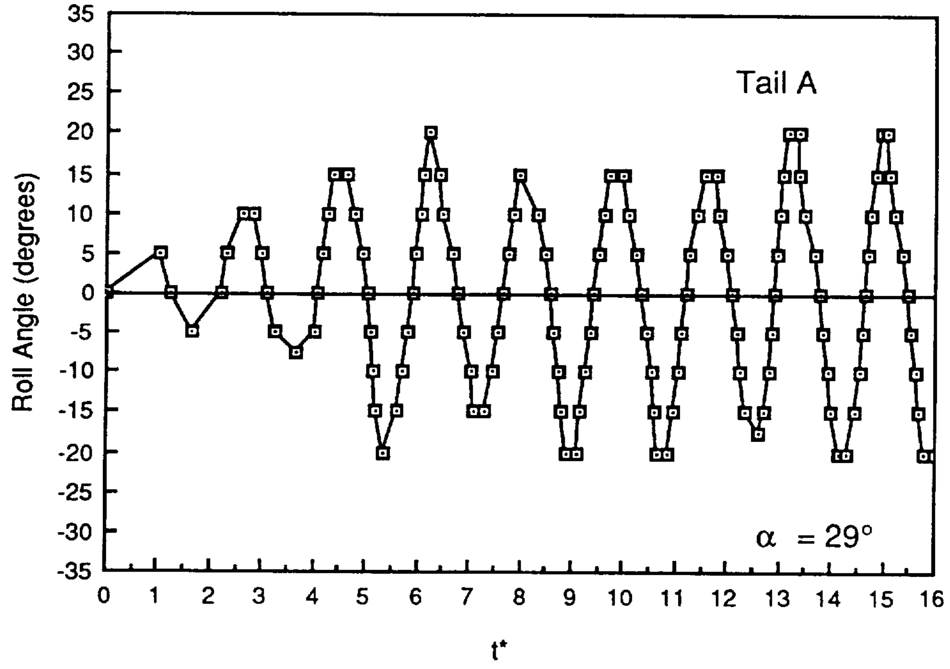

Figure 3 - Roll Angle History of Model A (Tail A)

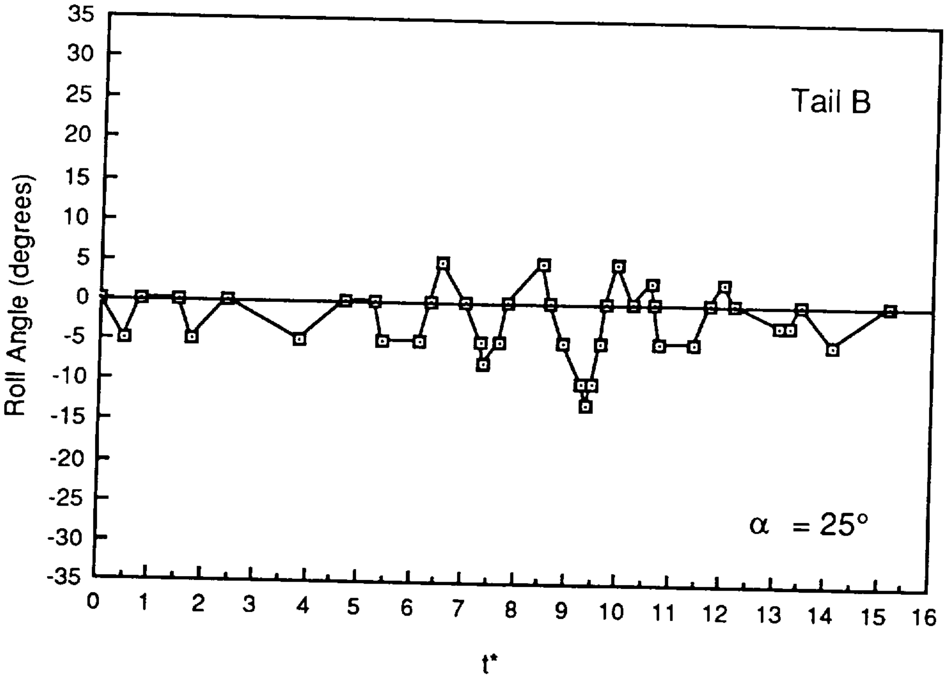

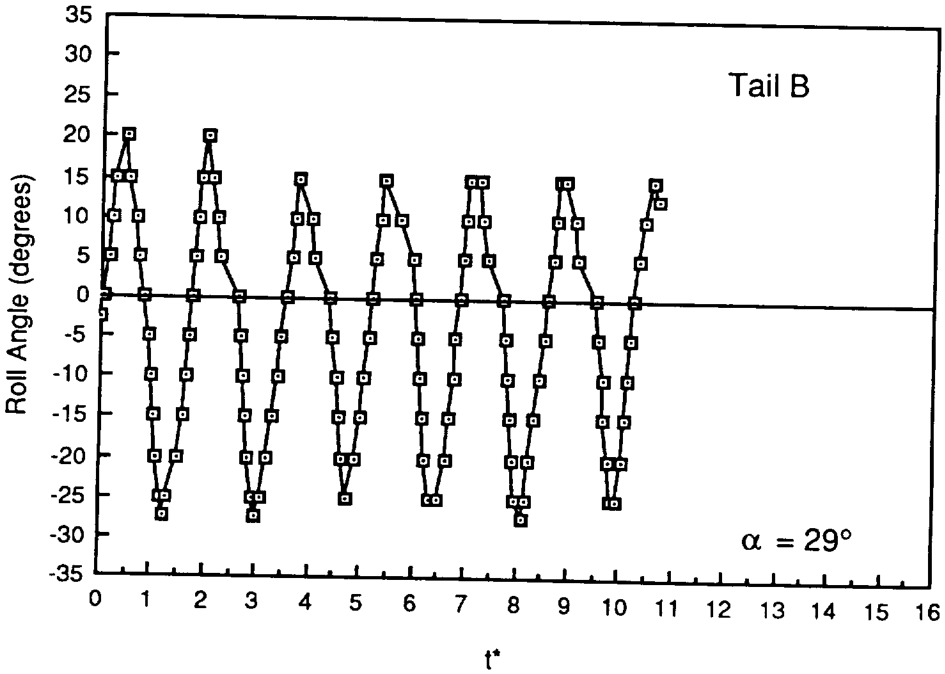

Figure 4 - Roll Angle History of Model B (Tail B)

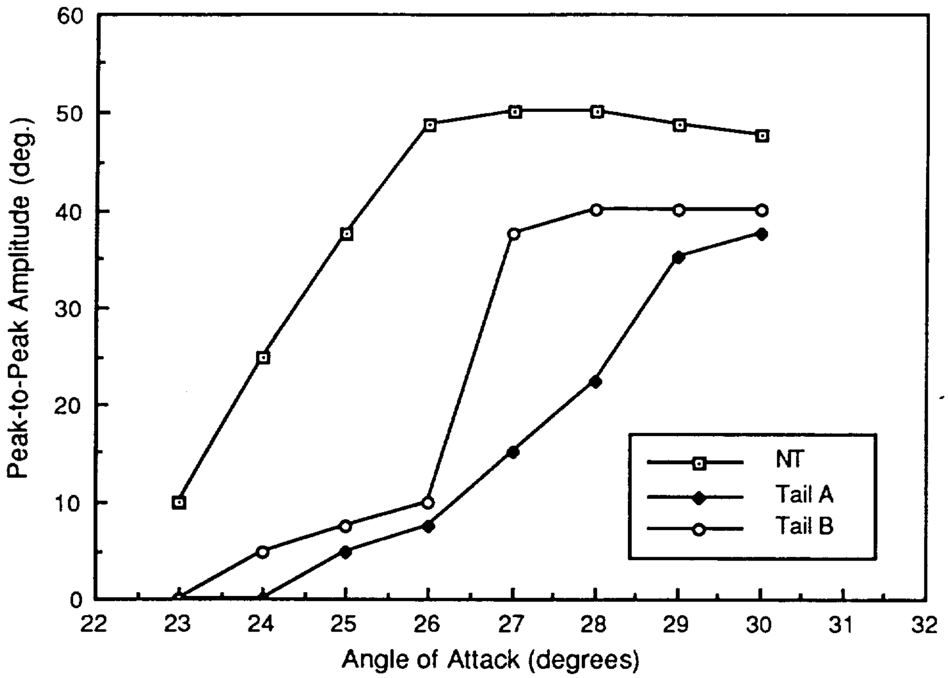

Figure 5 - Amplitude of the Wing Rock Motion

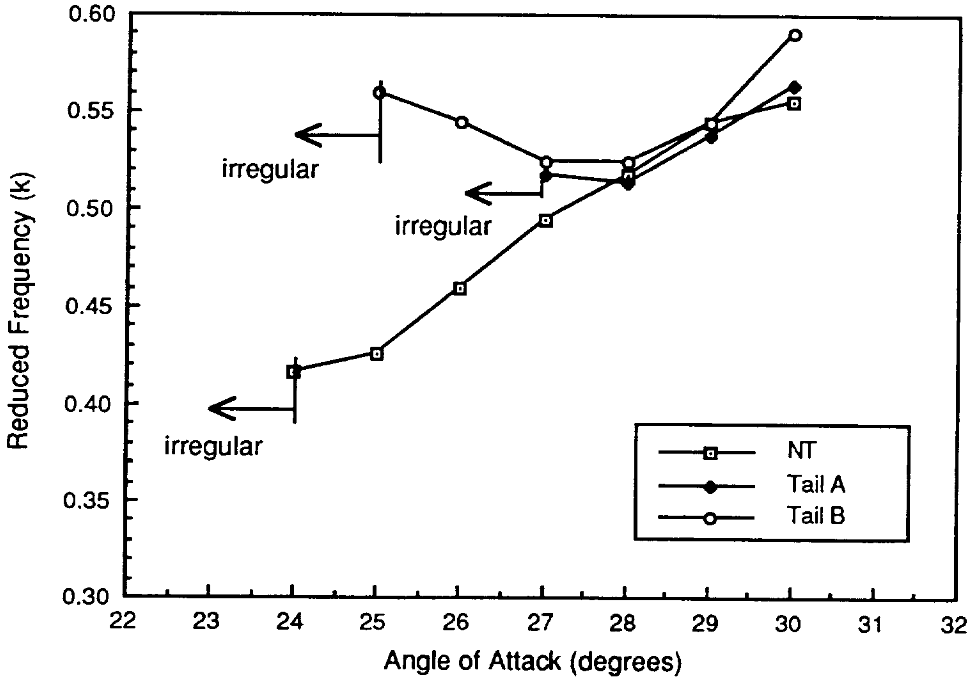

Figure 6 - Reduced Frequency of the Wing Rock Motion

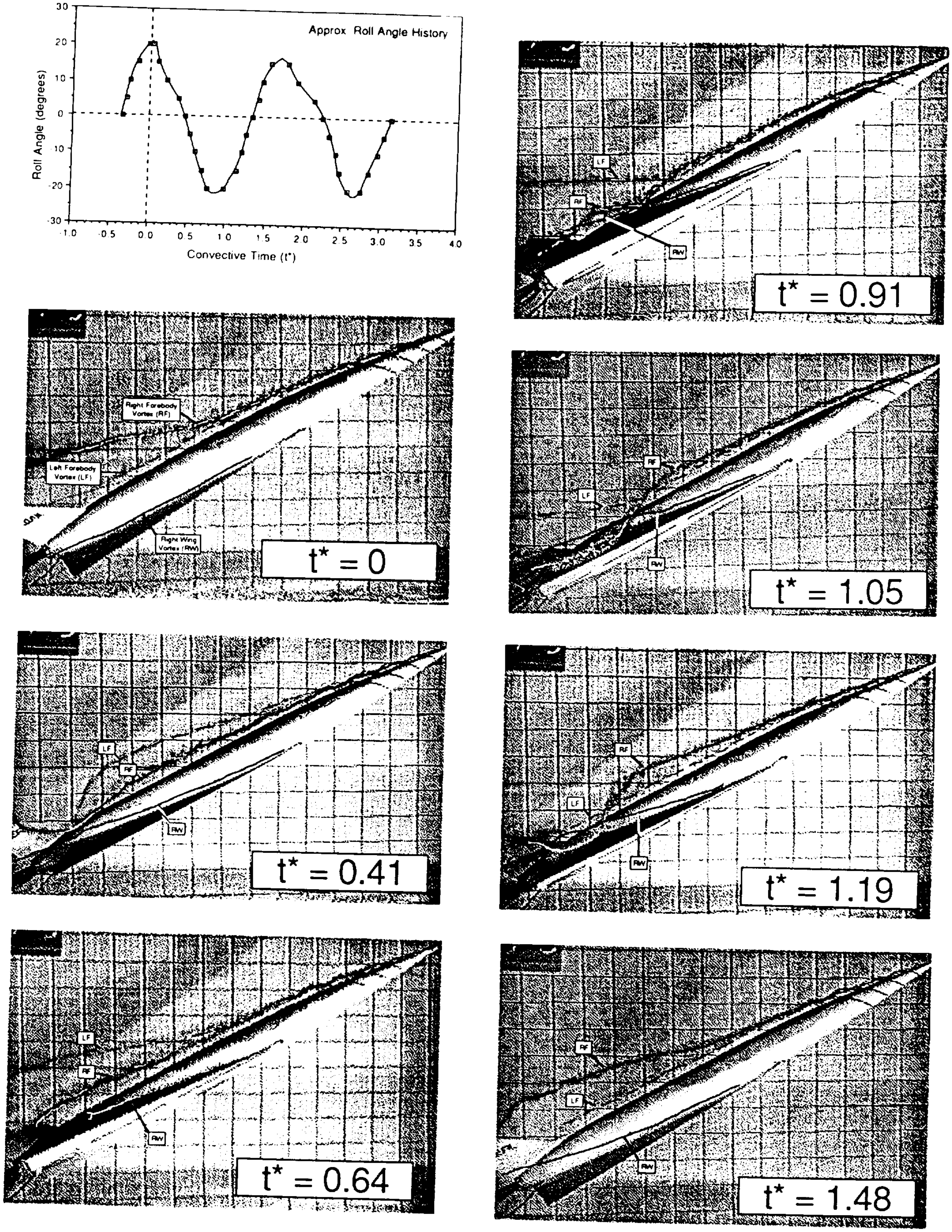

Figure 7 - Digitized Video Recordings of the Vortex Flow During the Wing Rock; Model A at $\alpha = 29°$

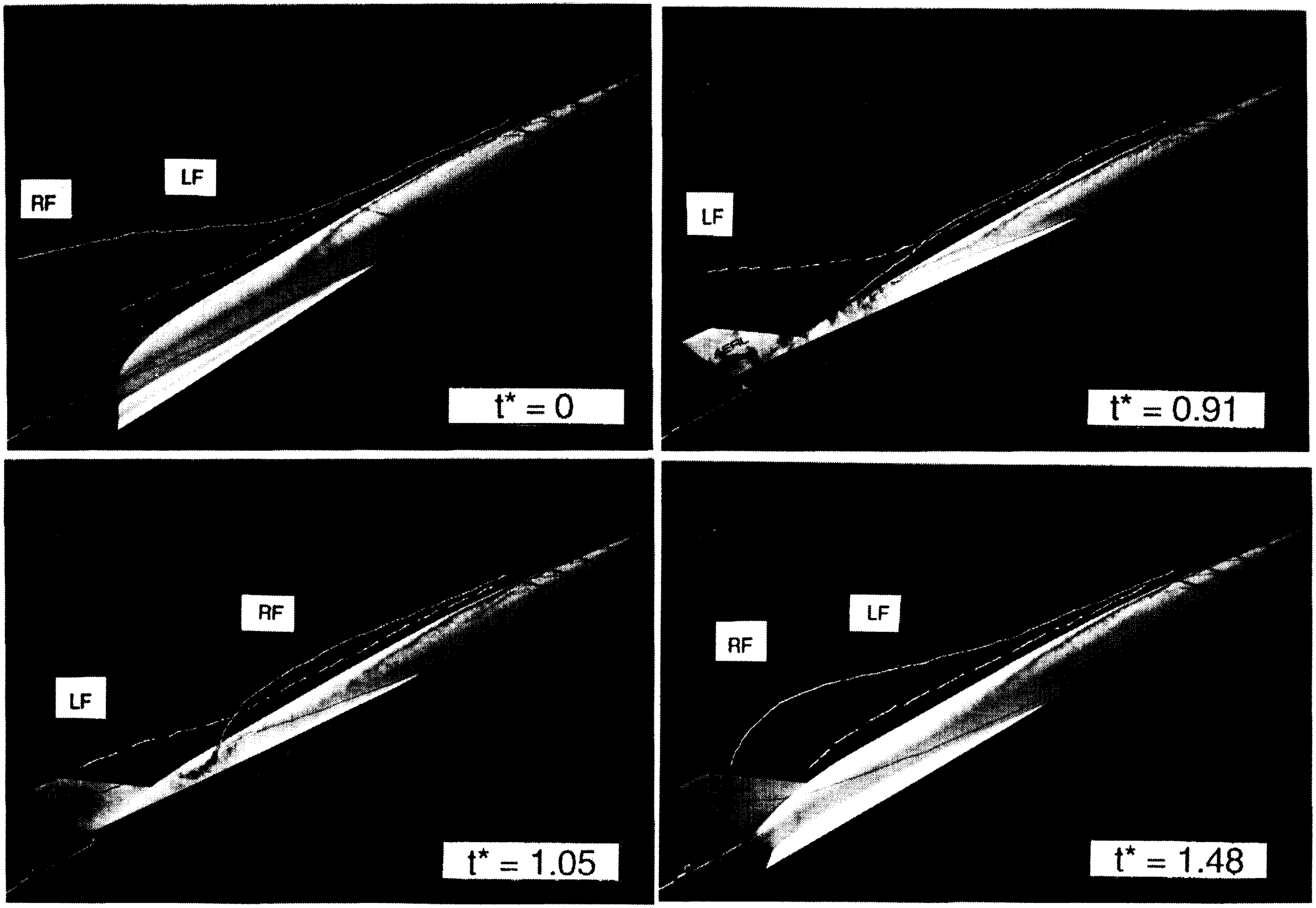

Figure 8 - Photos of Model A During Wing Rock at $\alpha = 29°$

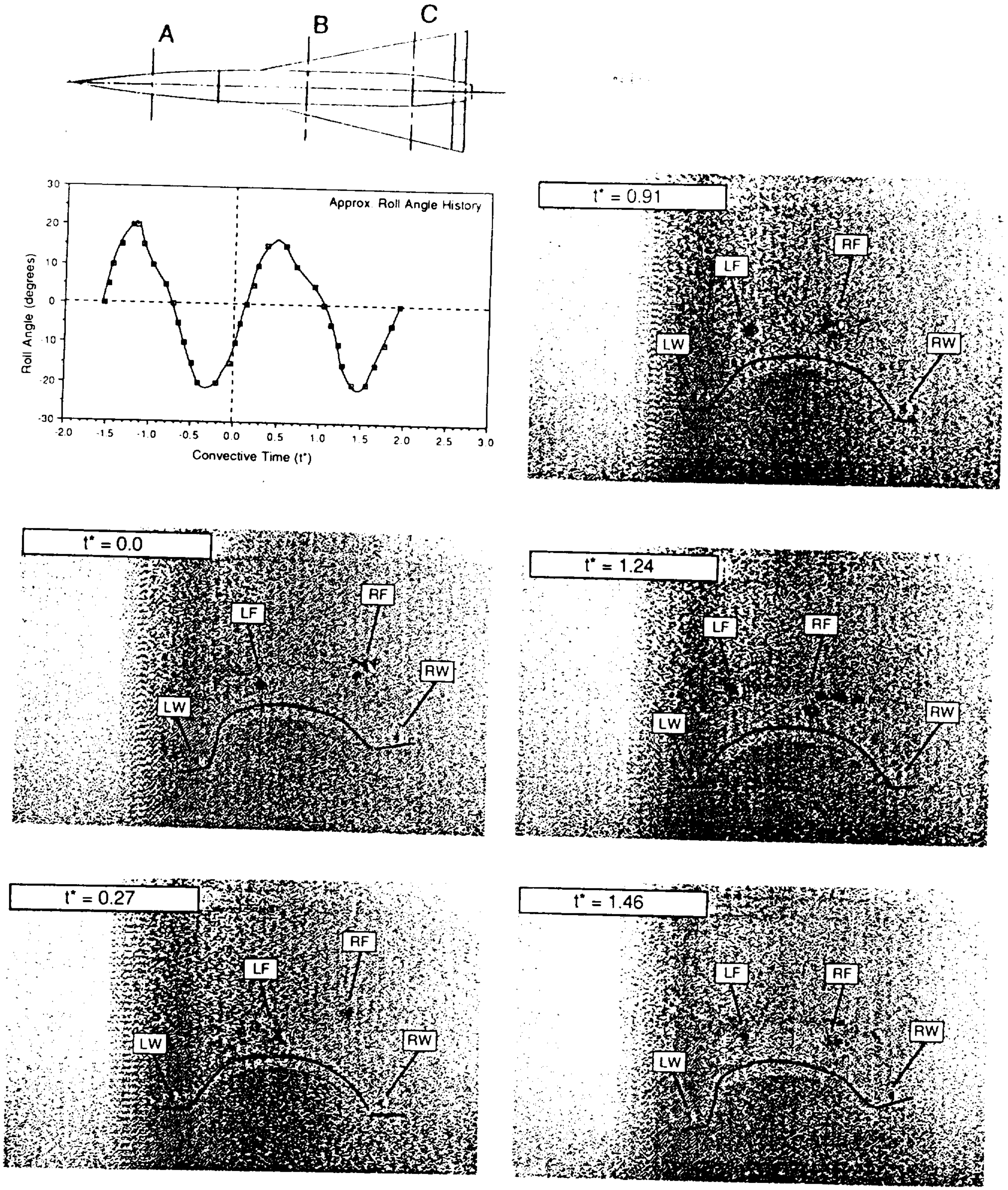

Figure 9 - Digitized Video Recordings of the Vortex Motion at Station B Laser Sheet Visualization; Model A at $\alpha = 29°$

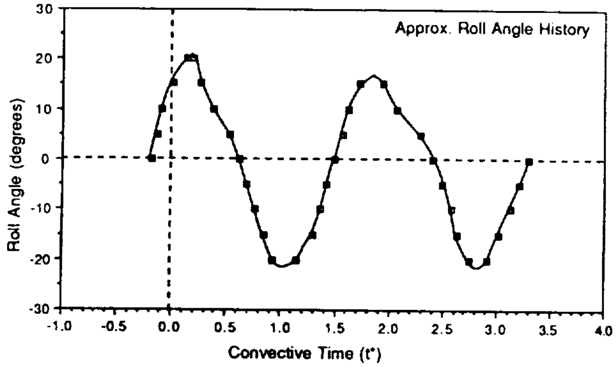

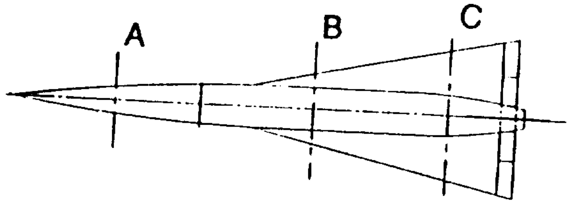

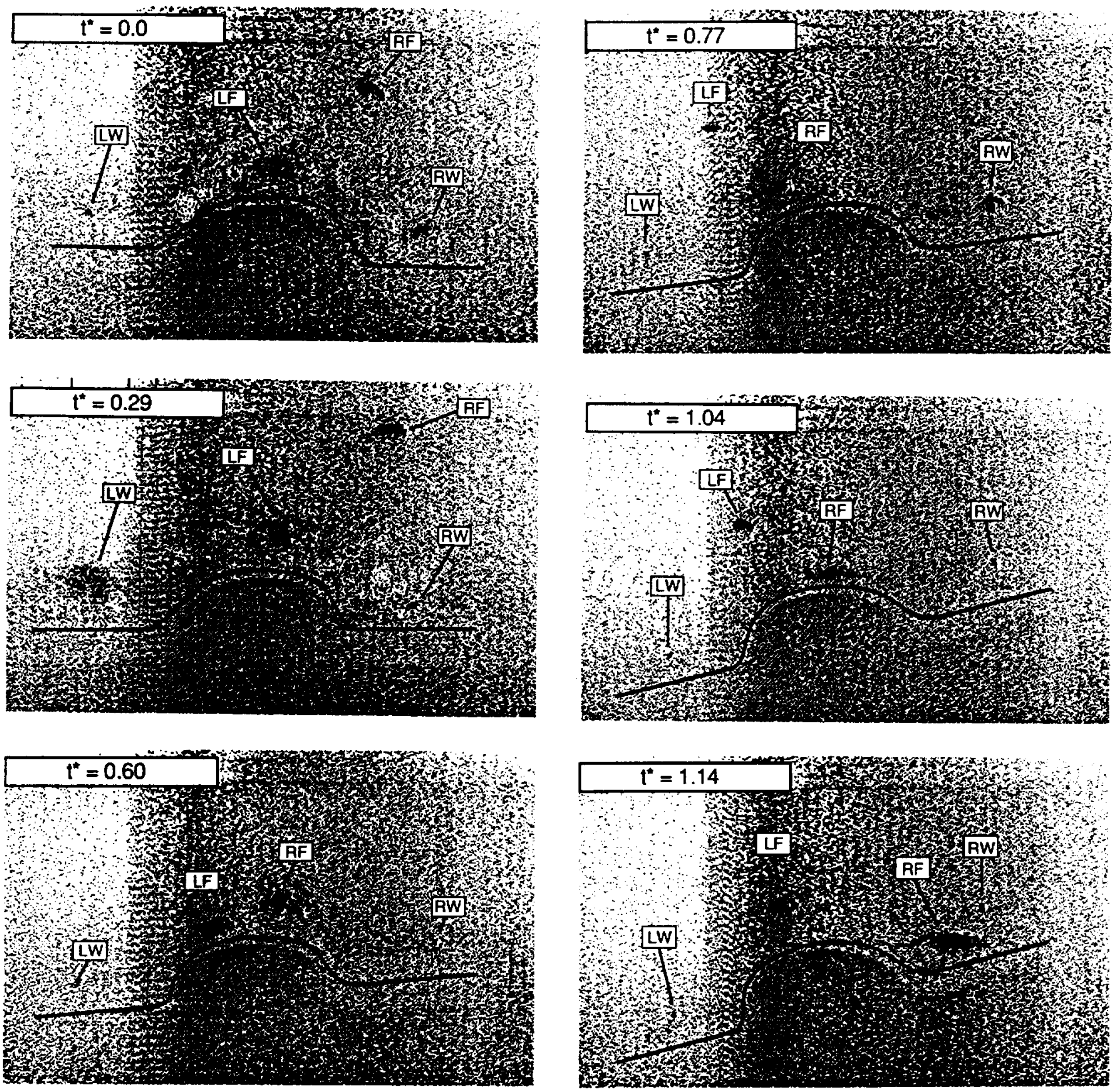

Figure 10 - Digitized Video Recordings of the Vortex Motion at Station C
Laser Sheet Visualization; Model A at $\alpha = 29°$

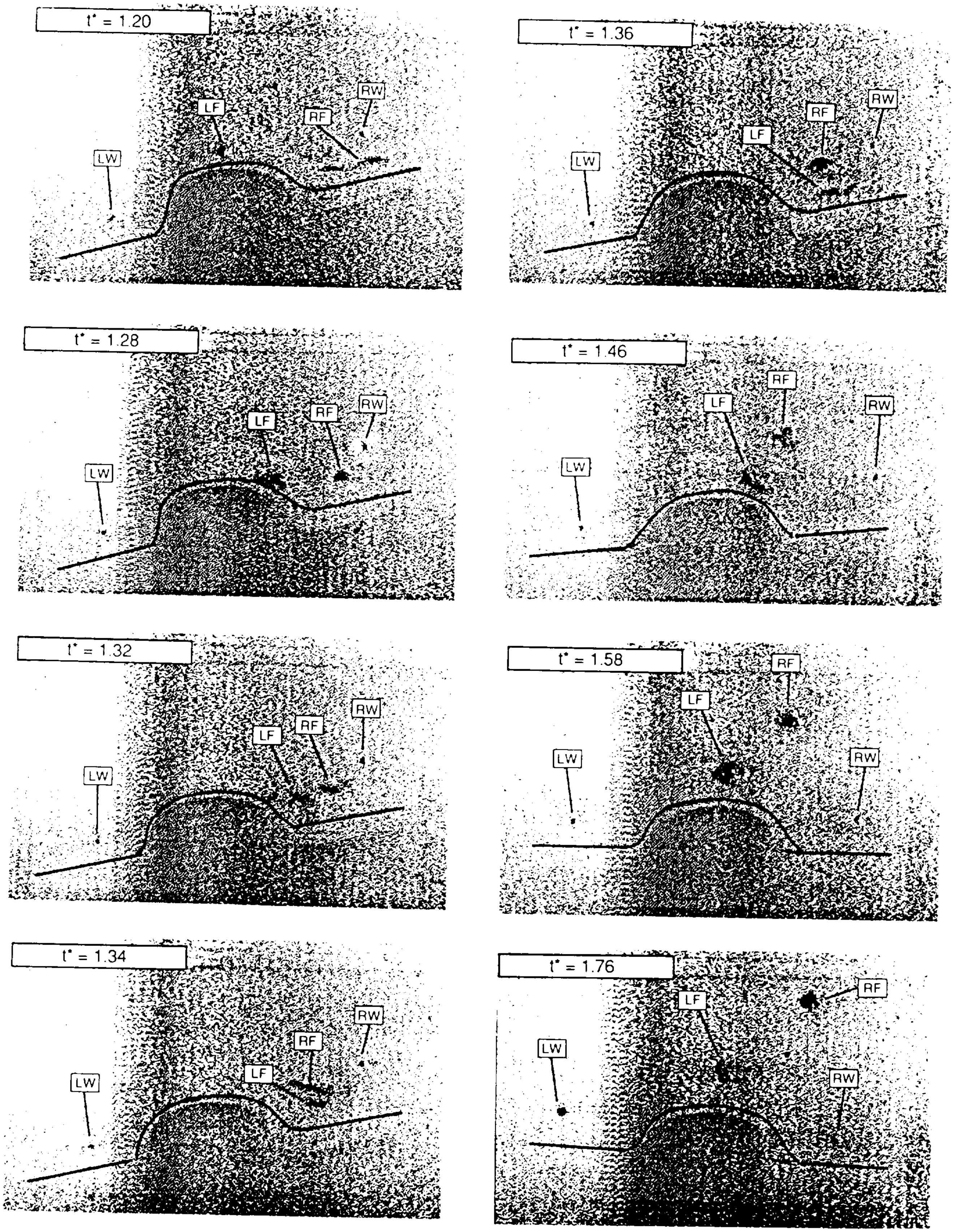

Figure 10 - Concluded

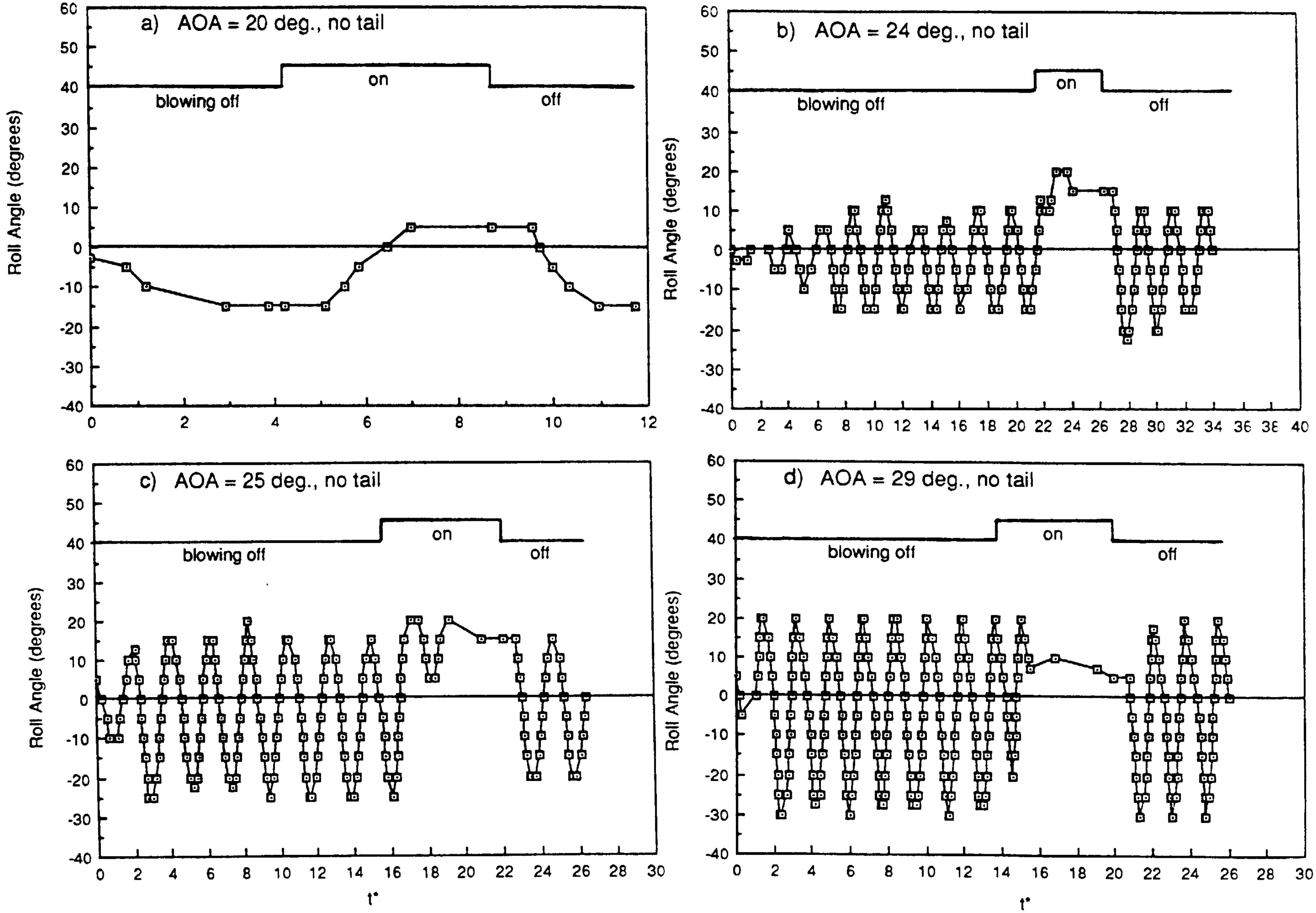

Figure 11 - Effect of Steady Blowing on the Left Side of Model O (No Tail) on the Roll Angle History

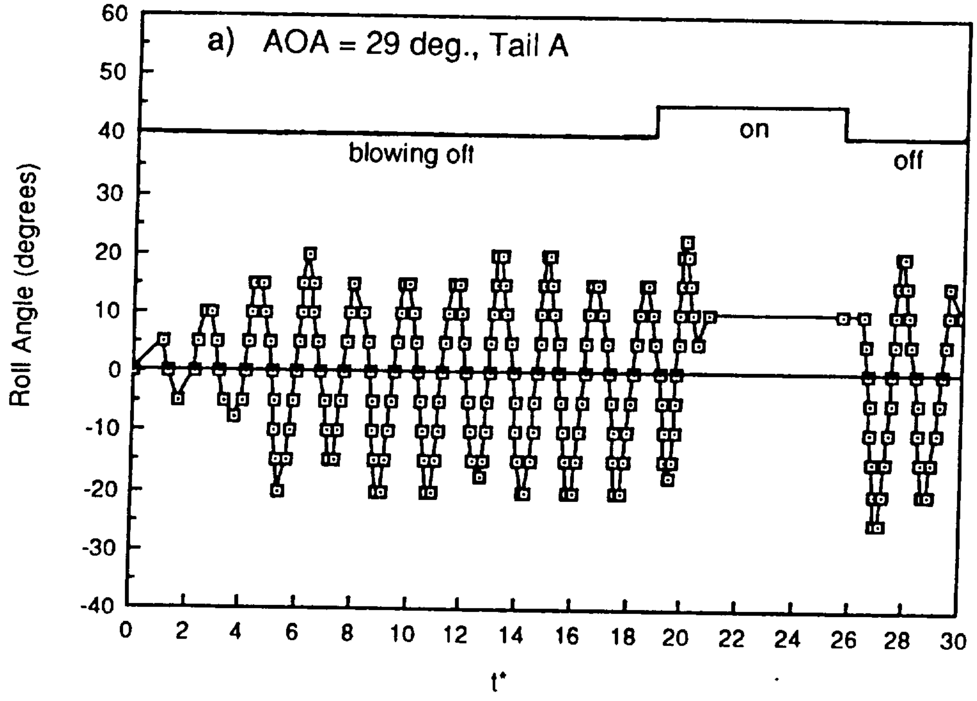

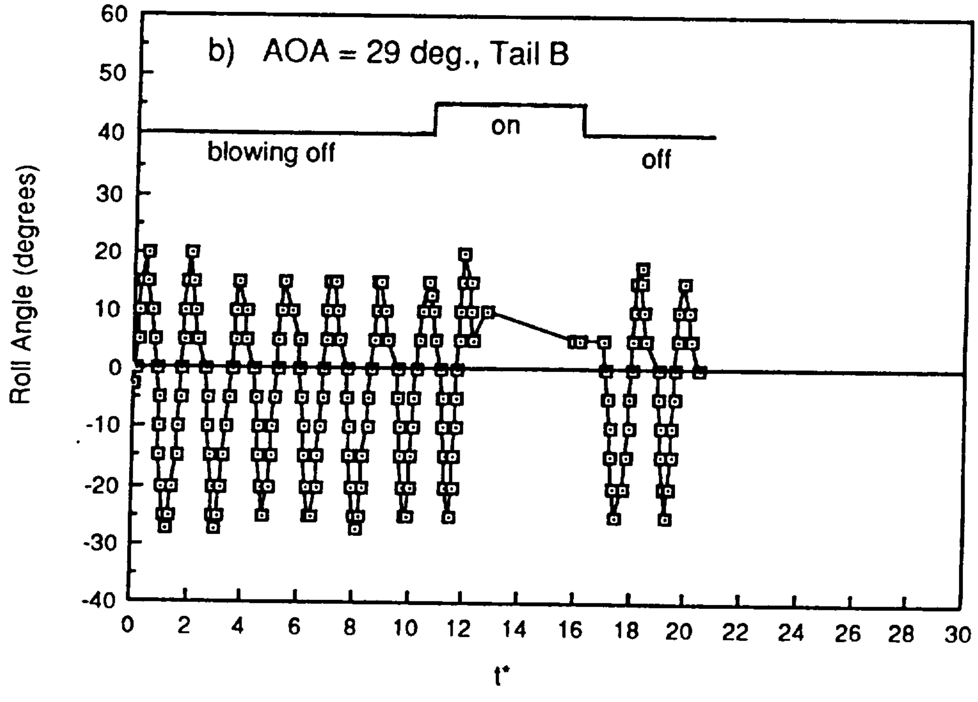

Figure 12 - Effect of Steady Blowing on the Left Side at $\alpha = 29°$
a) Model A; b) Model B

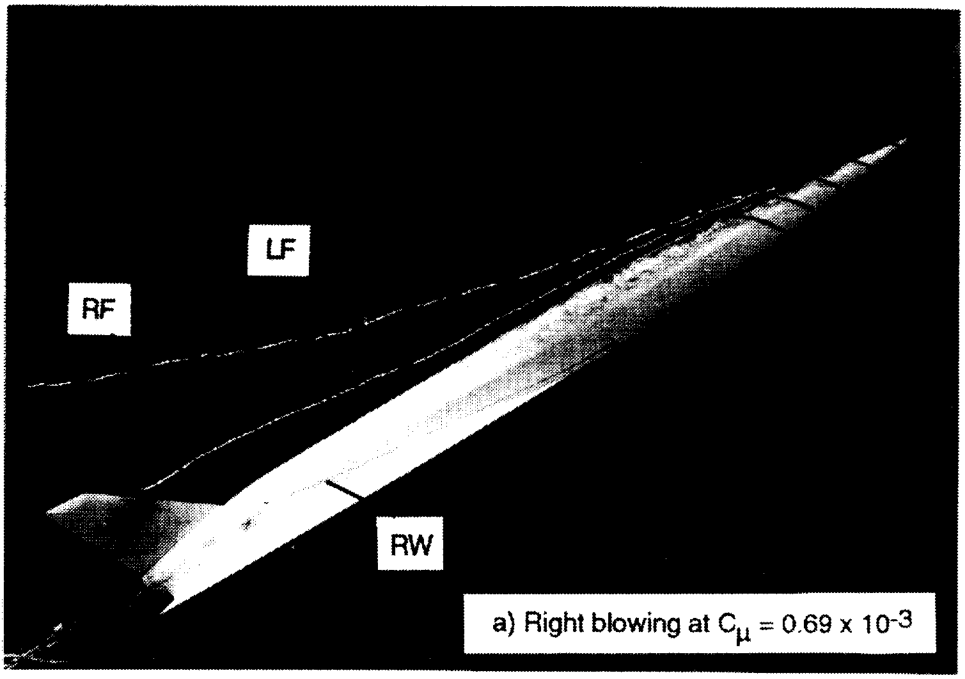

a) Right blowing at $C_\mu = 0.69 \times 10^{-3}$

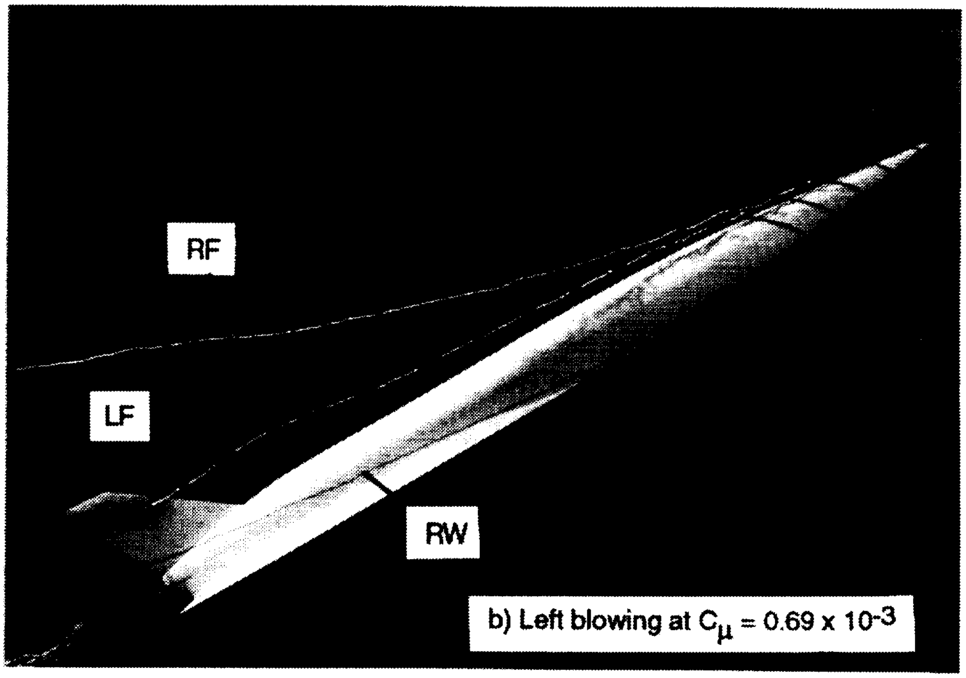

b) Left blowing at $C_\mu = 0.69 \times 10^{-3}$

Figure 13 - Flow Visualization of the Effect of Blowing on Model A at $\alpha = 29°$; a) Right Blowing, b) Left Blowing

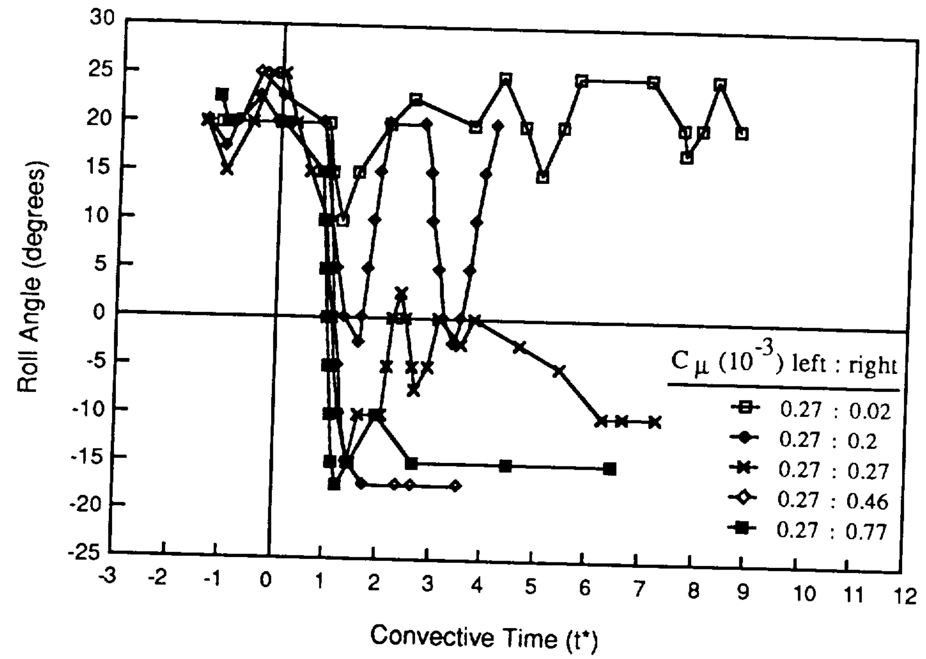

Figure 14 - Effect of Simultaneous Steady Blowing on Both Sides of the Forebody (Left Blowing Rate Fixed: $C\mu = 0.27 \times 10^{-3}$, Right Blowing Rate Variable), Model A at $\alpha = 29°$

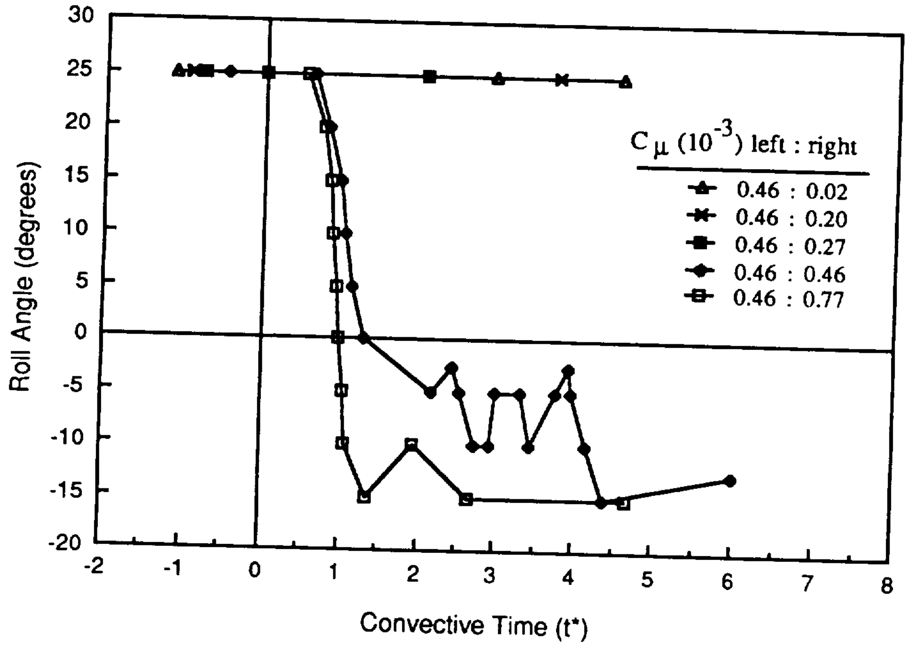

Figure 15 - Effect of Simultaneous Steady Blowing on Both Sides of the Forebody (Left Blowing Rate Fixed: $C\mu = 0.46 \times 10^{-3}$, Right Blowing Rate Variable), Model A at $\alpha = 29°$

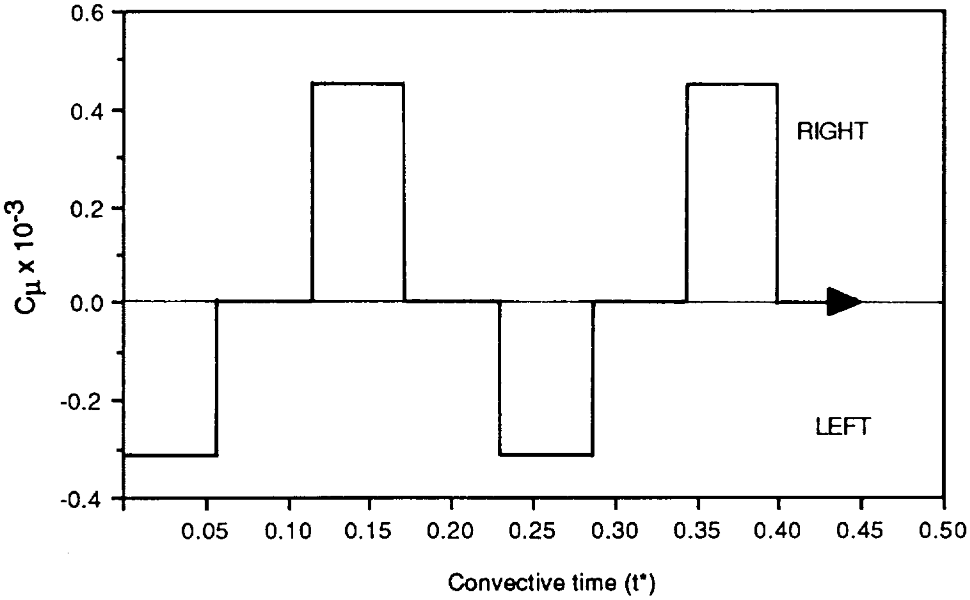

a) Blowing Scheme

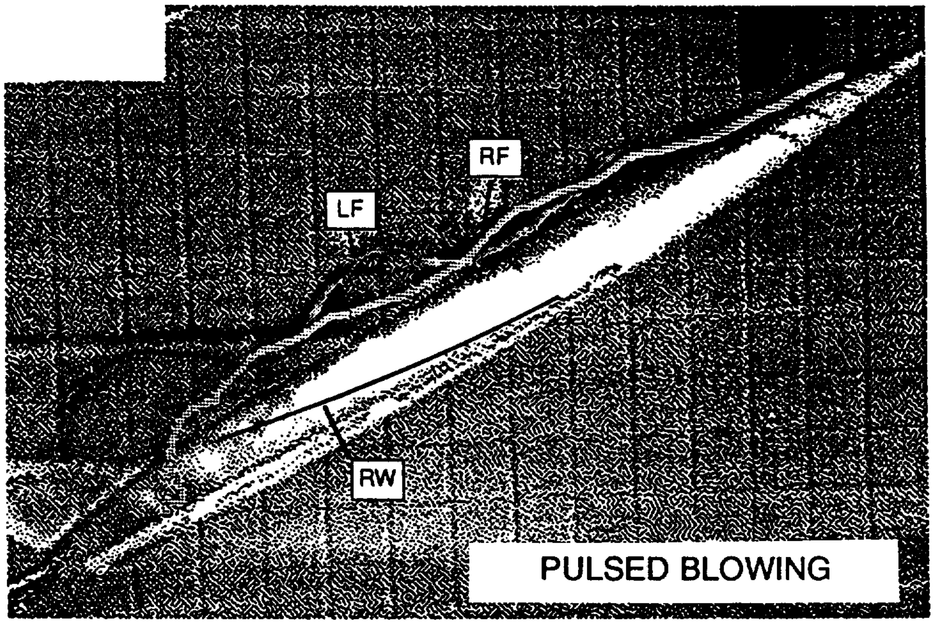

b) Flow Visualization, Model A at $\alpha = 29°$

Figure 16 - Effect of Alternating Pulsed Blowing on the Left and Right Sides of the Forebody

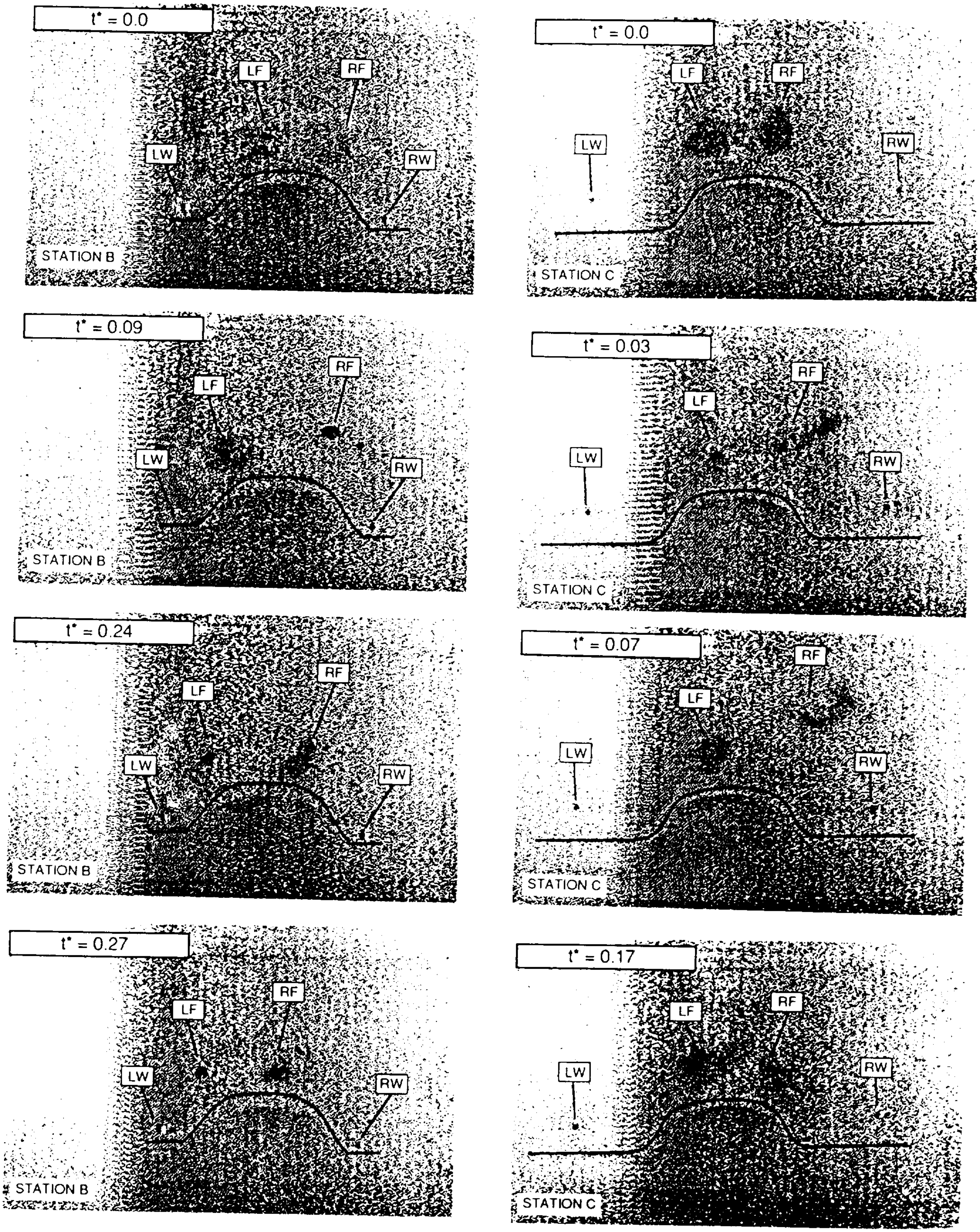

Figure 17 - Digitized Video Recordings of the Vortex Flow During Alternating Pulsed Blowing (Laser Sheet Visualization) Model A at $\alpha = 29°$

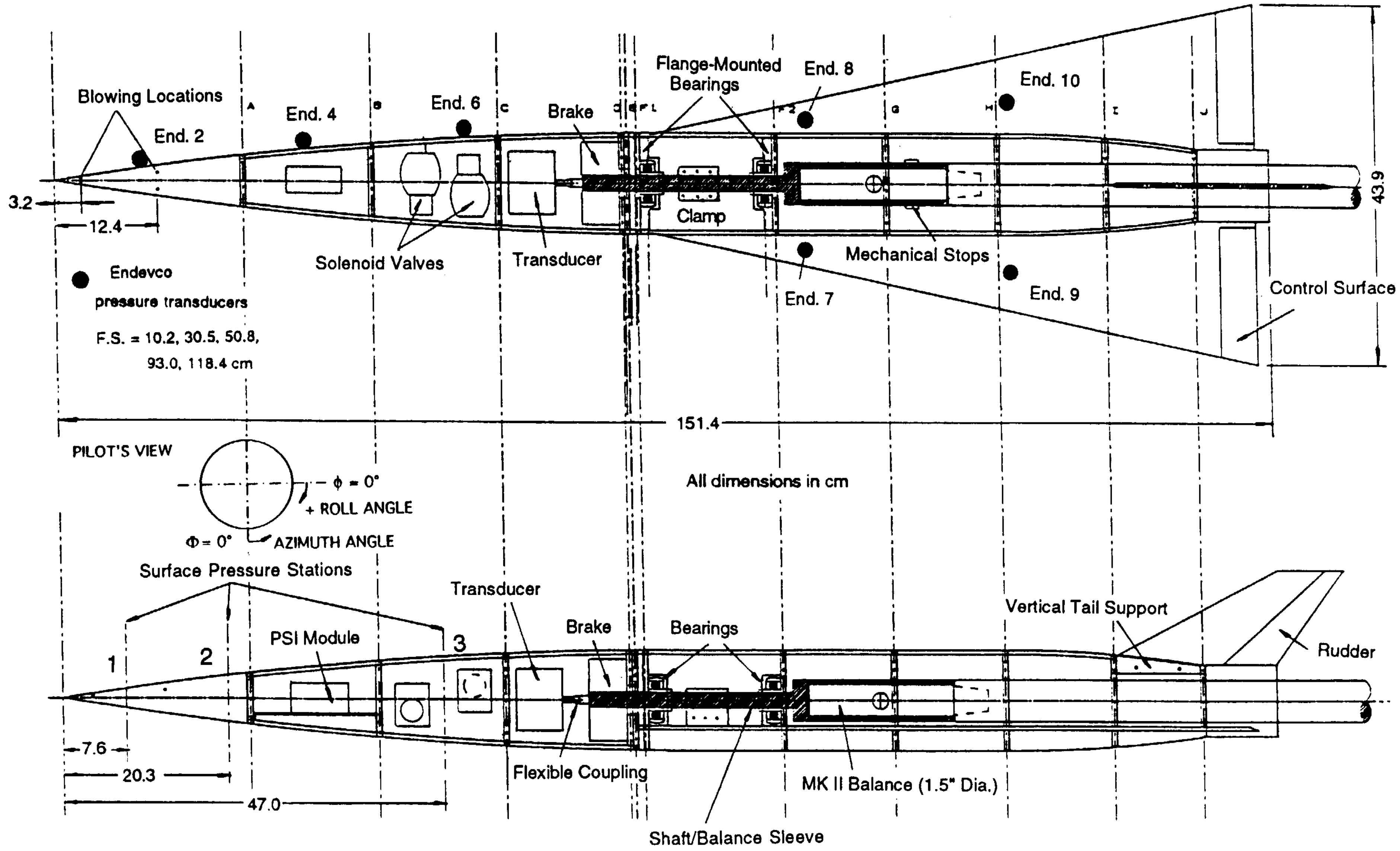

Figure 18 - Schematic of the Wind Tunnel Model

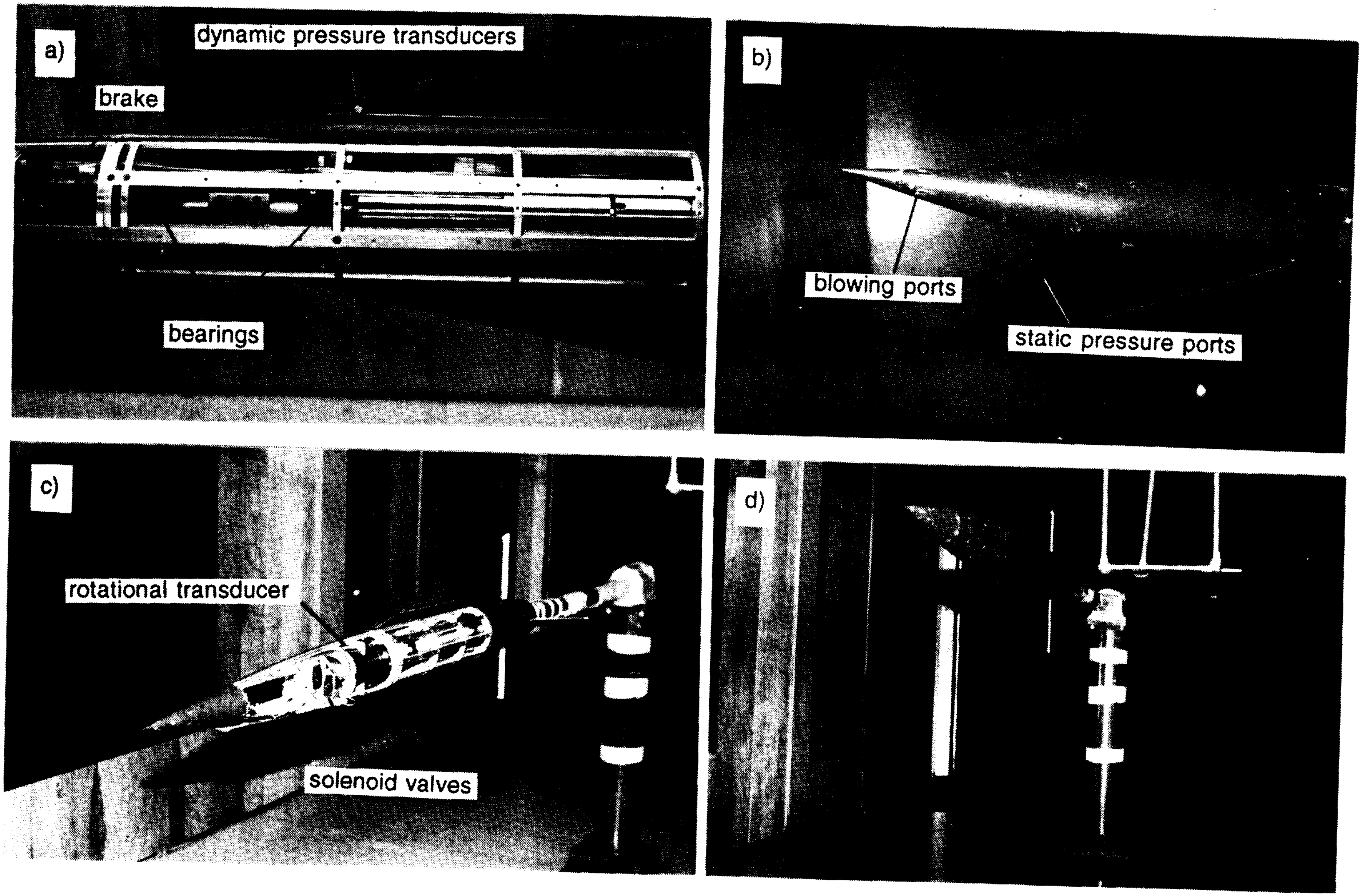

Figure 19 - Wind Tunnel Model; a) Free-to-roll Hardware, b) Blowing Ports, c) General Instrumentation, d) Sting Setup

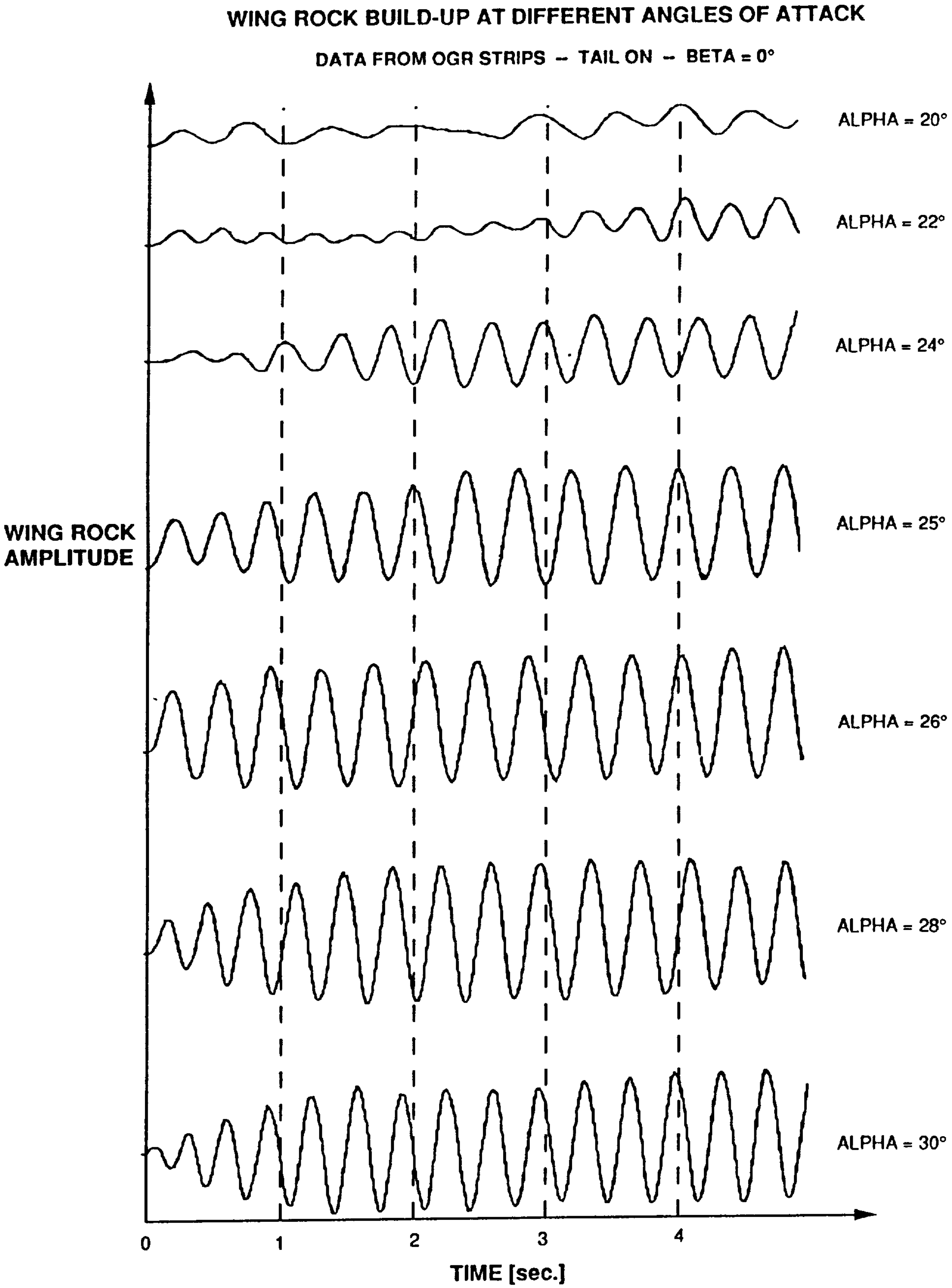

Figure 20 - Wing Rock Buildup at Different Angles of Attack (q = 958 Pa, Tail On)

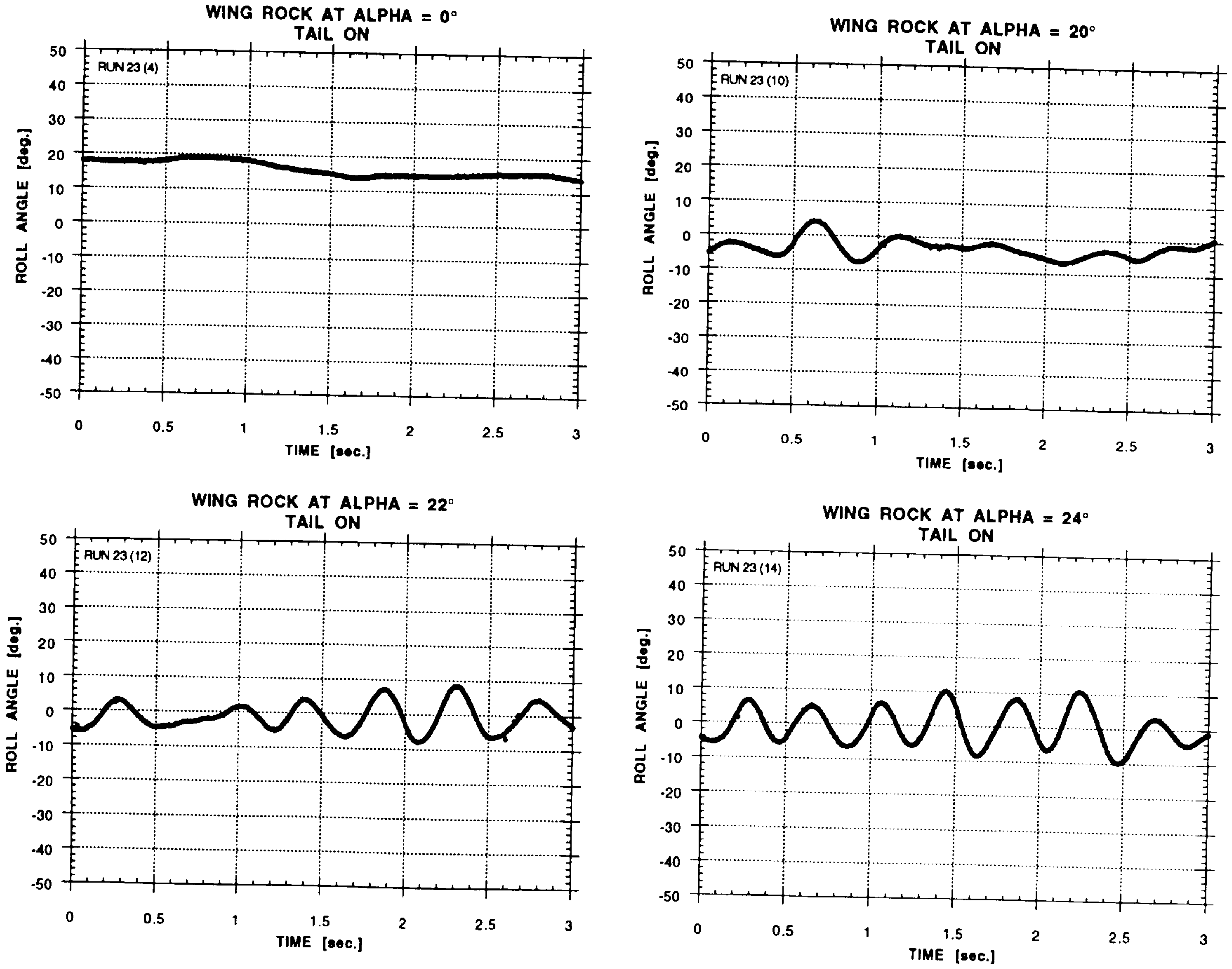

Figure 21 - Wing Rock at Different Angles of Attack (q = 718 Pa, Tail On)

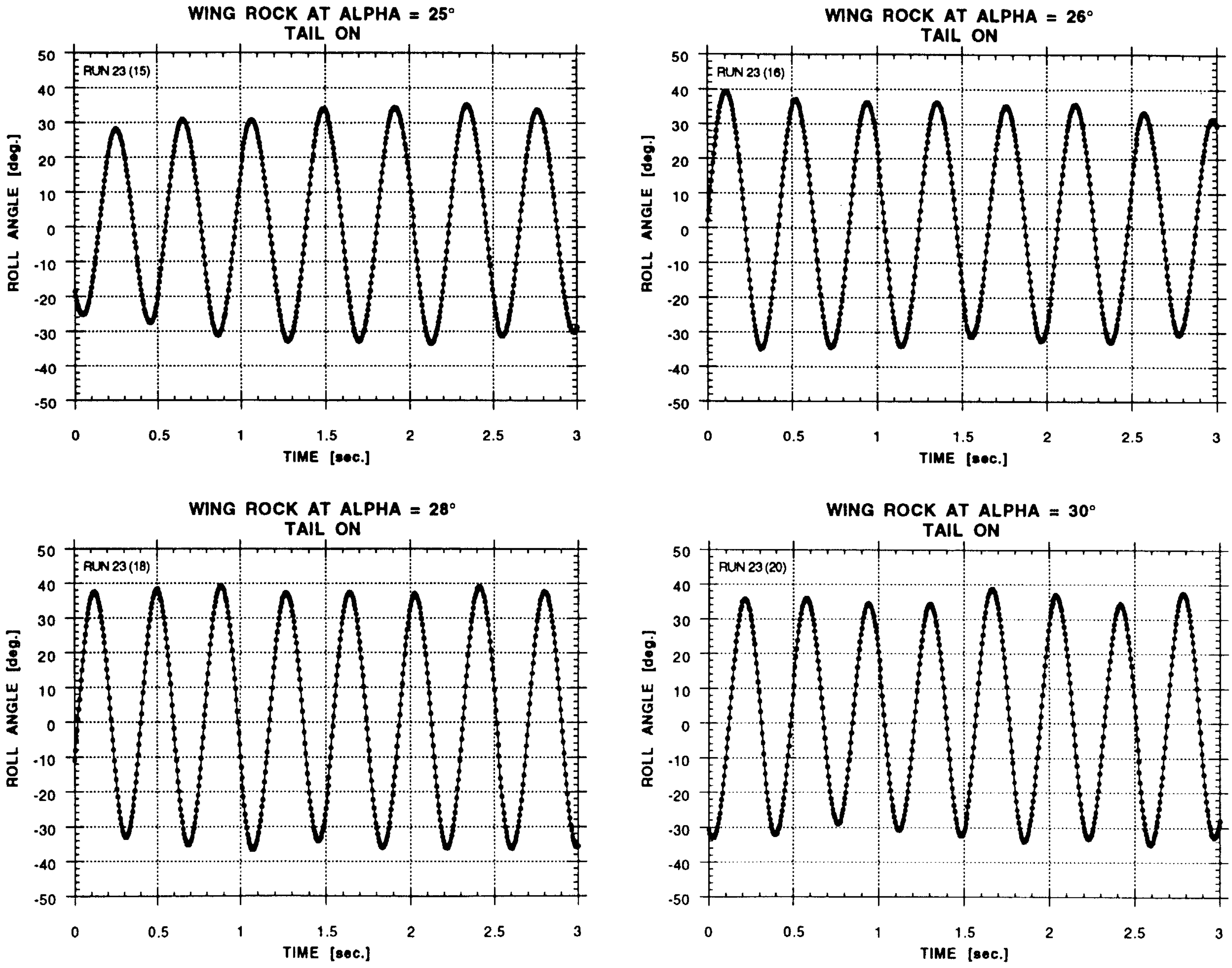
WING ROCK AT ALPHA = 25° TAIL ON

WING ROCK AT ALPHA = 26° TAIL ON

WING ROCK AT ALPHA = 28° TAIL ON

WING ROCK AT ALPHA = 30° TAIL ON

Figure 21 - Concluded

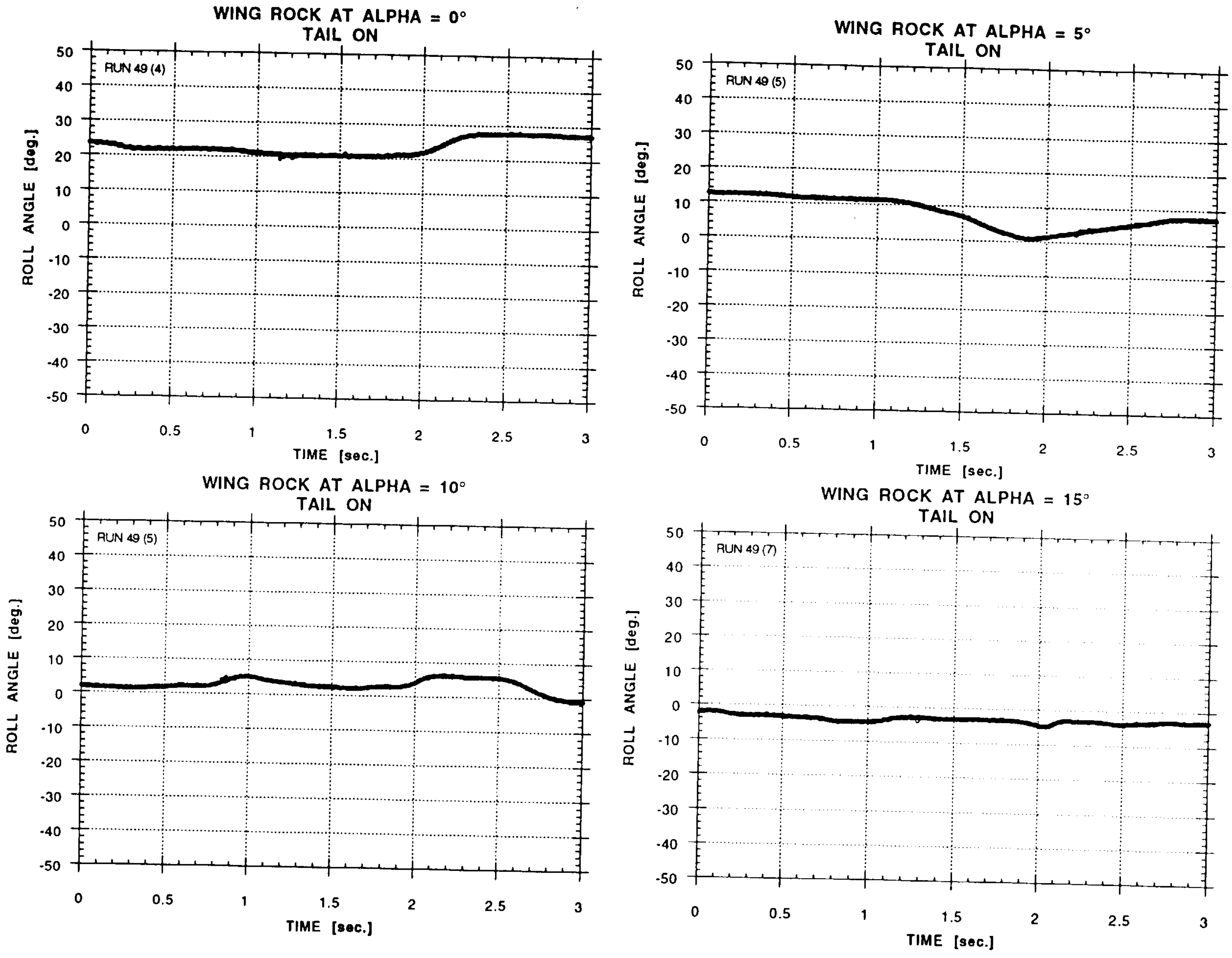

Figure 22 - Wing Rock at Different Angles of Attack (q = 958 Pa, Tail On)

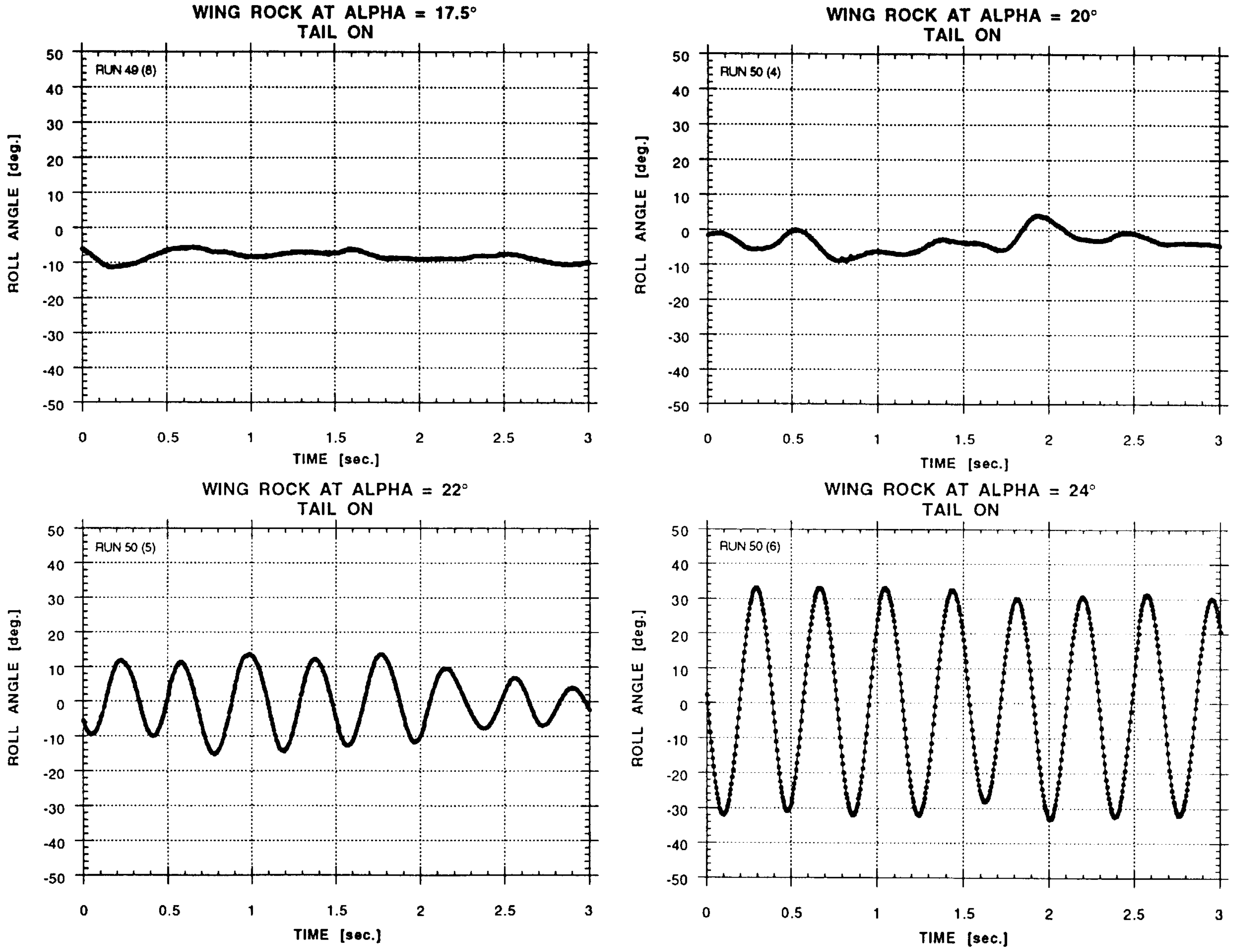

Figure 22 - Continued

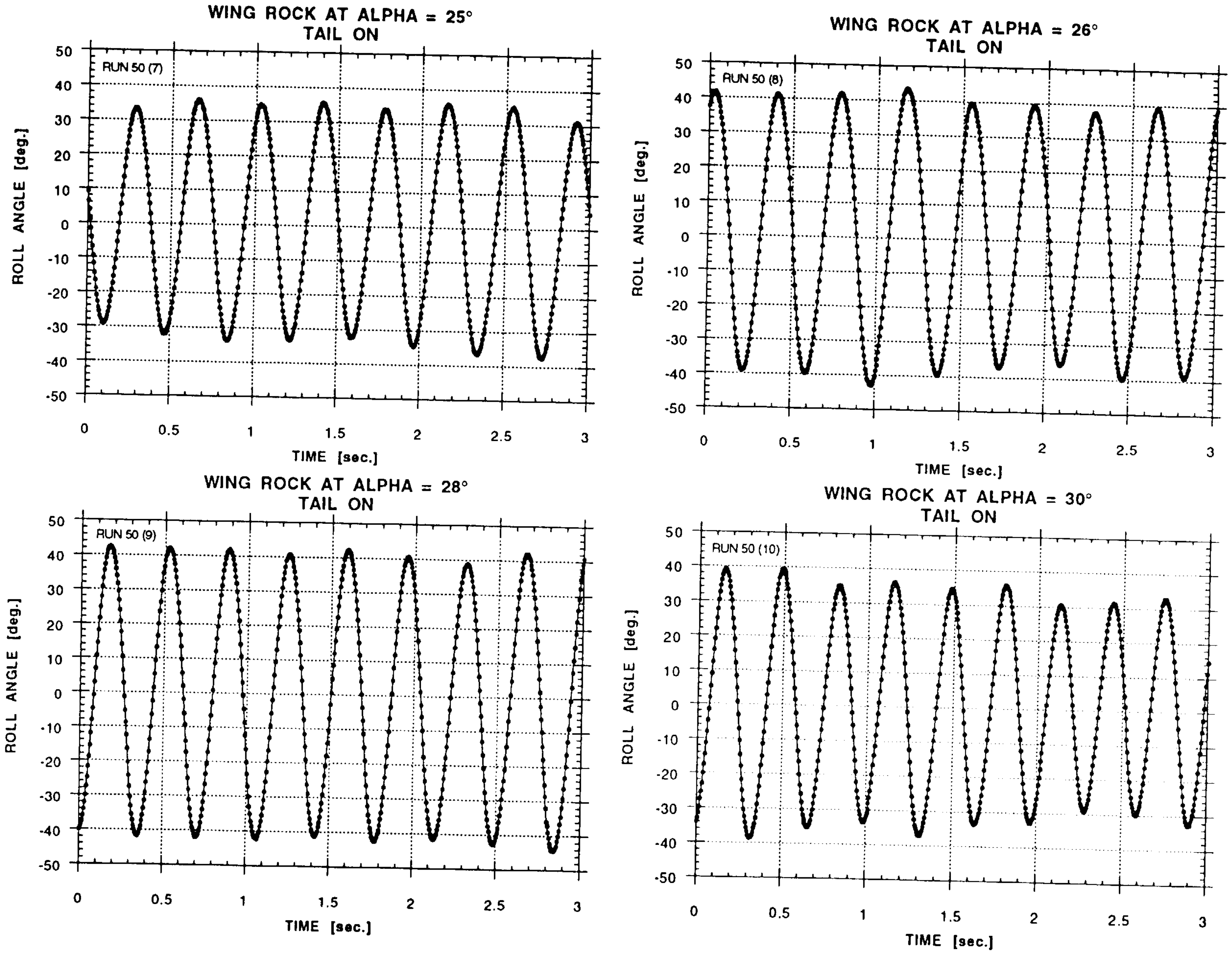

WING ROCK AT ALPHA = 25°
TAIL ON

WING ROCK AT ALPHA = 26°
TAIL ON

WING ROCK AT ALPHA = 28°
TAIL ON

WING ROCK AT ALPHA = 30°
TAIL ON

Figure 22 - Concluded

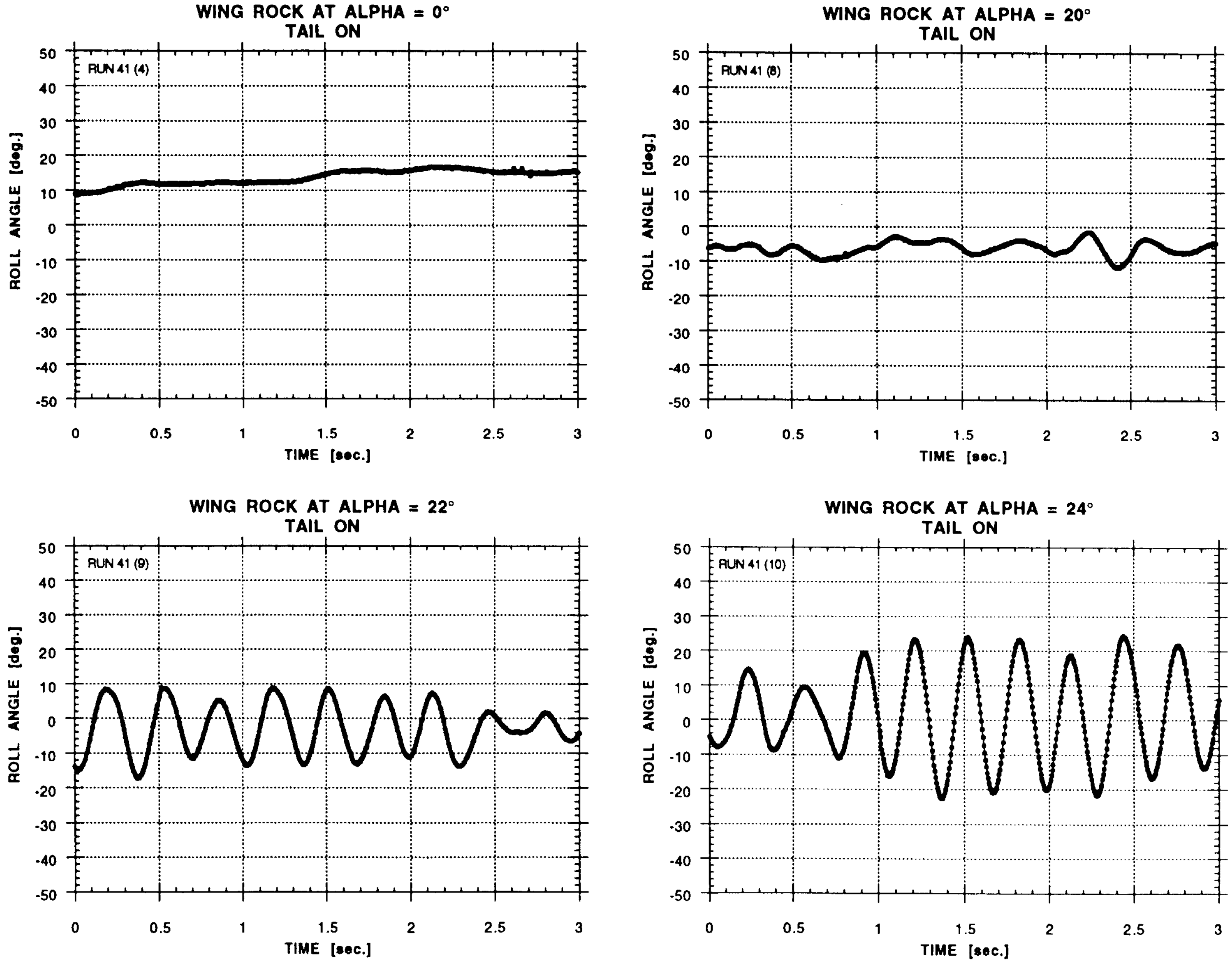
WING ROCK AT ALPHA = 0°
TAIL ON

WING ROCK AT ALPHA = 20°
TAIL ON

WING ROCK AT ALPHA = 22°
TAIL ON

WING ROCK AT ALPHA = 24°
TAIL ON

Figure 23 - Wing Rock at Different Angles of Attack (q = 1436 Pa, Tail On)

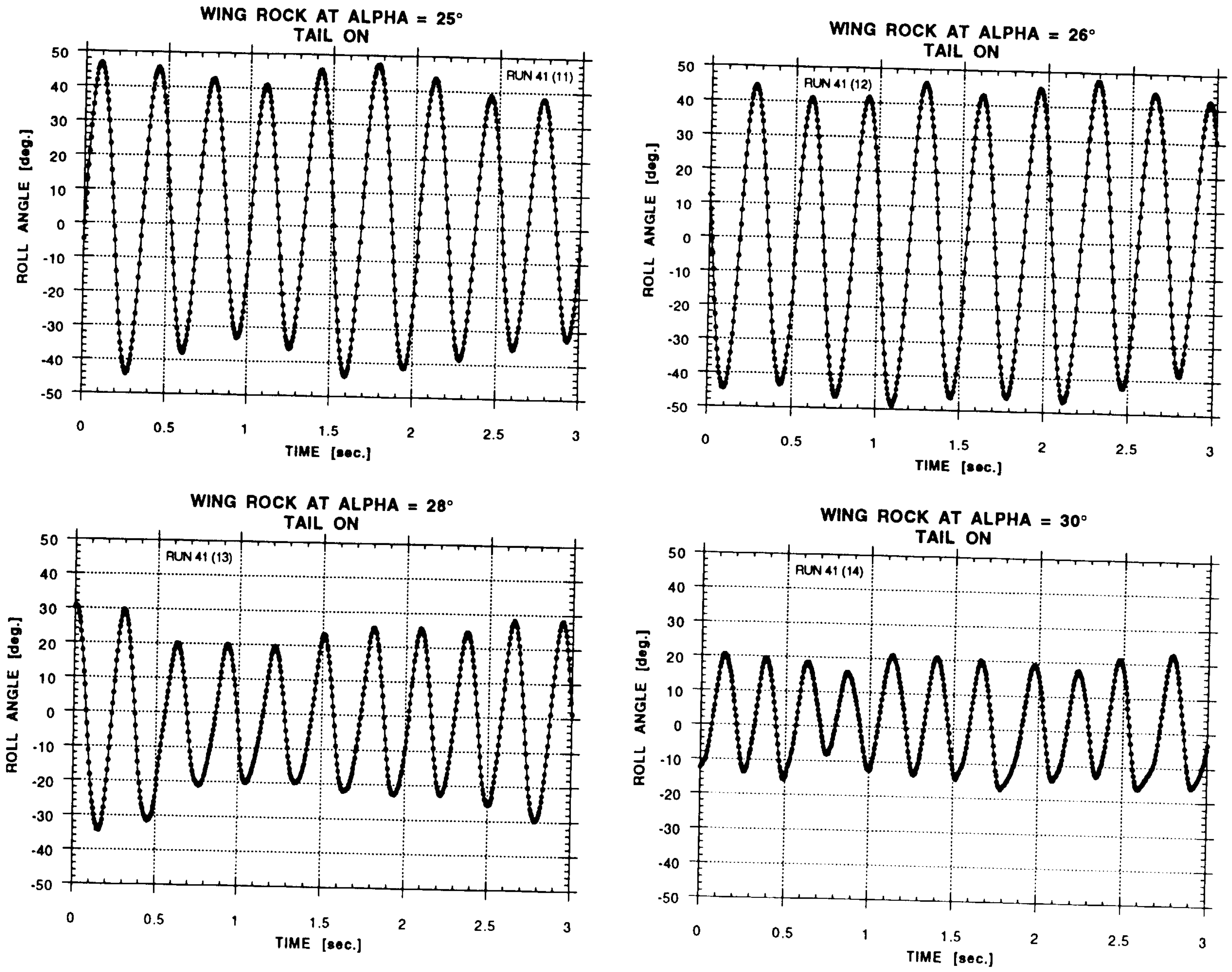
WING ROCK AT ALPHA = 25°
TAIL ON

WING ROCK AT ALPHA = 26°
TAIL ON

WING ROCK AT ALPHA = 28°
TAIL ON

WING ROCK AT ALPHA = 30°
TAIL ON

Figure 23 - Concluded

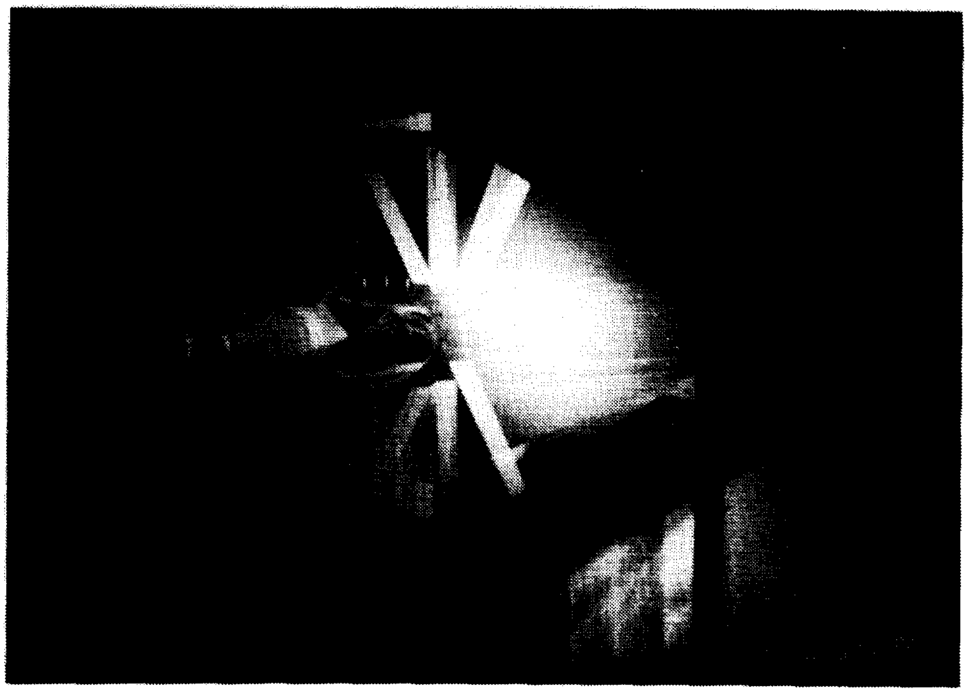

Figure 24 - Multi-exposure Photo of Wing Rock at α = 30°

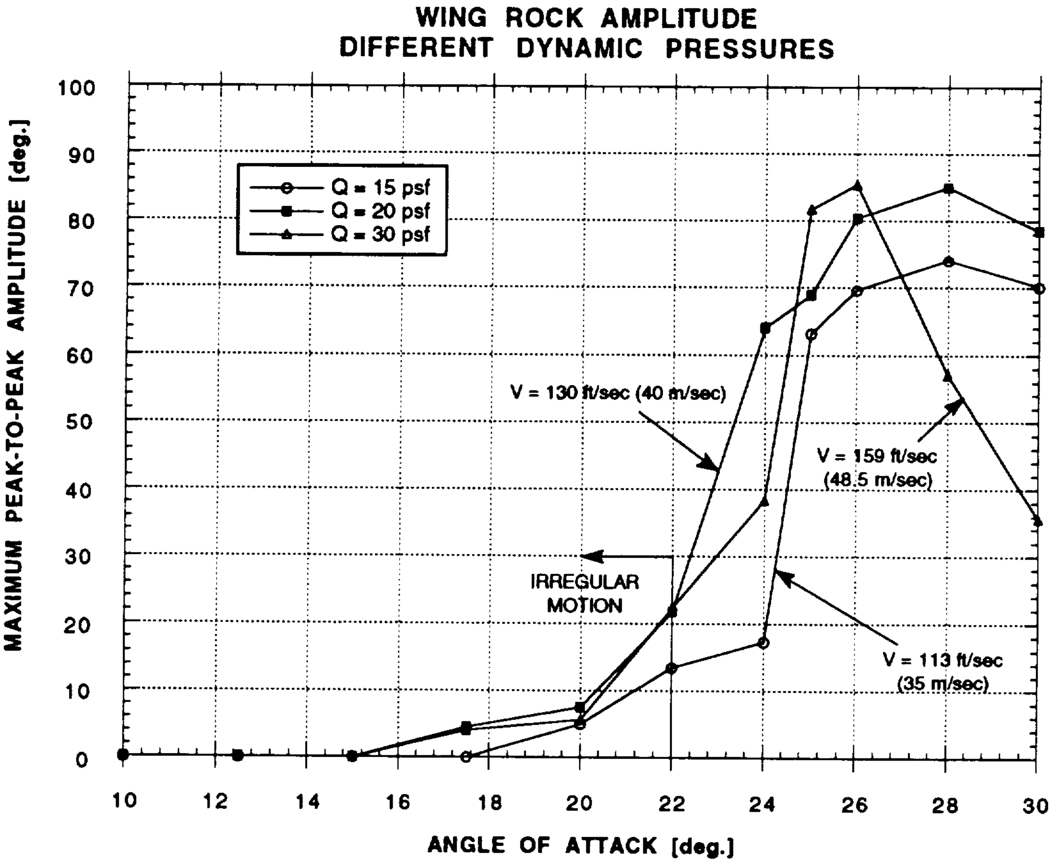

Figure 25 - Effect of Free-Stream Velocity on Wing Rock Amplitude

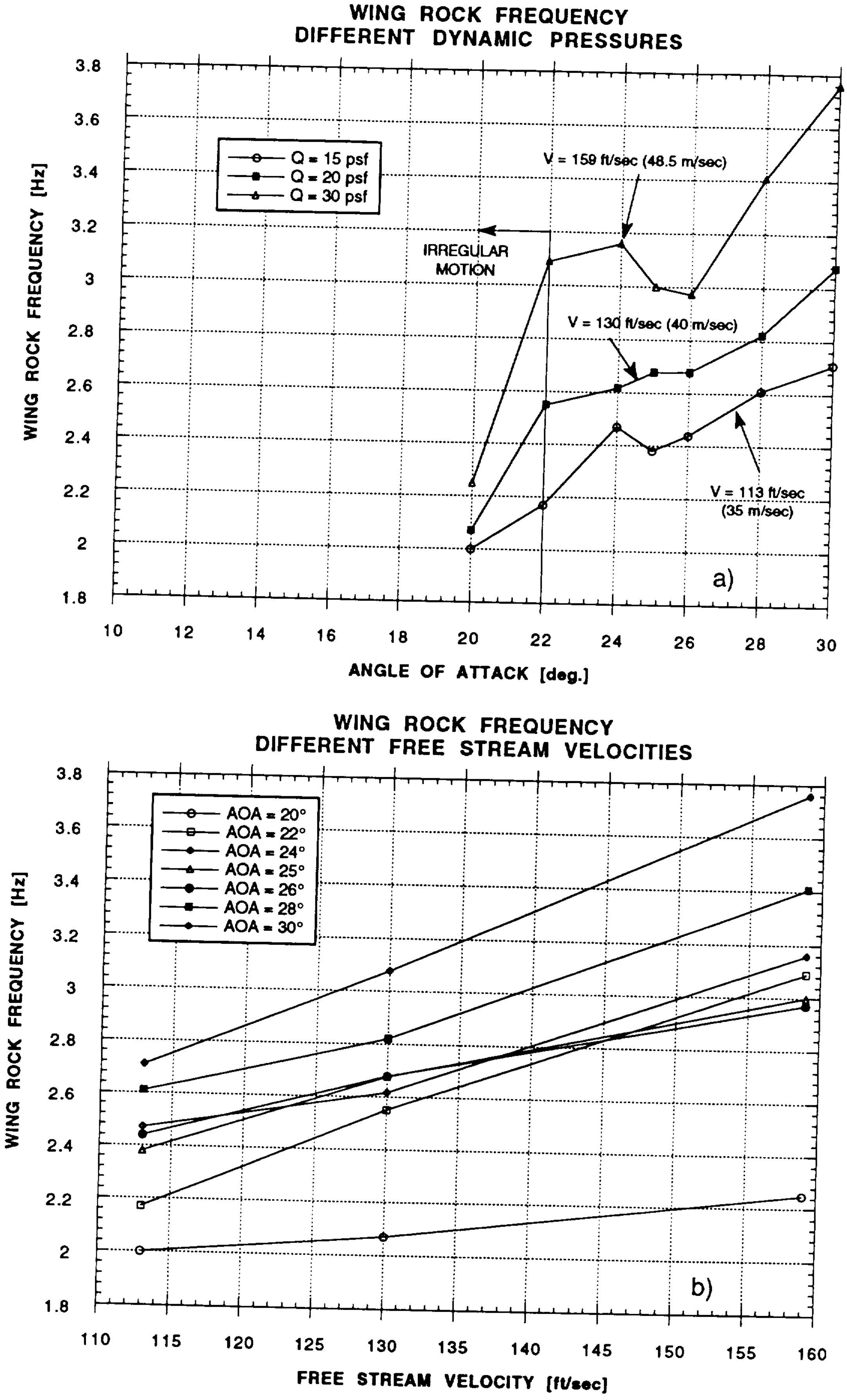

Figure 26 - Effect of Free-Stream Velocity on Wing Rock Frequency

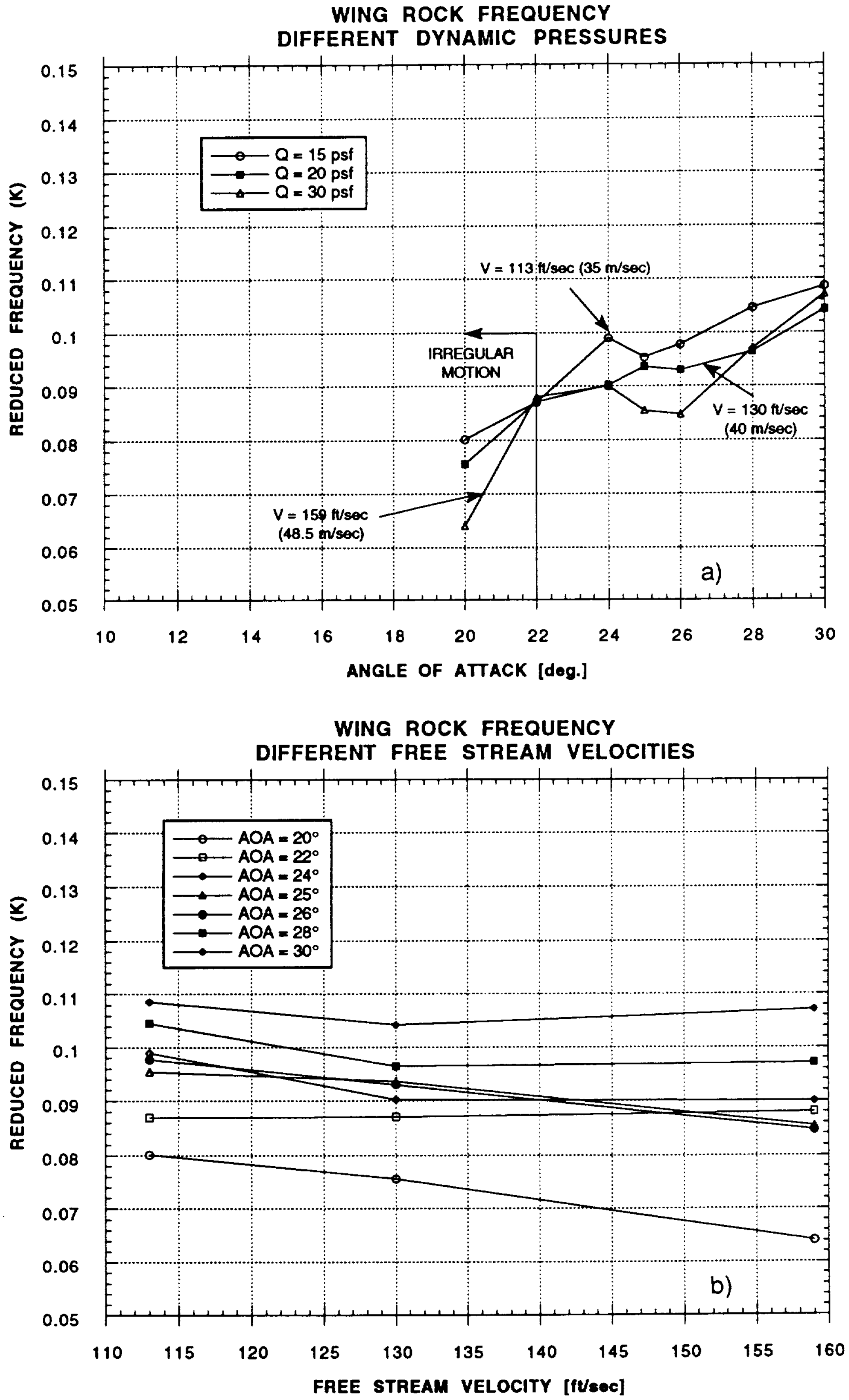

Figure 27 - Effect of Free-Stream Velocity on Wing Rock Reduced Frequency

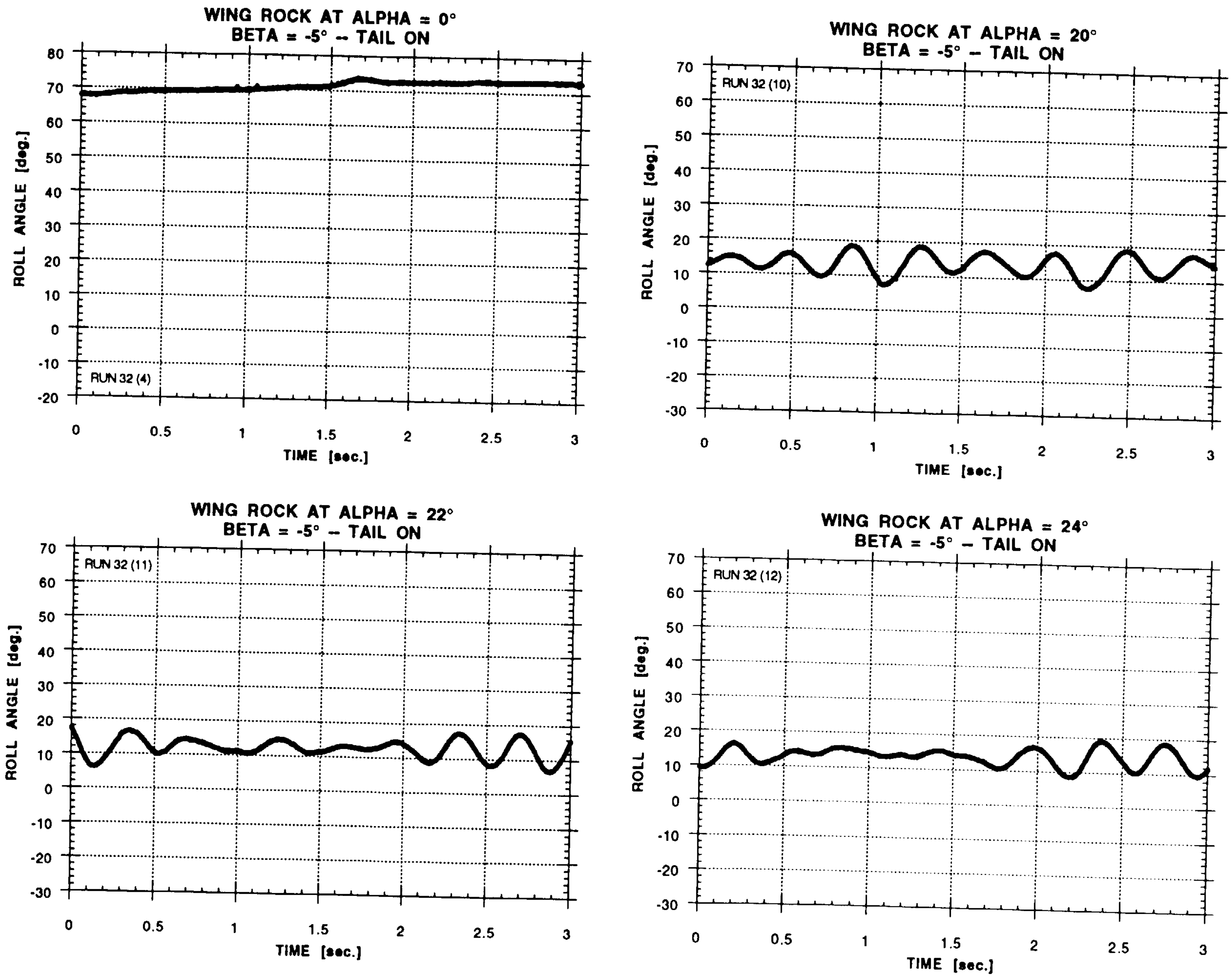

Figure 28 - Wing Rock at Different Angles of Attack (β = -5°, q = 718 Pa, Tail On)

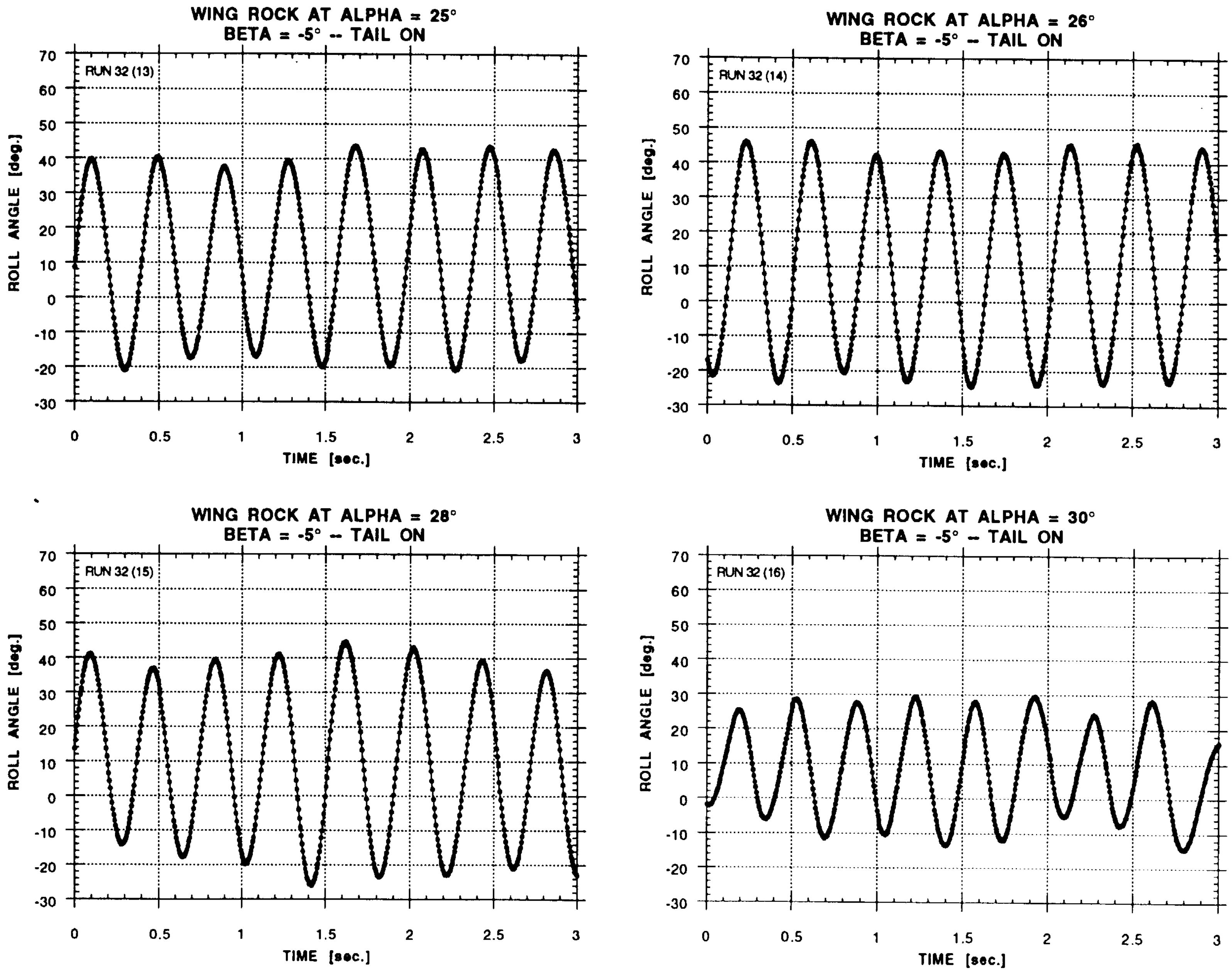

Figure 28 - Concluded

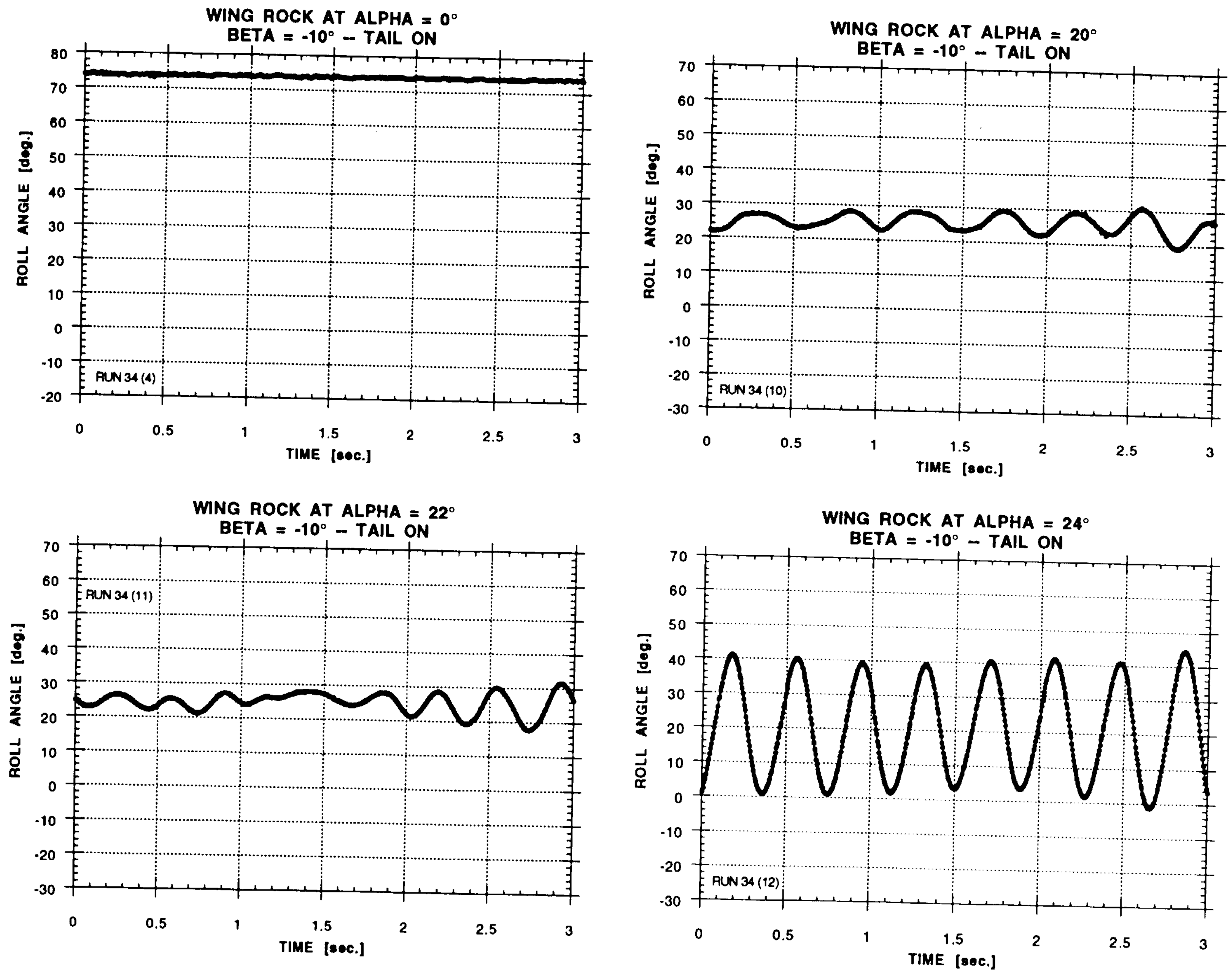

Figure 29 - Wing Rock at Different Angles of Attack (β = -10°, q = 718 Pa, Tail On)

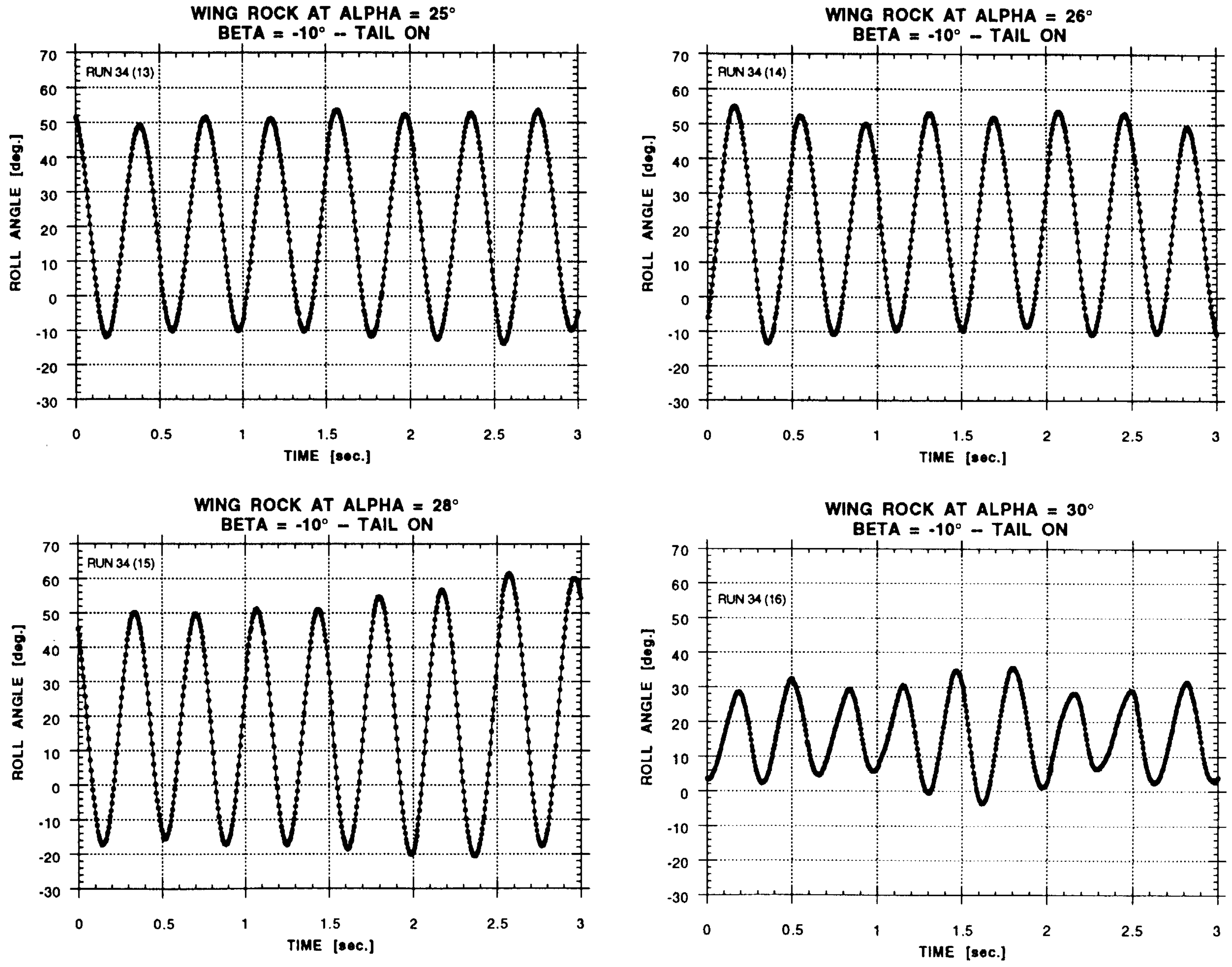

Figure 29 - Concluded

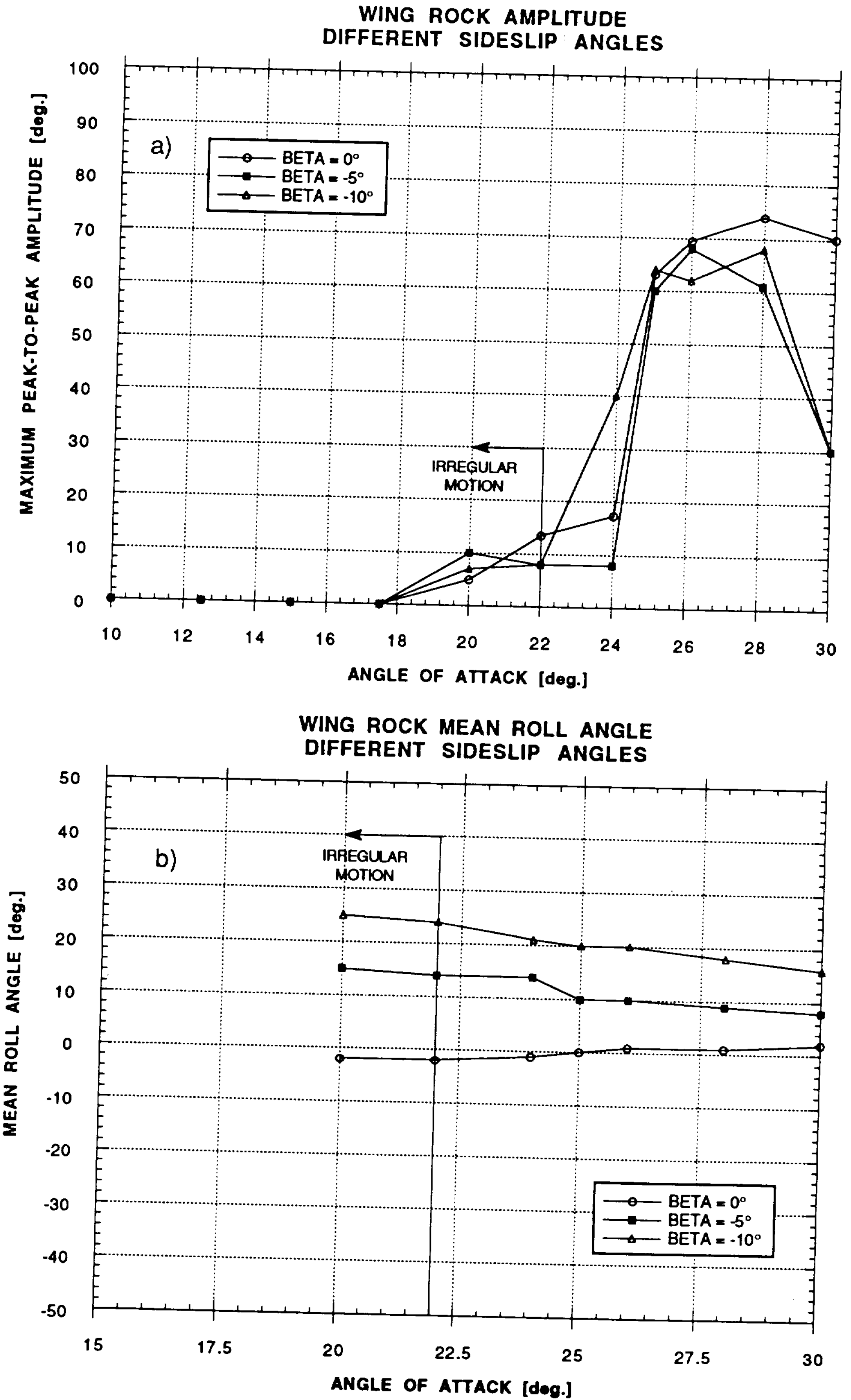

Figure 30 - Effect of Mean Sideslip Angle on Wing Rock
a) Maximum Peak-to-Peak Amplitude, b) Mean Roll Angle

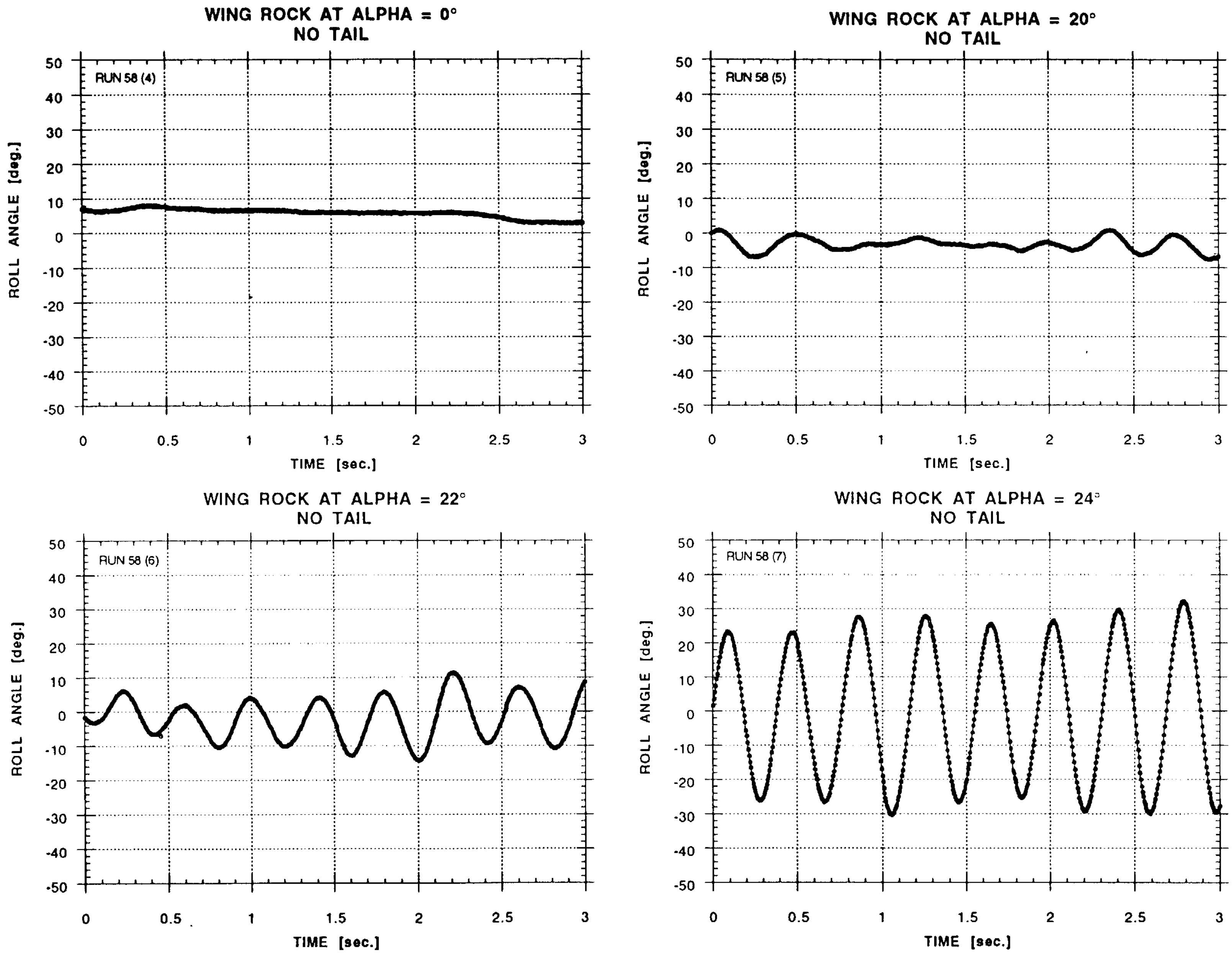

Figure 31 - Wing Rock at Different Angles of Attack (q = 958 Pa, Tail Off)

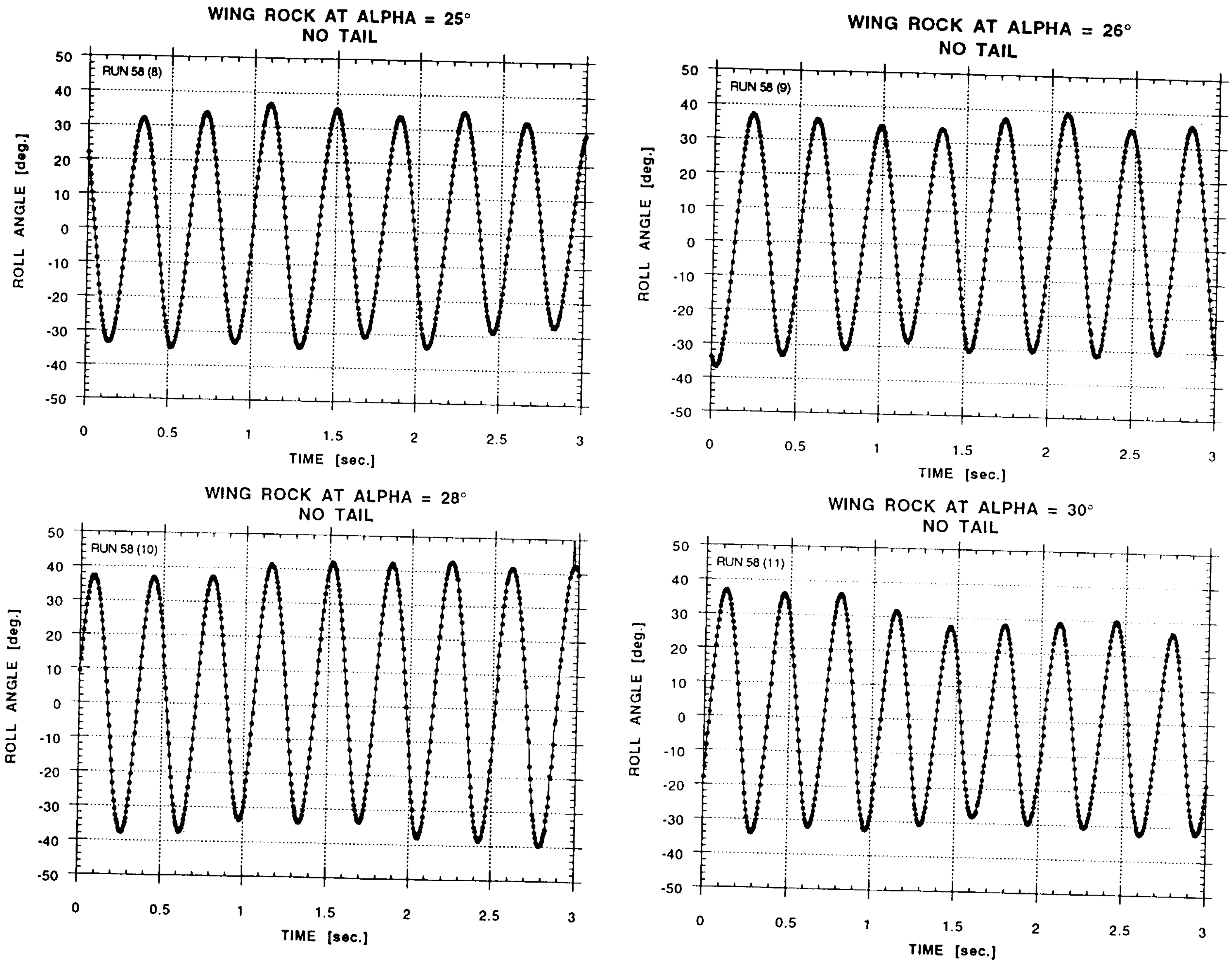
WING ROCK AT ALPHA = 25° NO TAIL

WING ROCK AT ALPHA = 26° NO TAIL

WING ROCK AT ALPHA = 28° NO TAIL

WING ROCK AT ALPHA = 30° NO TAIL

Figure 31 - Concluded

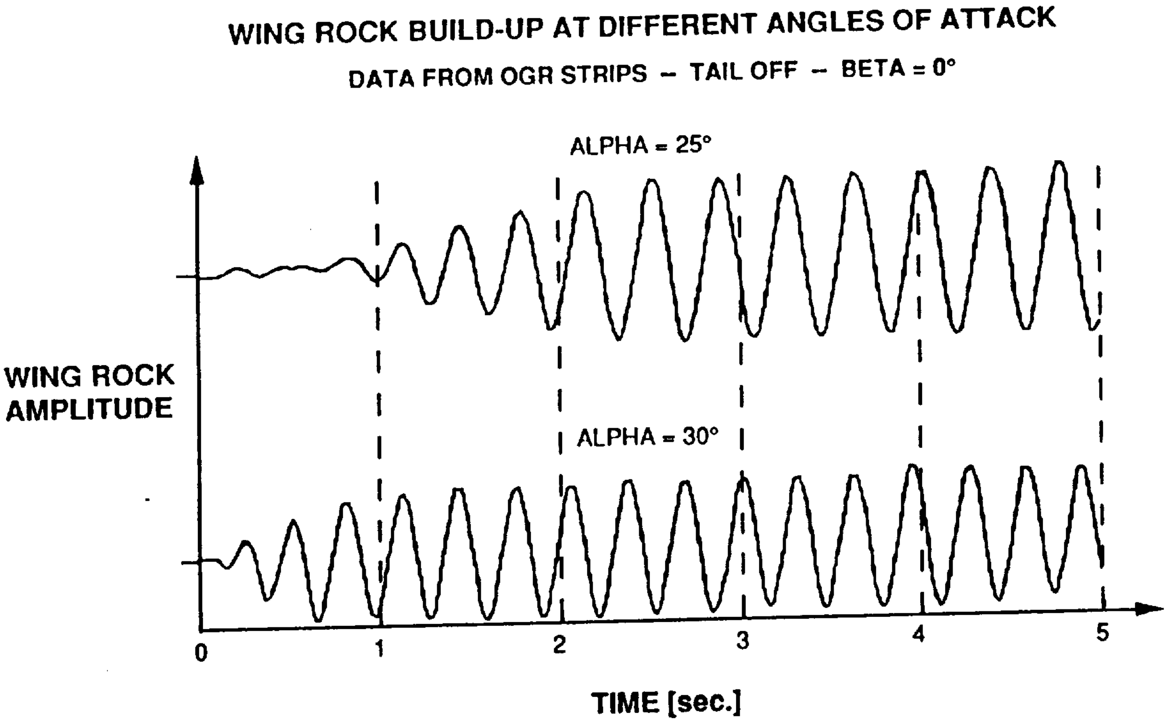

Figure 32 - Wing Rock Buildup at Different Angles of Attack (q = 958 Pa, Tail Off)

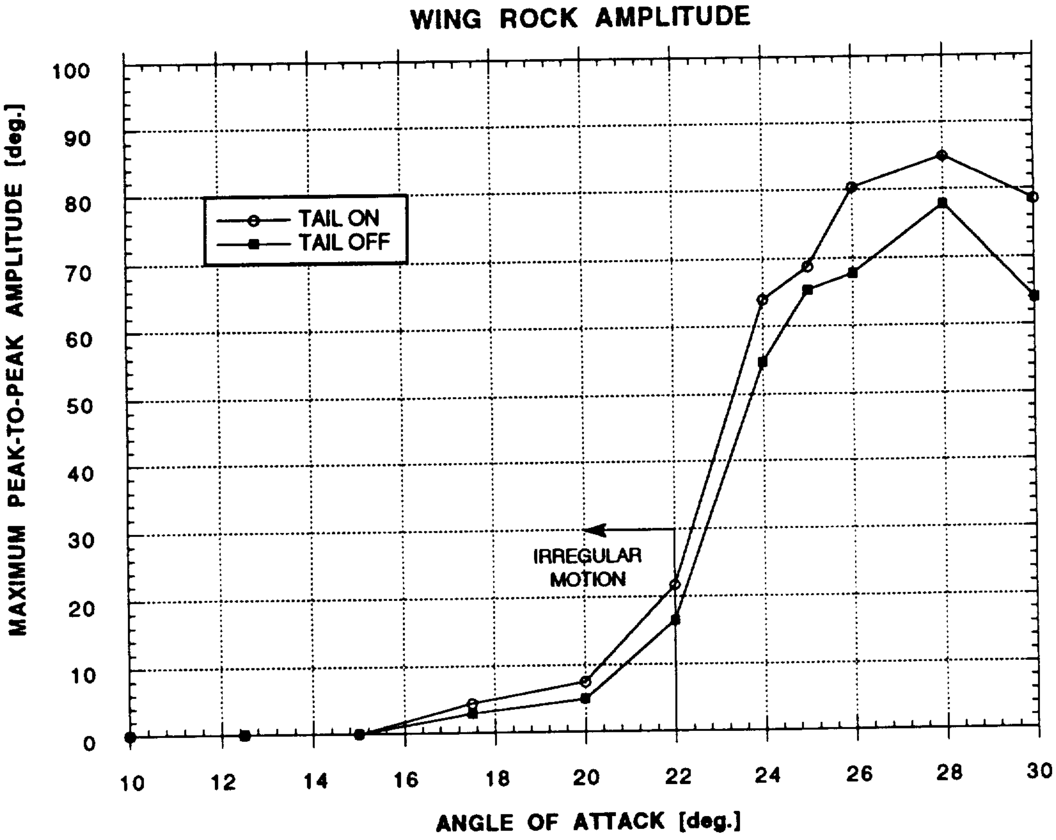

Figure 33 - Effect of Vertical Tail on Wing Rock Amplitude

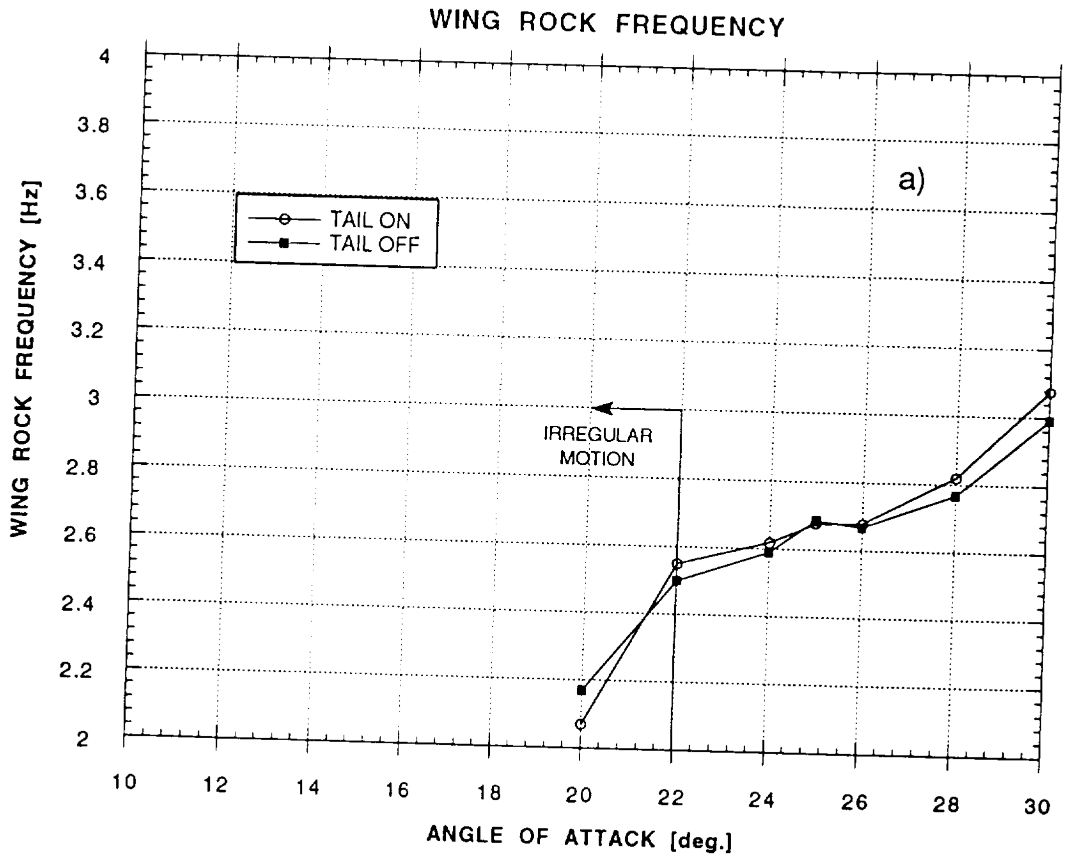

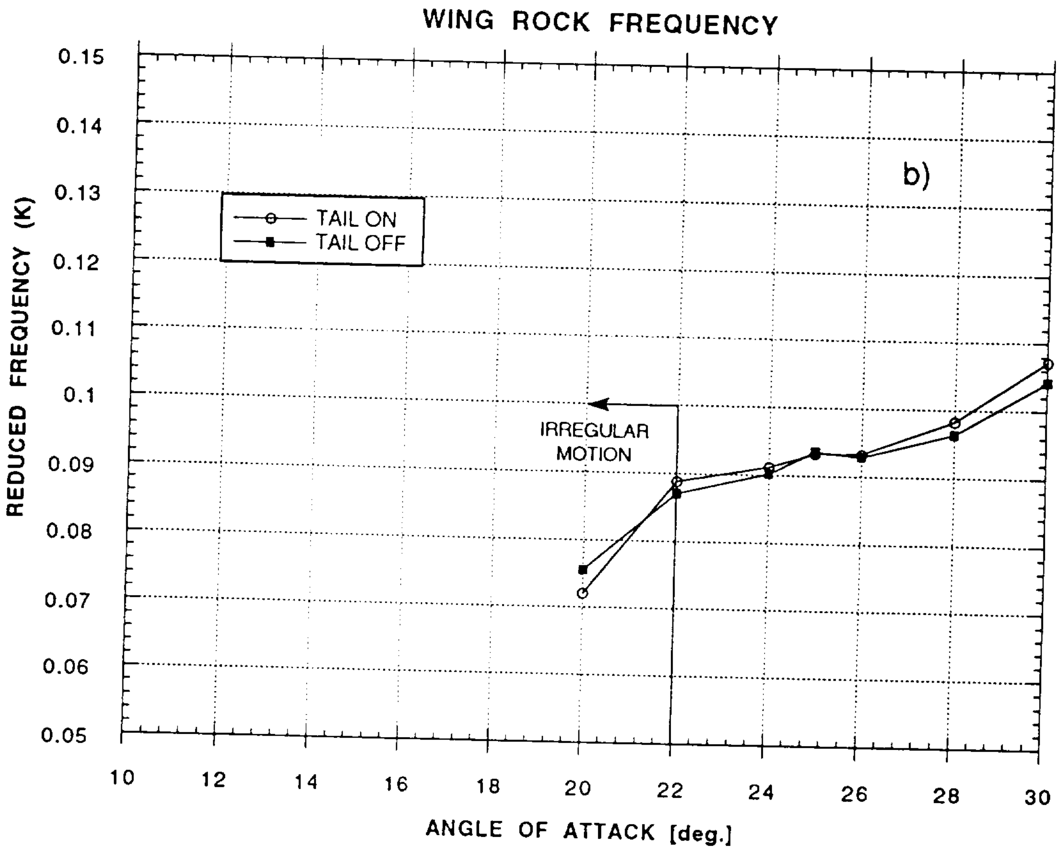

Figure 34 - Effect of Vertical Tail on Wing Rock Frequency

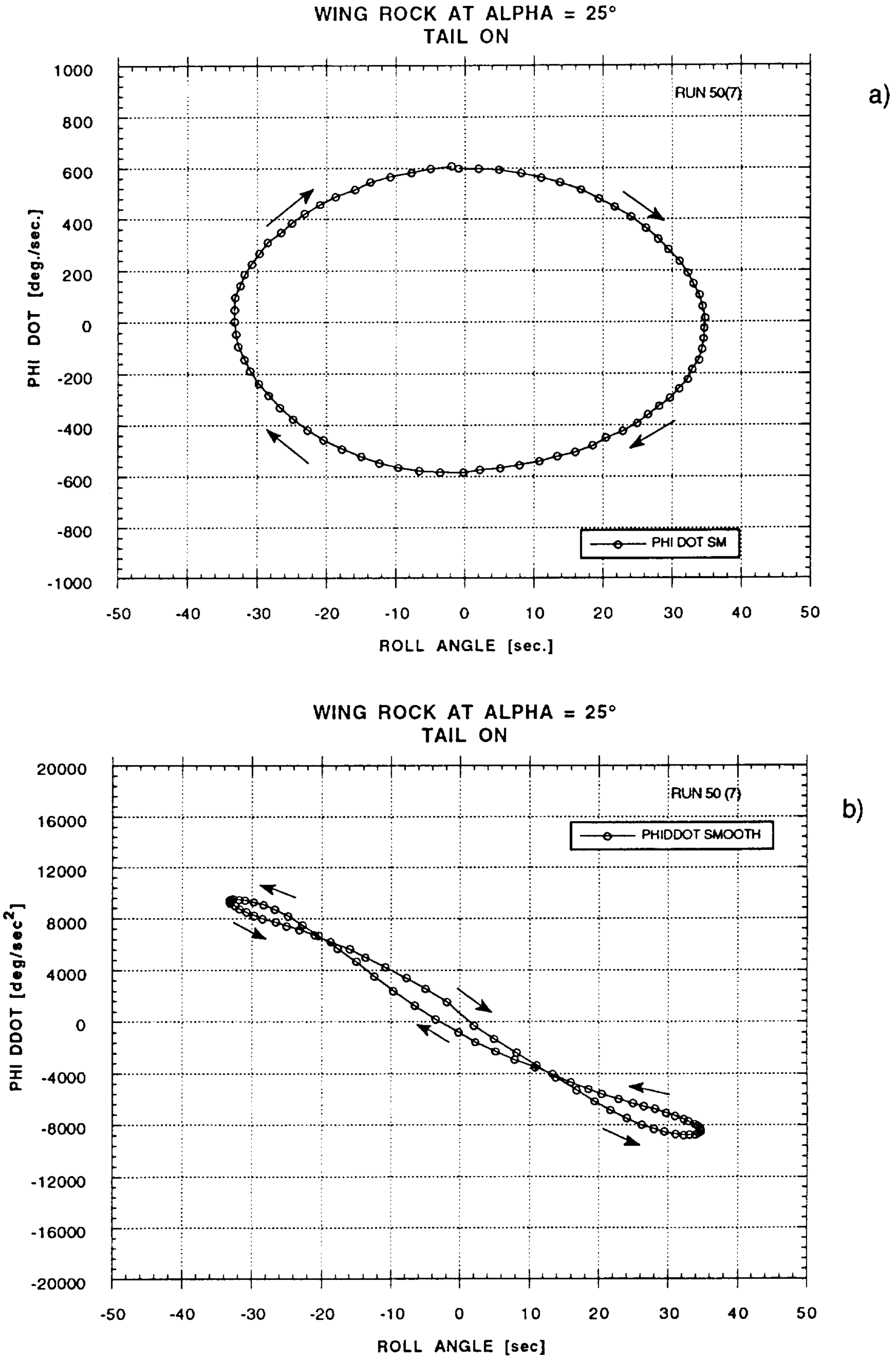

Figure 35 - Phase Plots at $\alpha = 25°$ (q = 958 Pa, Tail On)

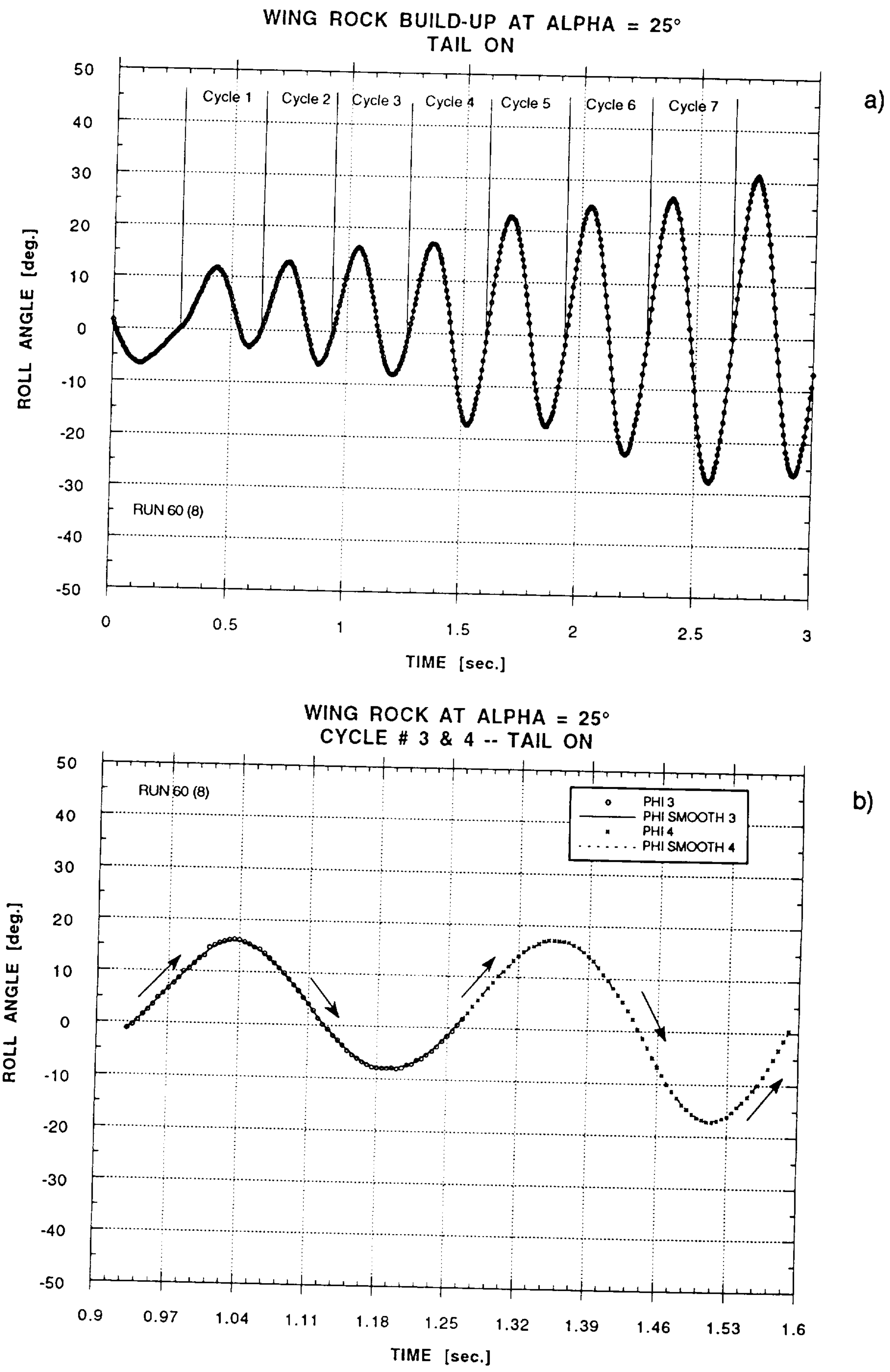

Figure 36 - Wing Rock Buildup at α = 25° (q = 958 Pa, Tail On)

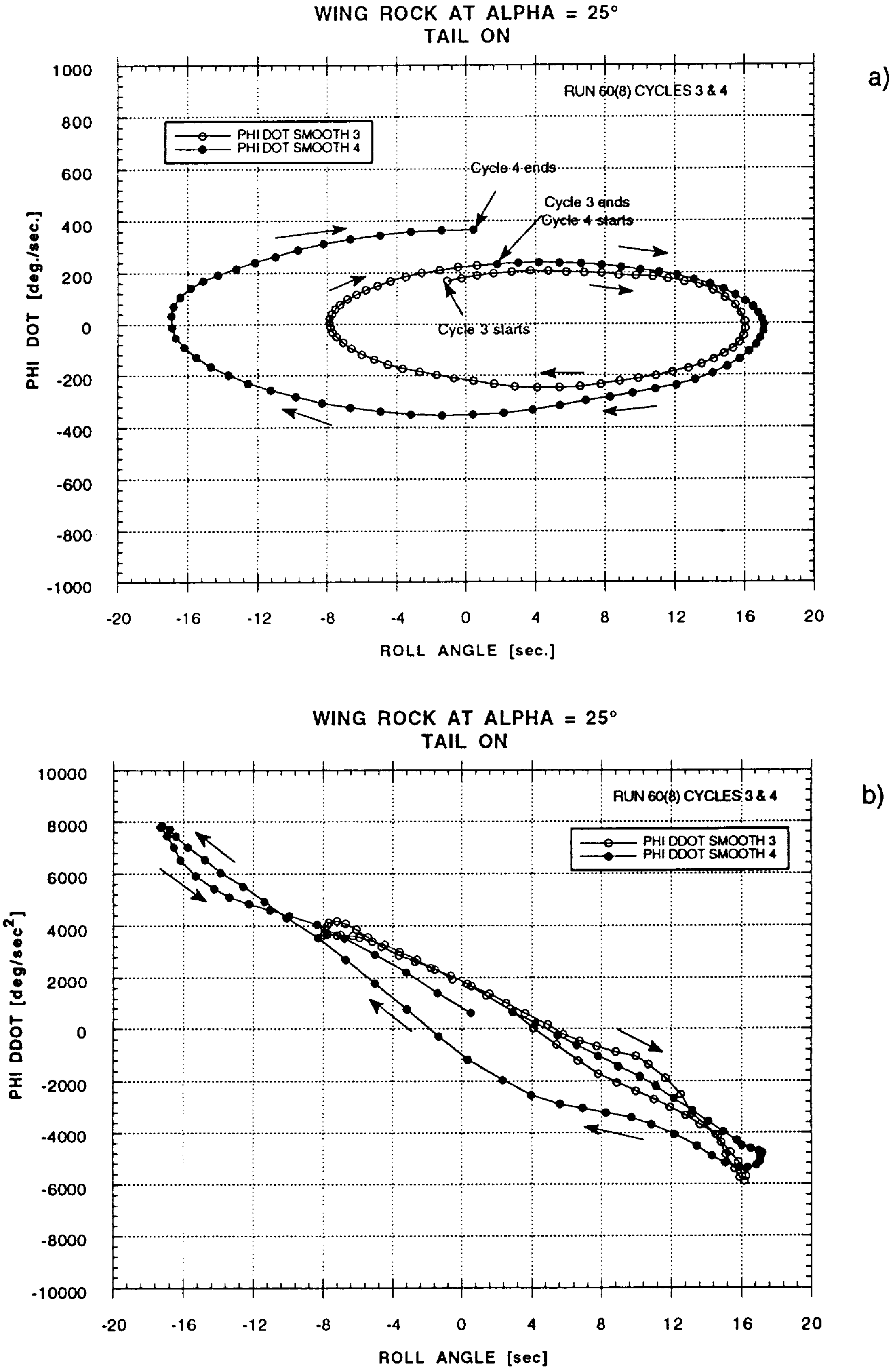

Figure 37 - Phase Plots at α = 25° (q = 958 Pa, Tail On)

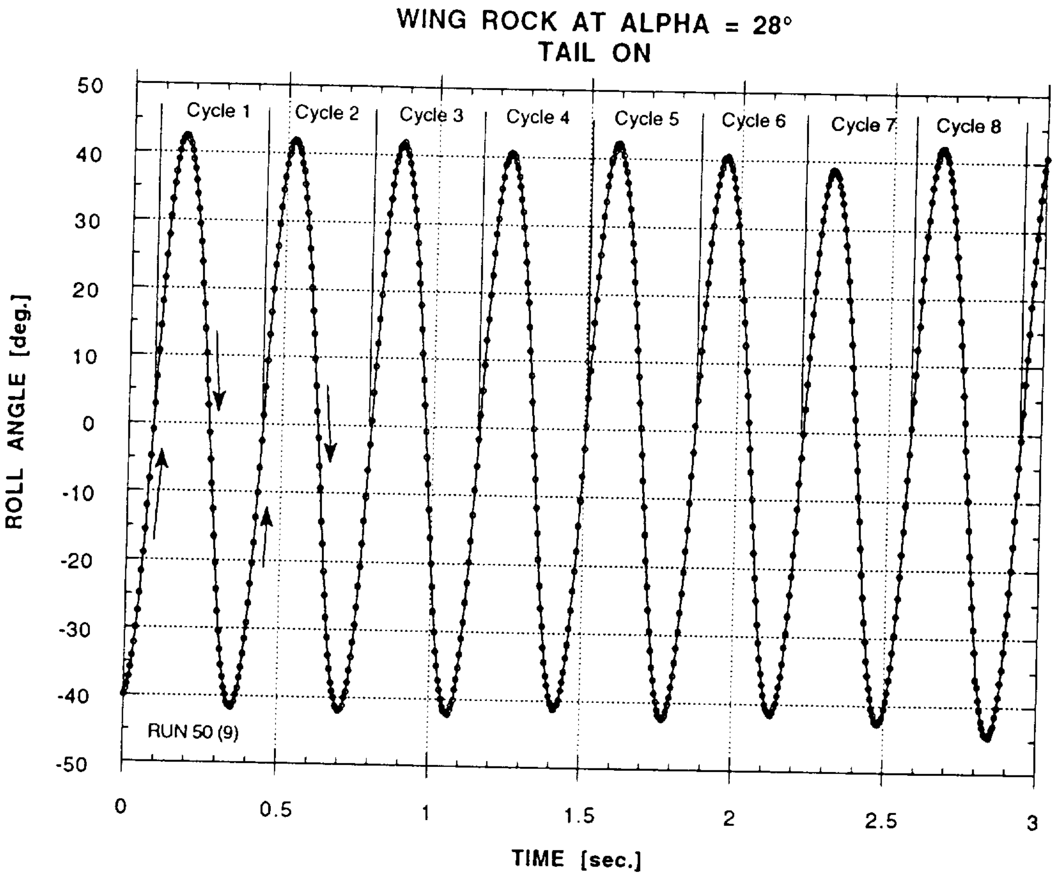

Figure 38 - Wing Rock at α = 28°

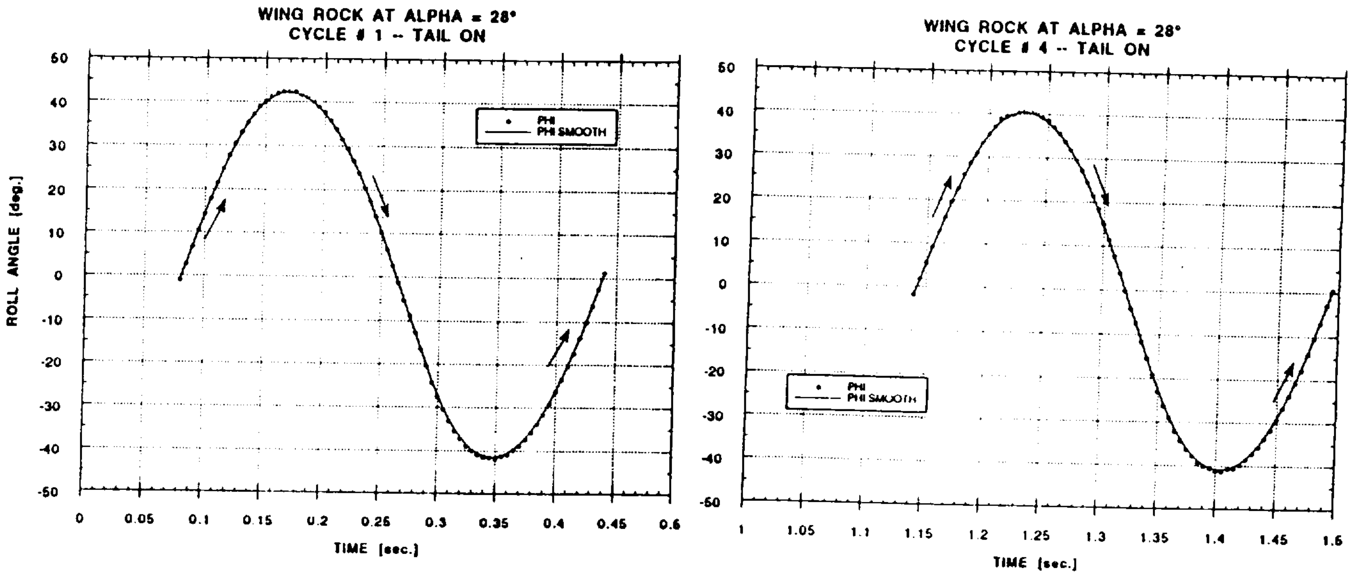

Figure 39 - Different Wing Rock Motion Cycles at α = 28°
(q = 958 Pa, Tail On)

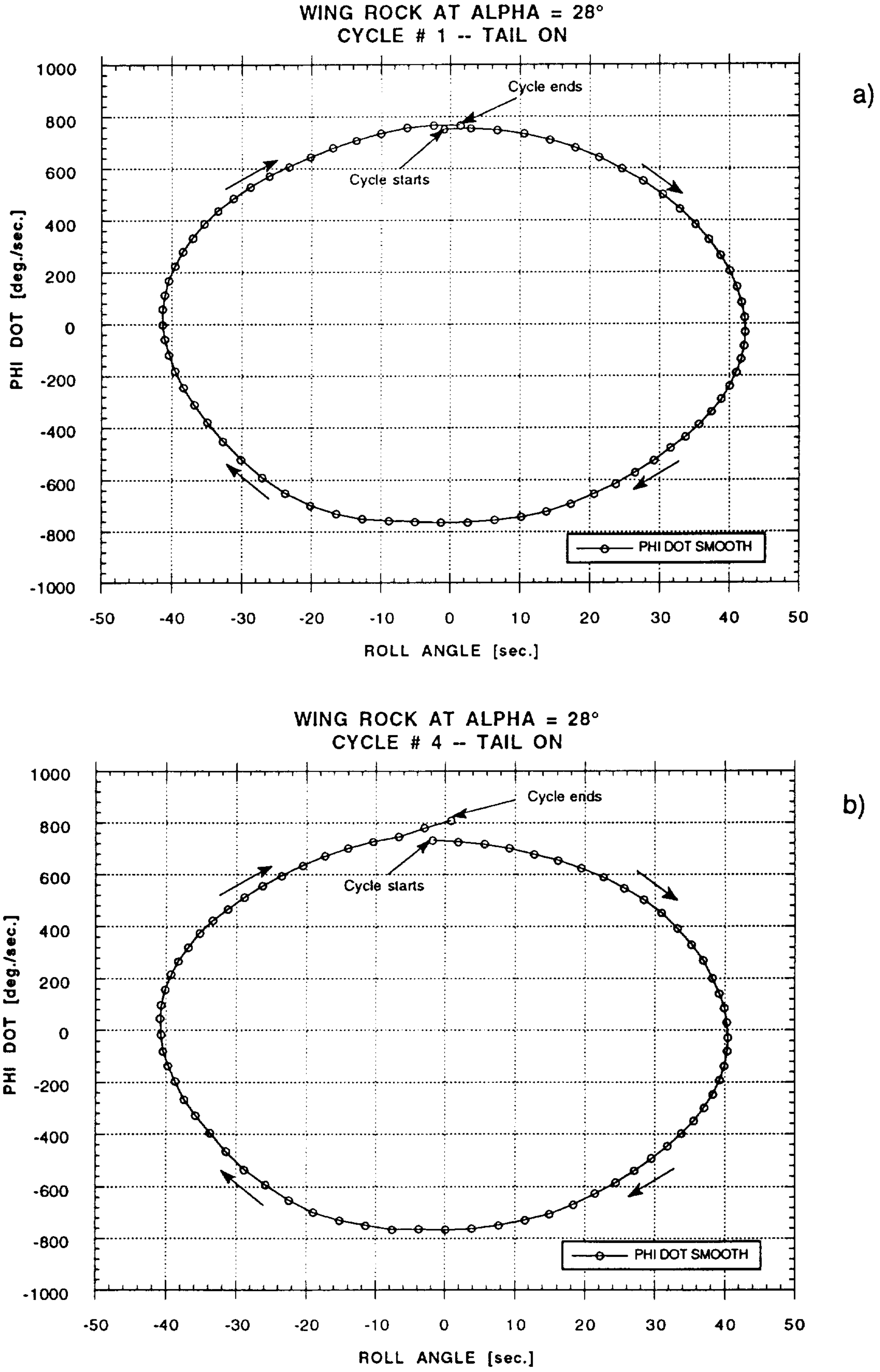

Figure 40 - Phase Plots at α = 28° (Angular Velocity)

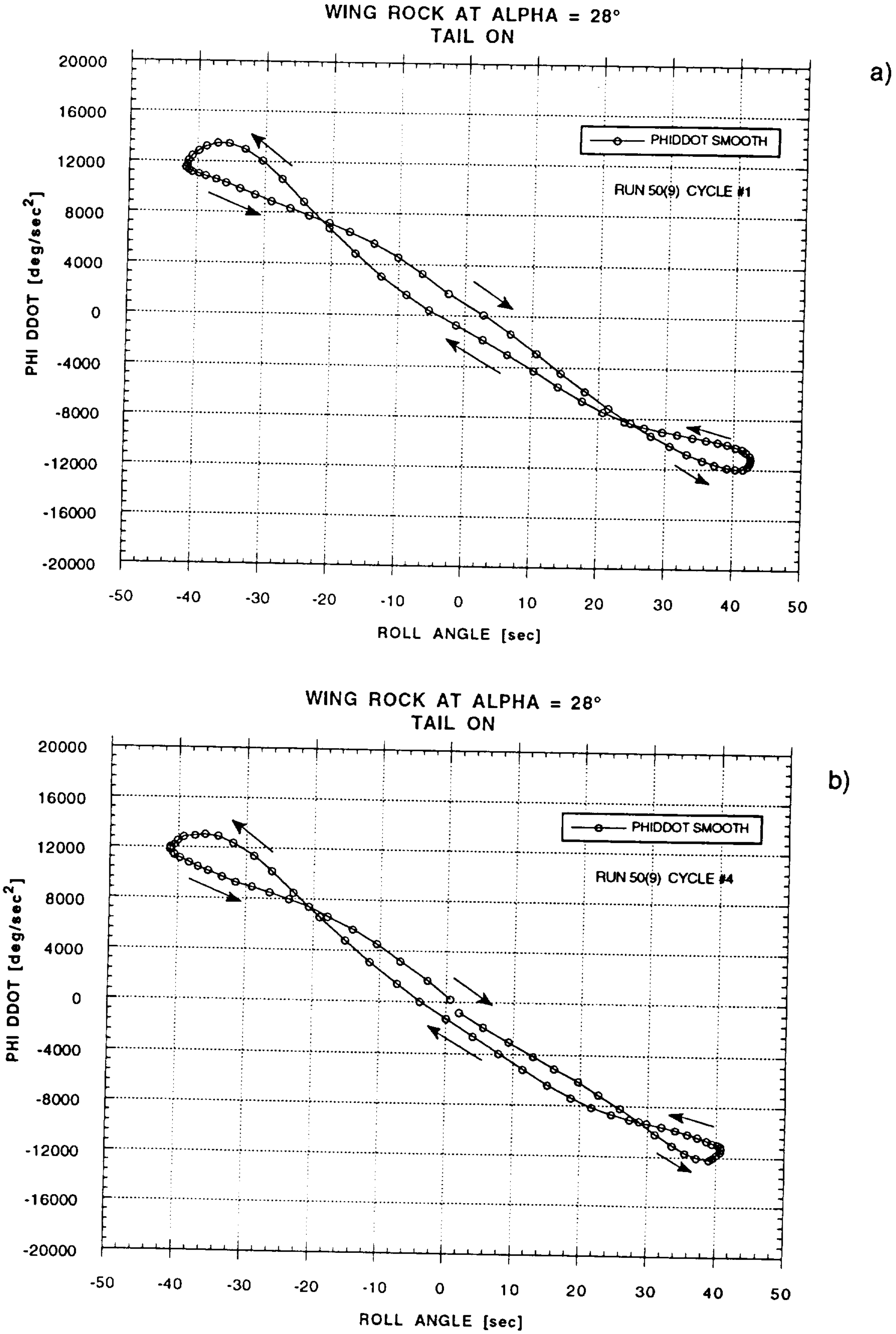

Figure 41 - Phase Plots at α = 28° (Angular Acceleration)

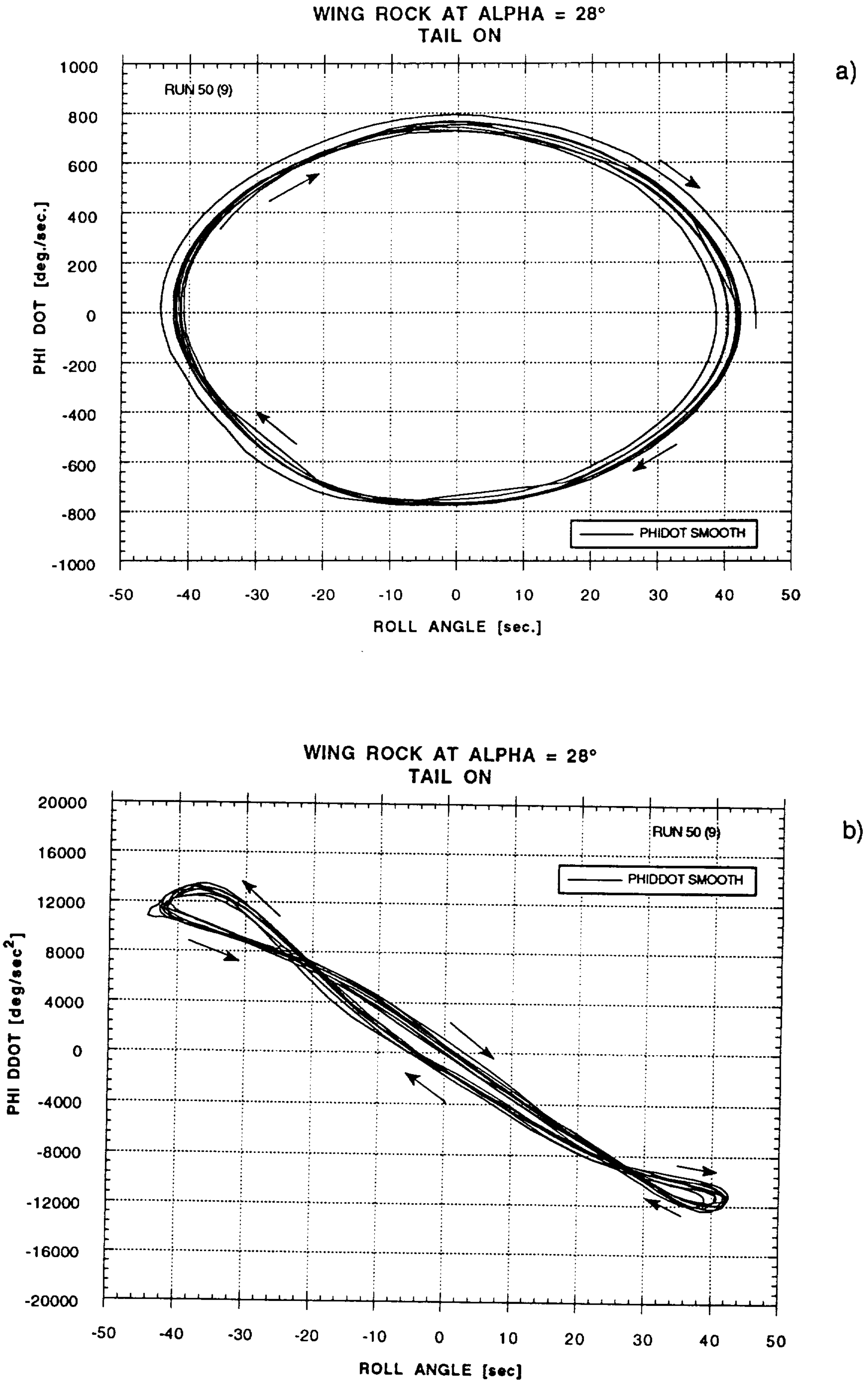

Figure 42 - Phase Plots at α = 28° (All Cycles)

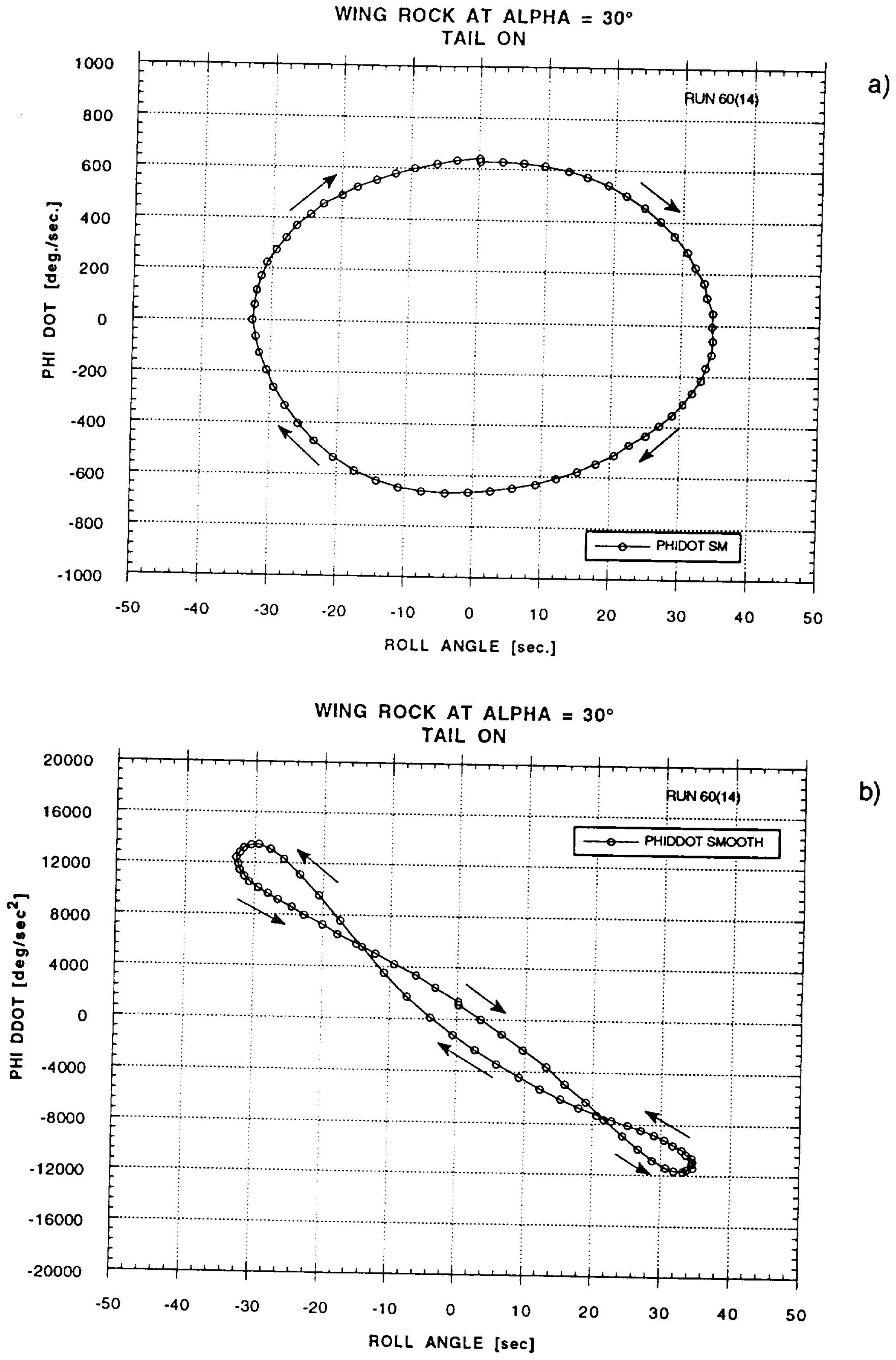

Figure 43 - Phase Plots at α = 30°

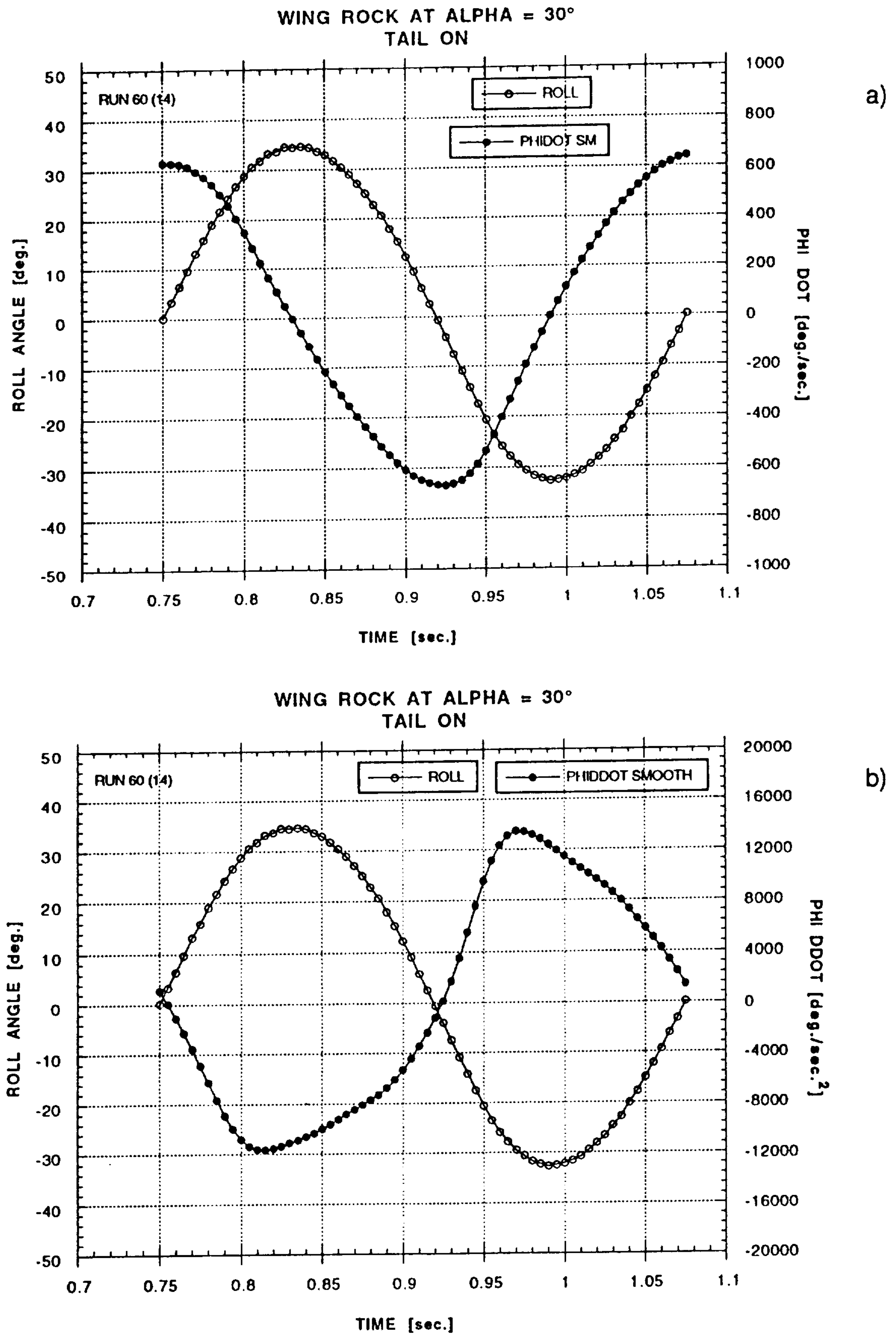

Figure 44 - Angular Velocity and Acceleration at α = 30°

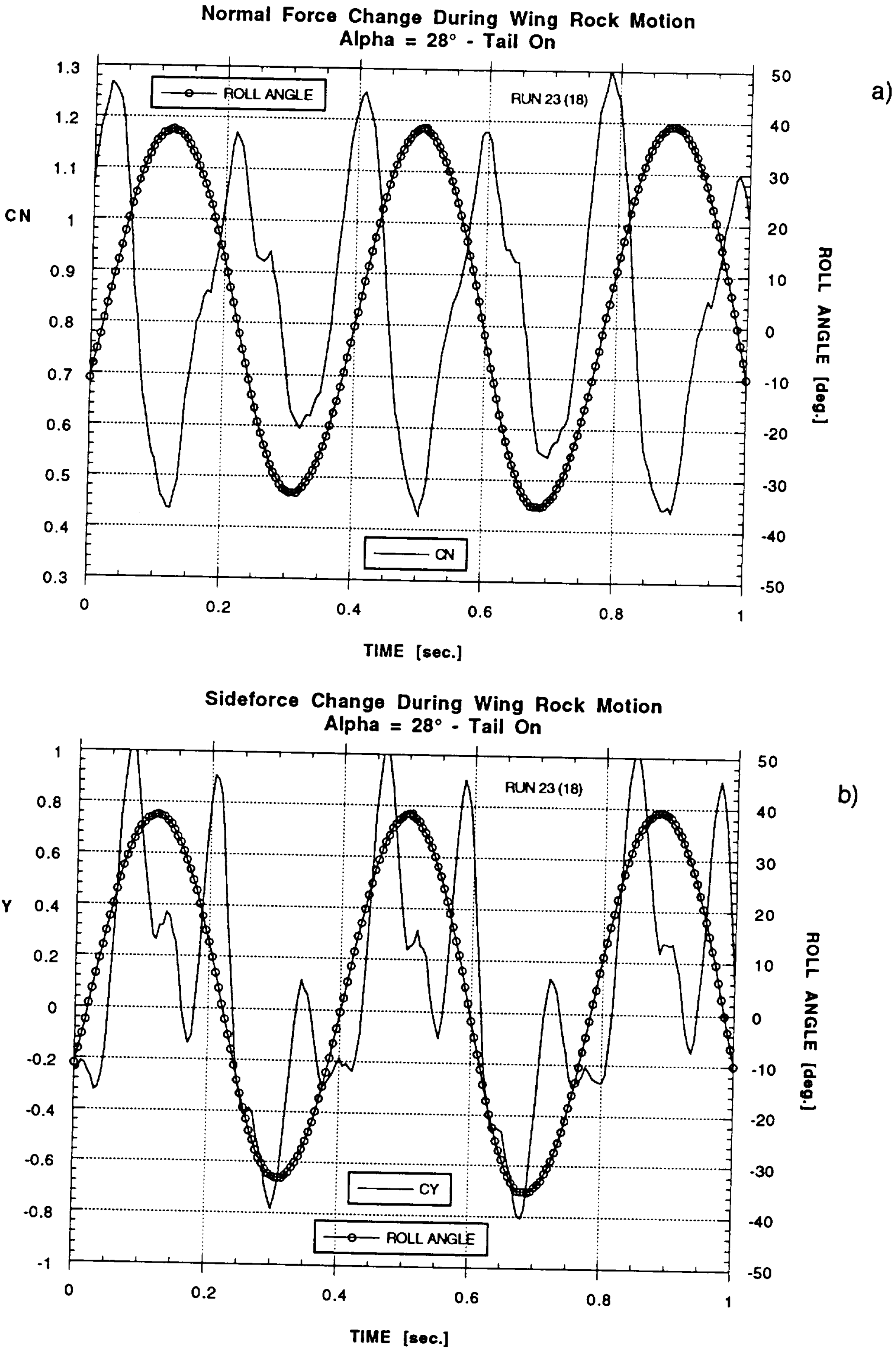

Figure 45 - Force Measurements During Wing Rock, Tail On
a) Normal Force, b) Side Force

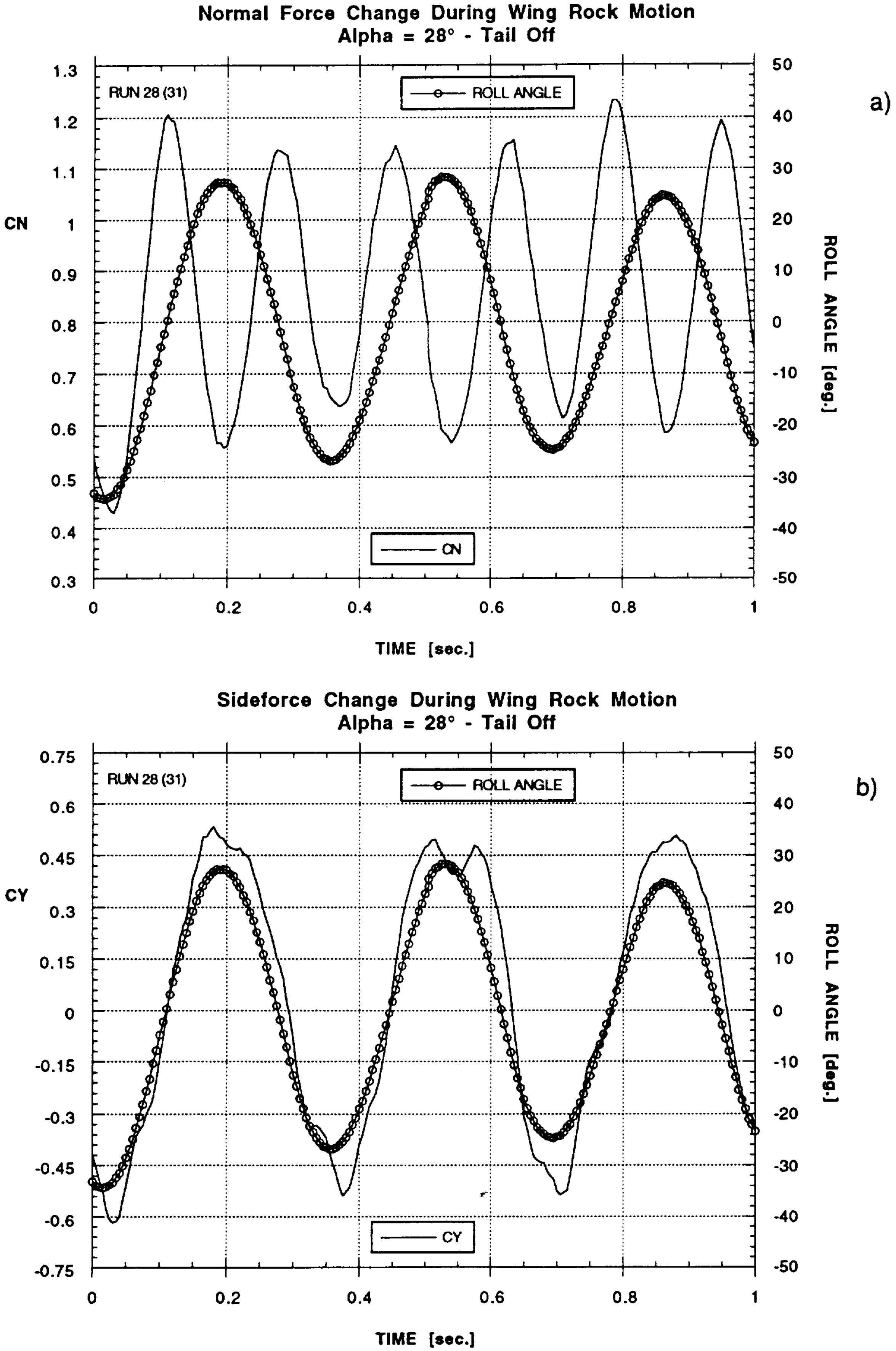

Figure 46 - Force Measurements During Wing Rock, Tail Off
a) Normal Force, b) Side Force

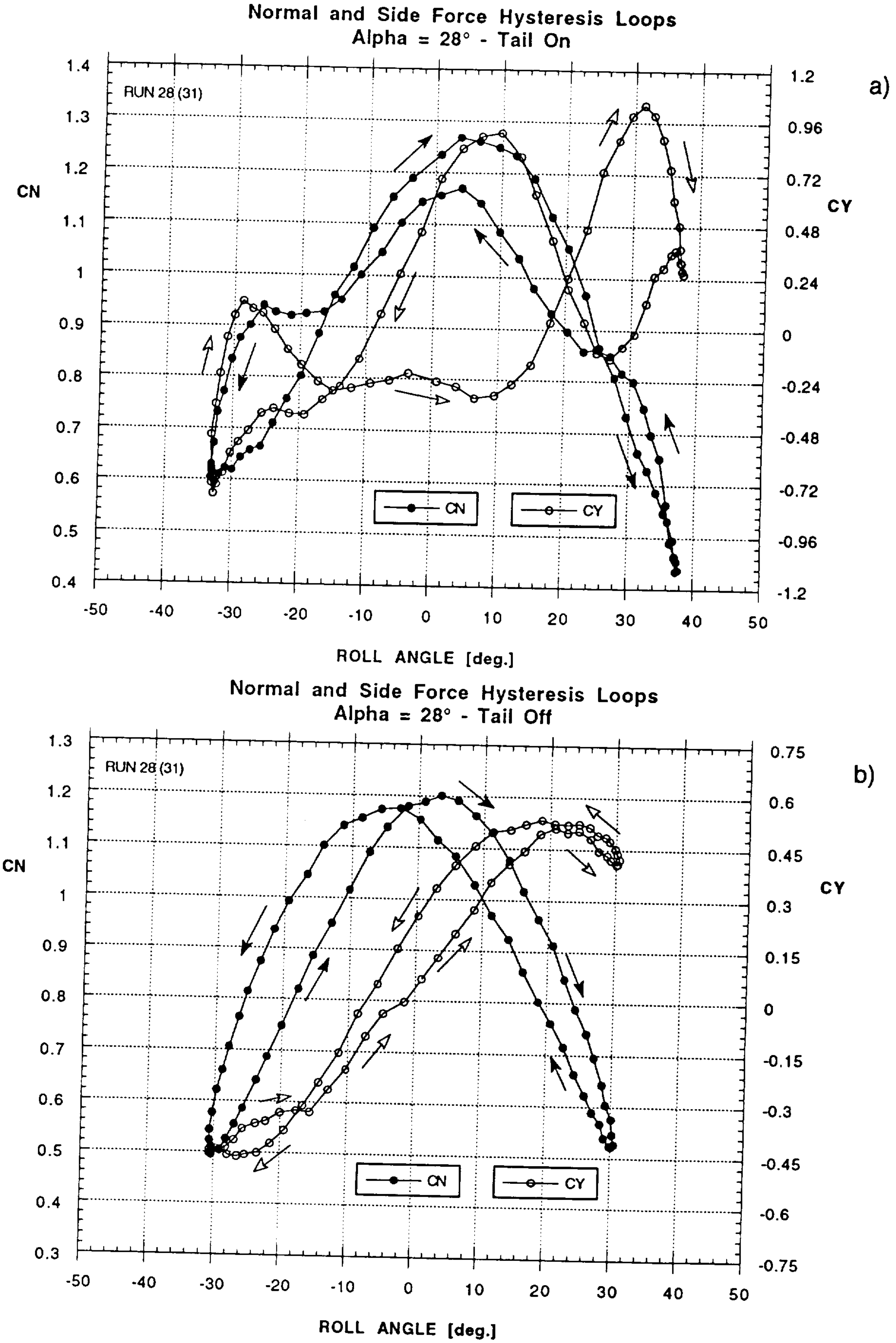
Normal and Side Force Hysteresis Loops
Alpha = 28° - Tail On

Normal and Side Force Hysteresis Loops
Alpha = 28° - Tail Off

Figure 47 - Normal and Side Force Hysteresis Loops
a) Tail On, b)Tail Off

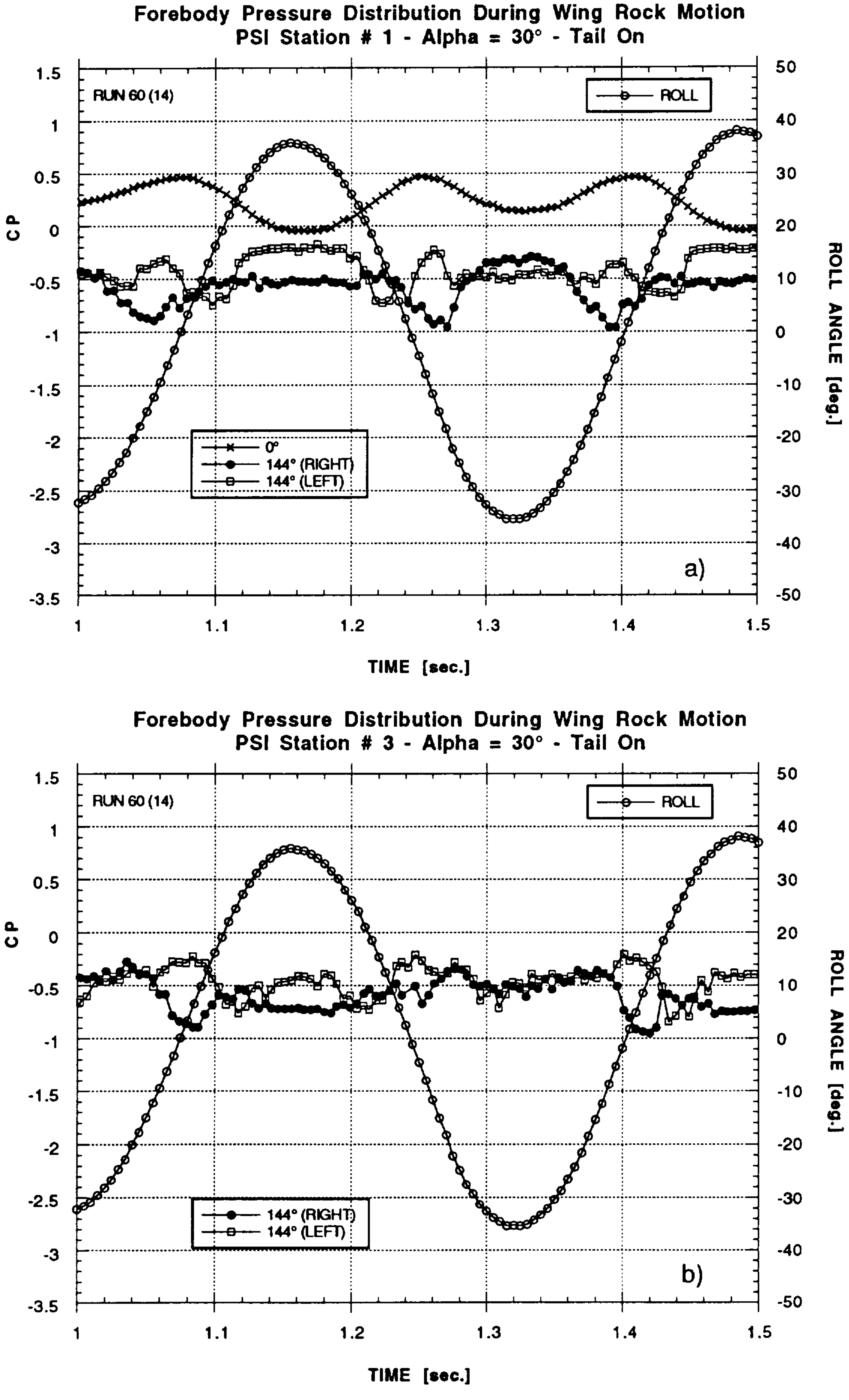

Forebody Pressure Distribution During Wing Rock Motion
PSI Station # 1 - Alpha = 30° - Tail On

Forebody Pressure Distribution During Wing Rock Motion
PSI Station # 3 - Alpha = 30° - Tail On

Figure 48 - Forebody Pressures During Wing Rock at $\alpha = 30°$
a) Station #1, b) Station #3

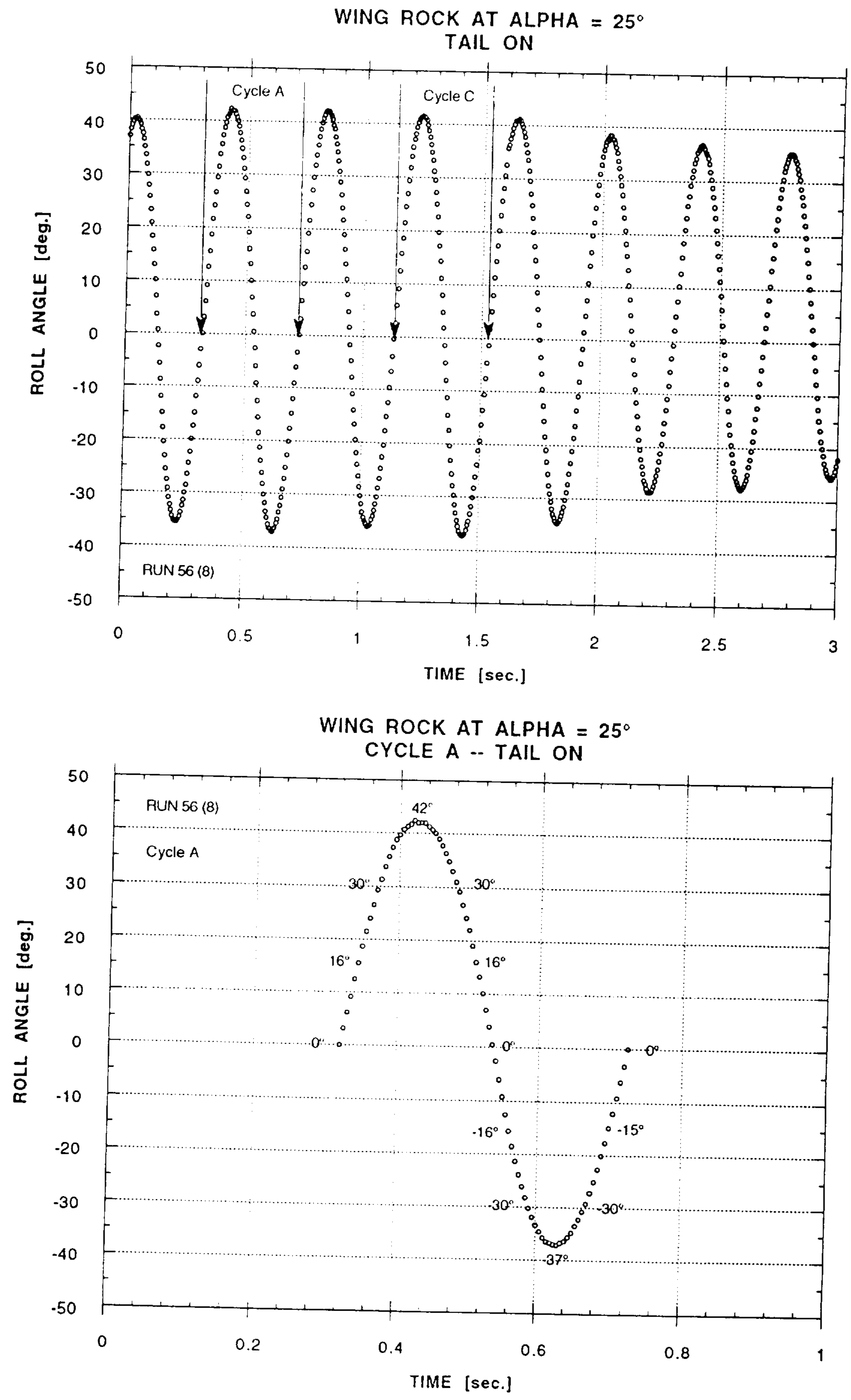

Figure 49 - Wing Rock at $\alpha = 25°$

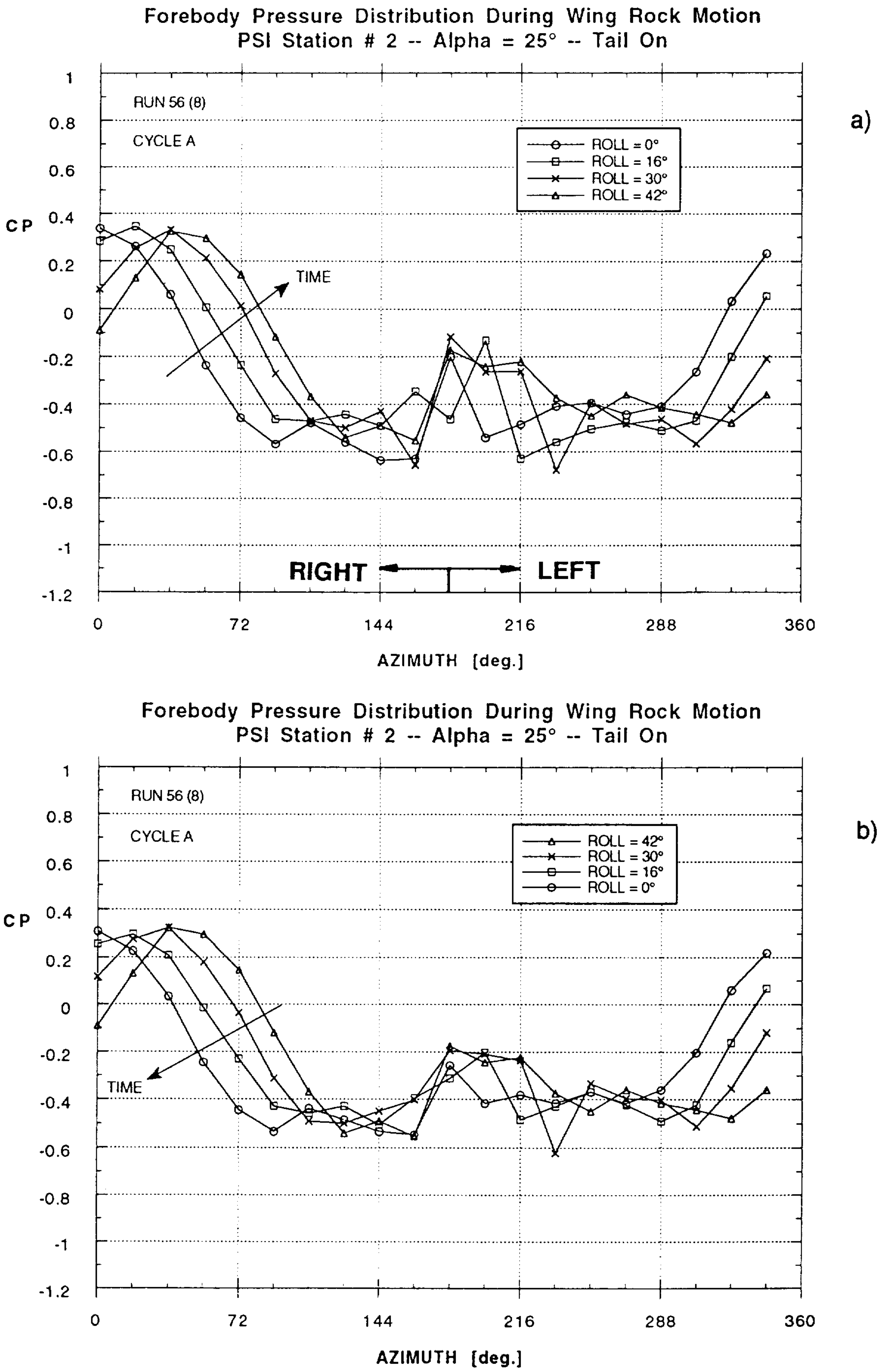

Figure 50 - Forebody Pressure Distribution During Wing Rock at α = 25° (Cycle A, q = 958 Pa, Tail On, uncorrected azimuth)

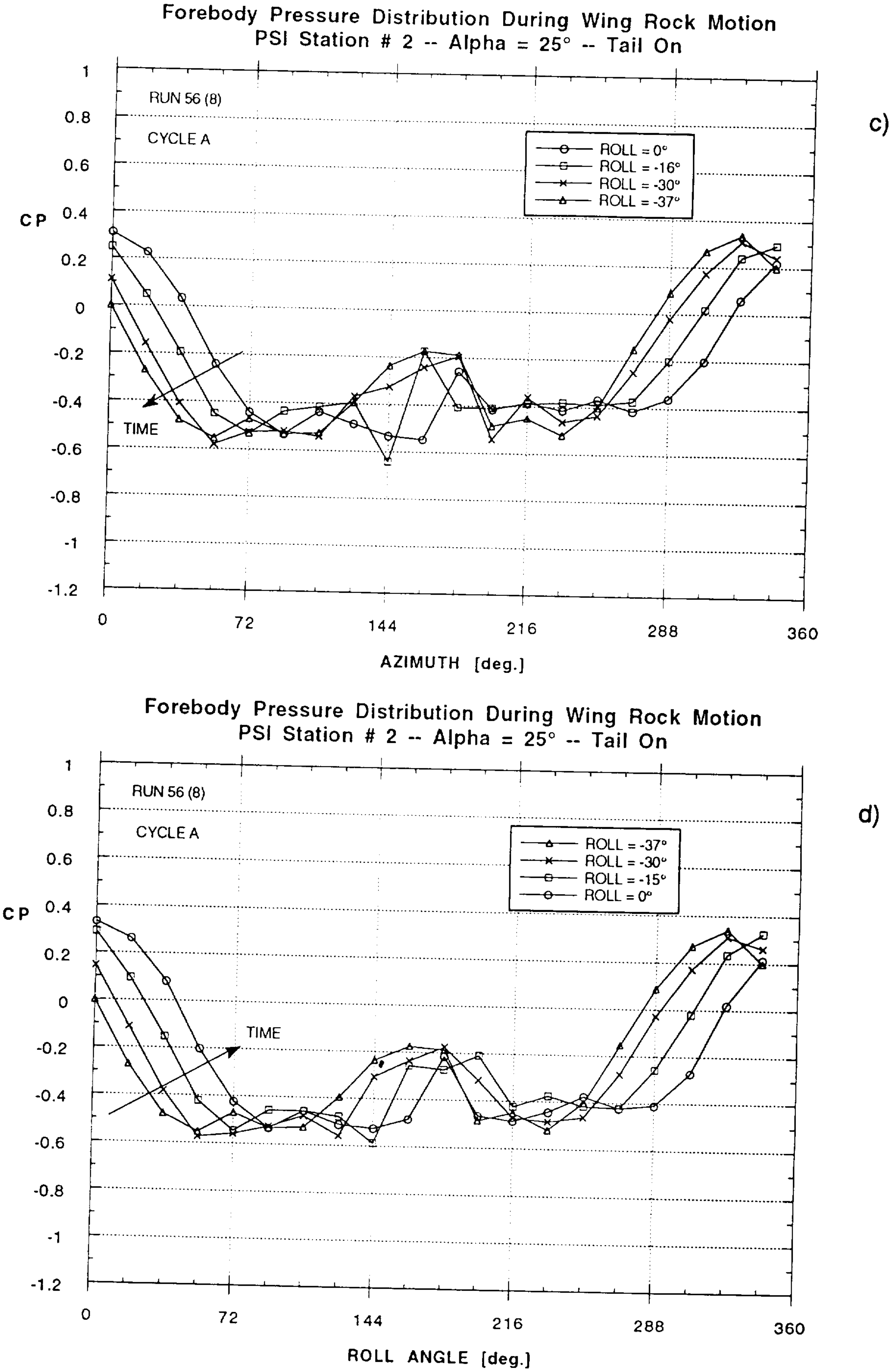

Figure 50 - Concluded

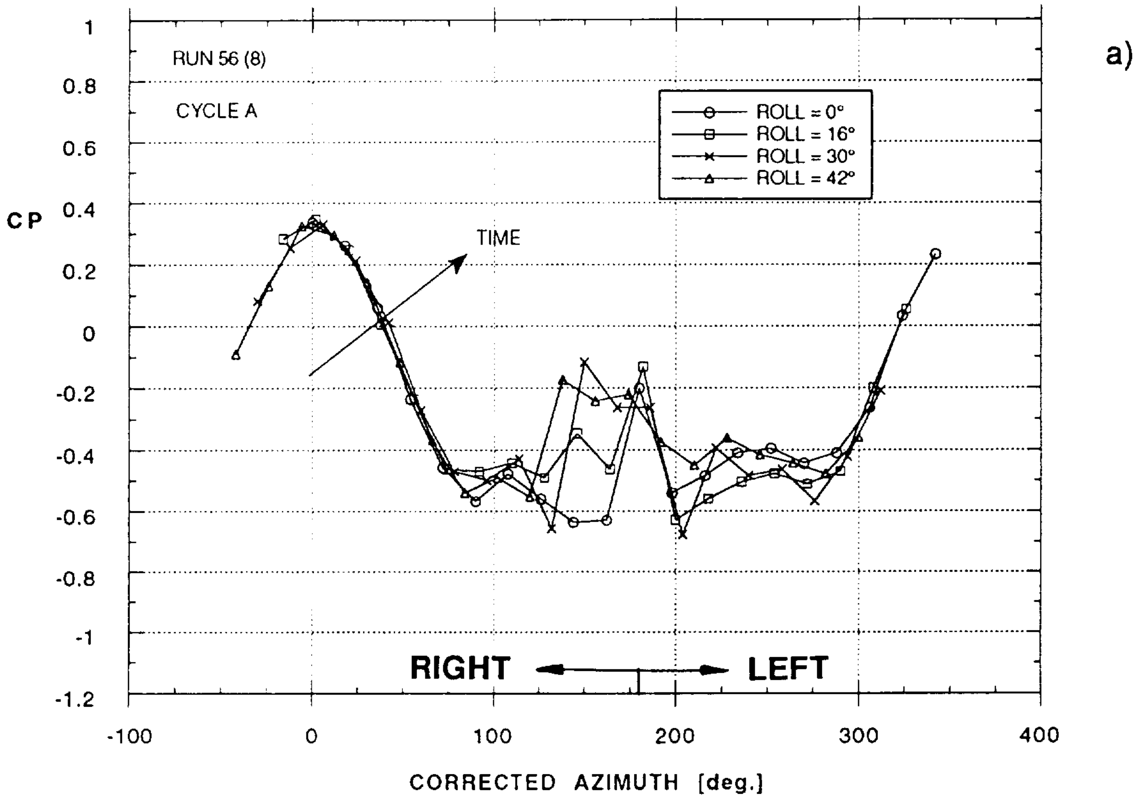

Forebody Pressure Distribution During Wing Rock Motion
PSI Station # 2 -- Alpha = 25° -- Tail On

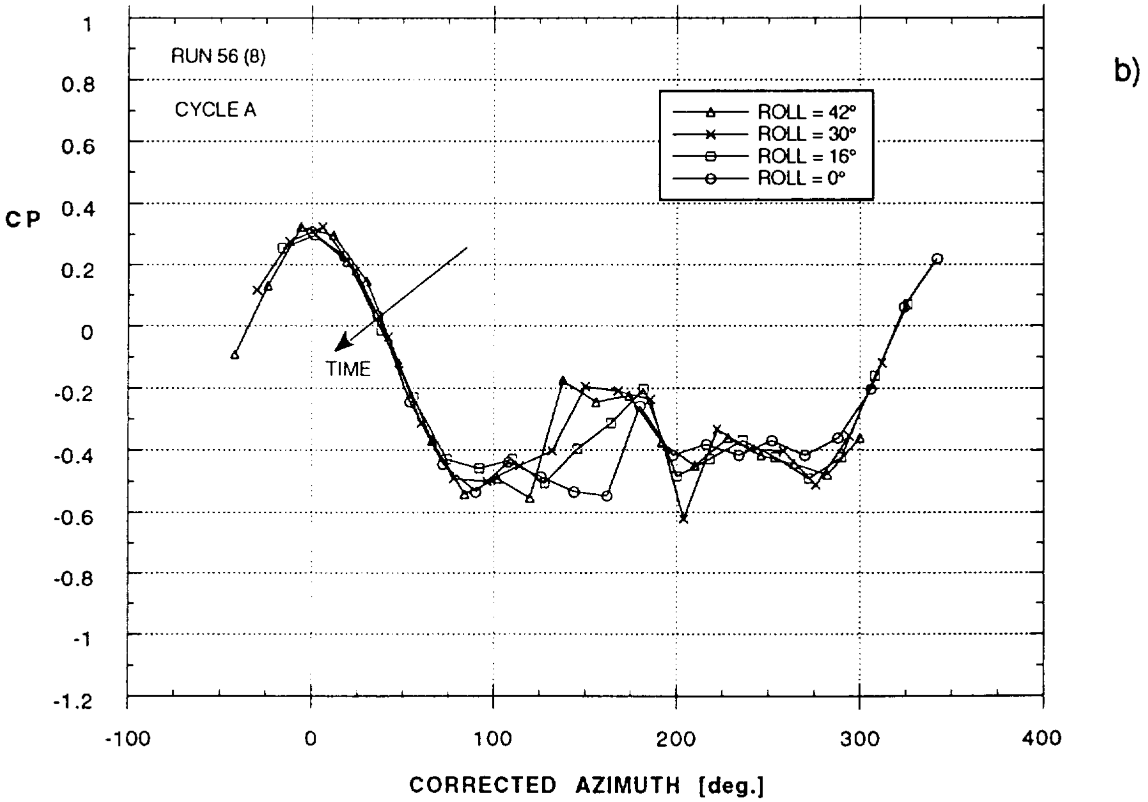

Forebody Pressure Distribution During Wing Rock Motion
PSI Station # 2 -- Alpha = 25° -- Tail On

Figure 51 - Forebody Pressure Distribution During Wing Rock at $\alpha = 25°$ (Cycle A, q = 958 Pa, Tail On, corrected azimuth)

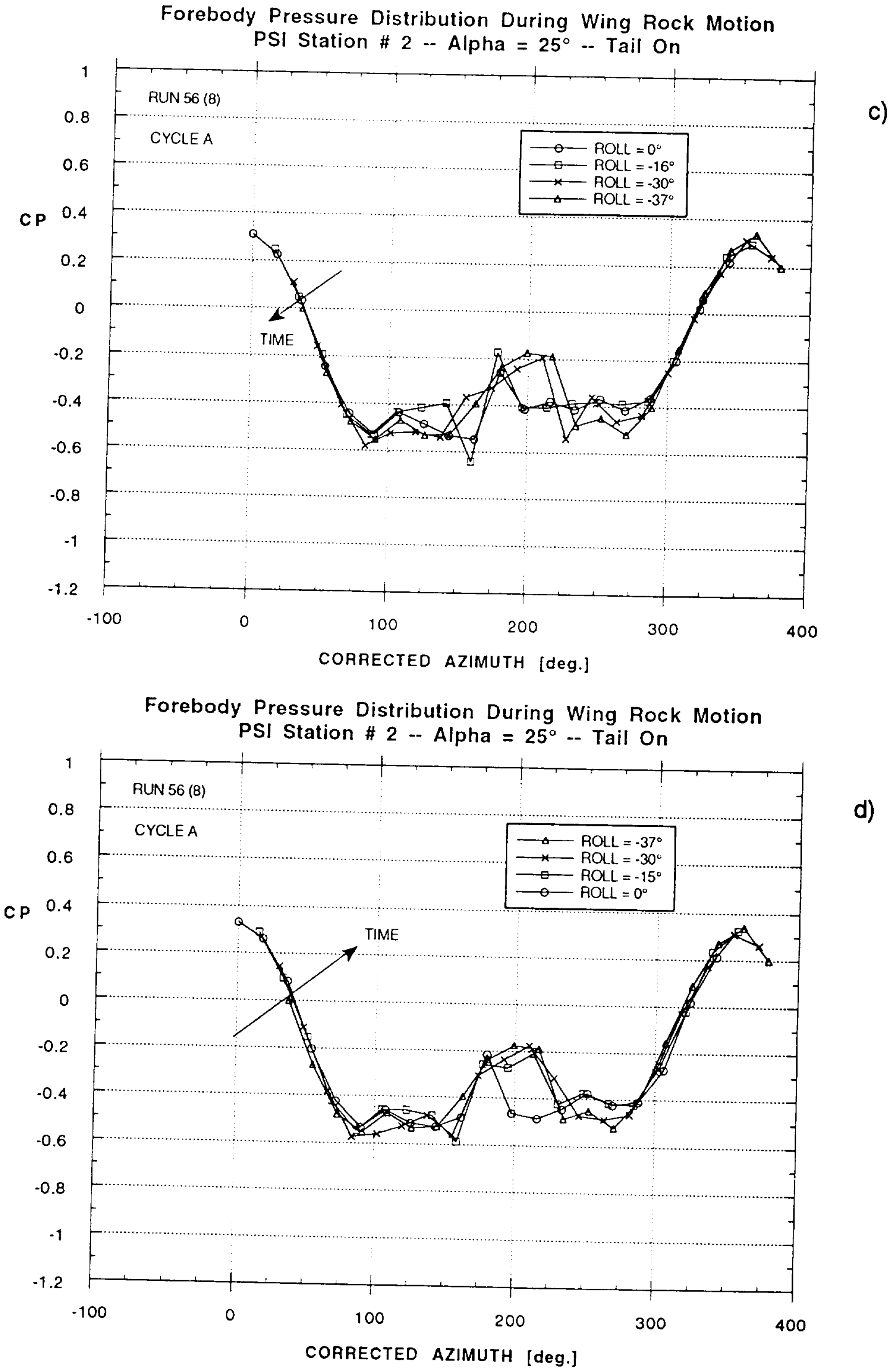

Figure 51 - Concluded

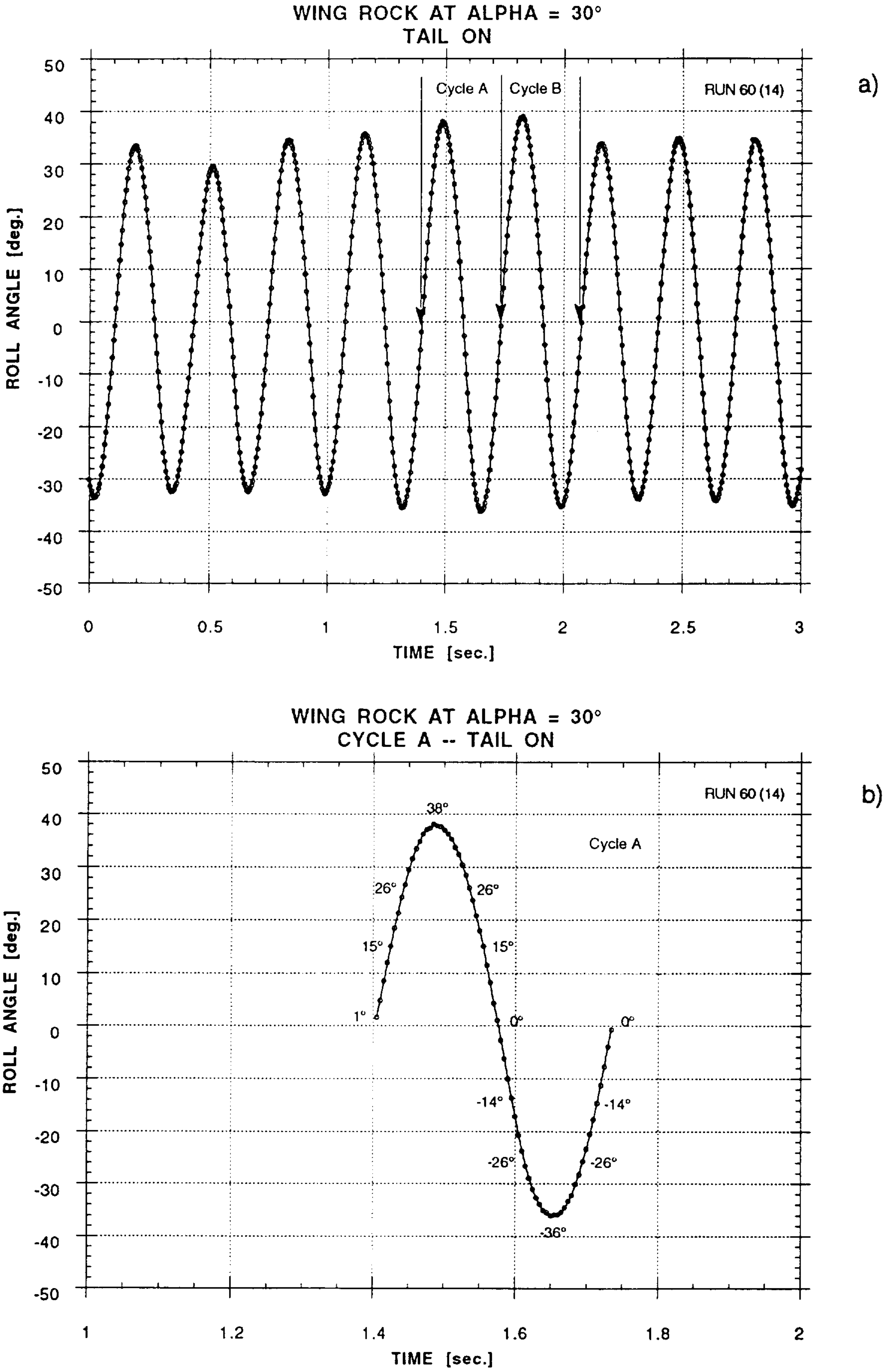

Figure 52 - Wing Rock at α = 30° (Cycle A)

C-2

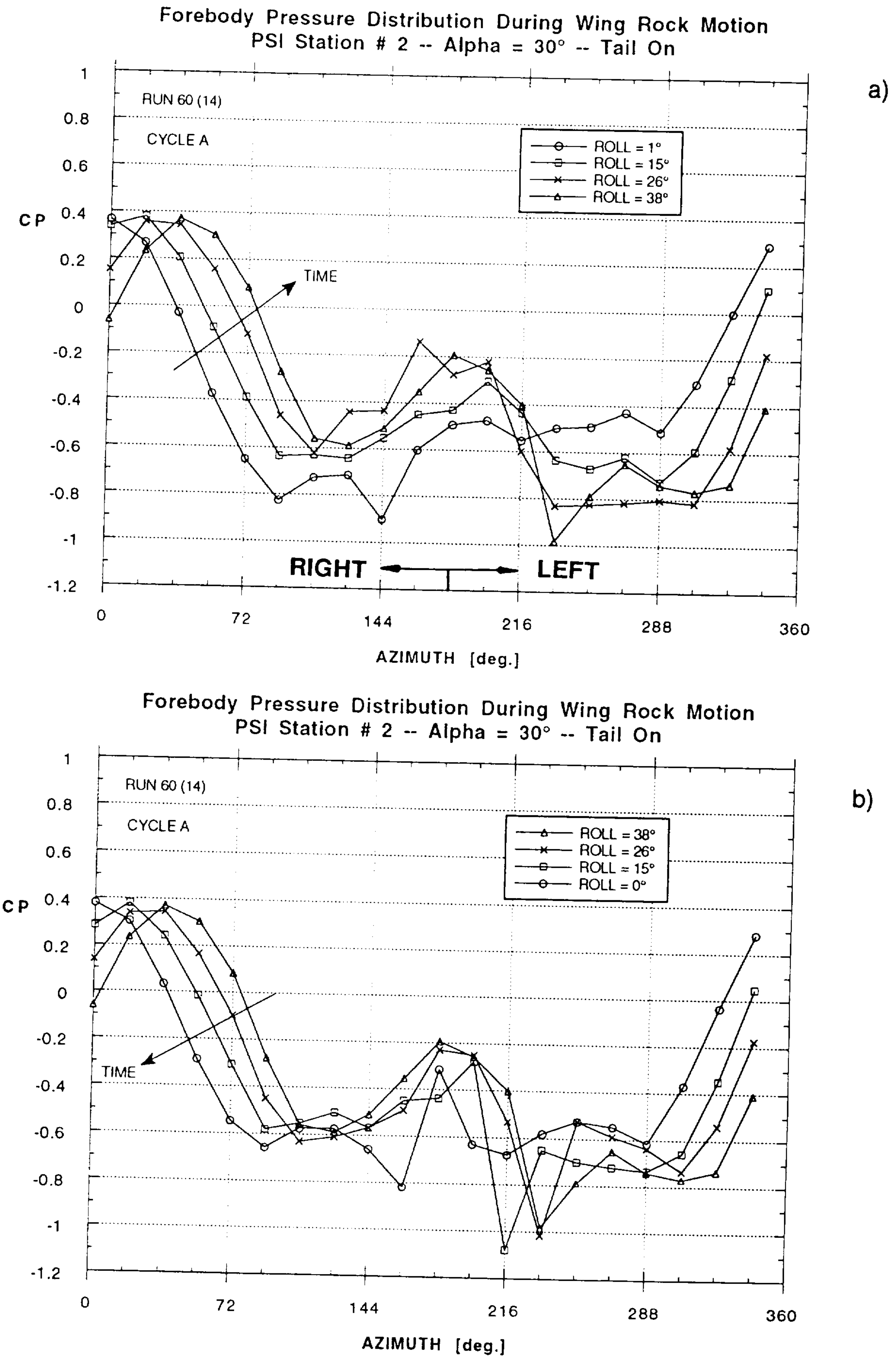

Figure 53 - Forebody Pressure Distribution During Wing Rock at α = 30° (Cycle A, q = 958 Pa, Tail On, uncorrected azimuth)

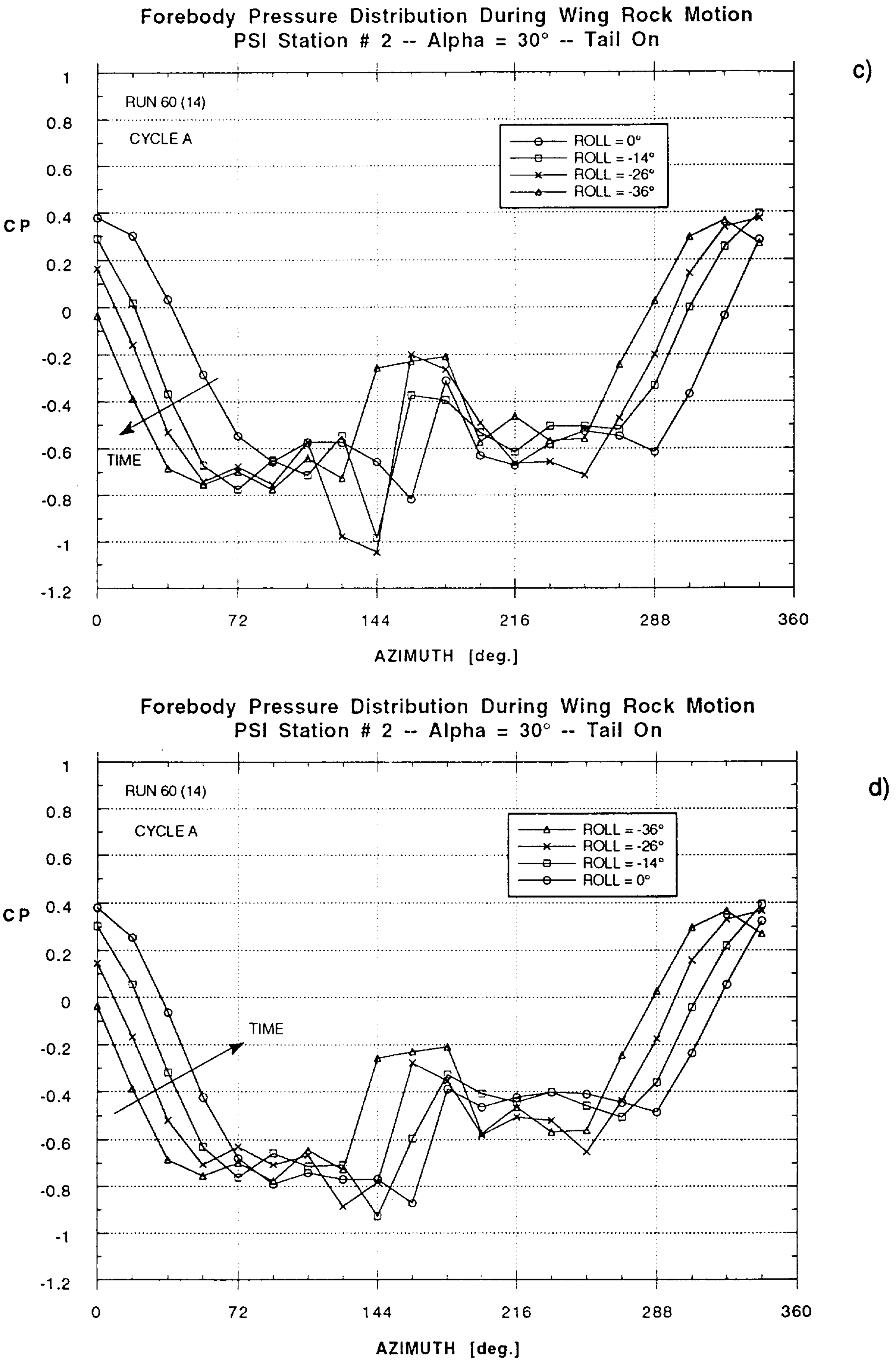

Figure 53 - Concluded

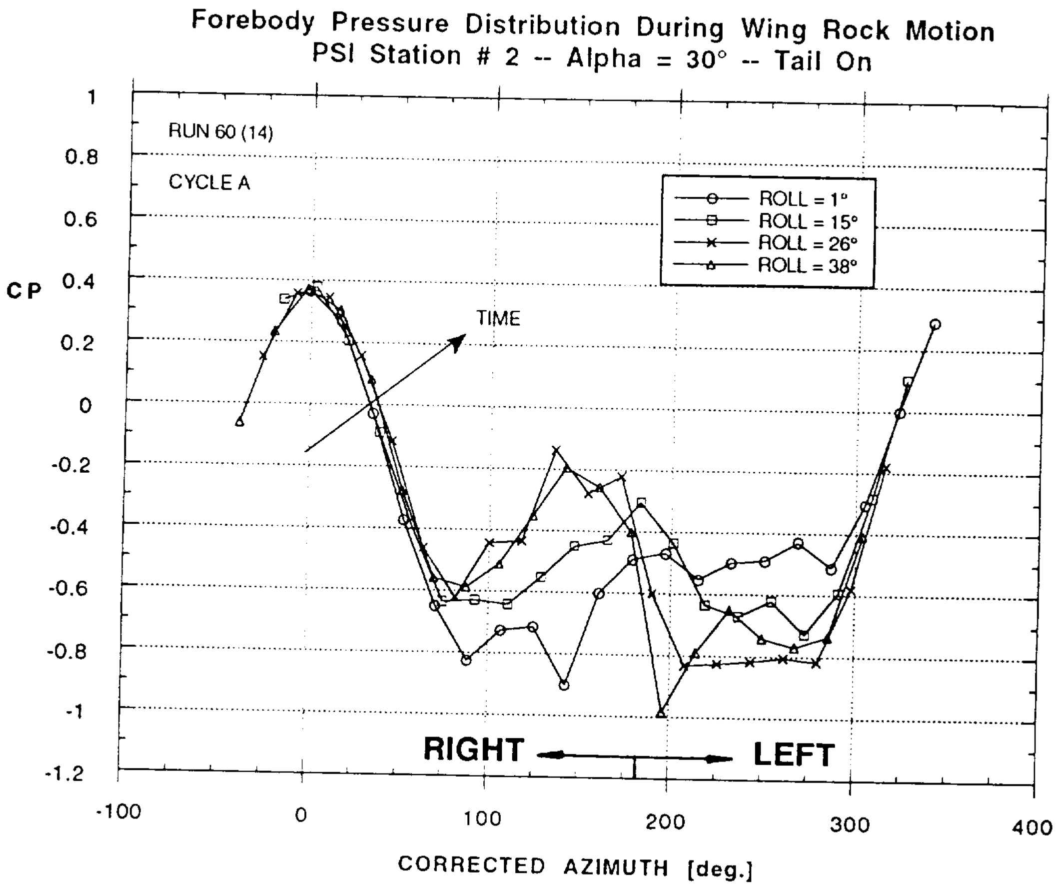

a)

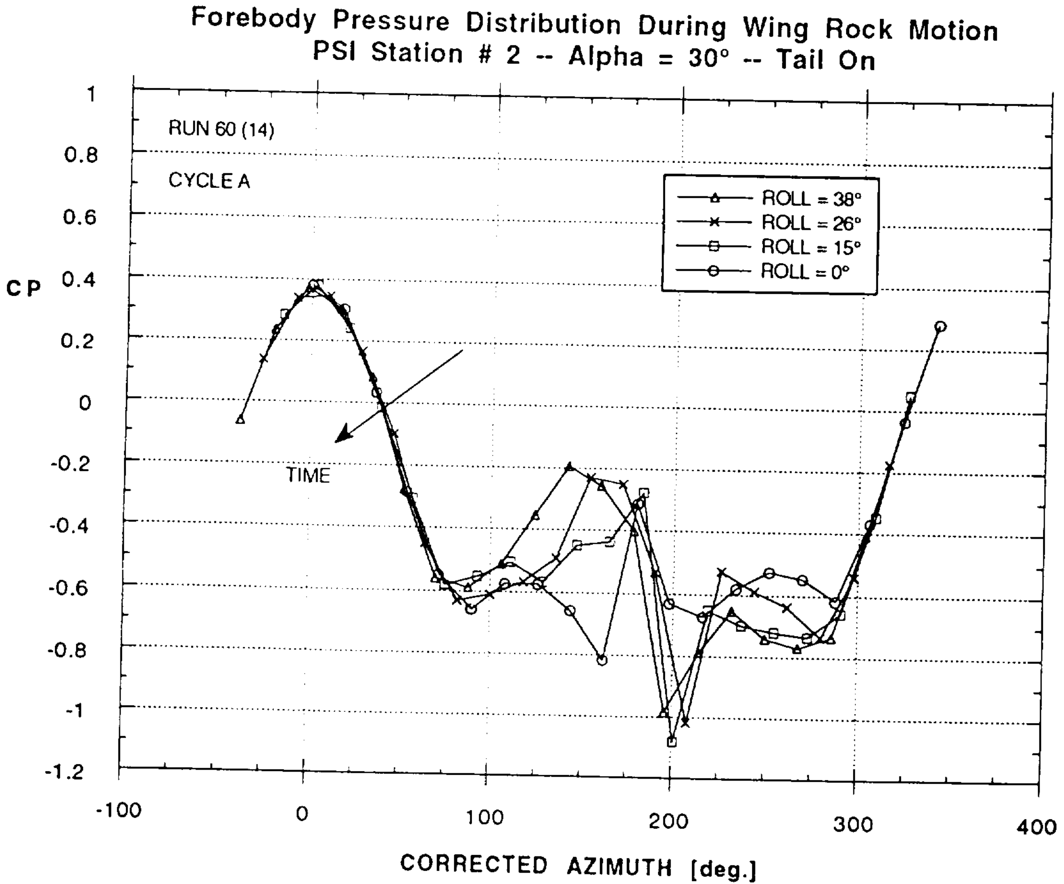

b)

Figure 54 - Forebody Pressure Distribution During Wing Rock at $\alpha = 30°$ (Cycle A, q = 958 Pa, Tail On, corrected azimuth)

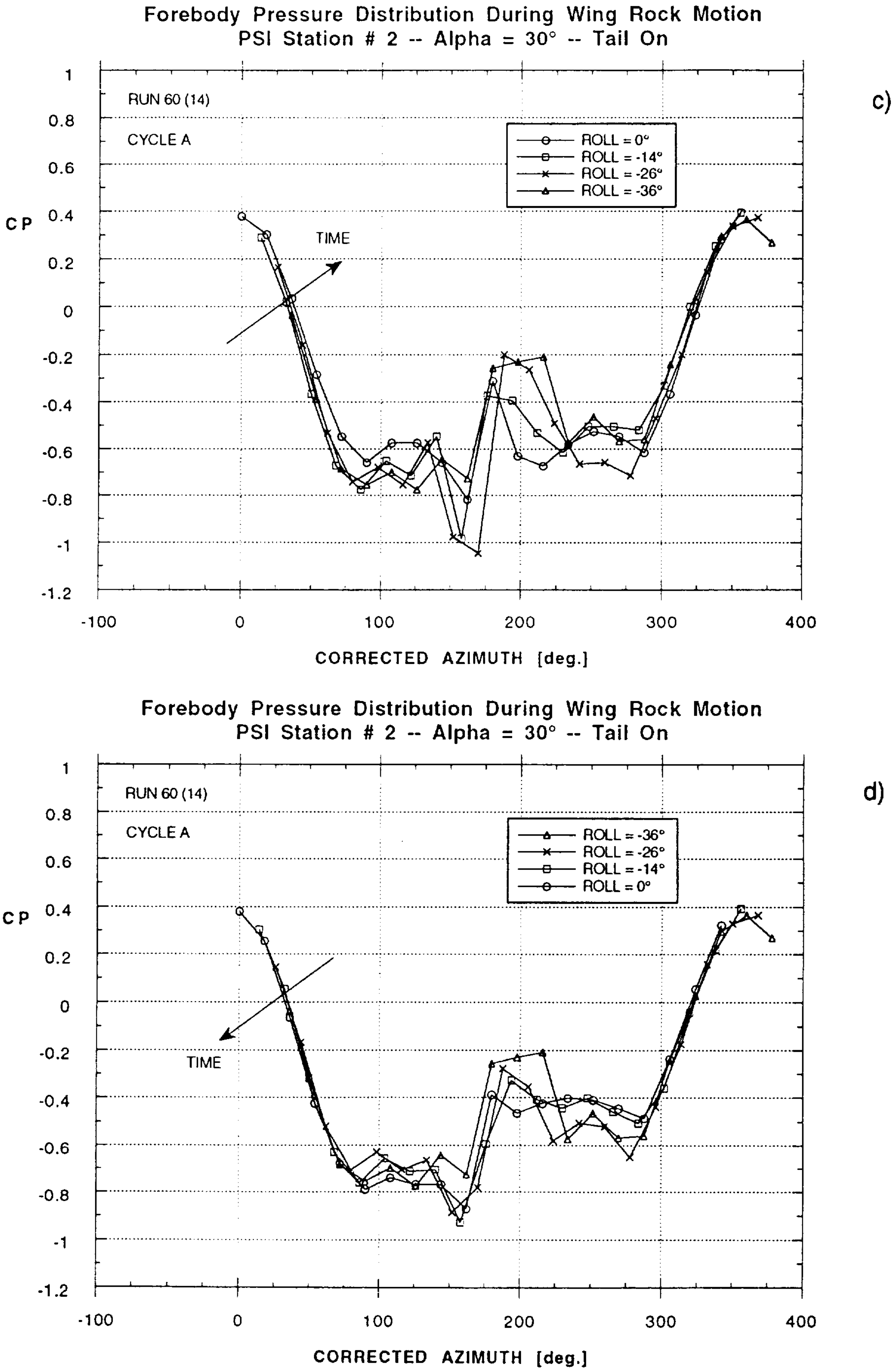

Figure 54 - Concluded

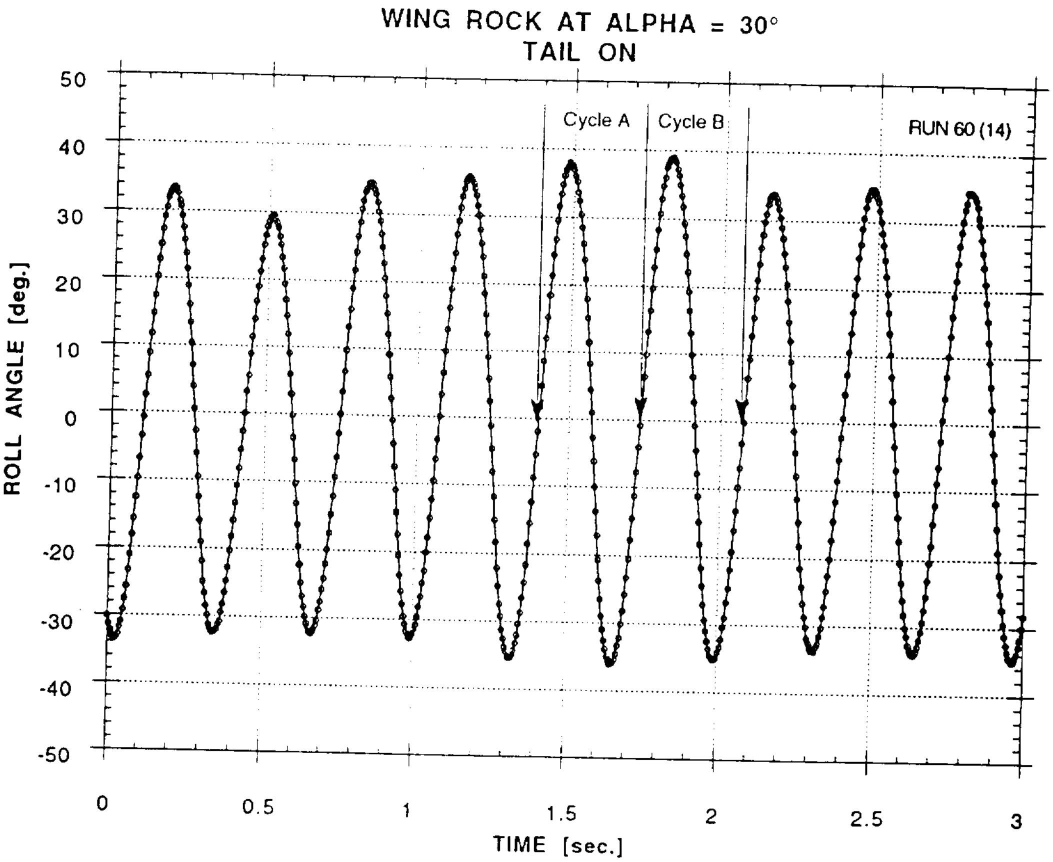

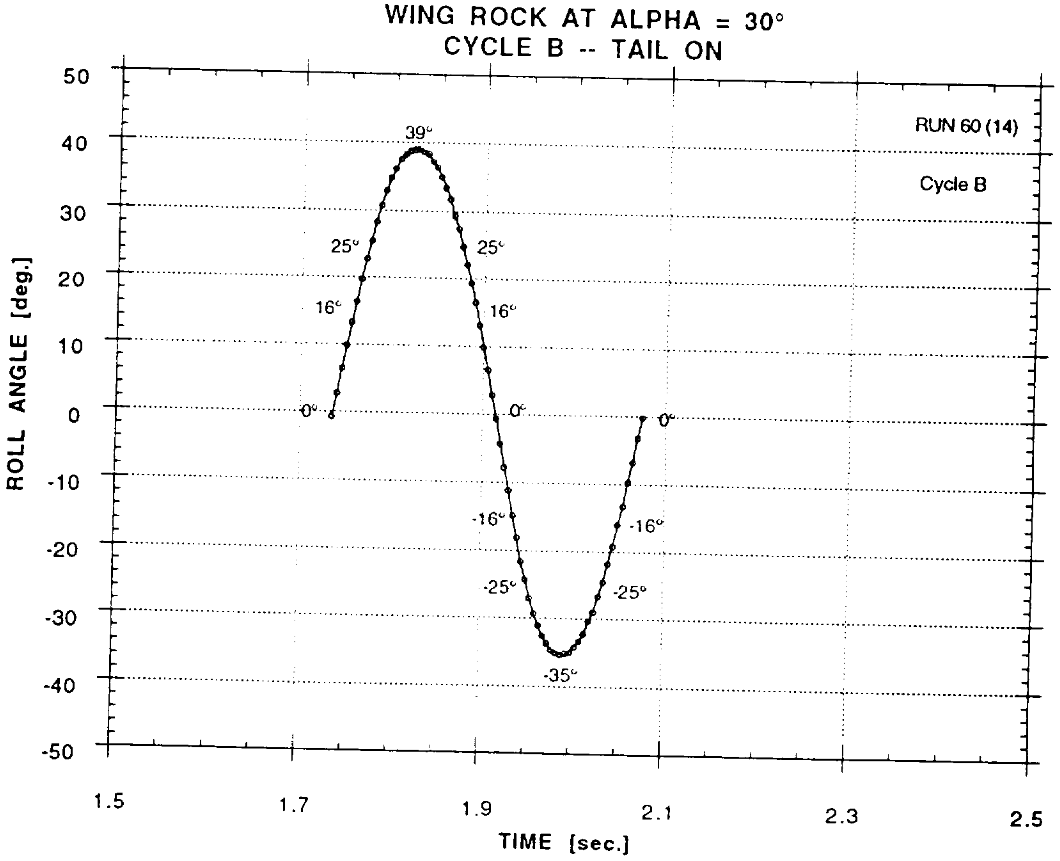

Figure 55 - Wing Rock at $\alpha = 30°$ (Cycle B)

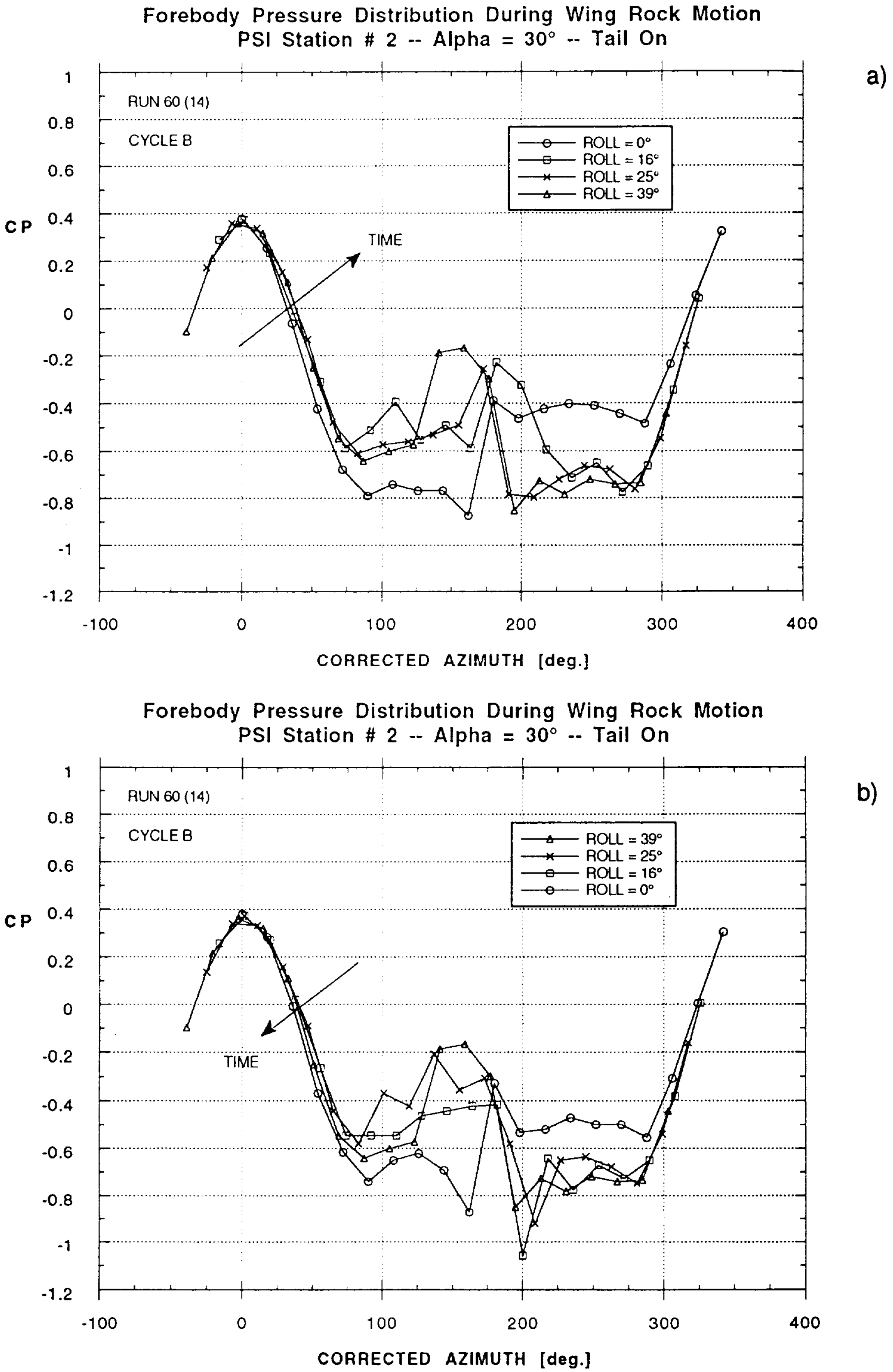

Figure 56 - Forebody Pressure Distribution During Wing Rock at $\alpha = 30°$ (Cycle B, q = 958 Pa, Tail On, corrected azimuth)

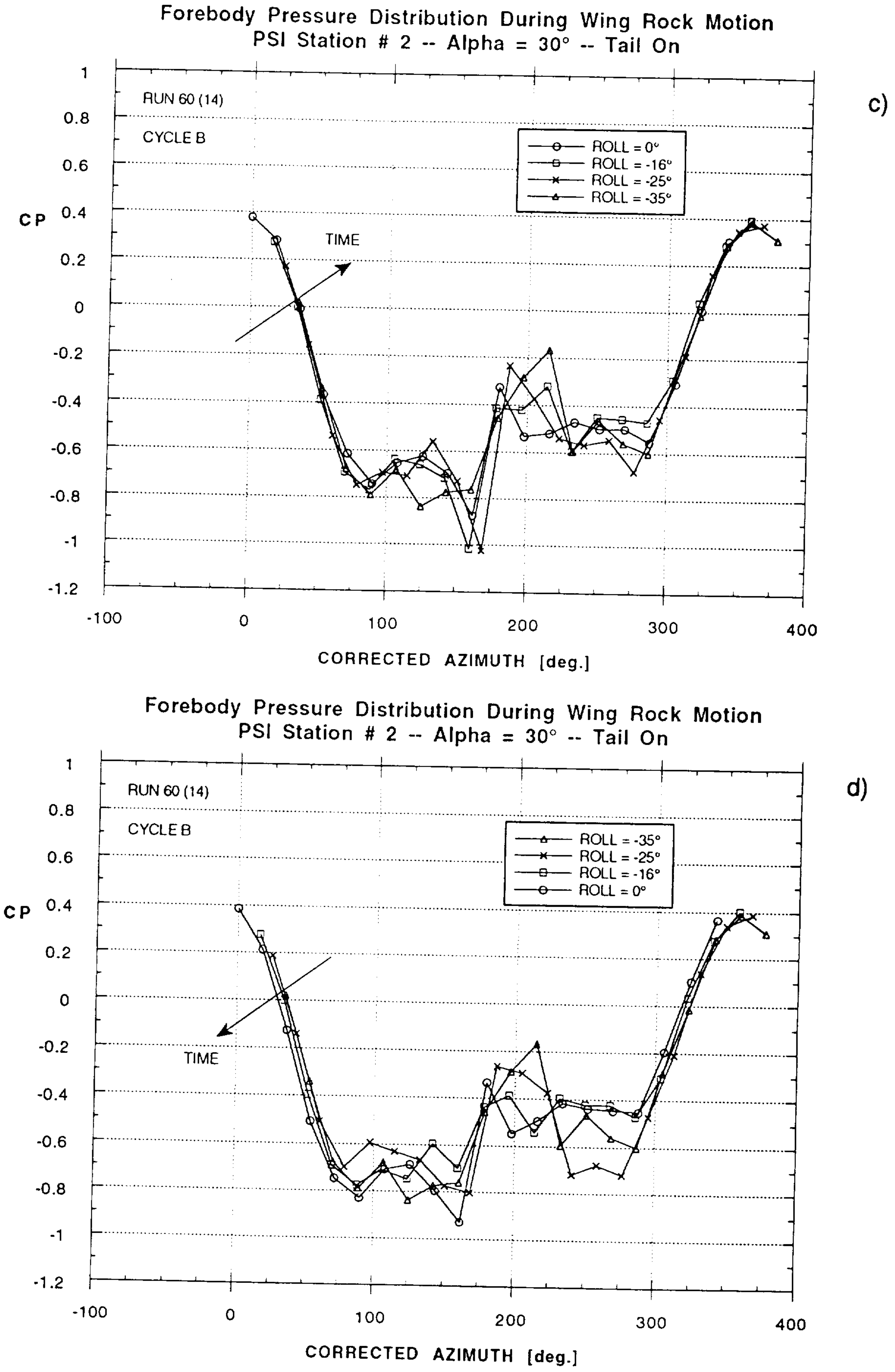

Figure 56 - Concluded

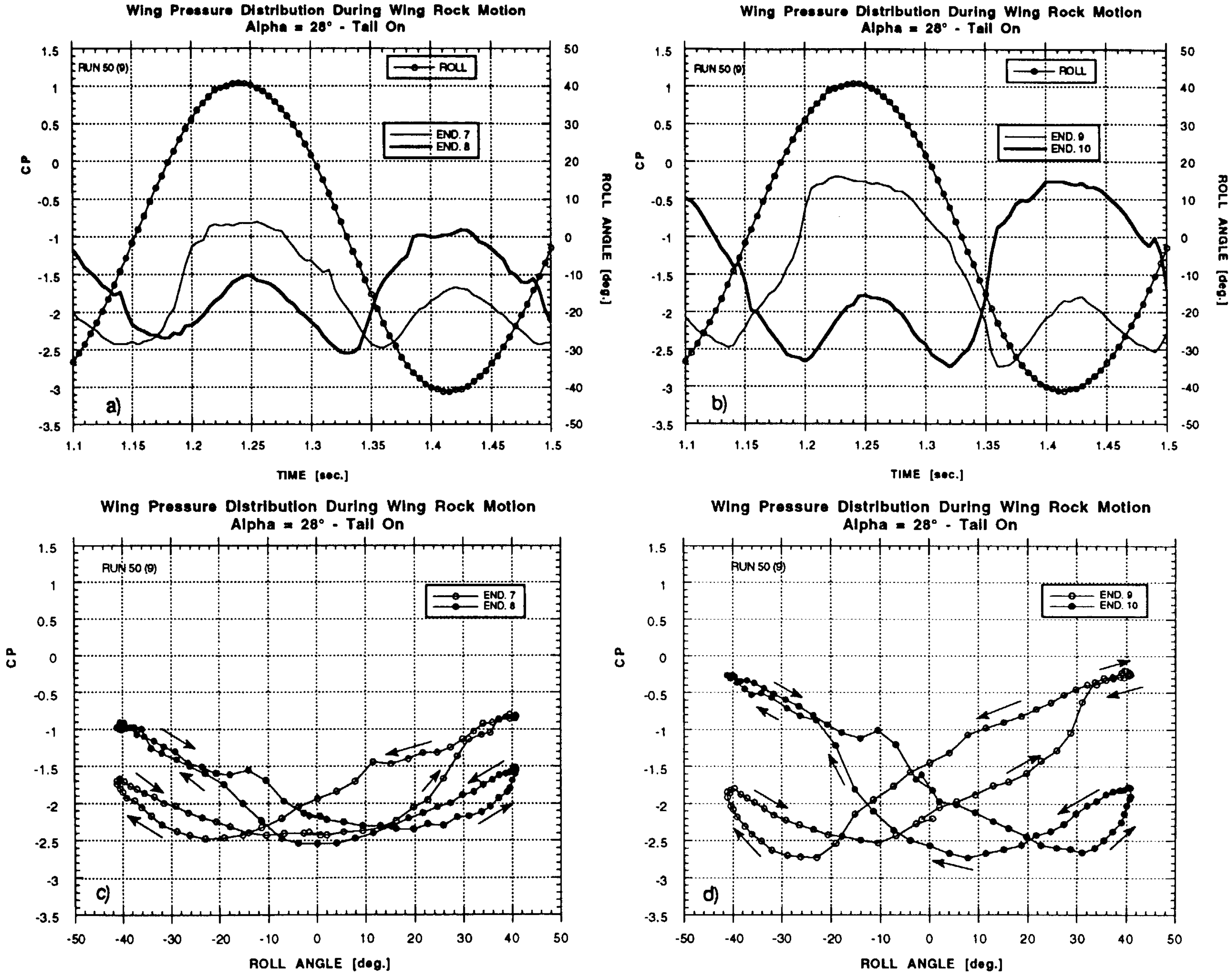

Figure 57 - Wing Pressure Distribution During Wing Rock (Tail On, α = 28°)

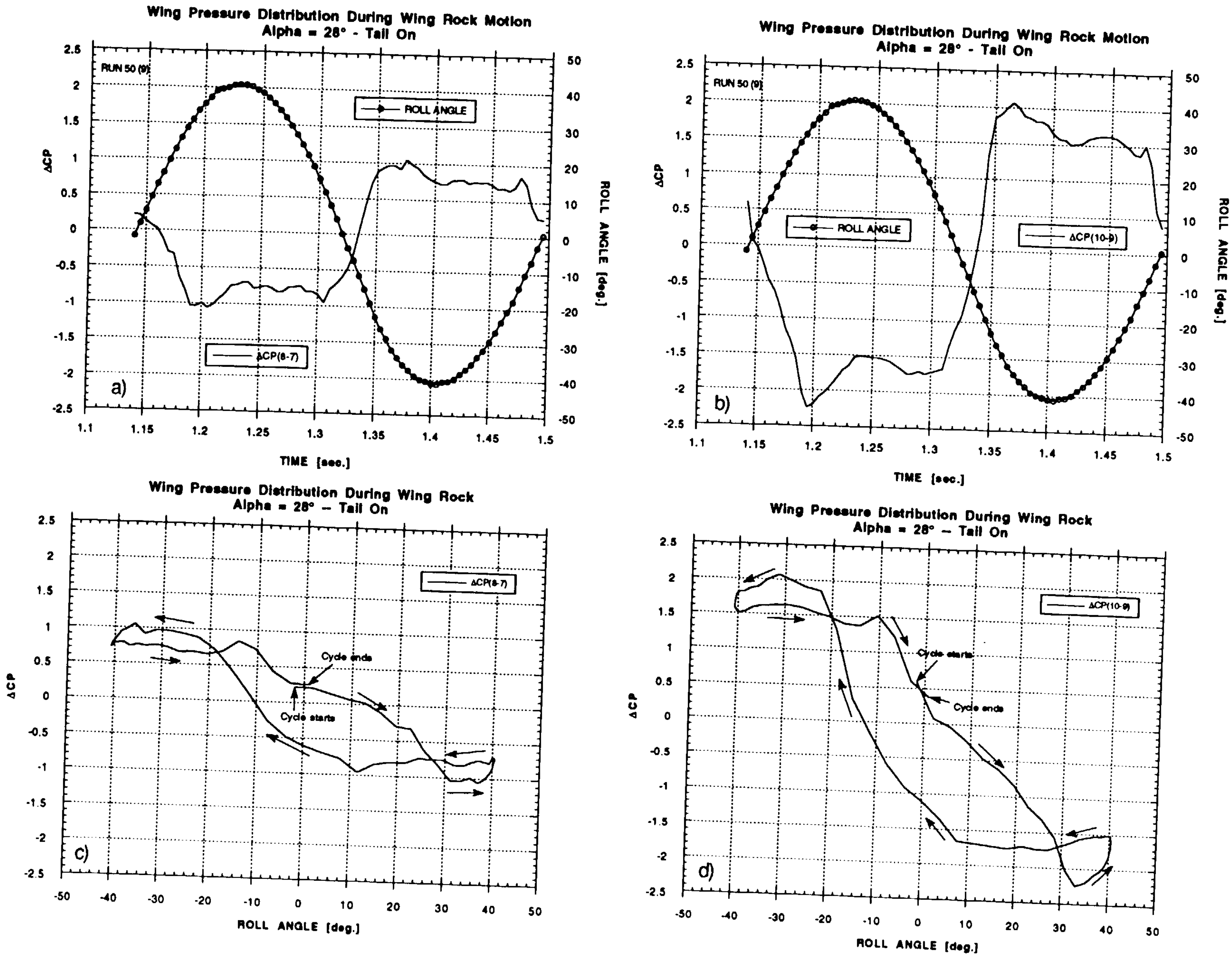

Figure 58 - Pressure Differential Between Left and Right Wings (α = 28°)

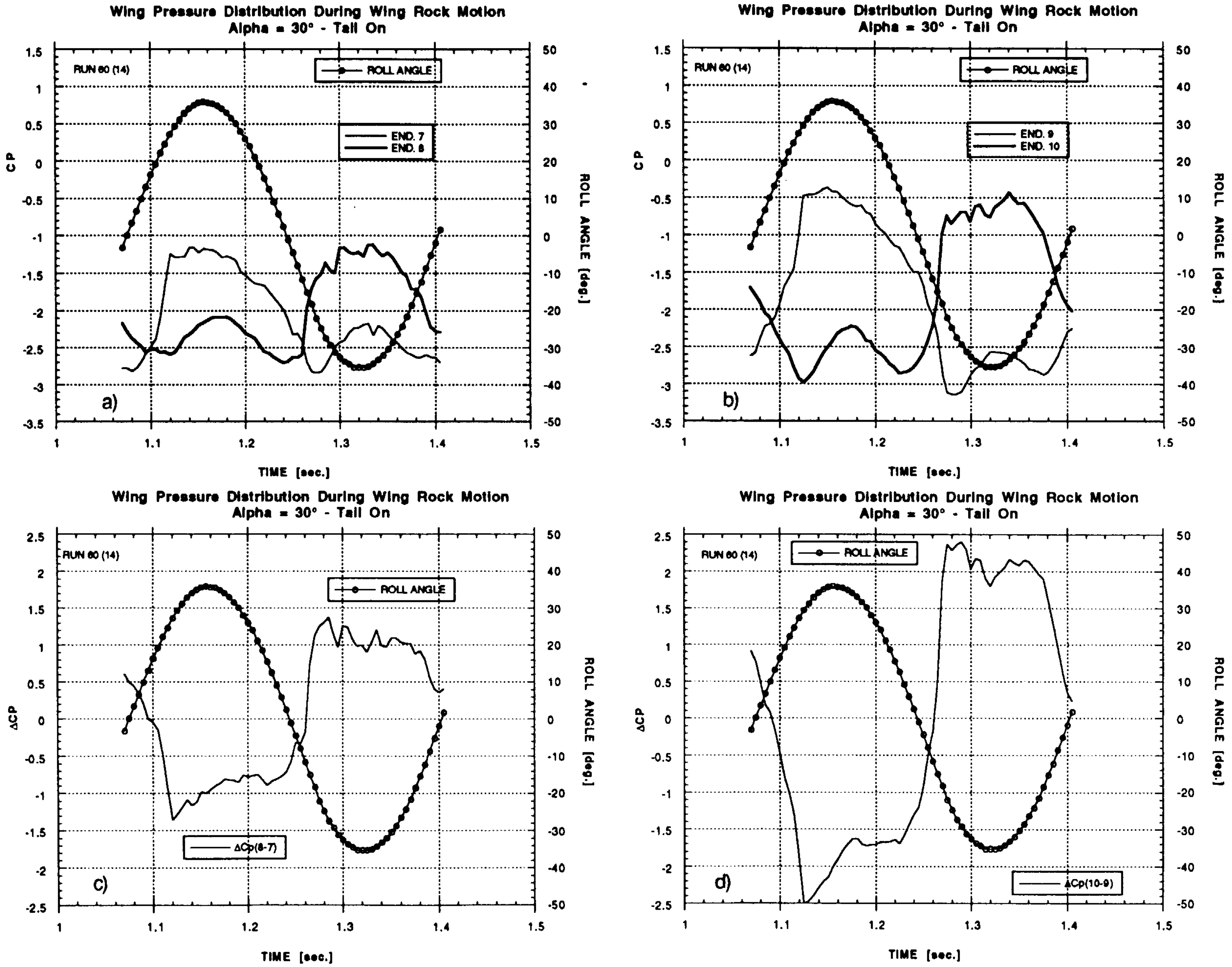

Figure 59 - Wing Pressure Distribution and Pressure Differential (α = 30°)

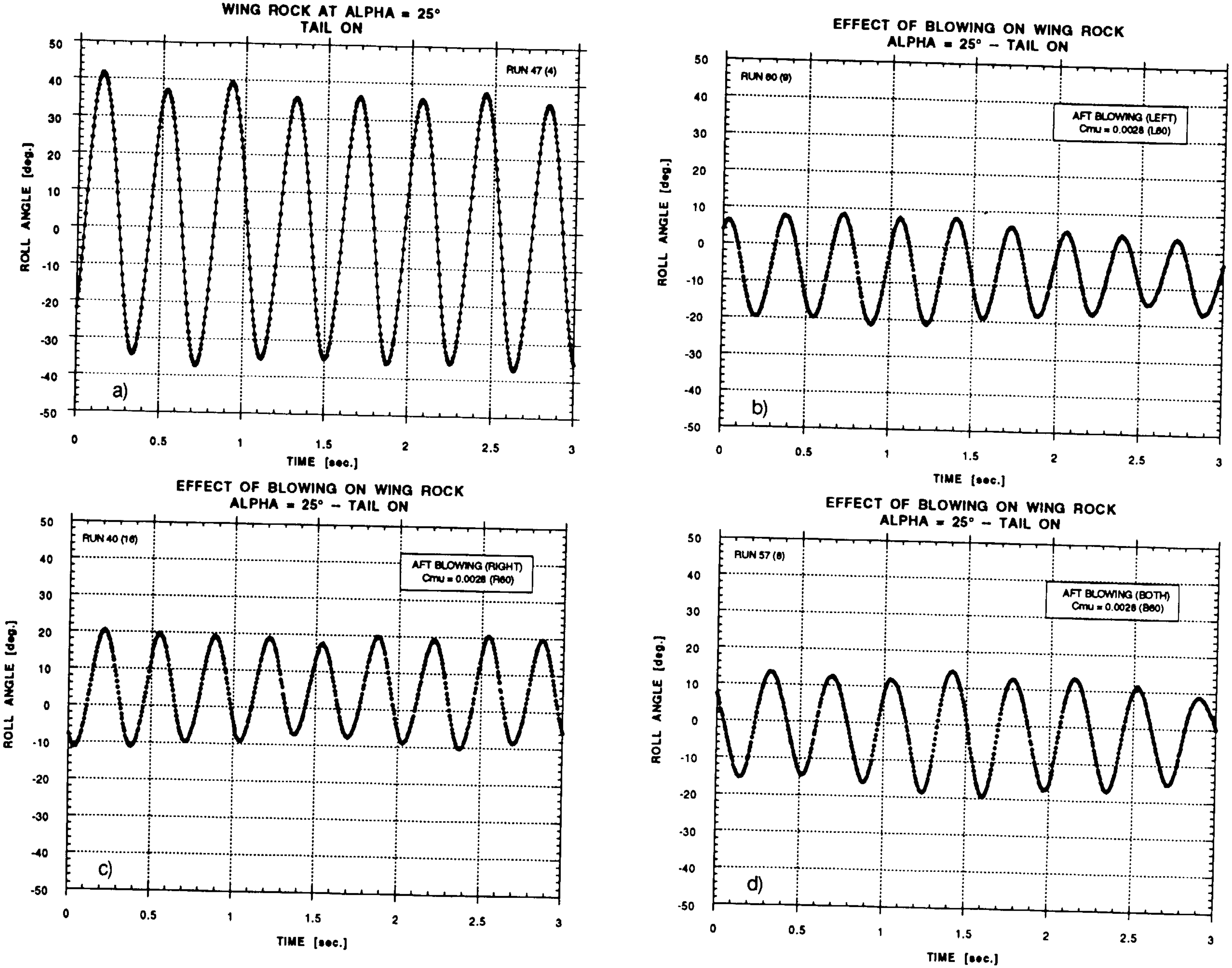

Figure 60 - Effect of Aft Blowing on Wing Rock at α = 25°; (Tail On, Cμ = 0.0028); a) No Blowing, b) Left Nozzle, c) Right Nozzle , d) Simultaneous

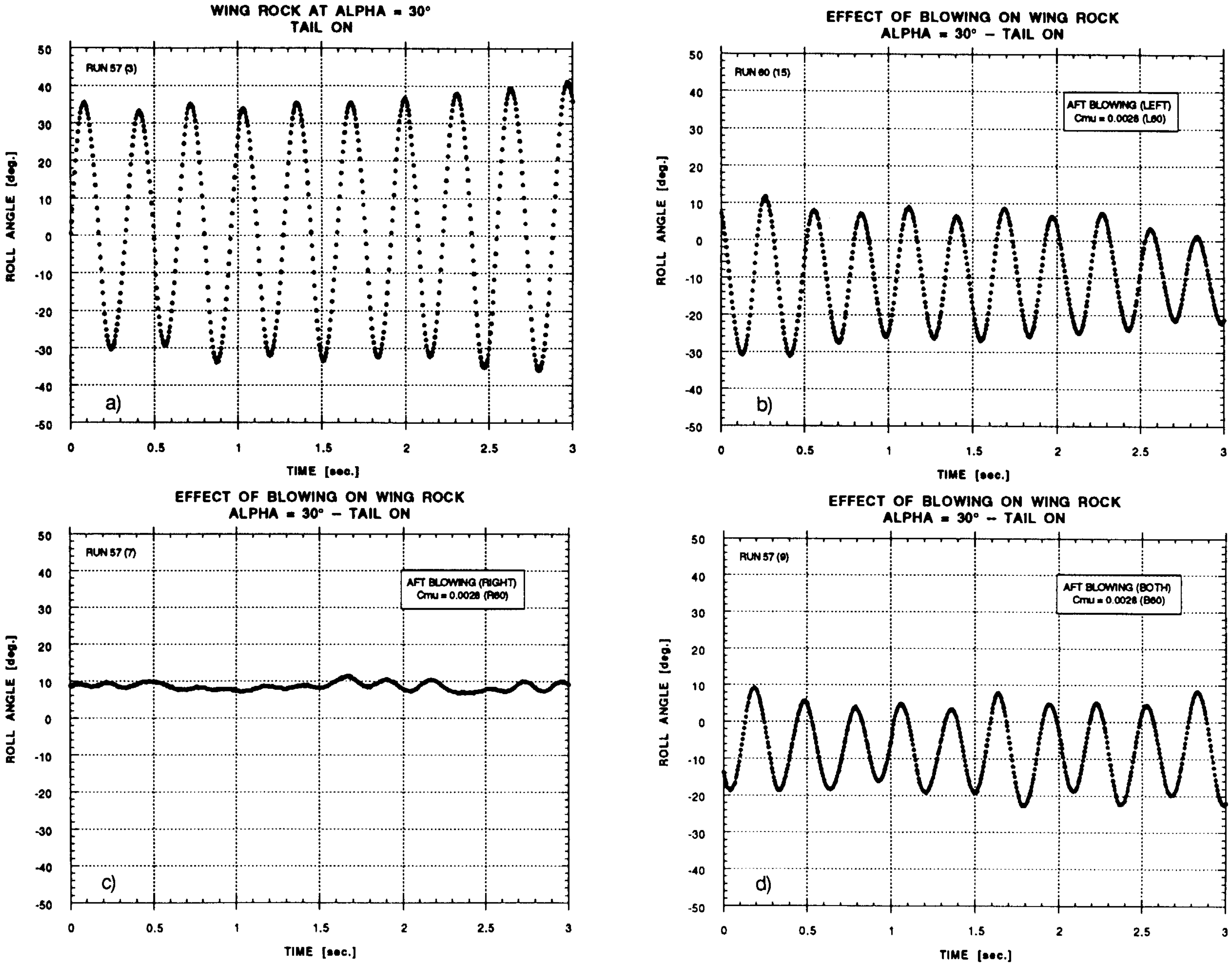

Figure 61 - Effect of Aft Blowing on Wing Rock at α = 30°; (Tail On, Cμ = 0.0028); a) No Blowing, b) Left Nozzle, c) Right Nozzle , d) Simultaneous

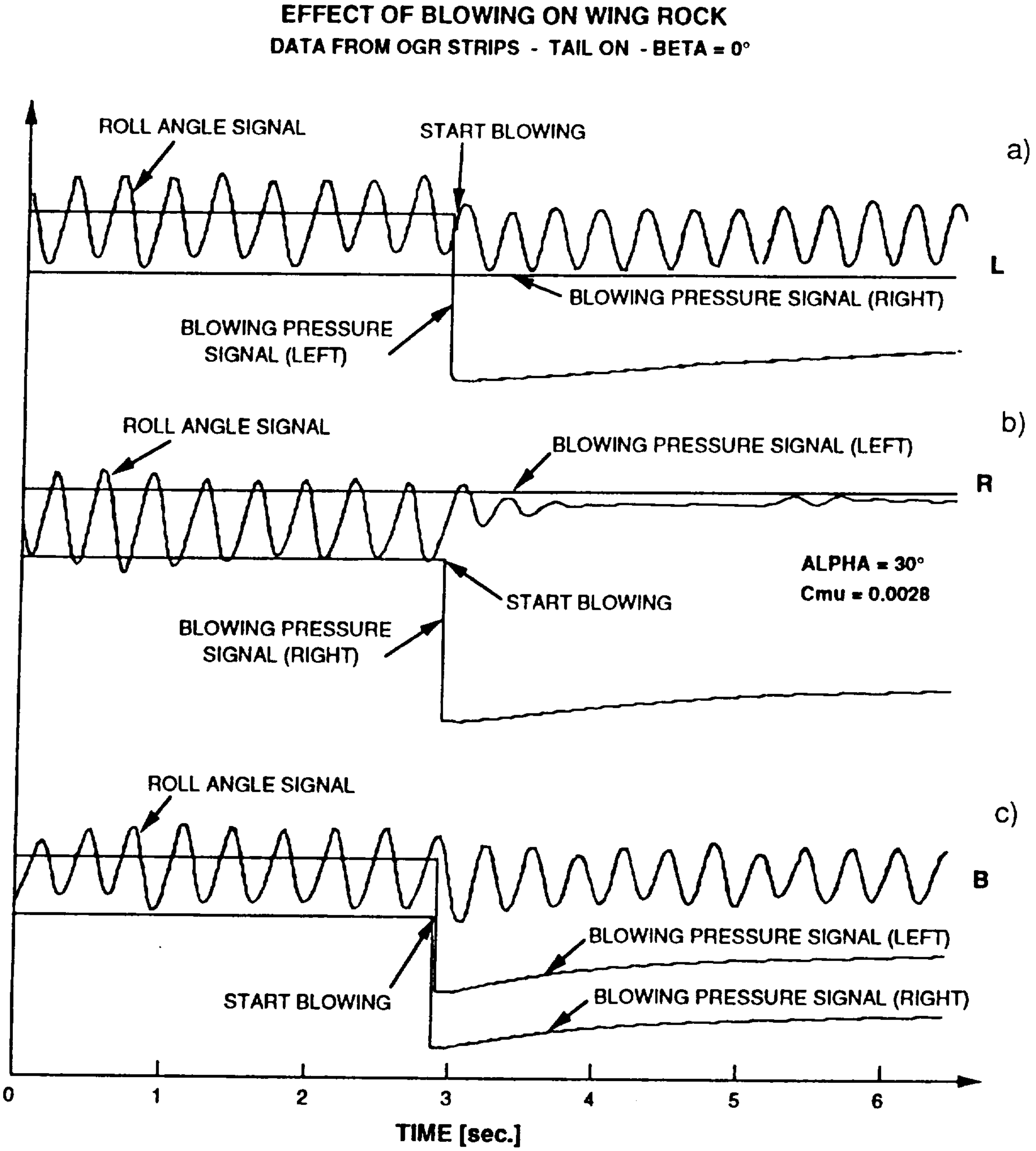

Figure 62 - Effect of Aft Blowing on Wing Rock at $\alpha = 30°$; (Tail On, $C\mu = 0.0028$); a) Left Nozzle, b) Right Nozzle , c) Simultaneous

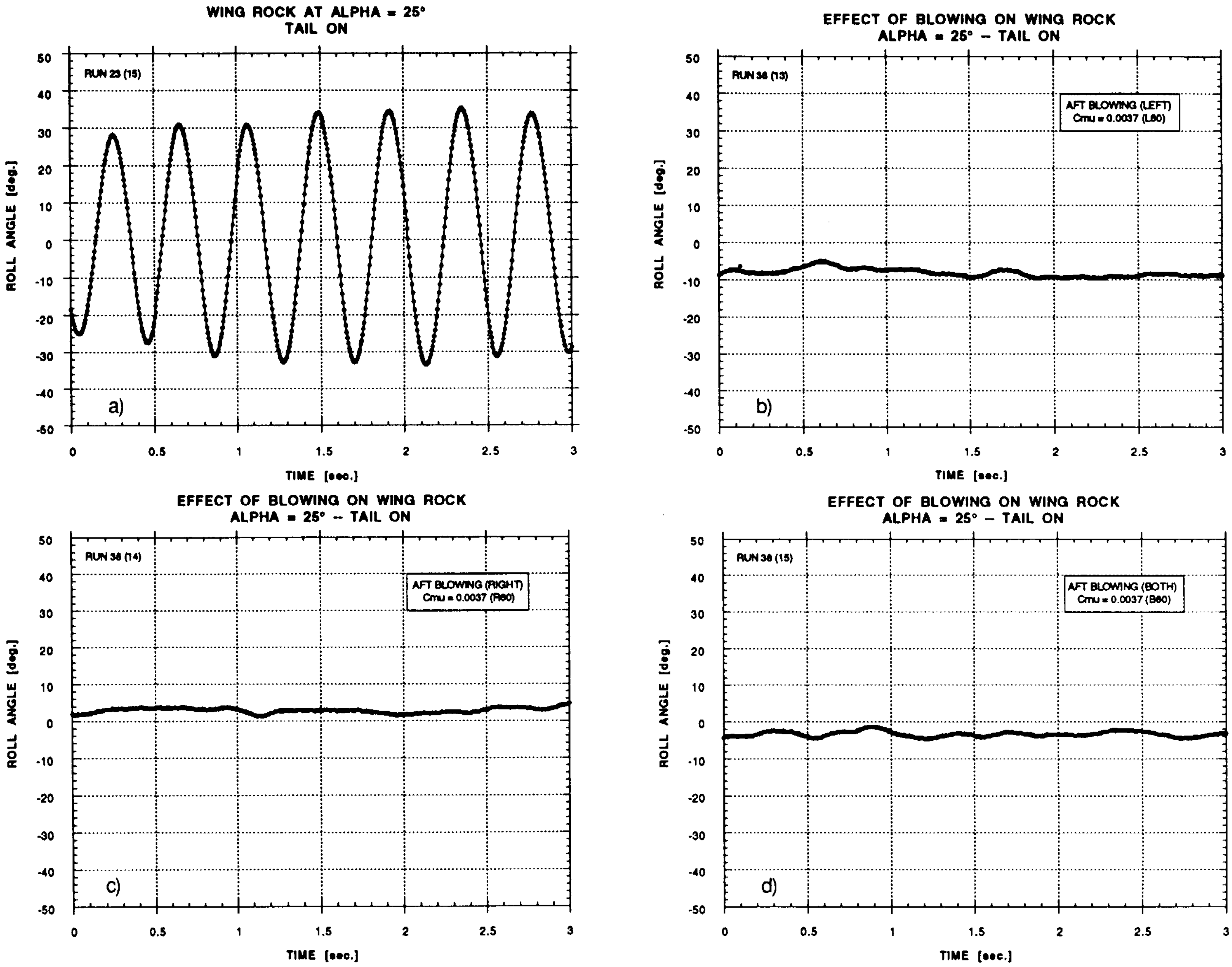

Figure 63 - Effect of Aft Blowing on Wing Rock at $\alpha = 25°$; (Tail On, $C\mu = 0.0037$); a) No Blowing, b) Left Nozzle, c) Right Nozzle , d) Simultaneous

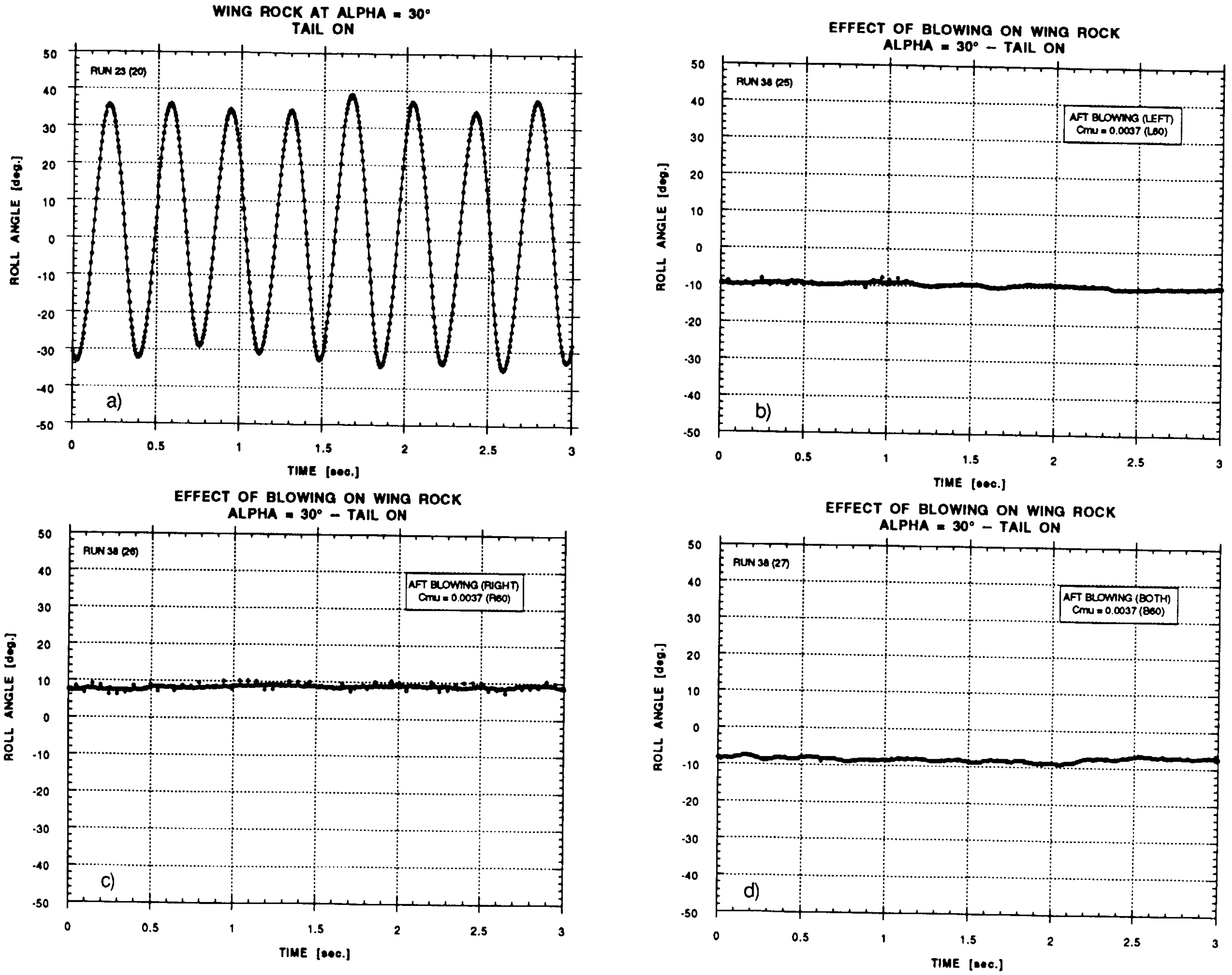

Figure 64 - Effect of Aft Blowing on Wing Rock at $\alpha = 30°$; (Tail On, $C_\mu = 0.0037$); a) No Blowing, b) Left Nozzle, c) Right Nozzle , d) Simultaneous

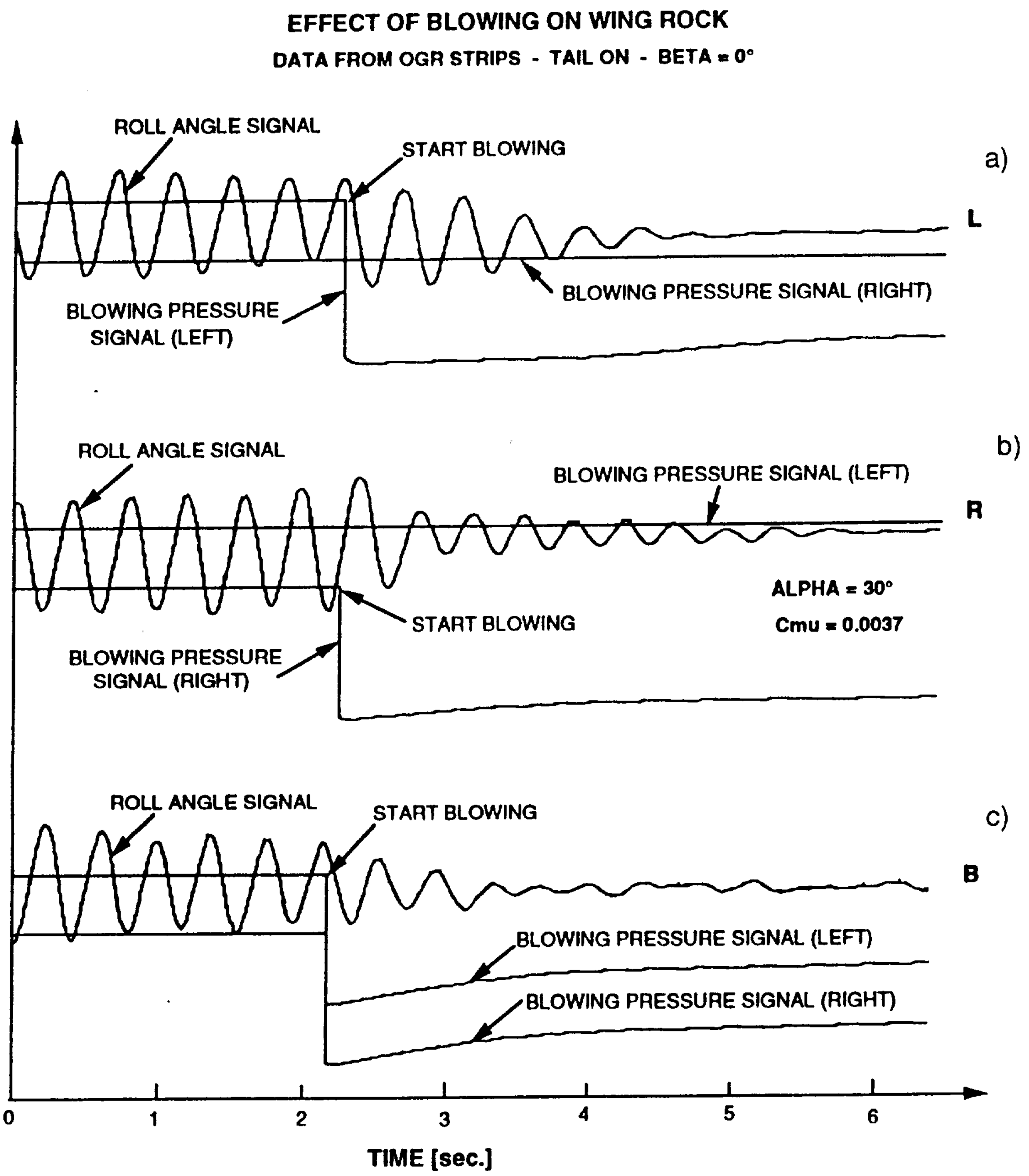

Figure 65 - Effect of Aft Blowing on Wing Rock at $\alpha = 30°$; (Tail On, $C\mu = 0.0037$); a) Left Nozzle, b) Right Nozzle , c) Simultaneous

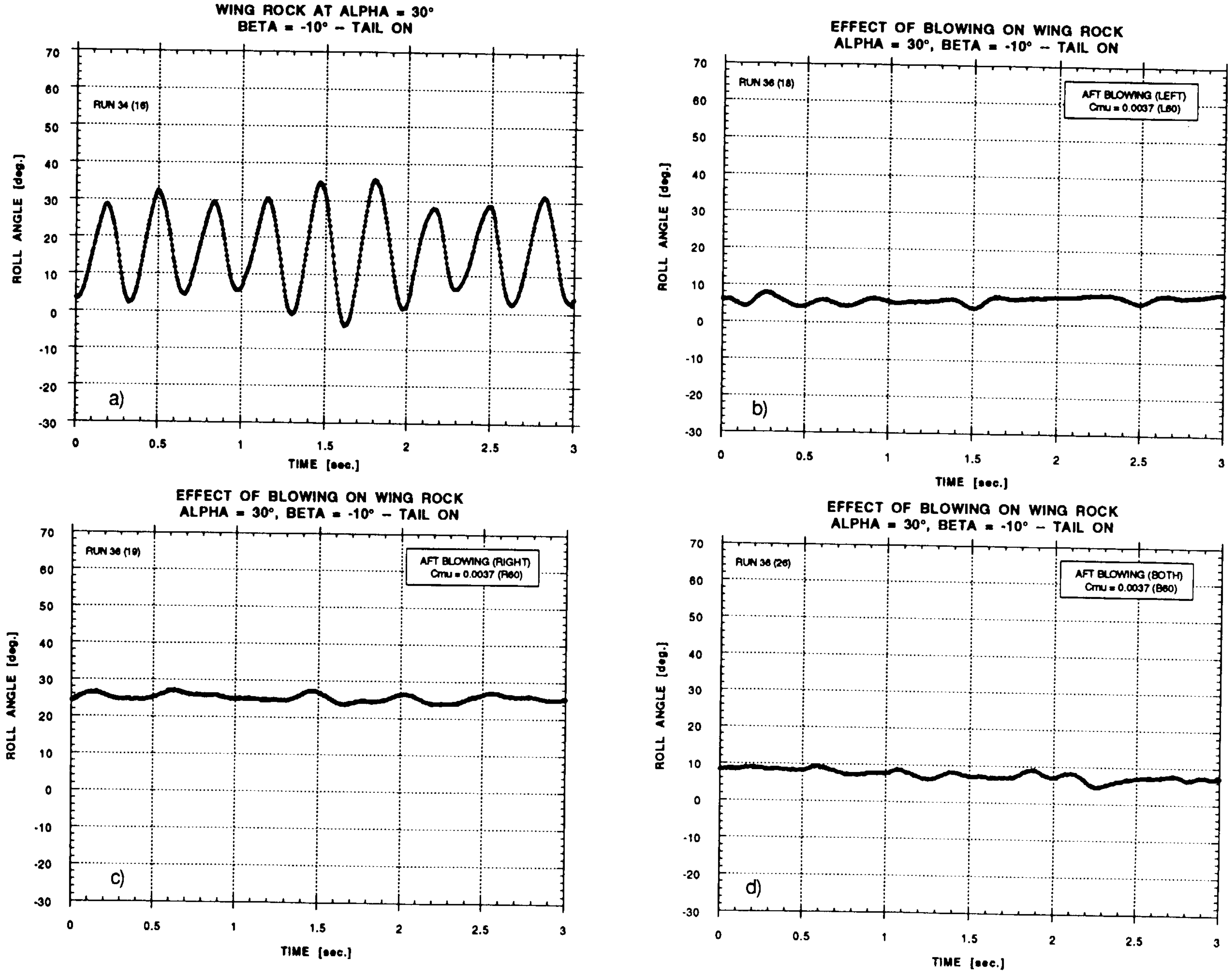

WING ROCK AT ALPHA = 30°
BETA = -10° -- TAIL ON

EFFECT OF BLOWING ON WING ROCK
ALPHA = 30°, BETA = -10° -- TAIL ON

EFFECT OF BLOWING ON WING ROCK
ALPHA = 30°, BETA = -10° -- TAIL ON

EFFECT OF BLOWING ON WING ROCK
ALPHA = 30°, BETA = -10° -- TAIL ON

Figure 66 - Effect of Aft Blowing on Wing Rock at $\alpha = 30°$ and $\beta = -10°$; (Tail On, $C\mu = 0.0037$); a) No Blowing, b) Left Nozzle, c) Right Nozzle , d) Simultaneous

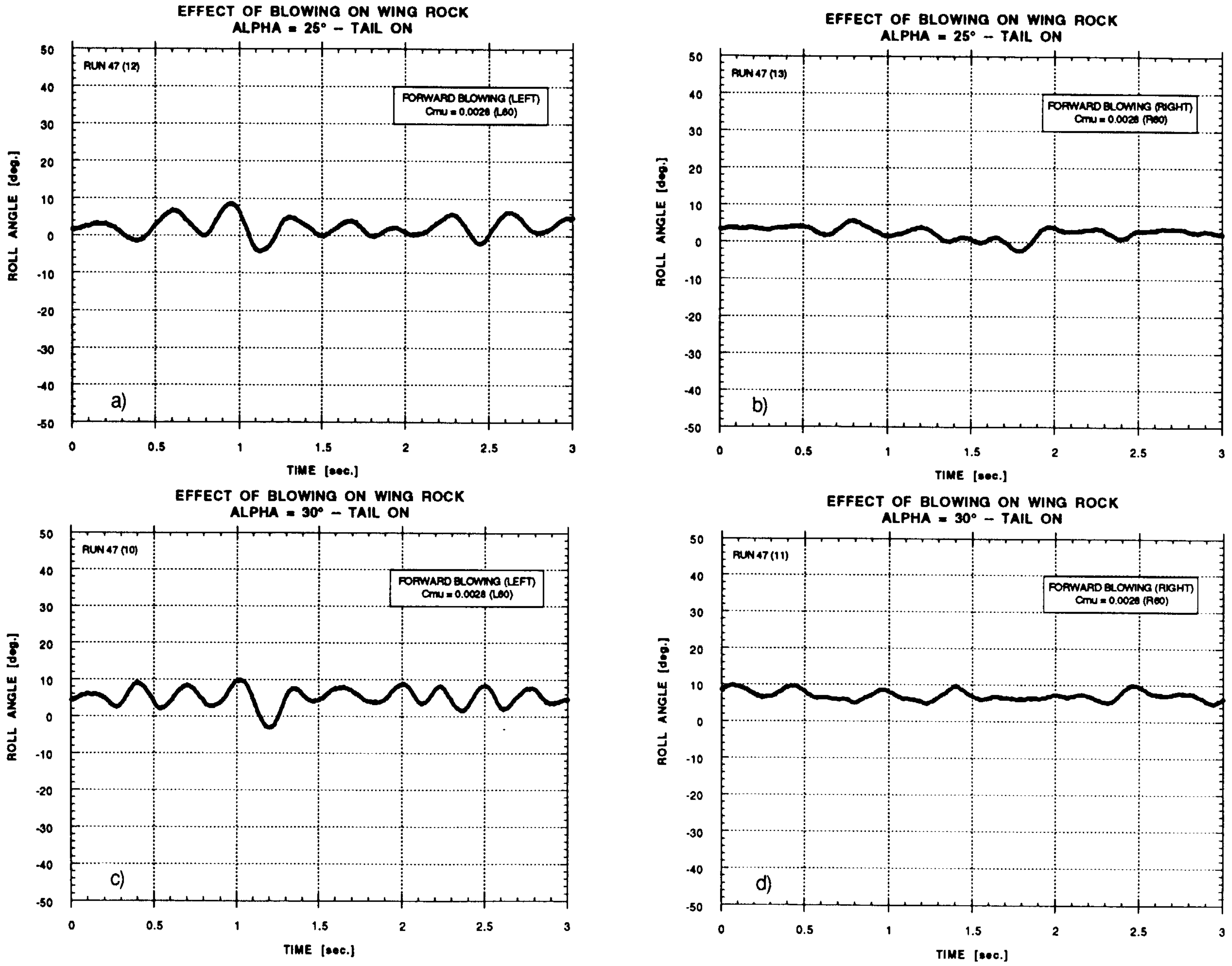

Figure 67 - Effect of Forward Blowing on Wing Rock (Tail On, $C\mu = 0.0028$); a) $\alpha = 25°$, left, b) $\alpha = 25°$, right, c) $\alpha = 30°$, left, d) $\alpha = 30°$, right

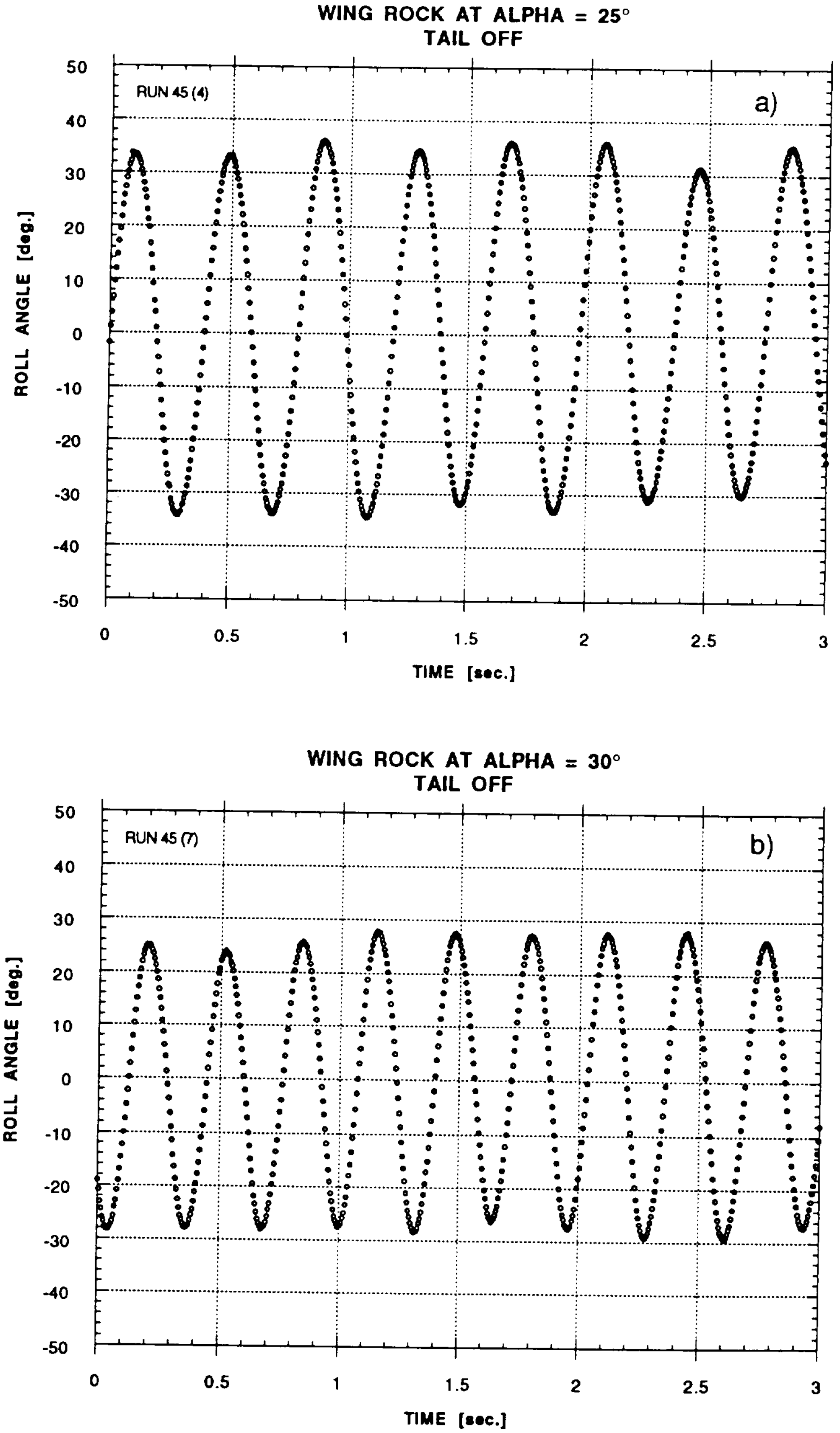

Figure 68 - Wing Rock Motion (Tail Off); a) $\alpha = 25°$, b) $\alpha = 30°$

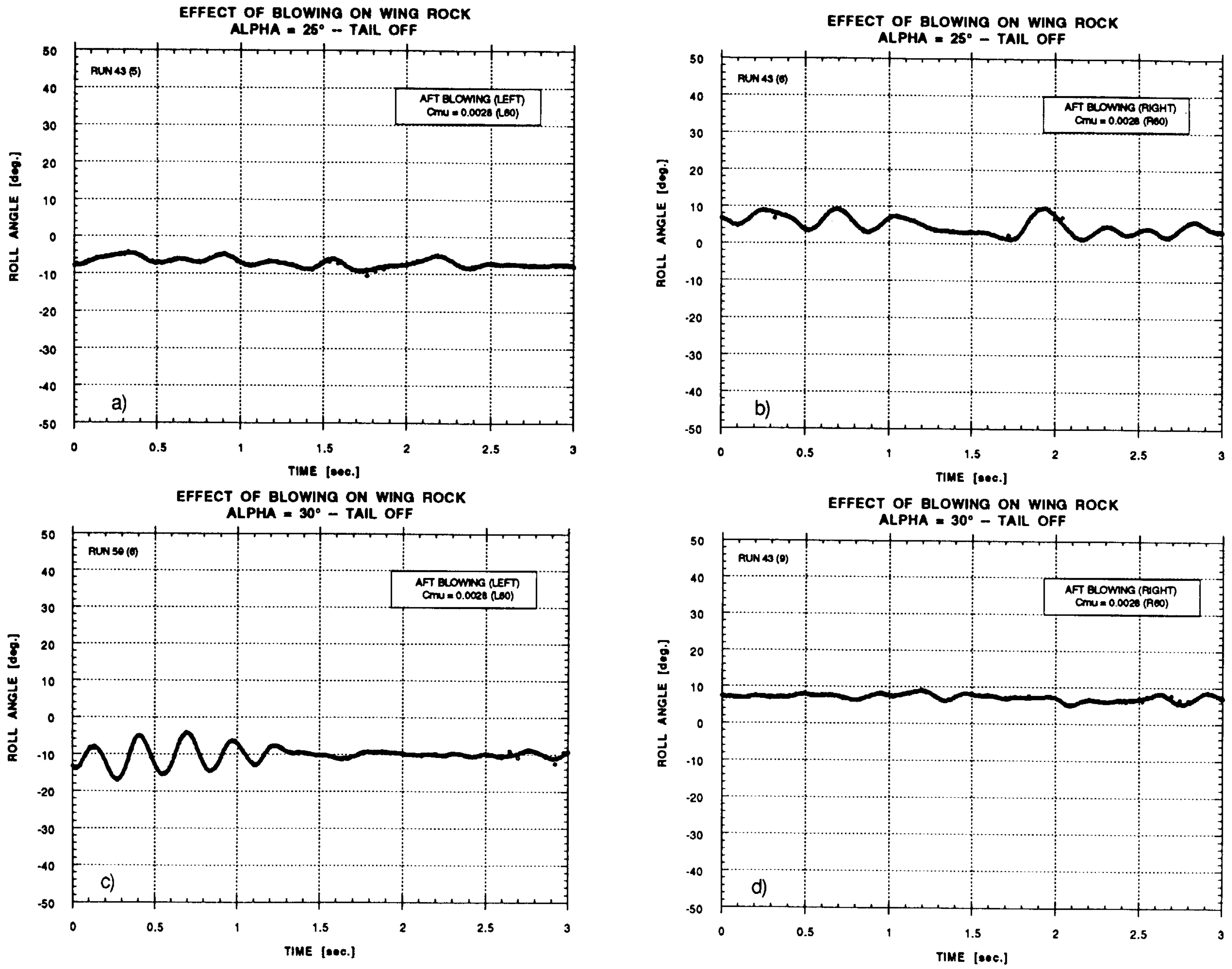

Figure 69 - Effect of Aft Blowing on Wing Rock (Tail Off, $C\mu = 0.0028$); a) $\alpha = 25°$, left, b) $\alpha = 25°$, right, c) $\alpha = 30°$, left, d) $\alpha = 30°$, right

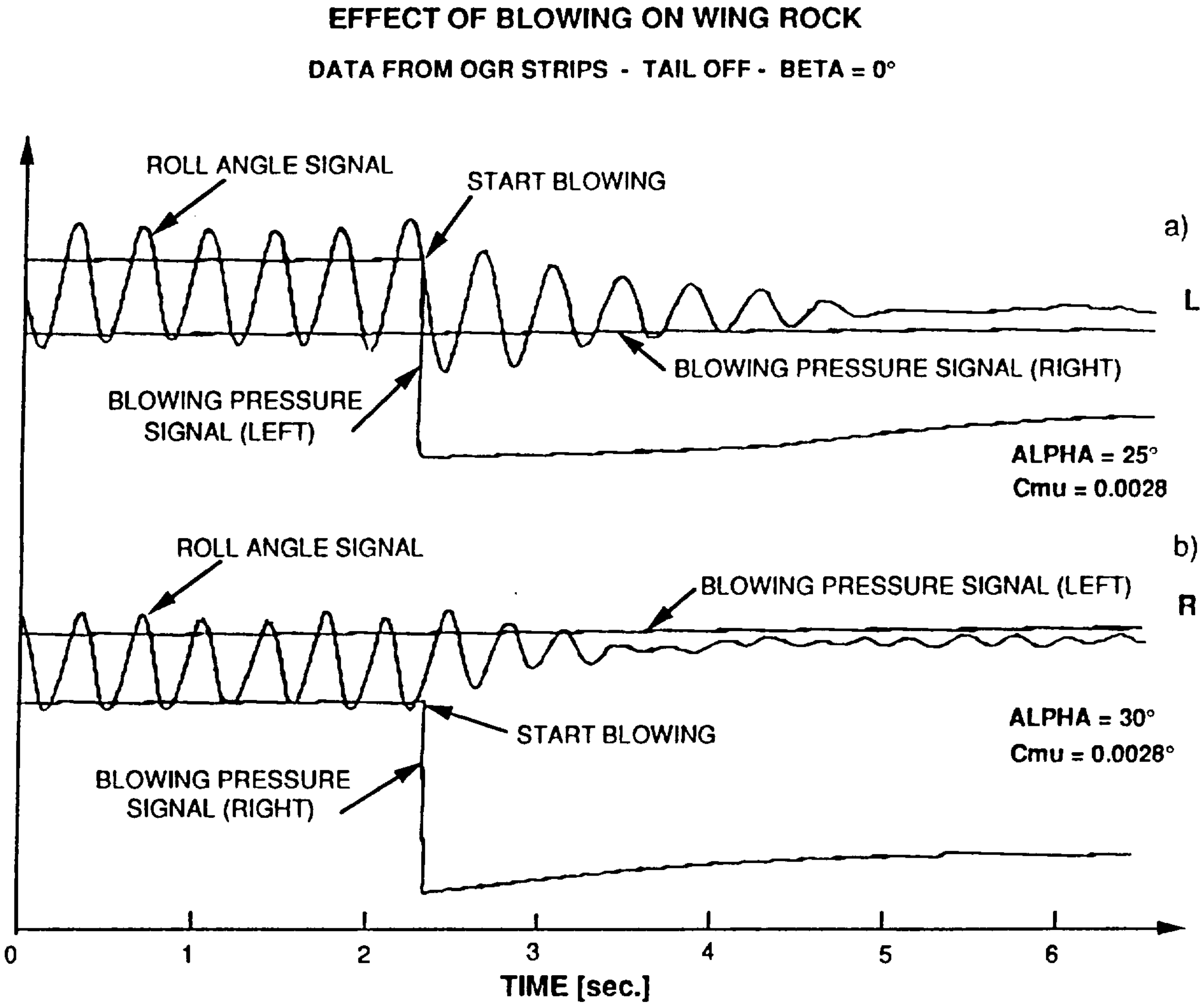

Figure 70 - Effect of Aft Blowing on Wing Rock (Tail Off, $C\mu = 0.0028$); a) $\alpha = 25°$, left, b) $\alpha = 30°$, right

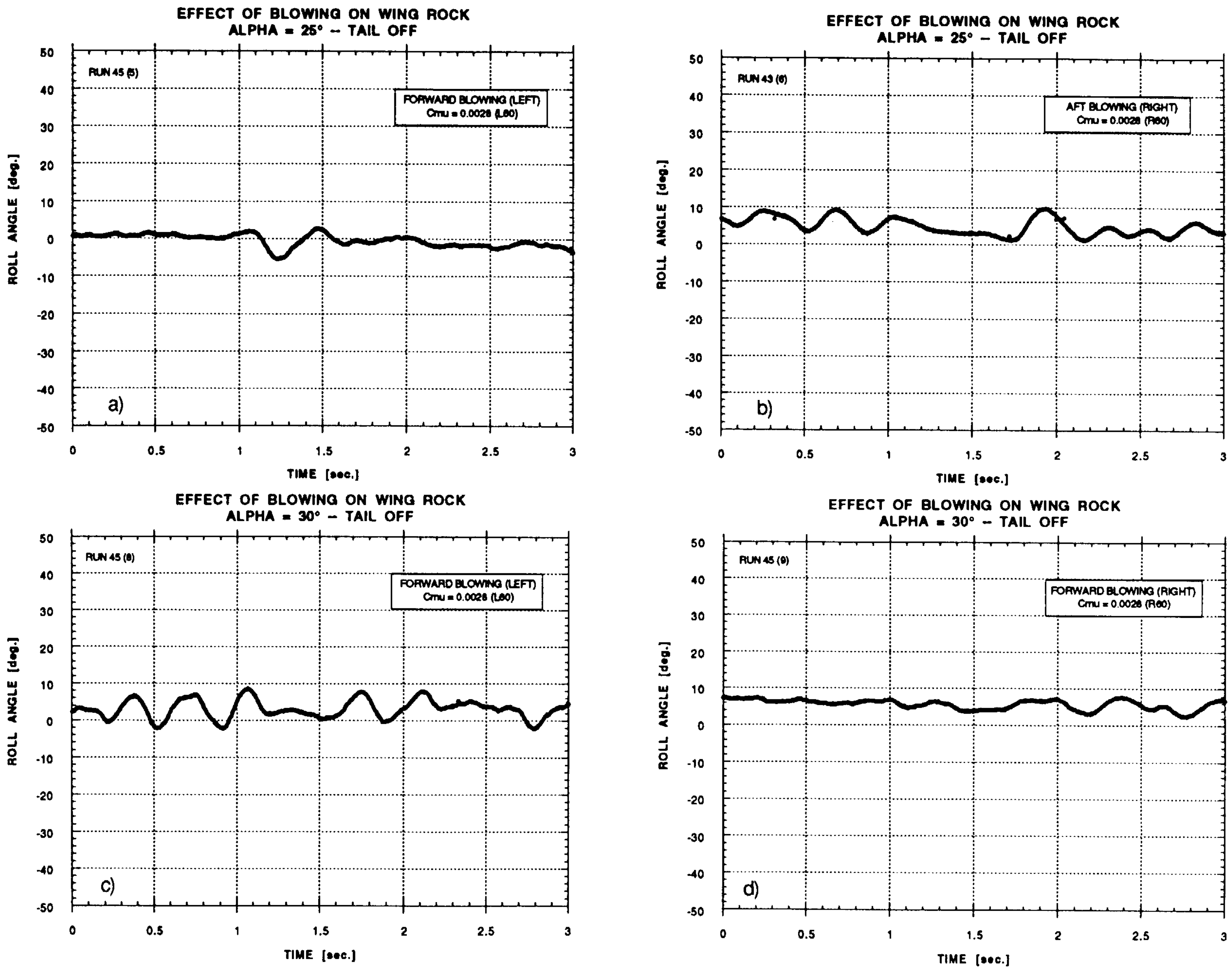

Figure 71 - Effect of Forward Blowing on Wing Rock (Tail Off, $C\mu = 0.0028$); a) $\alpha = 25°$, left, b) $\alpha = 25°$, right, c) $\alpha = 30°$, left, d) $\alpha = 30°$, right

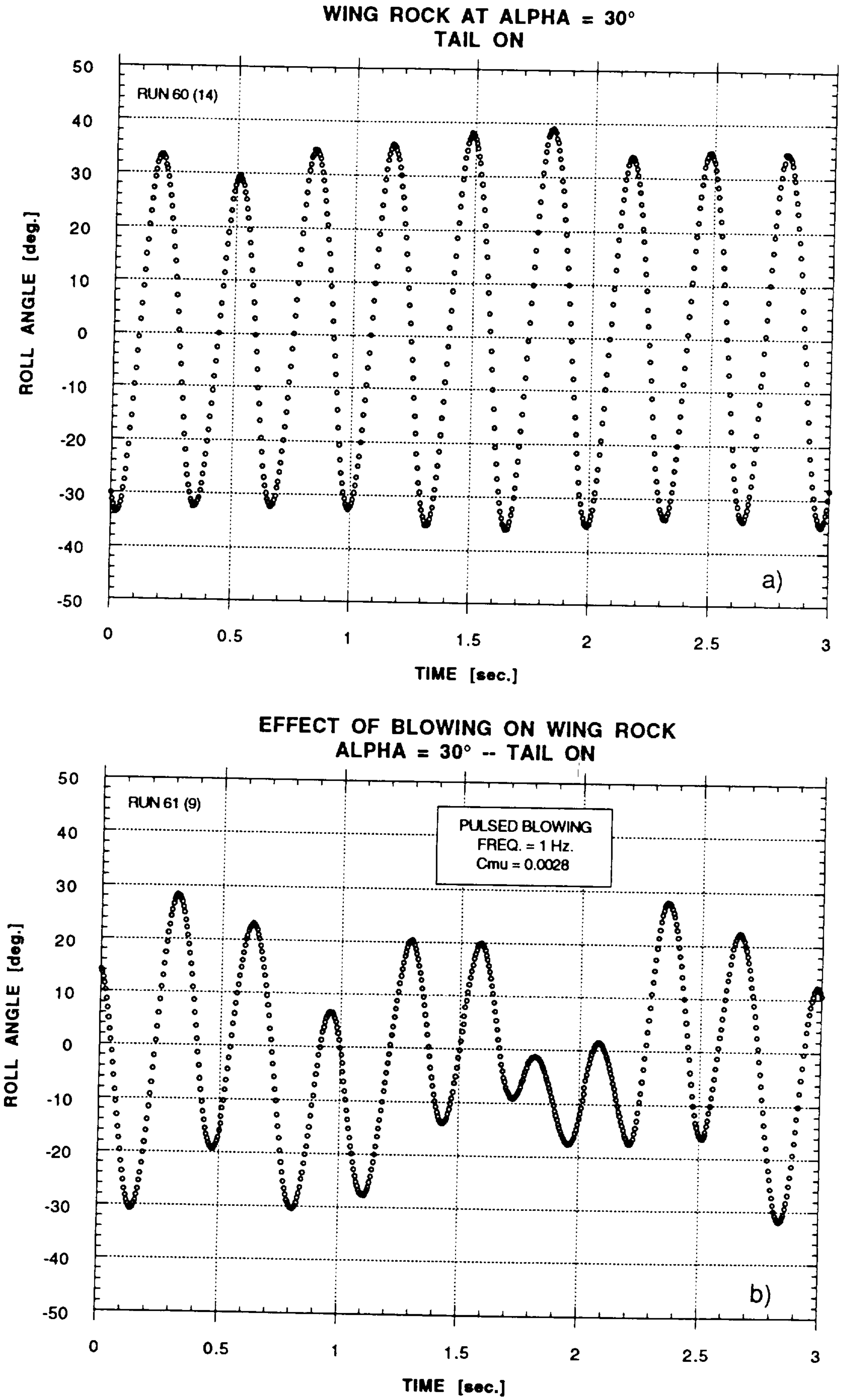

Figure 72 - Effect of Alternating Pulsed Blowing at $\alpha = 30°$ (Tail On); a) No Blowing, b) 1 Hz, c) 3 Hz, d) 6 Hz, e) 9 Hz, f) 12 Hz

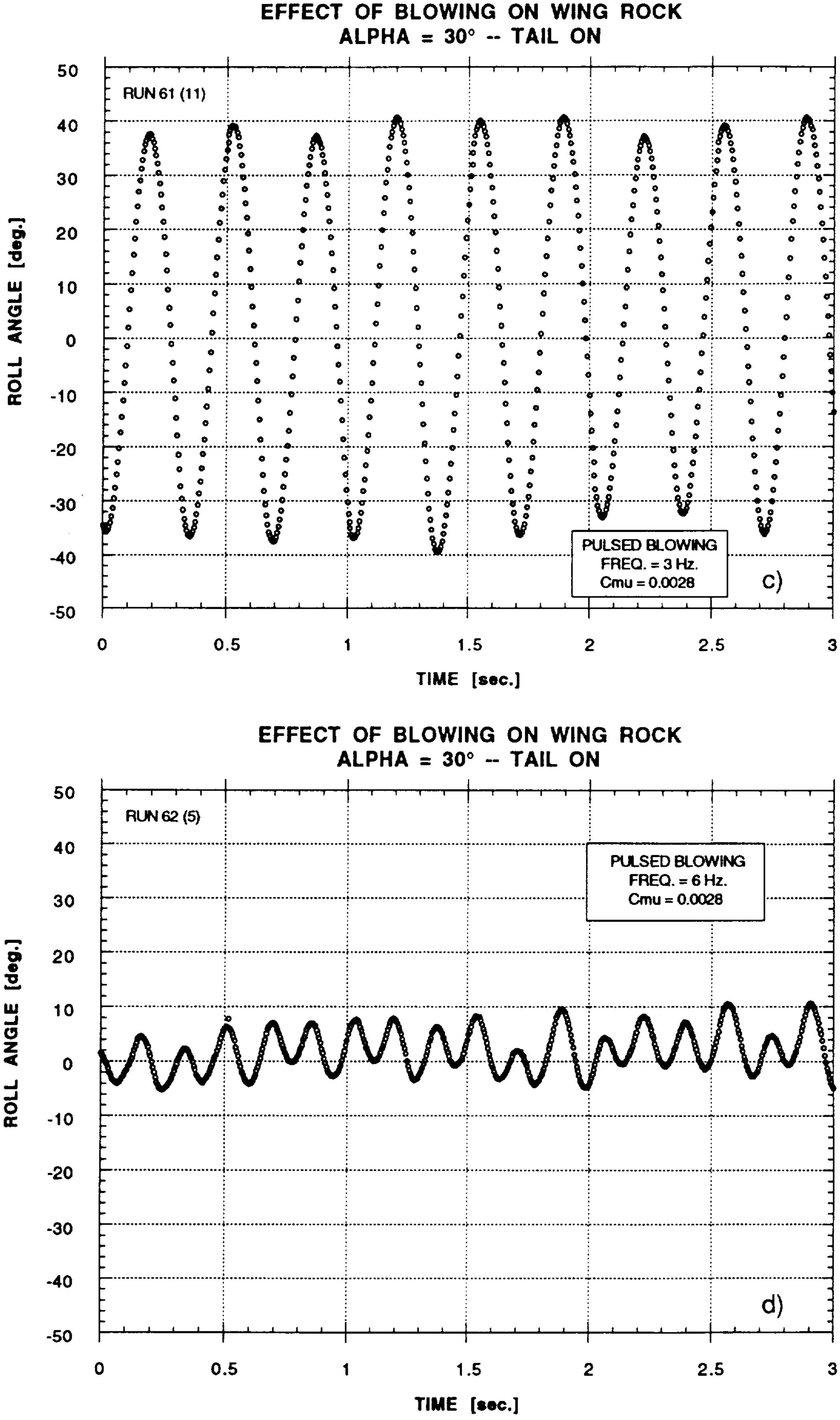

EFFECT OF BLOWING ON WING ROCK
ALPHA = 30° -- TAIL ON

EFFECT OF BLOWING ON WING ROCK
ALPHA = 30° -- TAIL ON

Figure 72 - Continued

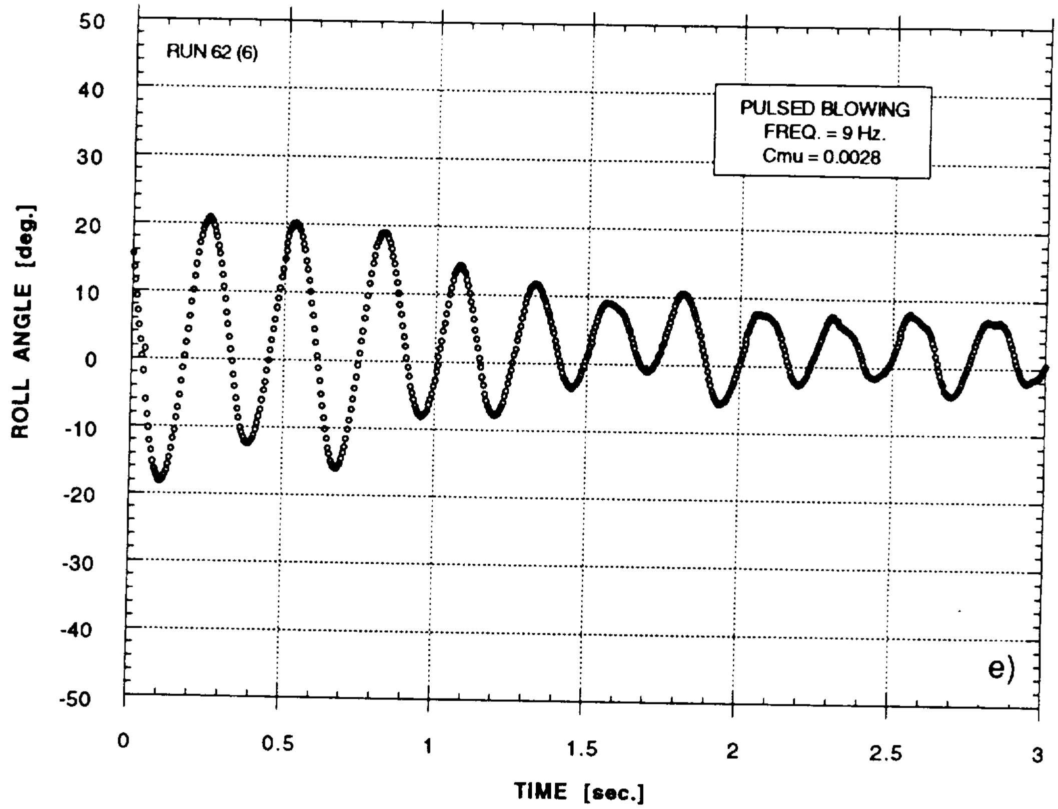
EFFECT OF BLOWING ON WING ROCK
ALPHA = 30° -- TAIL ON

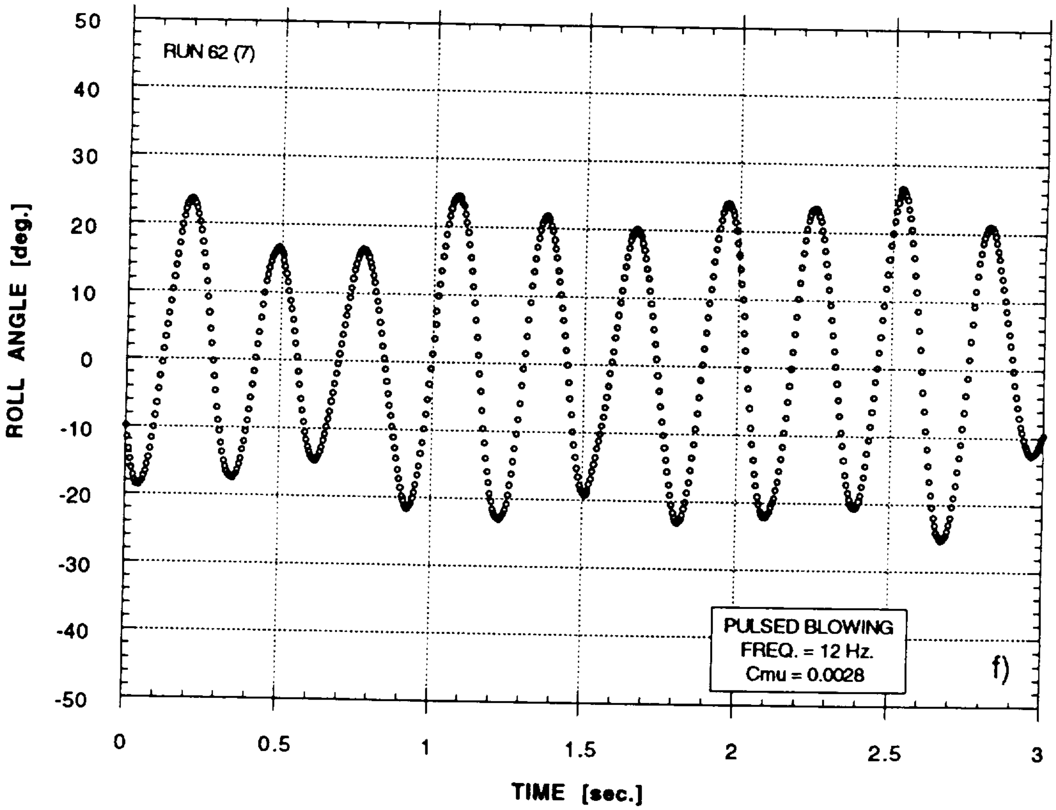
EFFECT OF BLOWING ON WING ROCK
ALPHA = 30° -- TAIL ON

Figure 72 - Concluded

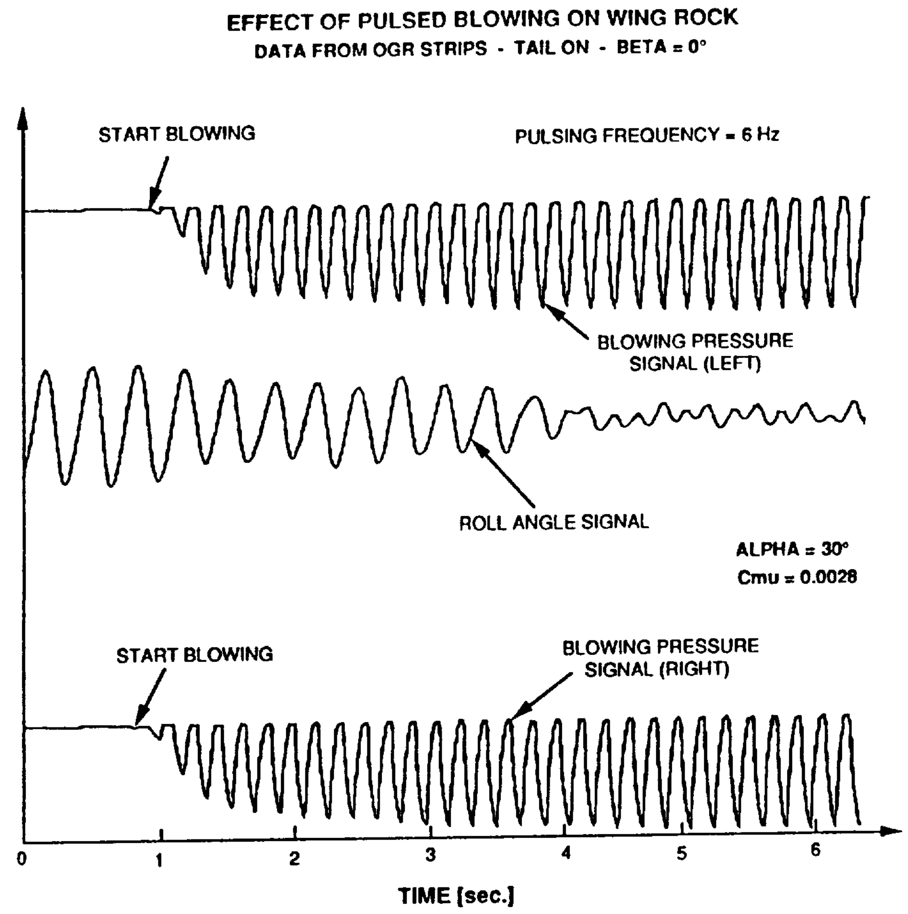

Figure 73 - Effect of Alternating Pulsed Blowing at α = 30° (Tail On, 6 Hz)

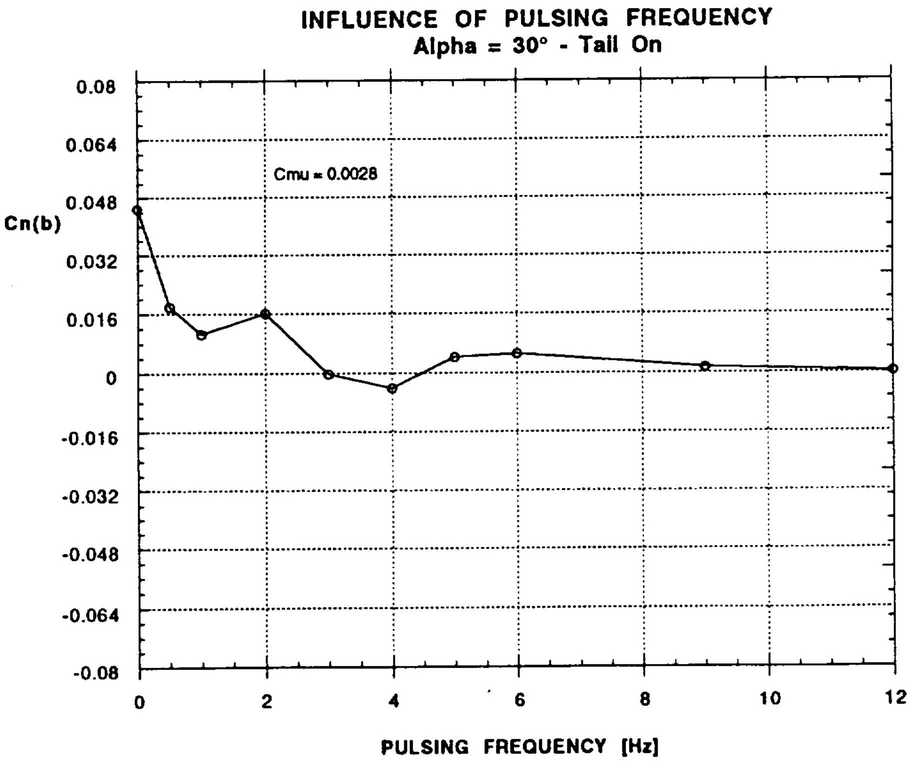

Figure 74 - Influence of Pulsing Frequency

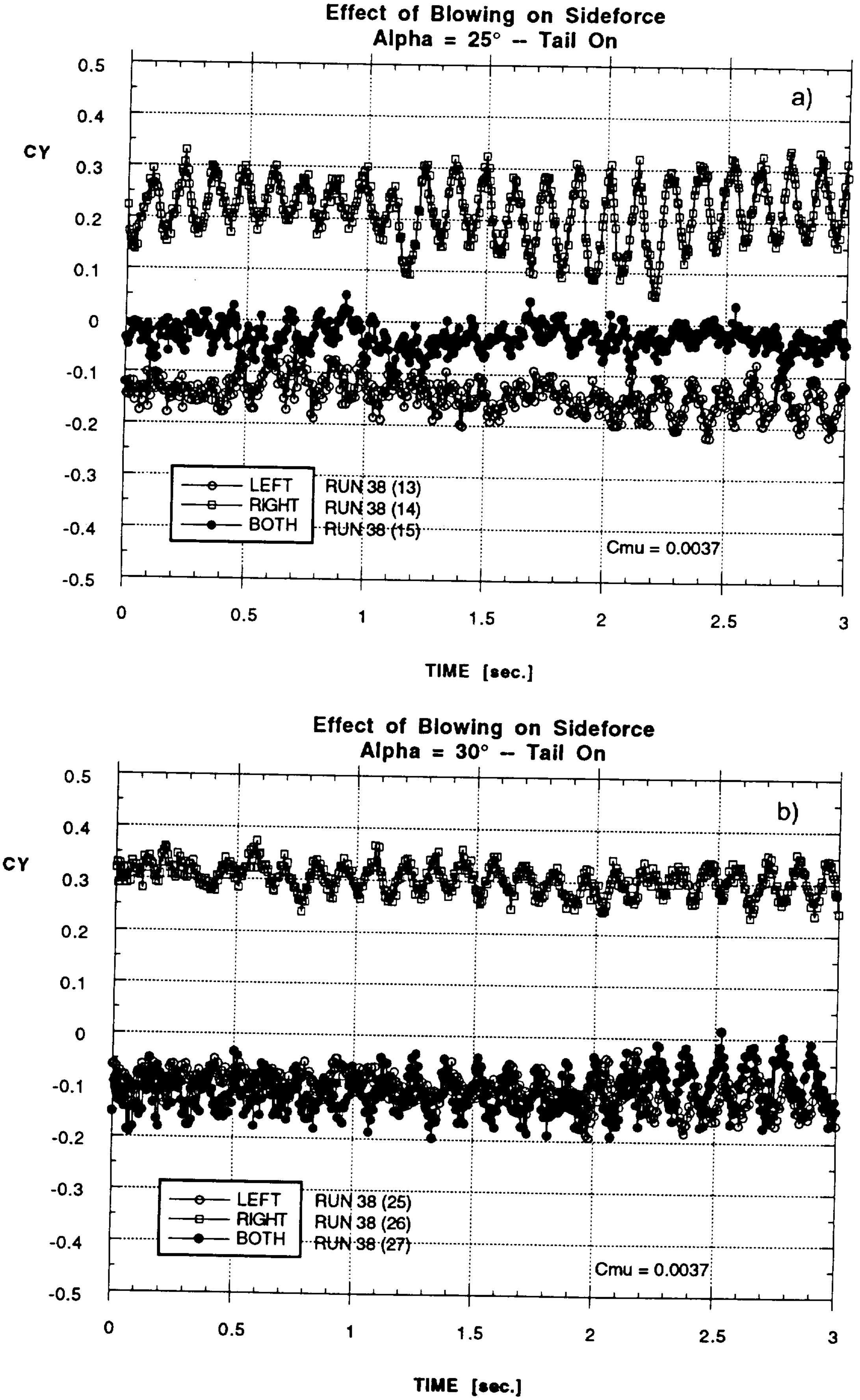

Figure 75 - Effect of Aft Blowing on Side Force, a) α = 25°, b) α = 30°

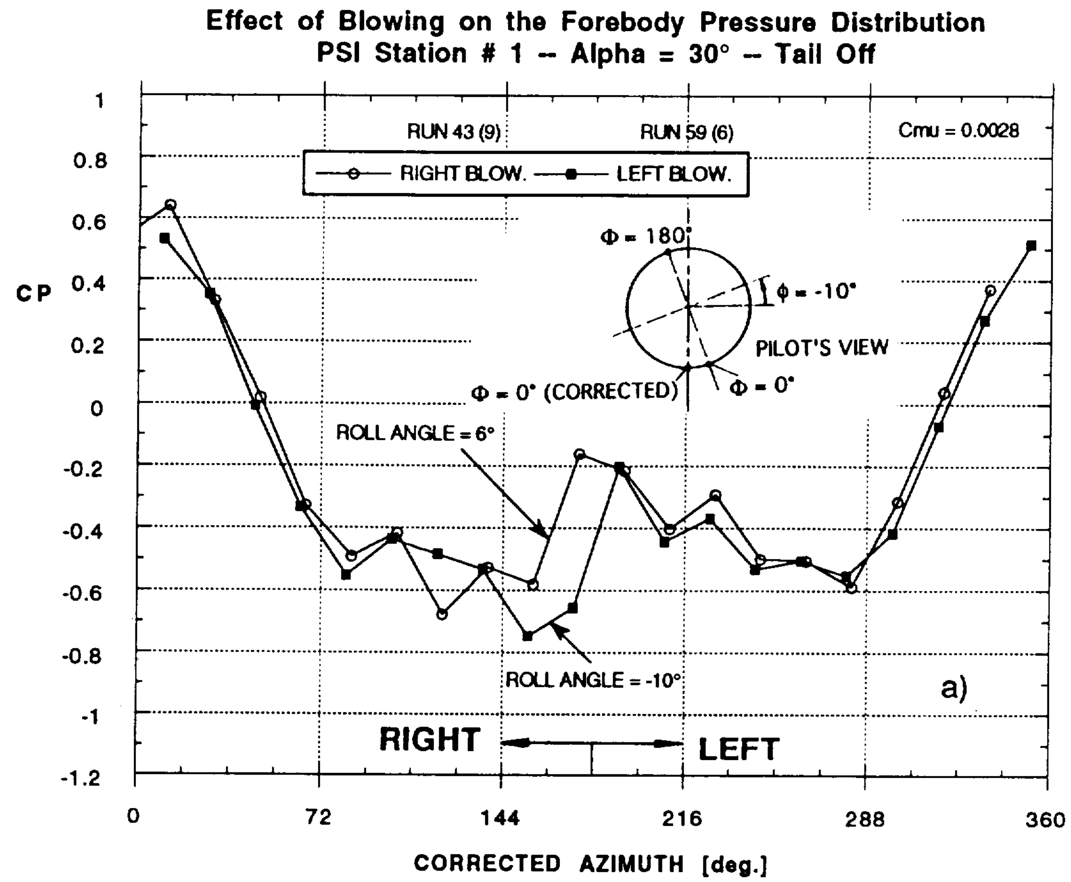

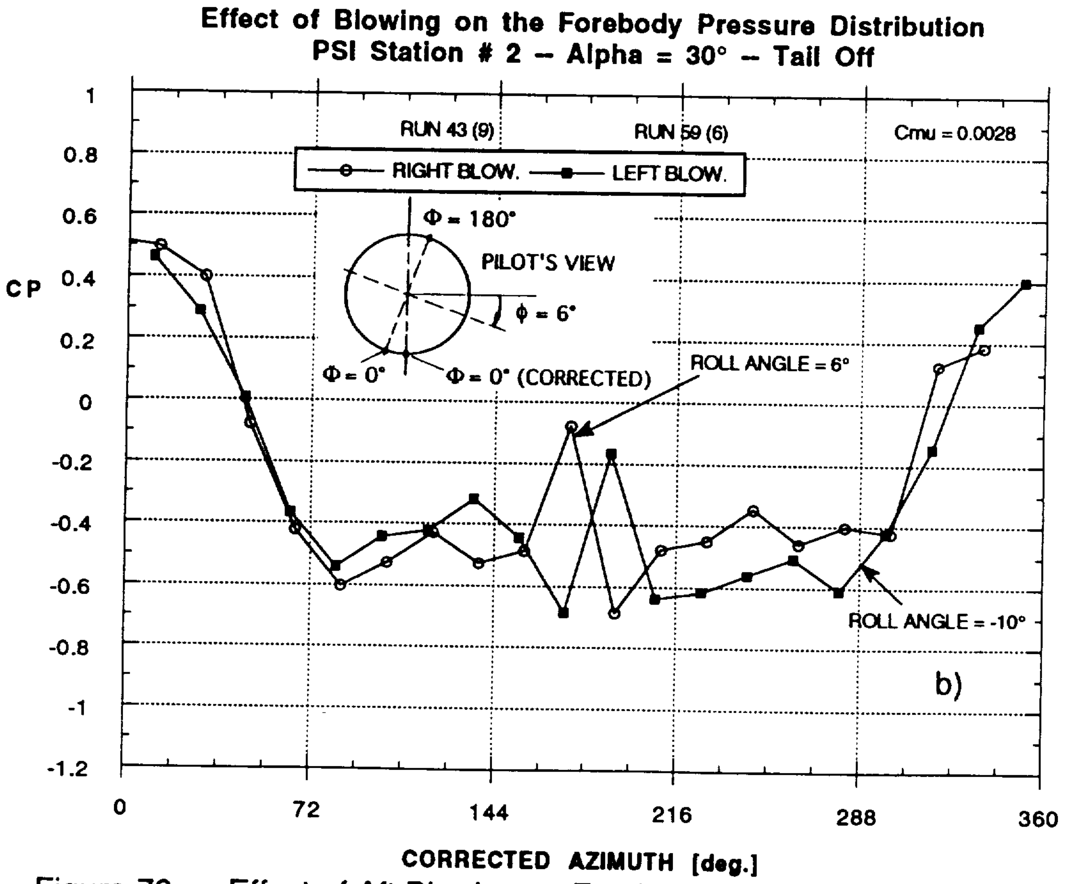

Figure 76 - Effect of Aft Blowing on Forebody Pressure Distribution at $\alpha = 30°$ (Tail Off, $C\mu = 0.0028$); a) Station #1, b) Station #2, c) Station #3

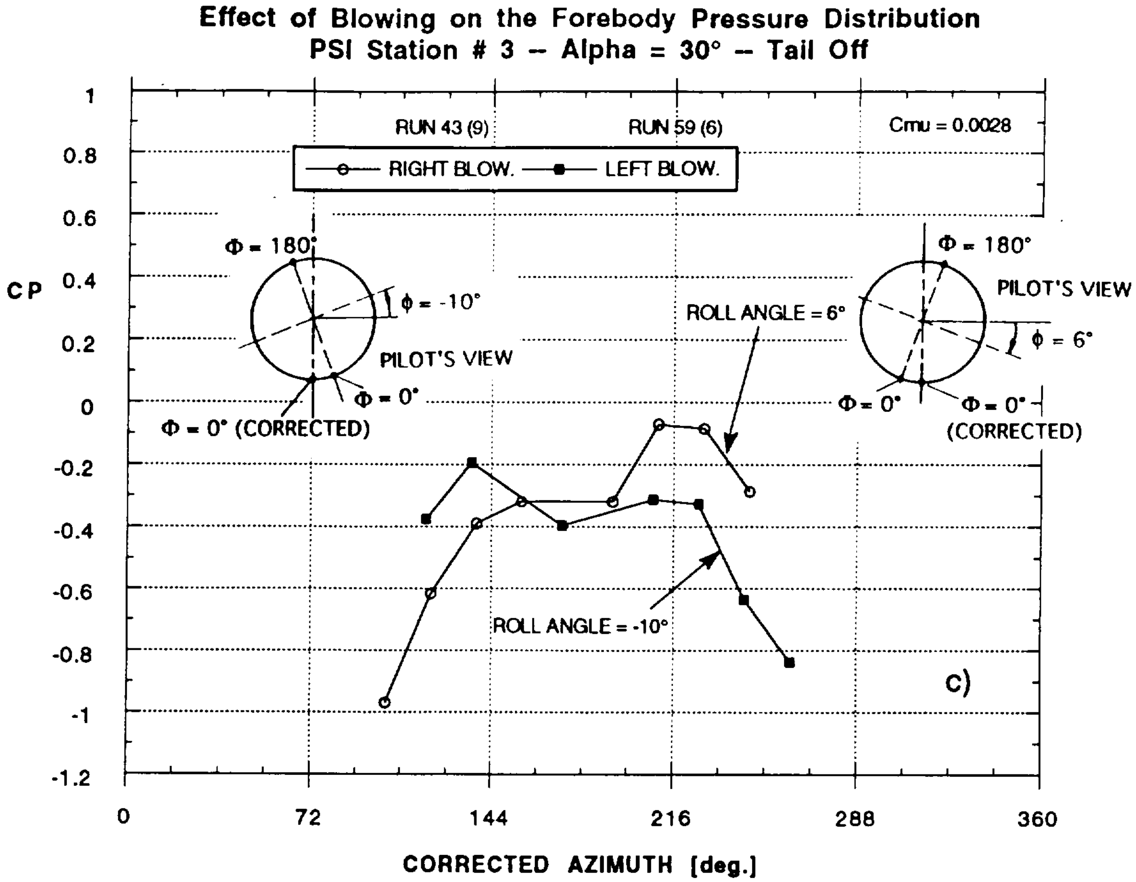

Effect of Blowing on the Forebody Pressure Distribution
PSI Station # 3 -- Alpha = 30° -- Tail Off

Figure 76 - Concluded

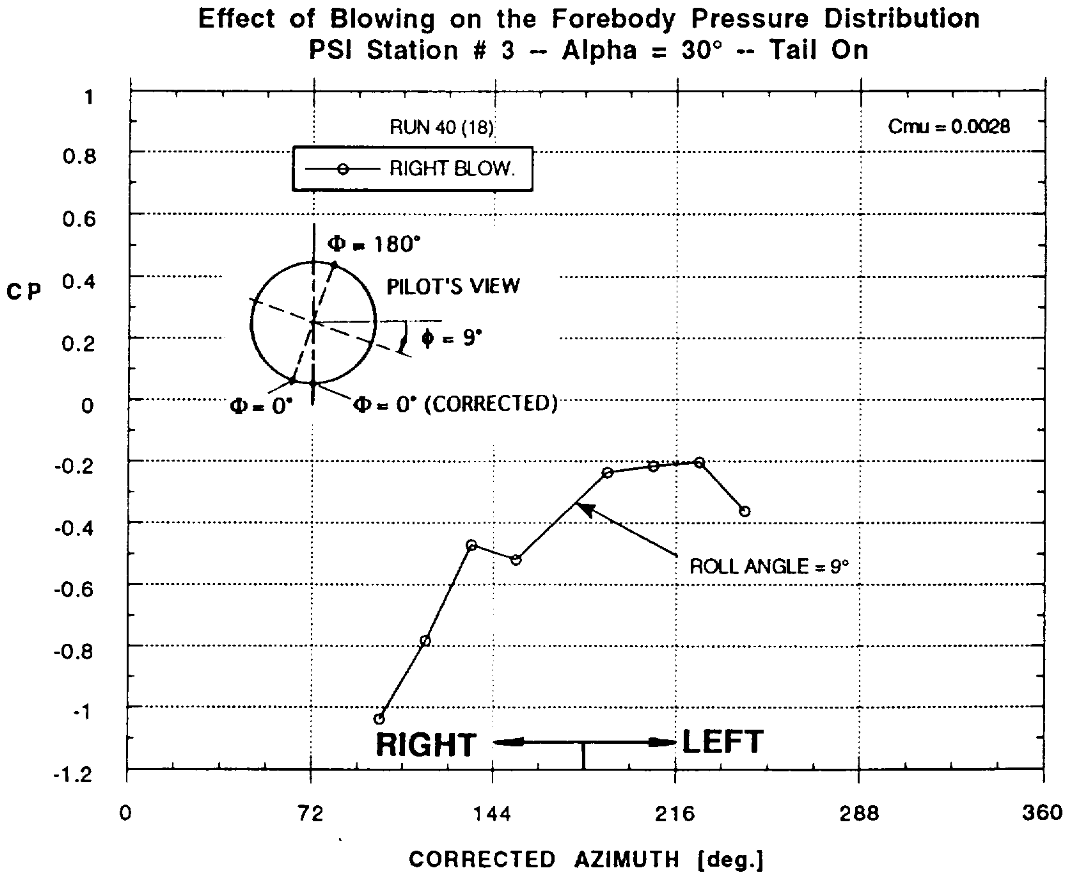

Effect of Blowing on the Forebody Pressure Distribution
PSI Station # 3 -- Alpha = 30° -- Tail On

Figure 77 - Effect of Aft Blowing on Forebody Pressure Distribution at α = 30°; (Tail On, Cμ = 0.0028, Station #3)

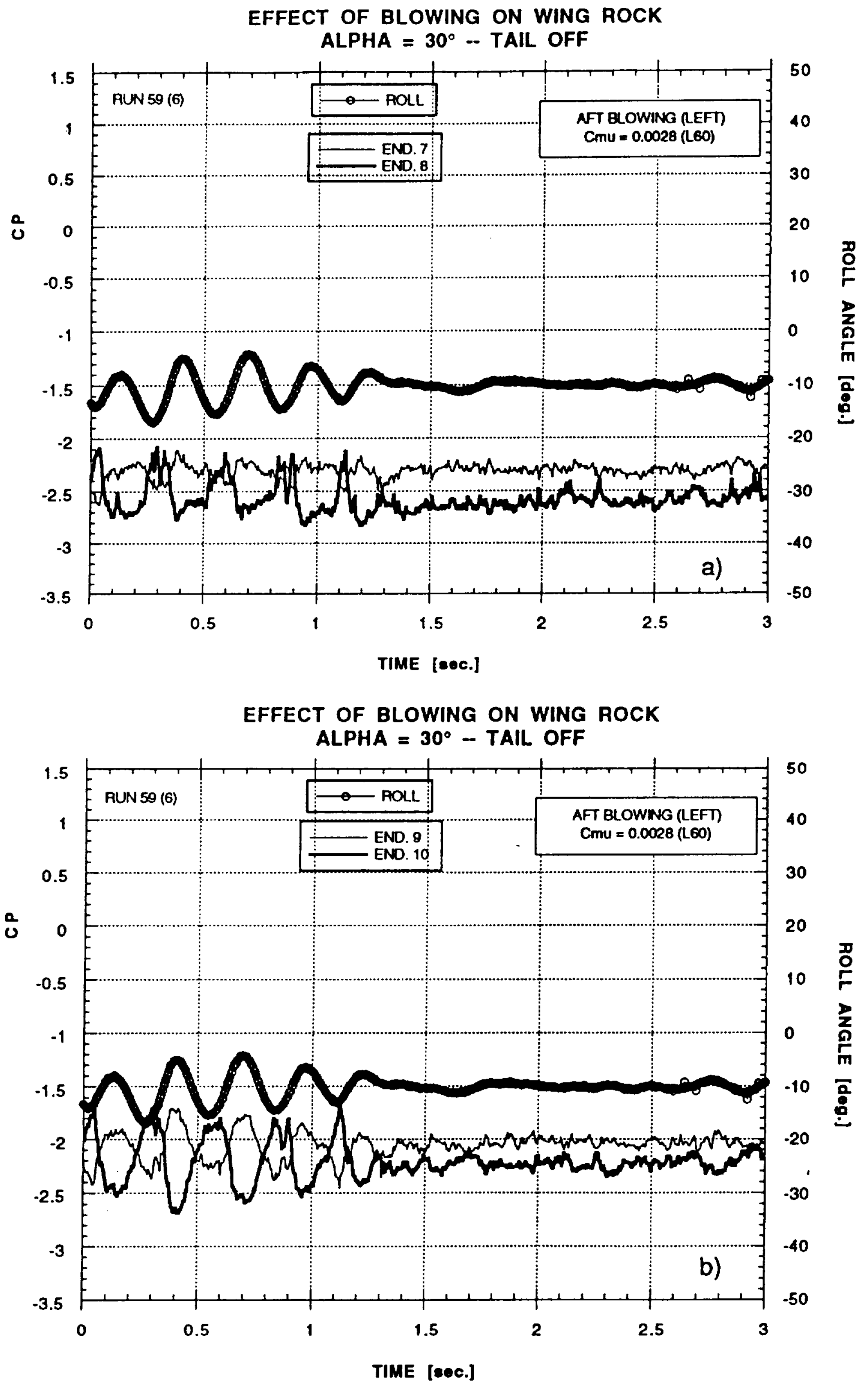

Figure 78 - Effect of Aft Blowing on Wing Pressure Distribution at $\alpha = 30°$; (Tail Off, $C\mu = 0.0028$); a-b) Left Nozzle, c-d) Right Nozzle

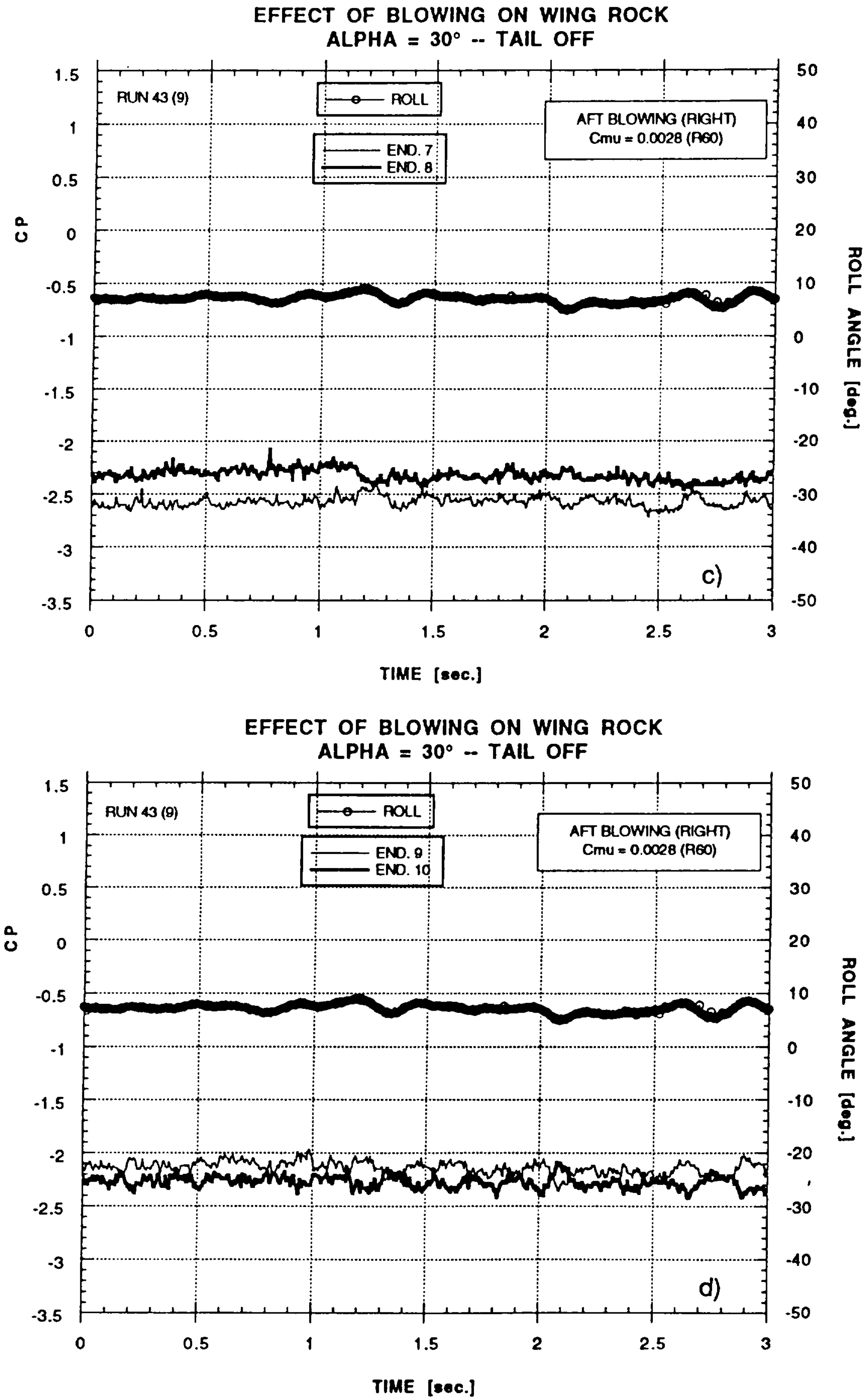

Figure 78 - Concluded

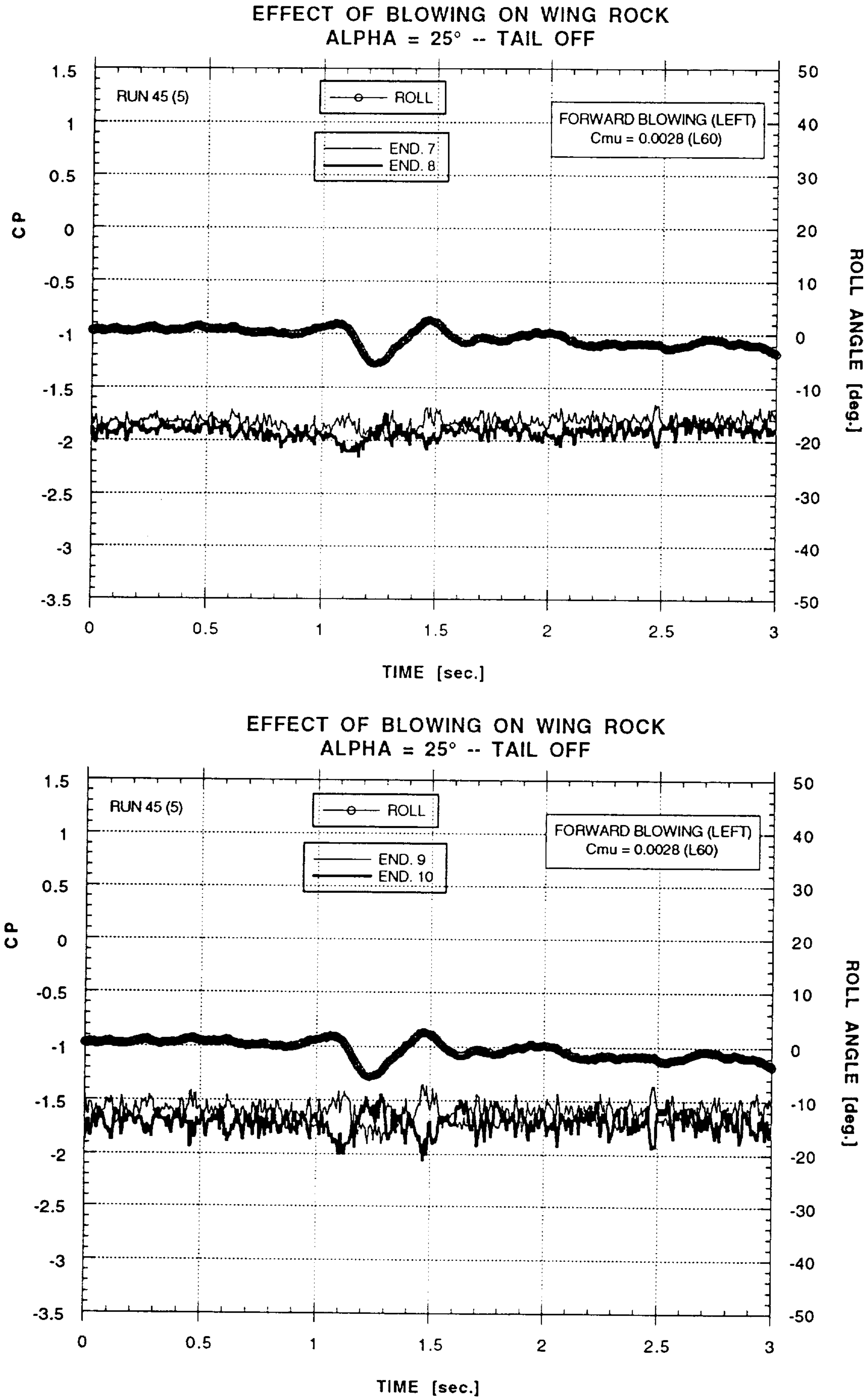

Figure 79 - Effect of Forward Blowing on Wing Pressure Distribution at $\alpha = 25°$ (Tail Off, $C\mu = 0.0028$); a-b) Left Nozzle, c-d) Right Nozzle

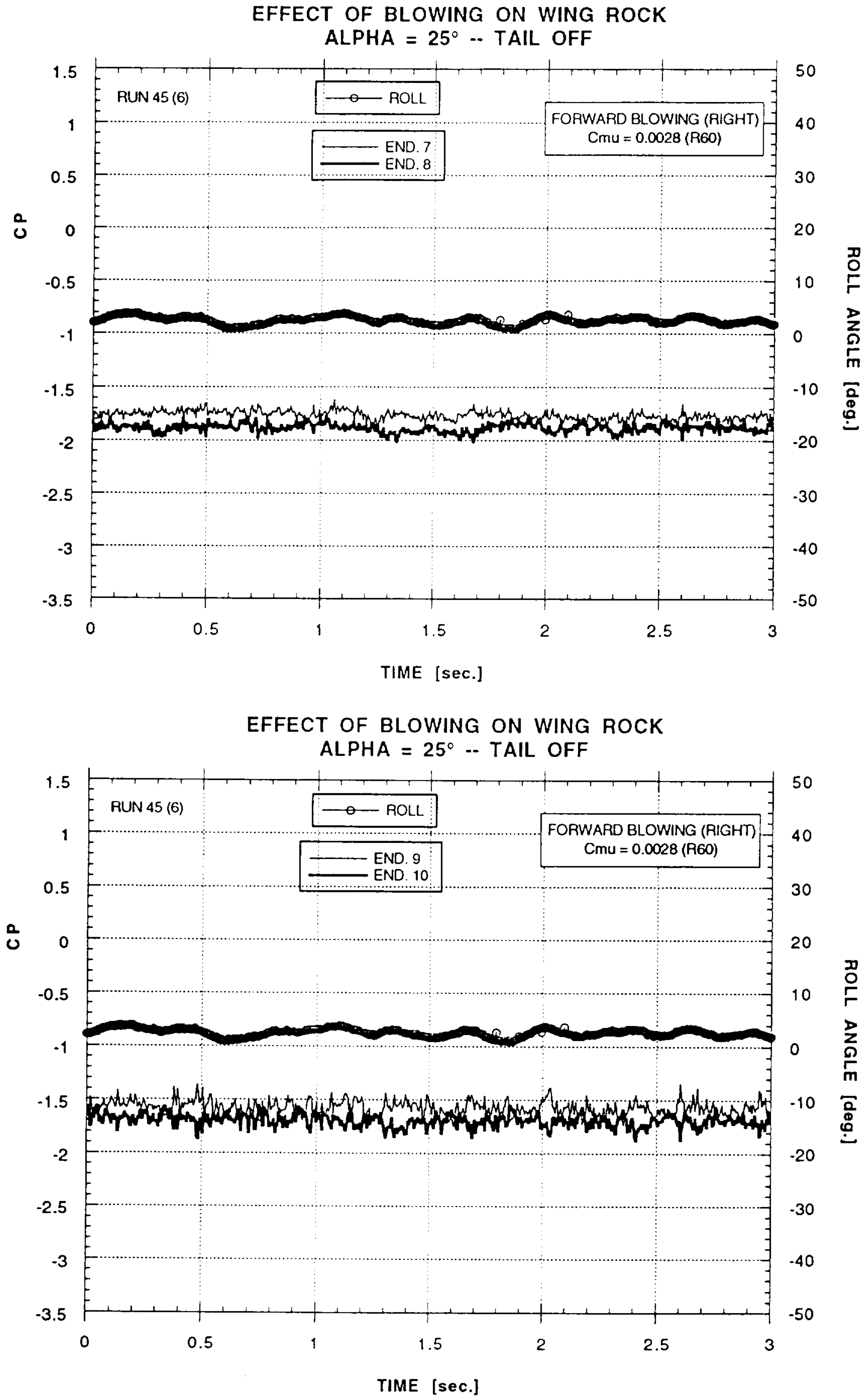

Figure 79 - Concluded

REPORT DOCUMENTATION PAGE

Form Approved
OMB No. 0704-0188

1. AGENCY USE ONLY *(Leave blank)*	**2. REPORT DATE** September 1993	**3. REPORT TYPE AND DATES COVERED** Contractor Report

4. TITLE AND SUBTITLE

Aerodynamic Control of NASP-Type Vehicles Through Vortex Manipulation, Volume III: Wing Rock Experiments

5. FUNDING NUMBERS

NAS2-13196

6. AUTHOR(S)

Carlos Suárez, Brooke C. Smith, Brian R. Kramer, T. Terry Ng, Lih-Yenn Ong, and Gerald N. Malcolm

7. PERFORMING ORGANIZATION NAME(S) AND ADDRESS(ES)

Eidetics International, Inc.
3415 Lomita Blvd.
Torrance, CA 90505

8. PERFORMING ORGANIZATION REPORT NUMBER

A-93138

9. SPONSORING/MONITORING AGENCY NAME(S) AND ADDRESS(ES)

National Aeronautics and Space Administration
Washington, DC 20546-0001

10. SPONSORING/MONITORING AGENCY REPORT NUMBER

NASA CR-177626

11. SUPPLEMENTARY NOTES

Point of Contact: Larry Meyn, Ames Research Center, MS 247-2, Moffett Field, CA 94035-1000
(415) 604-5038

12a. DISTRIBUTION/AVAILABILITY STATEMENT

Unclassified-Unlimited
Subject Category – 02

12b. DISTRIBUTION CODE

13. ABSTRACT *(Maximum 200 words)*

Free-to-roll tests were conducted in water and wind tunnels in an effort to investigate the mechanisms of wing rock on a NASP-type vehicle. The configuration tested consisted of a highly-slender forebody and a 78° swept delta wing. In the water tunnel test, extensive flow visualization was performed and roll angle histories were obtained. In the wind tunnel test, the roll angle, forces and moments, and limited forebody and wing surface pressures were measured during the wing rock motion. A limit cycle oscillation was observed for angles of attack between 22° and 30°. In general, the experiments confirmed that the main flow phenomena responsible for the wing-body-tail wing rock are the interactions between the forebody and the wing vortices. The variation of roll acceleration (determined from the second derivative of the roll angle time history) with roll angle clearly slowed the energy balance necessary to sustain the limit cycle oscillation. Different means of suppressing wing rock by controlling the forebody vortices using small blowing jets were also explored. Steady blowing was found to be capable of suppressing wing rock, but significant vortex asymmetrices are created, causing the model to stop at a non-zero roll angle. On the other hand, alternating pulsed blowing on the left and right sides of the forebody was demonstrated to be a potentially effective means of suppressing wing rock and eliminating large asymmetric moments at high angles of attack.

14. SUBJECT TERMS

Generic hypersonic configuration, Forebody vortex control, Wing rock suppression, Experimental/simulation, Aerodynamic control

15. NUMBER OF PAGES

132

16. PRICE CODE

A07

17. SECURITY CLASSIFICATION OF REPORT Unclassified	**18. SECURITY CLASSIFICATION OF THIS PAGE** Unclassified	**19. SECURITY CLASSIFICATION OF ABSTRACT**	**20. LIMITATION OF ABSTRACT**

NSN 7540-01-280-5500

Standard Form 298 (Rev. 2-89)
Prescribed by ANSI Std. Z39-18
298-102